2024
全球6G技术大会
GLOBAL 6G CONFERENCE

10.0N
6G Near-Field Technologies White Paper

未来移动通信论坛
FUTURE MOBILE COMMUNICATION FORUM

6G Near-Field Technologies White Paper

Consultants

Tiejun Cui (tjcui@seu.edu.cn), Southeast University

Ping Zhang (pzhang@bupt.edu.cn), Beijing University of Posts and Telecommunications

Xiaohu You (xhyu@seu.edu.cn), Southeast University

Yonina Eldar (yonina.eldar@weizmann.ac.il), Weizmann Institute of Science

Editors in Chief

Yajun Zhao (zhao.yajun1@zte.com.cn), ZTE Corporation

Linglong Dai (daill@tsinghua.edu.cn), Tsinghua University

Jianhua Zhang (jhzhang@bupt.edu.cn), Beijing University of Posts and Telecommunications

Chapter Editors

Chongwen Huang (chongwenhuang@zju.edu.cn), Zhejiang University

Yuanwei Liu (yuanwei.liu@qmul.ac.uk), Queen Mary University of London

Yifei Yuan (yuanyifei@chinamobile.com), China Mobile

Contributors ***(*Order by the first letter of names.)***

Ahmed Al Hammadi (ahmed.alhammadi@tii.ae), Technology Innovation Institute

Ahmed Elzanaty (a.elzanaty@surrey.ac.uk), University of Surrey

Ang Chen (chenang1122@mail.ustc.edu.cn), University of Science and Technology of China

Beixiong Zheng(bxzheng@scut.edu.cn), South China University of Technology

Bo Ai (boai@bjtu.edu.cn), Beijing Jiaotong University

Bohao Wang (bohaowang@zju.edu.cn), Zhejiang University

Bokai Xu (20251197@bjtu.edu.cn), Beijing Jiaotong University

Boqun Zhao (boqun1@ualberta.ca), University of Alberta

Boya Di (diboya@pku.edu.cn), Peking University

Chan-Byoung Chae(cbchae@yonsei.ac.kr), Yonsei University

Chau Yuen (chau.yuen@ntu.edu.sg), Nanyang Technological University

Chen Sun (chen.sun@sony.com), SONY China Research Lab

Chen Yang (shijianyc@163.com), Beijing Institute of Technology (Zhuhai)

Chenxi Zhu (zhucx1@lenovo.com), Lenovo Research

Chong Huang (chong.huang@ieee.org), Sun Yat-sen University

Chongjun Ouyang (chongjun.ouyang@ucd.ie), University College Dublin

Chongwen Huang (chongwenhuang@zju.edu.cn), Zhejiang University

Cunhua Pan (c.pan@seu.edu.cn), Southeast University

Dajie Jiang (jiangdajie@vivo.com), vivo Software Technology Co. Ltd.

Daniel Benevides da Costa (danielbcosta@ieee.org), King Fahd University of Petroleum & Minerals

Davide Dardari (davide.dardari@unibo.it), University of Bologna

Deyue Zou (zoudeyue@dlut.edu.cn), Dalian University of Technology

Di Zhang (dr.di.zhang@ieee.org), Zhengzhou University

Dongxuan He (dongxuan_he@bit.edu.cn), Beijing Institute of Technology

Du Pan (pandu@cmdi.chinamobile.com), China Mobile Group Design Institute Co., Ltd.

Ehsan Tohidi (tohidi@tu-berlin.de), Technische Universität Berlin

Emil Björnson(emilbjo@kth.se), KTH Royal Institute of Technology

Fambirai Takawira (Fambirai.takawira@wits.ac.za), University of Witwatersrand

Fan Liu (liuf6@sustech.edu.cn), Southern University of Science and Technology

Fan Zhang (zf22@mails.tsinghua.edu.cn), Tsinghua University

Fang Fang (fang.fang@uwo.ca), Western University

Fang Yang (fangyang@tsinghua.edu.cn), Tsinghua University

Faouzi Bader (carlos-faouzi.bader@tii.ae), Technology Innovation Institute

Feifei Gao (feifeigao@ieee.org), Tsinghua University

Feng Shu (shufeng0101@163.com), Hainan University

Fuwang Dong (dongfw@sustech.edu.cn), Southern University of Science and Technology

Gang Yang (yanggang@uestc.edu.cn), University of Electronic Science and Technology of China

Gaojian Huang (g.huang@hpu.edu.cn), Henan Polytechnic University

Gaojie Chen (gaojie.chen@ieee.org), Sun Yat-sen University

Gaurav Bhargava (gauravbhargav87@gmail.com), National institute of Technology Meghalaya

Gong Tierui (tierui.gong@ntu.edu.sg), Nanyang Technological University

Guiping Lu (344088386@qq.com), Beijing Institute of Technology (Zhuhai)

Güneş Karabulut-Kurt (gunes.kurt@polymtl.ca), Polytechnique Montréal

Haifan Yin (yin@hust.edu.cn), Huazhong University of Science and Technology

Haiquan Lu (haiquanlu@seu.edu.cn), Southeast University

Haixia Liu (hxliu@xidian.edu.cn), Xidian University

Haiyang Miao (hymiao@bupt.edu.cn), Beijing University of Posts and Telecommunications

Haiyang Zhang (haiyang.zhang@njupt.edu.cn),Nanjing University of Posts and Telecommunications

Hao Jiang (jianghao@nuist.edu.cn), Nanjing University of Information Science and Technology.

Hao Lei (19211425@bjtu.edu.cn), Beijing Jiaotong University

Hao Qin (hao.qin@ucdconnect.ie), University College Dublin

Hao Xue(xuehao@xidian.edu.cn), Xidian University

Haris Pervaiz (haris.pervaiz@essex.ac.uk), University of Essex

Hong Ren (hrenw@seu.edu.cn), Southeast University

Hongkang Yu (yu.hongkang@zte.com.cn), ZTE Corporation

Hongliang Luo (luohl23@mails.tsinghua.edu.cn), Tsinghua University

Huizhi Wang (wanghuizhi@seu.edu.cn), Southeast University

Jalil Kazim(Jalil.Kazim@glasgow.ac.uk), University of Glasgow

Ji Wang (jiwang@ccnu.edu.cn), Central China Normal University

Jiachen Tian (tianjiachen@seu.edu.cn), Southeast University

Jian Song (jsong@tsinghua.edu.cn), Tsinghua University

Jianchi Zhu (zhujc@chinatelecom.cn), China Telecom Research Institute

Jianhua Zhang (jhzhang@bupt.edu.cn), Beijing University of Posts and Telecommunications

Jianwu Dou (dou.jianwu@zte.com.cn), ZTE Corporation

Jiapeng Li (lijiapeng2023@mail.sustech.edu.cn), Southern University of Science and Technology

Jiaqi Han (jqhan@xidian.edu.cn), Xidian University

Jiaqi Xu (jiaqi.xu@qmul.ac.uk), Queen Mary University of London

Jiaxue Li (jiaxue_li@gs.zzu.edu.cn), Zhengzhou University/China

Jiayi Zhang (jiayizhang@bjtu.edu.cn), Beijing Jiaotong University

Jiayu Shen (shenjy@zju.edu.cn), Zhejiang University

Jie Hu (hujie@uestc.edu.cn), University of Electronic Science and Technology of China

Jie Feng(eejiefeng@mail.scut.edu.cn), South China University of Technology

Jiguang He (jiguang.he@tii.ae), Technology Innovation Institute

Jintao Wang (wangjintao@tsinghua.edu.cn), Tsinghua University

Josep Miquel Jornet (j.jornet@northeastern.edu), Northeastern University

Jun Du (jundu@tsinghua.edu.cn), Tsinghua University

Jun Liu (cnliujun93@gmail.com),University of Electronic Science and Technology of China

Kai-Kit Wong (kai-kit.wong@ac.ucl.uk), University College London

Kangda Zhi (k.zhi@tu-berlin.de), Technische Universität Berlin

Kun Yang (kun.yang.txyj@vivo.com), vivo Software Technology Co. Ltd.

Kun Yang(kunyang@nju.edu.cn), Nanjing University

Lexi Xu (xulx29@chinaunicom.cn), China Unicom Research Institute & Beijing University of Posts and Telecommunications

Leyi Zhang (leyi.zhang@zte.com.cn), ZTE Corporation

Li Chen (chenli87@ustc.edu.cn), University of Science and Technology of China

Lijuan Dong (donglijuan_2012@163.com), Shanxi Datong University

Linglong Dai (daill@tsinghua.edu.cn), Tsinghua University

Lipeng Zhu (zhulp@nus.edu.sg), National University of Singapore

Liyang Lu (luliyang@mail.tsinghua.edu.cn), Tsinghua University

Long Li (lilong@mail.xidian.edu.cn), Xidian University

Long Zhang (lzhang1224@qq.com), Sun Yat-sen University

Lulu Song (lulu_song@gs.zzu.edu.cn), Zhengzhou University

Marco DI RENZO (marco.di-renzo@universite-paris-saclay.fr), Paris-Saclay University

Mengnan Jian (jian.mengnan@zte.com.cn), ZTE Corporation
Mérouane Debbah (merouane.debbah@ku.ac.ae), Khalifa University of Science and Technology & CentraleSupelec, University Paris-Saclay
Miaowen Wen (eemwwen@scut.edu.cn), South China University of Technology
Mingyao Cui (cui-my16@tsinghua.org.cn), Tsinghua University
Muhammad Ali Imran (Muhammad.lmran@glasgow.ac.uk) , University of Glasgow
Nan Zhang (zhang.nan152@zte.com.cn), ZTE Corporation
Nan Zhao (zhaonan@dlut.edu.cn), Dalian University of Technology
Nanxi Li (linanxi@chinatelecom.cn), China Telecom Research Institute
Navneet Agrawal (navneet.agrawal@tu-berlin.de), Technische Universität Berlin
Neel Kanth Kundu (neelkanth@iitd.ac.in), Indian Institute of Technology Delhi
Nizar Zorba (nizarz@qu.edu.qa), Qatar University
Özlem Tugfe Demir (ozlemtd@kth.se), KTH Royal Institute of Technology
Pan Tang (tangpan27@bupt.edu.cn), Beijing University of Posts and Telecommunications
Pengfei Wang (wangpengfei1121@vivo.com), vivo Software Technology Co. Ltd.
Qammer H. Abbasi (Qammer.abbasi@glasgow.ac.uk), University of Glasgow
Qi Gu (guqi@chinamobile.com), China Mobile
Qi Zhang (zhang.qi33@zte.com.cn), ZTE Corporation
Qiang Feng (qfeng@xidian.edu.cn), Xidian University
Qingqing Wu (qingqingwu@sjtu.edu.cn), Shanghai Jiao Tong University
Qingxiao Huang (377145470@qq.com), University of Electronic Science and Technology of China
Qiuyan Liu (liuqy92@chinaunicom.cn), China Unicom
Qu Luo (q.u.luo@surrey.ac.uk), University of Surrey
Qurrat-Ul-Ain Nadeem (qurrat.nadeem@nyu.edu), New York University (NYU) Abu Dhabi and NYU Tandon
Ran Ji (ranji@zju.edu.cn), Zhejiang University
Ritao Cheng (chengritao@cmdi.chinamobile.com), China Mobile Group Design Institute Co., Ltd.
Robert W. Heath Jr (rwheathjr@ucsd.edu), University of California
Robert W. Heath Jr. (rwheathjr@ucsd.edu), University of California
Rui Zhang (rzhang@cuhk.edu.cn), The Chinese University of Hong Kong, Shenzhen / National University of Singapore
Ruiqi (Richie) Liu (richie.leo@zte.com.cn), ZTE Corporation
Ruirui Sun (sunrr@seu.edu.cn), Southeast University
Saber Hassouna (s.hassouna.1@research.gla.ac.uk), University of Glasgow
Shan Wang(wang.shan40@zte.com.cn), ZTE Corporation
Shaohua Yue (yueshaohua@pku.edu.cn), Peking University
Shengheng Liu (s.liu@seu.edu.cn), Southeast University
Shi Jin (jinshi@seu.edu.cn), Southeast University
Shihang Lu (lush2021@mail.sustech.edu.cn), Southern University of Science and Technology
Shiru Duan (duanshiru822@qq.com), Beijing Information Science and Technology University.
Shuang Zheng (zheng.shuang@zte.com.cn), ZTE Corporation
Shubhankar Majumdar (shubuit@gmail.com), National institute of Technology Meghalaya
Shupei Zhang (zhangshupei@pku.edu.cn), Peking University
Sicong Liu (liusc@xmu.edu.cn), Xiamen University
Sławomir Stańczak, (slawomir.stanczak@tu-berlin.de), Technische Universität Berlin
Songtao Gao (gaosongtao@cmdi.chinamobile.com), China Mobile Group Design Institute Co., Ltd.
Syed Tariq Shah (syed.shah@essex.ac.uk), University of Essex
Tianqi Mao (maotq@bit.edu.cn), Beijing Institute of Technology
Tiantian Ma(mitiantianma@mail.scut.edu.cn), South China University of Technology
Tianwei Hou (twhou@bjtu.edu.cn), Beijing Jiaotong University
Tingting Fan (Emme.Fan@sony.com), SONY China Research Lab
Victor Monzon Baeza (vmonzon@uoc.edu), Universitat Oberta de Catalunya
Wahab Almuhtadi (almuhtadi@ieee.org), Algonquin College
Wang Liu (w_liu@seu.edu.cn), Southeast University
Wanming Hao (iewmhao@zzu.edu.cn), Zhengzhou University
Wei E.I. Sha (weisha@zju.edu.cn), Zhejiang University
Wei Li (l_wei@ntu.edu.sg), Nanyang Technological University

Weidong Hu (hoowind@bit.edu.cn), Beijing Institute of Technology

Weidong Li (weidongli@hust.edu.cn), Huazhong University of Science and Technology

Weihua Yu (ywhbit@bit.edu.cn), Beijing Institute of Technology/BIT Chongqing Institute of Microelectronics and Microsystems

Wenjie Hou (byhhwj@163.com), Beijing Institute of Technology (Zhuhai)

Wenyan Ma (wenyan@u.nus.edu), National University of Singapore

Xiang Li (lix@docomolabs-beijing.com.cn), DOCOMO Beijing Labs

Xianjun Yang (yangxianjun@cictmobile.com),CICT Mobile Communication Technology Co., Ltd.

Xiaolin Hou (hou@docomolabs-beijing.com.cn), DOCOMO Beijing Labs

Xiaowen Tian (xtian8@ncsu.edu), North Carolina State University

Xidong Mu (xidong.mu@qmul.ac.uk), Queen Mary University of London

Xin Su (suxin@chinamobile.com), China Mobile

Xin Su (suxin@cictmobile.com), CICT Mobile Communication Technology Co., Ltd.

Xin Wang (wangxin01@stu.xidian.edu.cn), Xidian University

Xing Zhang (xing_zhang@njupt.edu.cn), Nanjing University of Posts and Telecommunications

Xingqi Zhang (xingqi.zhang@ualberta.ca), University of Alberta

Xingwang Li (lixingwang@hpu.edu.cn), Henen Polytechnic University

Xinrui Li (xinrui_li@seu.edu.cn), Southeast University

Xinwei Yue (xinwei.yue@bistu.edu.cn), Beijing Information Science and Technology University

Xinyu Xie (xinyuxie@sjtu.edu.cn), Shanghai Jiao Tong University

Xiyuan Liu (1910670@tongji.edu.cn), Tongji University

Xu Shi (shi-x19@mails.tsinghua.edu.cn), Tsinghua University

Xue Xiong(ftxuexiong@mail.scut.edu.cn), South China University of Technology

Xuehua Li (lixuehua@bistu.edu.cn), Beijing Information Science and Technology University

Xuesong Cai (xuesong.cai@eit.lth.se), Lund University

Xusheng Zhu (xushengzhu@sjtu.edu.cn), Shanghai Jiao Tong University

Yajun Zhao (zhao.yajun1@zte.com.cn), ZTE Corporation

Yan Gao (3220221590@bit.edu.cn), Beijing Institute of Technology

Yan Shi (yanshi@mail.xidian.edu.cn), Xidian University

Yang Zhang (y_zhang@seu.edu.cn), Southeast University

Yanxia Cao (caoyx28@chinaunicom.cn), China Unicom

Yasheng Jin (yashengjin@seu.edu.cn), Southeast University

Yifan Li (liyifan97@foxmail.com), Nanjing University of Science and Technology

Yifei Yuan (yuanyifei@chinamobile.com), China Mobile

Yiming Yu (yuyiming@cmdi.chinamobile.com), China Mobile Group Design Institute Co., Ltd.

Ying Gao (yinggao@sjtu.edu.cn), Shanghai Jiao Tong University

Yiwei Sun (sunyiweiyjy@chinamobile.com), China Mobile

Yizhe Zhao (yzzhao@uestc.edu.cn), University of Electronic Science and Technology of China

Yong Zeng (yong_zeng@seu.edu.cn), Southeast University

Yongpeng Wu (yongpeng.wu@sjtu.edu.cn), Shanghai Jiao Tong University

Yonina Eldar (yonina.eldar@weizmann.ac.il), Weizmann Institute of Science

You Changsheng (youcs@sustech.edu.cn), Southern University of Science and Technology

Yu Han (hanyu@seu.edu.cn), Southeast University

Yu Lu (y-lu19@mails.tsinghua.edu.cn), Tsinghua University

Yuan Xu (yuan_xu@zju.edu.cn), Zhejiang University

Yuanbin Chen (chen_yuanbin@163.com), Beijing University of Posts and Telecommunications

Yuanwei Liu (yuanwei.liu@qmul.ac.uk), Queen Mary University of London

Yuexia Zhang (zhangyuexia@bistu.edu.cn), Beijing Information Science and Technology University

Yuhua Jiang (jiangyh20@mails.tsinghua.edu.cn), Tsinghua University

Yuming Bai (bym@bit.edu.cn), Beijing Institute of Technology

Yunqi Sun (sun.yunqi@zte.com.cn), ZTE Corporation

Yutong Zhang (yutongzhang@pku.edu.cn), Peking University

Zhaohui Yang (yang_zhaohui@zju.edu.cn), Zhejiang University

Zhaolin Wang (zhaolin.wang@qmul.ac.uk), Queen Mary University of London
Zhaoyang Zhang (zhzy@zju.edu.cn), Zhejiang University
Zhe Wang (zhewang_77@bjtu.edu.cn), Beijing Jiaotong University
Zhen Gao(gaozhen16@bit.edu.cn), Beijing Institute of Technology
Zheng Li (stones_li@outlook.com), Zhengzhou University
Zhengyu Zhu (iezyzhu@zzu.edu.cn), Zhengzhou University
Zhenqiao Cheng (chengzq@chinatelecom.cn), China Telecom Research Institute
Zhiguo Ding (zhiguo.ding@ieee.org), Khalifa University
Zhiqiang Yuan (yuanzhiqiang@bupt.edu.cn), Beijing University of Posts and Telecommunications
Zhuo Xu (xz23@mails.tsinghua.edu.cn), Tsinghua University
Zidong Wu (wuzd19@mails.tsinghua.edu.cn), Tsinghua University

---

Citation: Y. J. Zhao, L. L. Dai, J. H. Zhang, et al. "6G Near-field Technologies White Paper," FuTURE Forum, Nanjing, China, Apr 2024. doi: 10.12142/FuTURE.202404002.

Acknowledgement

This white paper has been written by an international expert group, led by FuTURE Forum, within a series of 6G white papers.

Abstract

In the context of rapidly advancing 5G wireless network commercialization, there has been a concurrent intensification in the research and development of 6G wireless networks. These networks are envisioned to surpass their predecessors with more ambitious objectives and elevated performance benchmarks. Traditional wireless networks, spanning from 1G to 5G, predominantly utilize the spectrum below 6 GHz bands. This spectrum range, constrained by physical array dimensions and wavelength, typically incorporates not so many antennas, thereby limiting the range of the radiative near-field to a few meters or even centimeters. However, 6G networks are breaking these boundaries by employing larger antenna apertures and exploring higher frequency bands, such as new mid-frequency, millimeter wave and terahertz bands. This shift enhances the prominence of near-field characteristics. The integration of cutting-edge technologies such as reconfigurable intelligent surface (RIS), extremely large aperture arrays (ELAA), movable antenna (MA), and cell-free networks will further expand the near-field range and construct an almost ubiquitous near-field propagation environment in future wireless networks.

From a spatial resource utilization standpoint, while traditional far-field systems can only separate signals in the angular domain, the shift to near-field operation adds the ability to exploit the depth domain in wireless communications. The near-field technology with many antennas is gaining traction for its potential to deliver higher data rates, precise angle-depth localization and sensing, and efficient wireless energy transfer through beamfocusing in 6G networks. The research in near-field technology indicates a paradigm shift in the propagation characteristics of electromagnetic waves. These waves can no longer be simply regarded as plane waves. They should be accurately modeled as spherical waves, making previously negligible electromagnetic phenomena such as spatial non-stationarity, finite-depth beamfocusing, tri-polarization, and evanescent waves important to consider for model and system design. In addition, totally new wavefronts such as self-healing Bessel beams or curving Airy beams become available. Traditional communication algorithms tailored for far-field conditions experience performance degradation in the 6G near-field context, while model-agnostic algorithms fail to exploit these new characteristics fully.

This white paper commences with the foundational definition of near-field in electromagnetic theory, delving into the root causes of near-field electromagnetic effects and their implications for existing communication systems. It thoroughly examines the influence of near-field effects on system design and performance, focusing particularly on the two critical metrics, the degree of freedom and capacity. Understanding channel characteristics and models is vital for the design of communication systems. Therefore, this white paper discusses near-field channel research from the angles of measurement and modeling and explores near-field transmission technologies such as channel estimation, beamforming, and codebook design. Additionally, it addresses the synergy between near-field technology and other domains, such as integrated sensing and communication, wireless power transfer, and physical layer security. The white paper's aim is to offer a comprehensive and systematic overview of near-field technology, fostering further research and development in this emerging field.

Table of Contents

List of Figure

1 Introduction

As the commercialization of 5G wireless networks gains momentum, there is a growing emphasis on exploratory research into the upcoming 6G wireless networks. This era of technological advancement sees 6G networks characterized by a more visionary and performance-driven ethos compared to their predecessors. Traditional wireless networks, spanning from 1G to 5G, predominantly operate within a spectrum below 6 GHz, often below 3 GHz. Due to the physical constraints on antenna arrays and the proportional relationship between element spacing and wavelength, these spectrum bands necessitate the use of relatively small numbers of antennas. Consequently, the combined effect of these lower-dimensional antenna arrays and lower frequency bands confines the range of wireless near-field communication to mere meters or even centimeters, thereby shaping the design of these systems around far-field assumptions.

However, the transition to 6G networks is marked by the adoption of larger antenna apertures and higher frequency bands, such as new mid frequency, millimeter wave, and terahertz bands, which accentuate near-field characteristics, as shown in Table 1.1. The integration of emerging technologies such as Reconfigurable Intelligent Surface (RIS)[1][2][3], extremely large aperture arrays (ELAA)[4], movable antenna (MA)[5] and cell-free networks[6] is expected to amplify the prevalence of the near-field scenario in future wireless networks. This shift challenges traditional far-field plane wave assumptions and underscores the need to rethink strategies for spatial resource utilization[7]. While conventional systems have effectively exploited far-field spatial resources, the exploration and utilization of near-field spatial resources in 6G networks promise to introduce novel physical dimensions to wireless communication systems. This shift towards near-field regions in 6G networks catalyzes a new wave of research in near-field technology paradigms.

Table 1.1 Near field range of typical scenarios (Rayleigh distance)

D *f*	2.6 GHz (low band)	7 GHz (Mid band)	28 GHz (mmWave band)	220 GHz (THz band)
0.5m	**4 m**	12 m	48	372
1.6m	60 m	**119 m**	476	/
3.0m	210 m	420 m	/	/

In the realm of near-field technology, the nuanced propagation behaviors of electromagnetic waves necessitate a departure from plane wave approximations to embrace spherical wave treatments. This paradigm shift brings forth a plethora of hitherto overlooked electromagnetic phenomena, including spatial non-stationarity, tri-polarization, evanescent waves, and the capacity for near-field focusing, all of which pose challenges to the efficacy of traditional communication algorithms within the context of 6G's near-field environment.

Harnessing near-field effects holds the promise of better realizing a broader range of application scenarios and key performance indicators outlined in IMT-2030. This article comprehensively explores potential application scenarios based on near-field technology, as shown in Fig. 1.1.

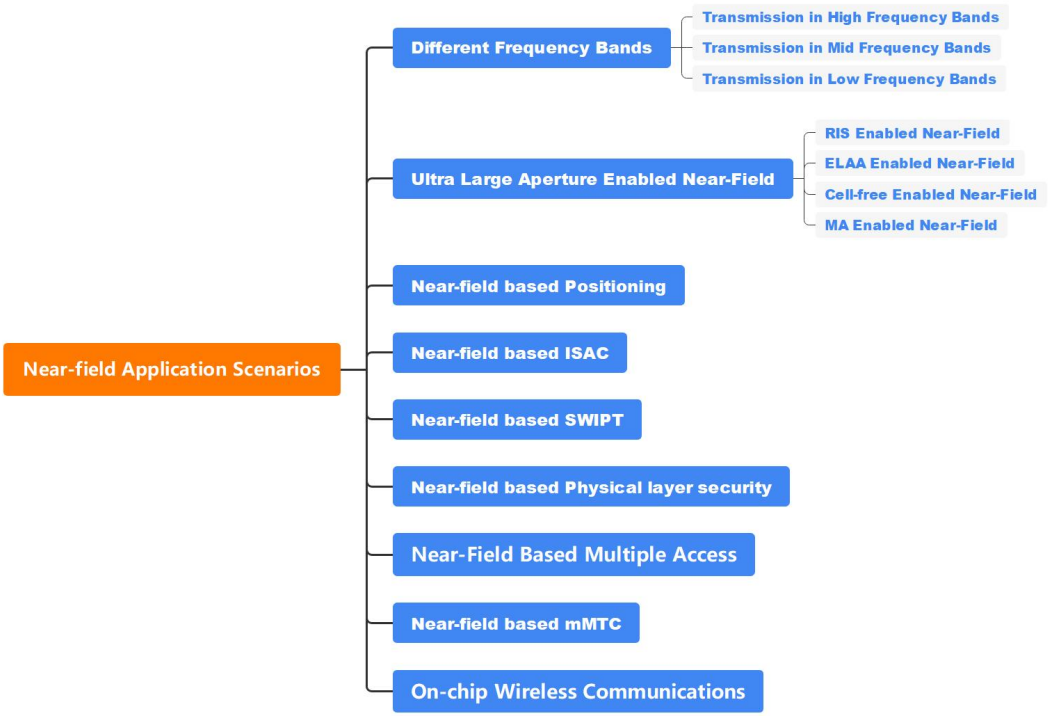

Fig. 1.1 Near-field Application Scenarios

Through meticulous examination of both theoretical foundations and technological advancements, we have meticulously crafted a preliminary framework for near-field technology, as illustrated in Fig. 1.2. Our discourse commences with an exploration of the definition of near-field in electromagnetic theory, tracing the origins of near-field electromagnetic effects and their ramifications on existing communication systems. Drawing upon an extensive body of literature, we provide an encompassing synthesis of near-field effects on communication system design and performance, with particular emphasis on degrees of freedom and communication capacity.

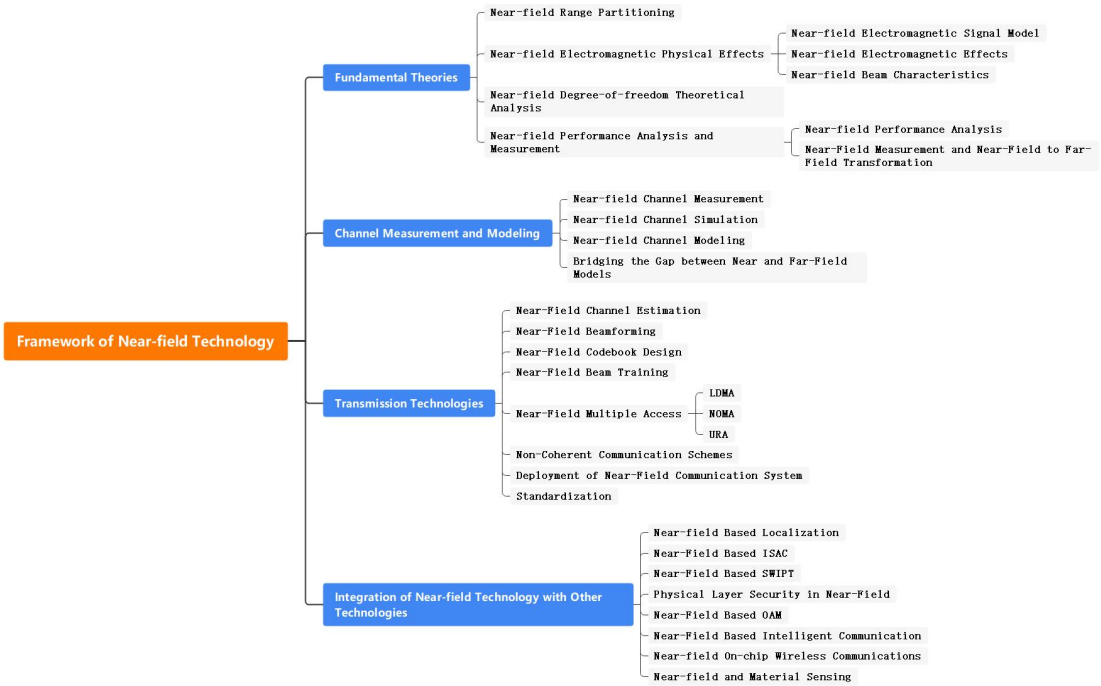

Fig. 1.2 Framework of Near-field Technology

A nuanced comprehension of near-field channel characteristics and models is pivotal for communication system design and evaluation. Thus, our article underscores the imperative for exhaustive channel measurements and precise channel characterization. Furthermore, we delve into near-field transmission technologies, encompassing facets such as channel estimation, beamforming, codebook design, beam training, multiple access technology, system architecture, deployment considerations, and implications for standardization. Additionally, we explore the convergence of near-field technology with other domains, including positioning, wireless power transfer, physical layer security, orbital angular momentum-based near-field, AI-driven communication, and Near-field On-chip Wireless Communications.

Despite notable advancements in the research on near-field propagation characteristics, a dearth of literature offers a systematic synthesis of near-field technology. Therefore, this article endeavors to bridge this gap by furnishing an all-encompassing summary of near-field technology's application scenarios, fundamental theories, channel measurement and modeling methodologies, transmission technologies, and integration with allied fields. Our overarching aim is to cultivate and propel the advancement of near-field technology research.

2 Near-field Application Scenarios

In November 2023, the International Telecommunication Union's 5D Working Group on Wireless Communications (ITU-R WP5D) released a framework and overall goal proposal for the development of IMT towards 2030 and the future , proposing typical 6G scenarios and capability indicator systems, as shown in Fig. 2.1 [1][8]. 6G scenarios include immersive communication, ultra large-scale connections, extremely high reliability and low latency, artificial intelligence and communication, integration of perception and communication, ubiquitous connections, etc. The key 6G capability indicators include 9 enhanced 5G capabilities and 6 new capability dimensions, including peak data rate, user experienced data rate, spectrum efficiency, regional traffic, connection density, mobility, latency, reliability, security privacy elasticity, coverage, sensing related indicators, applicable AI related indicators, sustainability and positioning [9]. 6G is expected to continue the efforts of 5G advanced in terms of keeping enhancing connection experiences for mobile users and enabling more vertical industries [10].

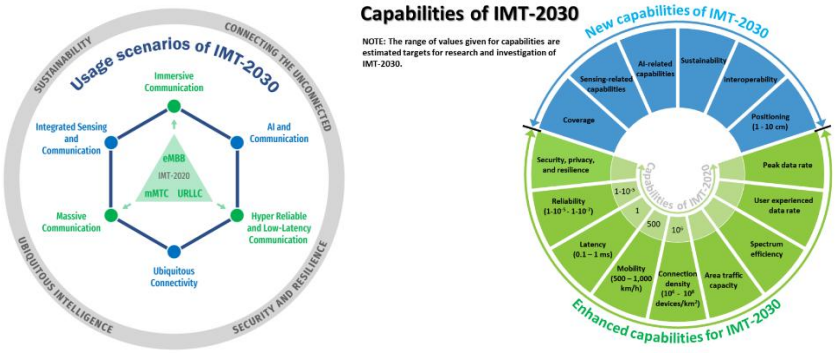

Fig. 2.1 IMT-2030 application scenarios and key capability indicators[1]

To meet the spectral efficiency requirements of IMT-2030, it is necessary to further explore the application potential of higher frequency bands and larger scale arrays. Simultaneously, the ultra large-scale arrays in higher frequency bands will bring near-field effects. The so-called near-field effect refers to the situation where, under certain distance conditions, the assumption of electromagnetic waves as plane waves in the far-field no longer holds and needs to be modeled as spherical wave. The spherical wavefront carries not only angle information, but also depth information. The electromagnetic beam focusing happens simultaneously in both the angle and depth domains, forming near-field beam focusing [11]. By utilizing the near-field effect, more application scenarios and key performance indicators of IMT-2030 can be better achieved, such as the integration of perception and communication, positioning, security, mobility, etc. This section will explain the application scenarios of near field based on the above analysis.

2.1 Near-field in Different Frequency Bands

The expansion of bandwidth and the increase of antennas will bring greater capacity and higher spectral efficiency to wireless communication systems. Typical 2G, 3G, 4G, and 5G communication systems use bandwidths of 0.2 MHz, 5 MHz, 20 MHz, and 100 MHz, respectively, and larger bandwidths will be required for 6G in the future.

In May 2023, China's Ministry of Industry and Information Technology (MIIT) issued a new version of the Regulations of the People's Republic of China on the Division of Radio Frequencies (MIIT Decree No. 62), which is the first in the world to use all or part of the bandwidth of the 6425-7125 MHz frequency band, totaling 700 MHz, for the 5G-A/6G system [12]. In December of the same year, the International Telecommunication Union (ITU) held the World Radiocommunication Conference 2023 (WRC-23) in Dubai, UAE, and completed a new round of revisions to the Radio Rules, newly dividing 6G spectrum resources in the mid-band of 6425-7125 MHz with a total of 700 MHz of bandwidth for most of the countries in the world [13]. In December 2023, the international standardization organization, 3GPP, held its Edinburgh, UK meeting, in which the first projects for Rel-19, the second version of the 5G-Advanced standard, including eight areas such as channel modeling studies for the new 7-24 GHz spectrum are established [14]. As reported in study of 6G mid band frequency by Nokia, a new spectrum ranges: 4.400–4.800 GHz, 7.125–8.400 GHz and 14.800–15.350 GHz are potentially available for 6G, subject to further study in the WRC-27 cycle [15]. The report also highlights about a US spectrum pipeline outside the WRC process concerning the lower 3 GHz band (3.100–3.450 GHz), which is being considered for shared use with military radar, and the 12.7 GHz band (12.700–13.250 GHz), which will be exclusively used for licensed mobile broadband.

Compared to the sub-6 GHz low-frequency band, which is widely used in 5G, and the high-frequency bands, such as millimeter wave and terahertz, which may be used in 6G in the future, the mid-frequency band, which combines the advantages of both coverage and capacity, is of great value for the wide-area high-capacity coverage of 6G, and it is expected to be one of the fundamental frequency bands for 6G, as shown in **Fig. 2.2**.

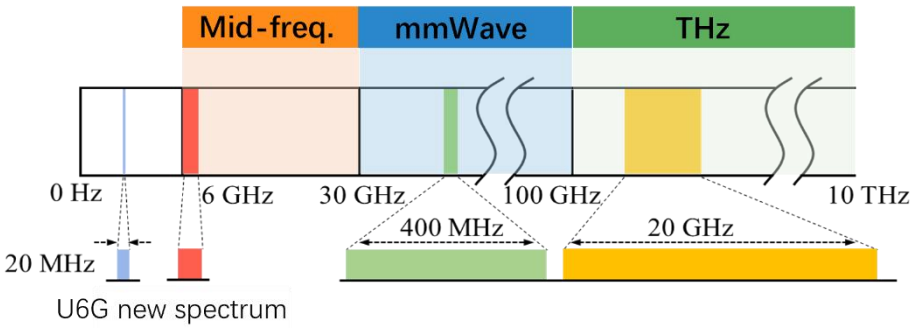

Fig. 2.2 Full spectrum of high, medium and low bands for the future 6G

In the future, 6G high, medium, and low frequency bands are likely to face near-field communication. 6G Technologies, a research report published by the 6G Alliance in June 2022, also clearly points out the necessity of researching near-field in 6G high, medium, and low frequency bands [15].

2.1.1 High Frequency Band Transmission

Millimeter wave (mmWave) and terahertz (THz) wireless communication can utilize large available bandwidth to improve data transmission rates, making it one of the key technologies for the next generation of communication systems [16][17][18]. In order to compensate for the path loss of high-frequency transmission, base stations (BS) operating on these frequency bands will be equipped with large-scale antenna arrays. The application of large-scale antenna arrays will increase the possibility that the users in high-frequency communication falling into the near-field region, while

traditional wireless systems typically operating in the far-field range. Under millimeter wave and terahertz conditions, the near-field distance of relatively small antennas/surfaces can also reach several tens of meters. For example, the near-field distance of a uniform linear array with 128 antennas working at 300 GHz would be 65 meters, which covers a relatively large area. Namely, the far-field plane wave assumption on electromagnetic fields is no longer applicable at actual communications distances. Thus, a near-field model of spherical waves should be used. The management of spherical wavefront can be transformed into flexible beamforming ability. For example, utilizing the spherical wavefront can focus the electromagnetic waves into a spot rather than traditional beam steering under far-field condition, which is referred as the concept of beam focusing in recent literature[19]. Beam focusing can support multiple orthogonal links even at similar angles.

The ability to focus beams in large-scale multiple input multiple output (MIMO) systems largely depends on the signal processing capability of the antenna array, with different processing capabilities in different architectures. The most flexible solution for a given radiation element array is full-digital architecture, where each antenna element is connected to a dedicated radio frequency (RF) chain. Under this architecture, the transceiver can simultaneously control infinite beams in multiple directions, greatly improving spatial flexibility. However, when deploying large-scale arrays in 5G and more advanced communication systems, implementing full-digital architectures becomes extremely challenging due to increased costs and power consumption. To alleviate this, large-scale MIMO communications adopt a hybrid analog-digital architecture. This hybrid architecture combines low dimensional digital processing and high-dimensional analog precoding, typically achieved through phase shifter interconnections, resulting in fewer RF links than antenna components. Another emerging technology for effectively implementing large-scale arrays is dynamic meta-surface antennas, which can programmatically control the transmit/receive beam patterns, provide advanced analog signal processing capabilities, and naturally achieve frequency chain reduction without the use of dedicated analog circuits. This also densifies antenna components, thereby improving focusing performance. Reference[20] explores multi-user communications in near-field utilizing various antenna architectures, including all digital arrays, hybrid architectures based on phase shifters, and dynamic meta-surface antennas, as well as the impact on downlink multi-user systems when forming focused beams.

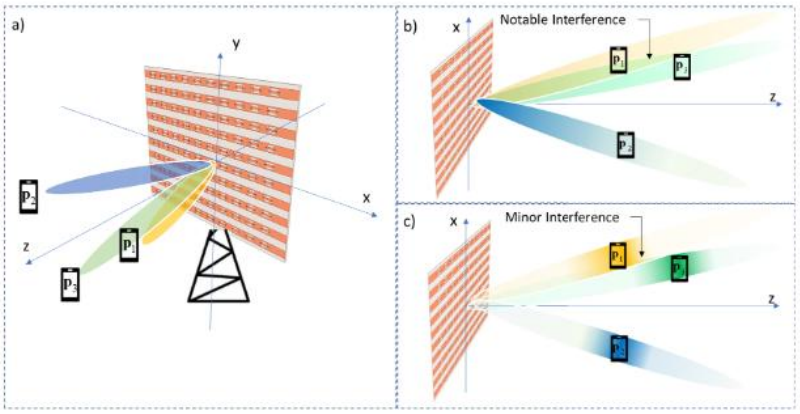

Fig. 2.3 Multi user near-field communication with beams pointing to each user

(a) towards each user in three-dimensional space; (b) beam steering in far-field, leads to interference between users at the same angle; (c) beam focusing in near-field, with minimal interference[20]

In addition, new types of wavefronts become available beyond spherical waves when operating in the near field[21]. By wavefront, we refer to the imaginary surface representing all points in a wave that are in the same phase at a given time. Among others, the use of Bessel beams has been recently proposed[22][23]. Bessel beams are no-diverging beams that focus the signal along a line. To generate an ideal Bessel beam, one would need an infinite aperture (i.e., an infinite lens or antenna array or reflect-array). When using a finite aperture, the Bessel beam only exist until a maximum distance delimited in the near-field. Focusing the power along a line, instead than on a point, can drastically reduce the amount of channel state information to ensure the reliable transmission of information. Moreover, Bessel beams are self-healing, i.e., even when they are partially blocked, the signal is regenerated to the original level after the obstacle [24][25]. This can be leveraged to overcome blockage, which is one of the main problems for high-frequency systems. Another type of non-conventional wavefronts that can be generated in the near field are Airy beams [26]. These are also non-diffracting beams that, in this case, focus along a curving line. This allows for example to circumvent obstacles (See Fig. 2.4).

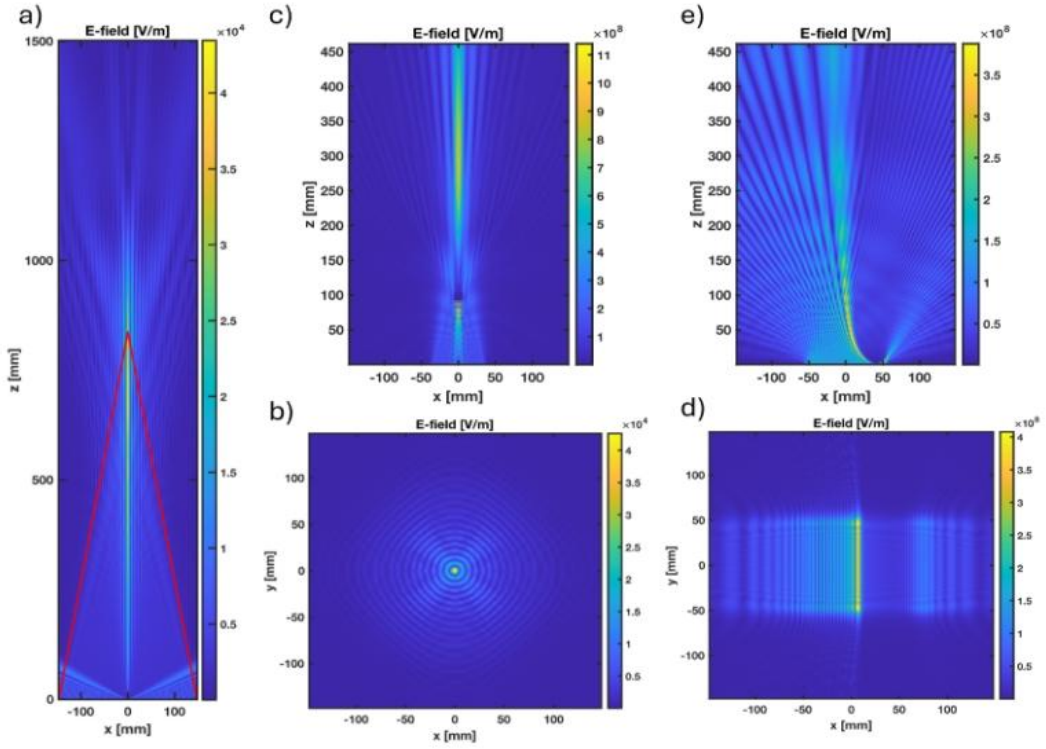

Fig. 2.4 Non-diffracting beams to circumvent obstacles
a) Illustration of a Bessel beam, focusing a long a line in the near field; b) Phase distribution of a Bessel beam; c) Bessel beam regeneration after an obstacle; d) Phase distribution of an Airy beam; e) A curving Airy beam.

Traditionally, Bessel beams and Airy beams have been generated at optical frequencies and utilizing different types of lenses. For example, axicons are utilized to generate Bessel beams. Nevertheless, these wavefronts can be generated utilizing arrays, reflect-arrays and meta-surfaces[27] with a large number of elements[28][29] at least phase control per element. Operating with new types of wavefronts drastically changes many well-known concepts [30], including the study of interference

across different type of beams, channel state information estimation, joint ultrabroadband waveform and wavefront design [28], and even physical layer security[31].

2.1.2 Mid Frequency Band Transmission

In September 2020, the Third Generation Partner Program (3GPP) completed the approval of the 6 GHz licensed frequency band, initiated the standardization of mid frequency band RF. Then, 3GPP successfully completed the standardization of the 6425-7125 MHz licensed frequency band in September 2022. Subsequently in December 2023, 3GPP further listed channel modeling in the 7-24 GHz mid frequency band as one of the earliest standard topics in the second standard version of 5G-Advance, continuing promoting the standardization process of the mid frequency band. At the same time, in May 2023, the Ministry of Industry and Information Technology of China issued a new version of the "Regulations on the Classification of Radio Frequency in the People's Republic of China", which clearly divides the 6 GHz mid frequency band for 5G/6G mobile communication systems. The 6 GHz frequency band has a continuous large bandwidth of 1200 MHz, which has lower propagation path loss and stronger coverage ability compared to the high-frequency band. It has both coverage and capacity advantages and can be used for wide area high-capacity coverage in 6G communication. Therefore, the mid frequency spectrum resources will become one of the important alternative frequency bands for 6G communication.

Compared to the sub-6 GHz frequency band of 5G communication, the increase in communication frequency leads to weaker coverage due to large propagation losses in materials and smaller antennas in mid frequency centimeter wave communication. In order to compensate for the high path loss during the propagation of intermediate frequency signals, the antenna size of intermediate frequency base stations needs to be further increased. With the increase of communication frequency band and base station antenna array aperture, the near-field range of intermediate frequency communication will also be significantly expanded. Taking the 7 GHz communication system and base station with 1.6-meter antenna array as an example, its near-field range exceeds 100 meters. In the formal project of the 3GPP intermediate frequency channel modeling standard, near-field characteristics and spatial non-stationary characteristics are considered as new characteristics of mid frequency channels, becoming important considerations for improving the 3GPP channel model [14]. Therefore, near-field spherical wave communication will become an important scenario for mid frequency transmission.

Due to the shorter wavelength of mid frequency centimeter waves and the further increase in antenna size, mid frequency system is more likely to form high-resolution narrow spatial beams, therefore achieving higher spatial degrees of freedom. Typical application scenarios for this band include single user multi-stream or higher-order multi-user multiplexing scenarios. The modeling and measurement of near-field spherical wave channels in the mid frequency range will provide a channel model foundation for mid frequency communication. The near-field spherical wave propagation model is expected to provide additional single user transmission spatial freedom. The focusing characteristics of near-field spherical waves can also be used for high-order multi-user multiplexing methods, further improving the throughput performance of 6G new mid frequency communication systems.

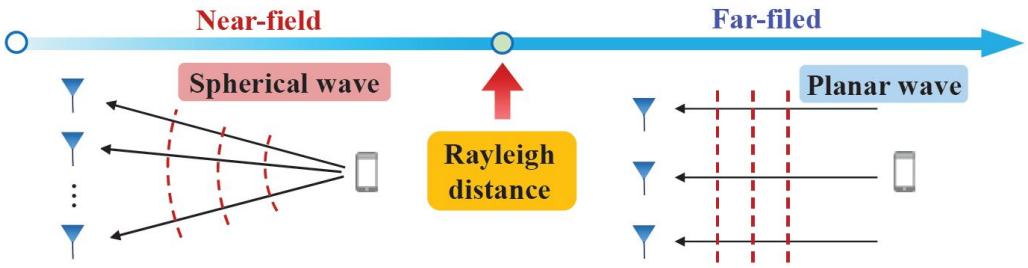

Fig. 2.5 An illustration for near field communication feature

For users located in the near field region, spherical wavefronts are utilized for communication compared to plane wavefronts in the far field region.[32]

2.1.3 Low Frequency Band Transmission

The low frequency band (FR1, Sub-6GHz) defines the baseline coverage range of cellular networks. While expanding to higher frequency bands, 6G will also fully utilize the advantages of FR1 frequency band for wide coverage and deep penetration to improve spectrum efficiency and break through bandwidth bottlenecks. Large scale MIMO can be used in the low frequency range to improve the spectral and energy efficiency of 6G systems while ensuring wide coverage.

If traditional large-scale MIMO is deployed in the low frequency range, it will face limitations on antenna size due to tower or base station deployment. Modular or distributed large-scale MIMO, as well as meta-surface antennas, are expected to overcome size limitations and reduce the requirement of half wavelength distance between antenna units through compact antenna arrays. On the other hand, traditional cell-based deployment strategies pose challenges such as feasibility, processing, and architectural complexity. Therefore, large-scale MIMO in the low frequency range may adopt multi panel, multi transceiver nodes, non-cellular, and irregular large-scale distributed network deployment. In this scenario, further research is needed on distributed deployment strategies, the potential demand for new channel models from non-uniform antenna panels, large antenna arrays, and near-field effects when users may approach access points. Also, research that focuses on exploring efficient reference signal designs, channel acquisition frameworks for far-field and near-field channels, further evaluating the potential of artificial intelligence in channel acquisition would be valuable.

2.2 Ultra Large Aperture Enabled Near-field

2.2.1 RIS Enabled Near-field

Reconfigurable Intelligent Surface (RIS) is considered as one of the key potential technologies in 6G, consisting of a large number of low-cost reconfigurable units [33]. Deploying RIS in wireless networks can effectively adjust the wireless channel between transmitters and receivers, thereby improving communication quality and coverage range, as already demonstrated by field trials [34]. One of the typical applications of RIS technology is to obtain sufficient beamforming gain through hundreds or even thousands of components for coverage blinding in millimeter wave and terahertz communications. The larger RIS array and higher operating frequency further expand the near-field area of RIS assisted communication links [35]. RIS is typically used to establish a direct connection channel between transmitters/receivers. In the far-field region, the rank of the channel is usually small, which restricts the spatial multiplexing gain of the channel. On the other hand, due to the nonlinear

changes in signal amplitude and phase caused by spherical waves, near-field channels have better rank conditions, which can effectively improve the multiplexing gain and spatial freedom of the system [36]. When users are located in the radiation near-field region, even if multiple users are at the same radiation angle, different near-field codebooks can be configured on the intelligent meta-surface to reduce co-channel interference through beam focusing, supporting multiple coexisting orthogonal links to achieve space division multiple access [37], as shown in Fig. 2.6. Similarly, the degrees of freedom provided by the spherical wavefront and the near-field radiation wave carrying both angle and distance information further enhances the accuracy of wireless positioning services and perception, as shown in Fig. 2.7 . On the other hand, this also means that the spatial non-stationarity of the channel is intensified, which will bring challenges to channel estimation, codebook design, beam training complexity, mobility management, signaling design, and other aspects.

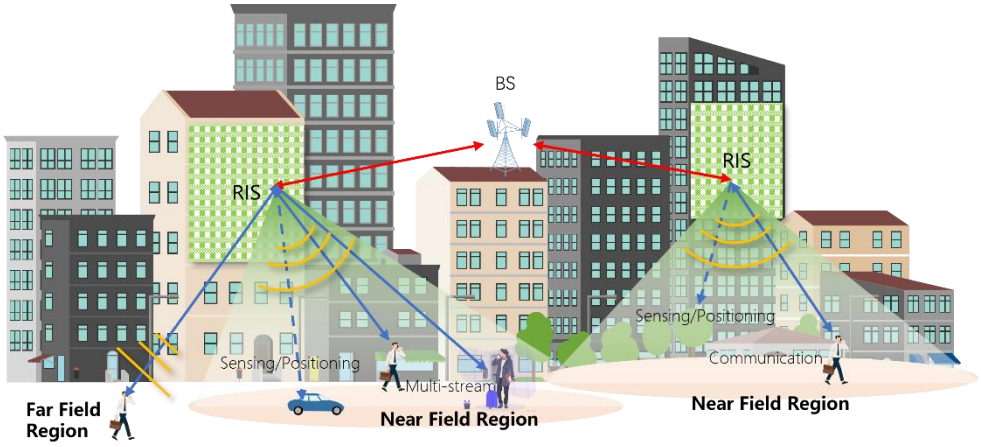

Fig. 2.6 RIS assisted near-field application scenarios.

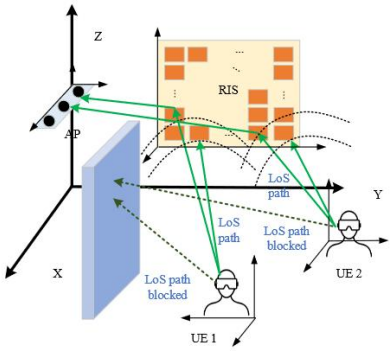

Fig. 2.7 Near field positioning model[38]

2.2.2 ELAA Enabled Near-field

Extremely Large Aperture Array (ELAA) is essential to the candidate technologies for 6G such as Extremely Large-Scale MIMO (XL-MIMO). Compared to 5G massive MIMO, ELAA for 6G not only means a sharp increase in the number of antennas but also results in a fundamental change of the electromagnetic (EM) characteristics. With the significant increase of the antenna number and carrier frequency in future 6G systems, the near-field region of ELAA will expand by orders of magnitude. The two commonly used ELAA architectures are co-located and distributed ELAAs, as shown in **Fig. 2.8 (a)** and **(b)**. The antenna elements of co-located ELAA are typically separated by half wavelength,

and its physical dimension is limited by the continuous platform [39]. By contrast, distributed ELAA is an architecture that antennas are widely distributed over a vast geographical region with multiple separated sites, which are interconnected by the backhaul/fronthaul links, so as to perform joint signal processing. However, distributed ELAA, e.g., cell-free ELAA, usually requires the sophisticated site coordination and high backhaul/fronthaul capacity.

In order to complement for existing ELAA architectures, the works [40][41] propose a novel modular ELAA architecture. As illustrated in **Fig. 2.8(c)**, the antenna elements of modular ELAA are regularly mounted on a shared platform in a modular manner. Each module is comprised of a moderate/flexible number of array antennas with the inter-element distance typically in the order of the signal wavelength, while different modules are separated by the relatively large inter-module distance, so as to enable conformal capability with the deployment structure in practice. For example, the modular ELAA with interlaced modules can be embedded into the discontinuous wall spaced by windows, like facade circumstances of shopping malls, factories or office buildings. Compared to co-located ELAA with the same number of antenna elements, modular ELAA not only has the characteristic of flexible deployment, but also a higher spatial resolution due to the larger physical dimension. However, since the inter-module distance is much larger than half wavelength, modular ELAA will lead to the undesired grating lobes. On the other hand, different from the distributed ELAA architecture, modular ELAA typically performs joint signal processing, without having to exchange or coordinate sophisticated inter-site information, which may ease the requirement of synchronization and reduce hardware cost associated with the backhaul/fronthaul links for distributed ELAA.

Uniform sparse ELAA is array architecture where the inter-element spacing is larger than half-wavelength, as illustrated in **Fig. 2.8 (d)**, which is a special case of modular ELAA. In general, uniform sparse ELAA results in a narrower main lobe due to the higher spatial resolution, which can provide a significant interference suppression gain in scenarios with densely located users [42]. Similar to modular ELAA, uniform sparse ELAA gives rise to the undesired grating lobes, due to the inter-element spacing much larger than half wavelength.

It is worth mentioning that the above four array architectures are suitable for different application scenarios. For example, co-located, modular and uniform sparse ELAAs can all be used to support cellular hotspot communications, while modular and uniform sparse ELAAs achieve a higher transmission rate in scenarios with densely located users. Besides, distributed ELAA is able to provide a better communication service for geographically widely distributed users. Thus, the above four architectures complement each other, and the choice of appropriate ELAA architecture depends on the actual application scenario.

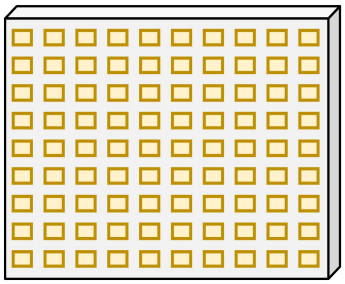

(a) co-located ELAA

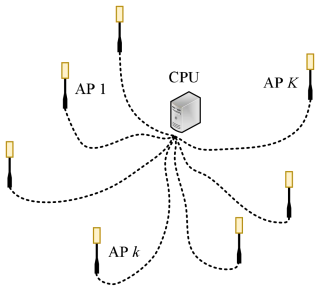

(b) Distributed ELAA

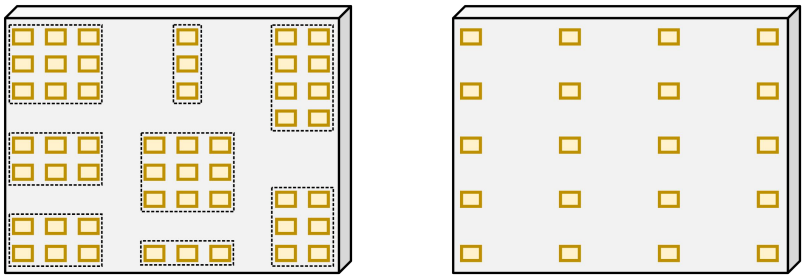

(c) Modular ELAA (d) Uniform sparse ELAA

Fig. 2.8 Different architectures of ELAA [39]

2.2.3 Cell-Free Enabled Near-field

Unlike the classic cellular communication architecture, the Cell-Free communication architecture achieves a user centered communication paradigm by deploying a large number of access nodes in a distributed manner, effectively overcoming inter cell interference, avoiding communication interruptions, and further improving the performance of next-generation 6G mobile communication. Based on the Cell-Free communication architecture, the equivalent array aperture is significantly expanded due to the distributed deployment of multiple arrays, and the near-field spherical wave effect is more significant. Meanwhile, due to the denser distribution of access nodes and shorter communication distances, users will have a higher probability of being in the near-field range. In addition, due to the collaborative nature of non-cellular communication architectures, users may be served simultaneously by multiple access nodes with different antenna sizes and distances, which may be located in the far-field or near-field range of different nodes, facing more complex mixed far-field and near-field communication scenarios. Therefore, cellular free near-field communication will be one of the important application scenarios for future 6G.

The modeling of near-field spherical wave channels can provide a model foundation for cellular free communication systems. Due to its significant near-field spherical wave effect, considering the near-field spherical wave property can further improve the optimization accuracy of access nodes in cellular free architectures. At the same time, beamforming methods that are compatible with near-field spherical waves and far-field plane waves, efficient far-field cellular free communication channel estimation, and beam training schemes can better adapt to near-field communication scenarios, further improving the performance of cellular free communication systems.

2.2.4 MA Enabled Near-Field

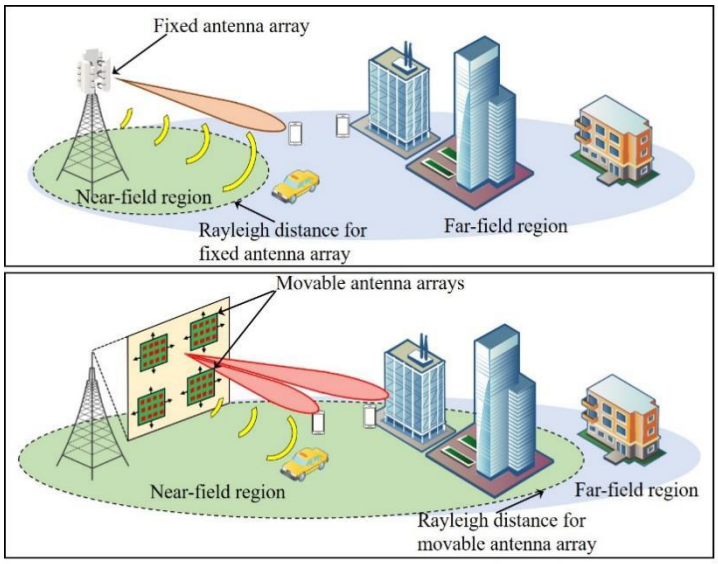

Fig. 2.9 MA for near-field communications and sensing

MA technology has recently been introduced in wireless communication systems to control the local movement (in position and/or rotation) of antennas at the Tx/Rx for improving wireless channel conditions and communication performance [43]. There are various practical methods that can be used to enable antenna movement, such as mechanical motors, microelectromechanical system (MEMS), etc. Due to their flexible movement capability, MAs can fully exploit the wireless channel spatial variation. For example, they can significantly enhance the spatial diversity performance, in terms of receiver signal power improvement and interference mitigation, as compared to conventional fixed-position antennas [44][45]. Besides, for multi-MA aided MIMO and/or multiuser communication systems, the channel matrices can be reshaped by antenna position optimization to increase the spatial multiplexing gain and thus the wireless channel capacity [46][47][48]. Moreover, by integrating multiple MAs into an array, more flexible beamforming can be realized by jointly designing the array geometry and beamforming vector [49][50]. Since the effective array aperture scales with the size of the antenna moving region, enlarging the antenna moving region expands the near-field region of the Tx/Rx for communication as well as sensing, as shown in Fig. 2.9.

Different from the ELAA which requires an extremely large number of antenna elements and radio frequency (RF) frontends, the number of MAs is moderate and can be kept constant even with the increasing moving region size. Thus, MAs can help reduce the hardware cost and RF power consumption as compared to ELAA. The performance advantages of MA systems, such as higher spatial diversity, enhanced multiplexing gain, and more flexible beamforming, become more appealing in 6G near-field communications because the spherical wave-based model renders more substantial channel variation in the spatial domain. Furthermore, distributed MAs can be seamlessly integrated into cell-free communication systems, providing additional degrees of freedom in antenna position and/or rotation for improving the performance of 6G networks. In wireless sensing and ISAC applications for 6G, the MA systems can effectively enlarge the antenna aperture such that the angular/ranging accuracy is increased manifoldly. For sufficiently large antenna moving regions, the MA-aided systems can realize super-resolution for near-field sensing. In summary, MAs opened up a new direction for research in 6G near-field communication and/or sensing. More collective efforts in theoretical research,

technical exploration, system design, experimental verification, and standardization activities are required to unleash the full potential of MAs in future 6G networks.

2.3 Integrated Sensing and Communication

In addition to high-capacity communication, the next generation of wireless networks also has the potential to achieve high-precision perception. Therefore, the integrated sensing and communication (ISAC) technology has also attracted widespread research interest in academia and industry [51]. Compared with traditional wireless positioning and channel estimation, wireless perception relies on the echo signal reflected by passive targets, rather than the pilot signal sent by active devices. Currently, many existing modulation waveforms have been proven to be applicable to wireless sensing, such as orthogonal frequency division multiplexing (OFDM) and orthogonal time frequency space (OTFS), indicating that sensing functions can be seamlessly integrated into existing wireless communication networks [52][53]. Besides, novel dual-functional waveform design strategies have been developed to balance the communication and sensing performances under different application scenarios, e.g., ISAC at mmWave/THz frequencies or communication/sensing-centric ISAC services.

In far-field sensing, increasing the size of the antenna array often only improves the resolution of angle estimation, while the resolution of distance and velocity mainly depends on signal bandwidth and perception duration. However, in the near-field region, the propagation of spherical waves allows large-scale antenna arrays able to estimate the distance and movement speed between objects. On the one hand, even within a limited bandwidth, near-field channels can still effectively contain distance information, improving the resolution of distance estimation in narrowband systems. On the other hand, the estimation of target velocity depends on the estimation of Doppler frequency. Compared with far-field sensing, near-field sensing may have significantly different Doppler frequencies when observing two antennas in a large-scale antenna array from different directions, which can enhance the estimation of object movement speed [37][54], as shown in Fig. 2.10 Based on the above discussion, near-field effects have the potential to promote high-precision perception in situations where time-frequency resources are limited. Therefore, near-field synesthesia integration is a highly promising technology.

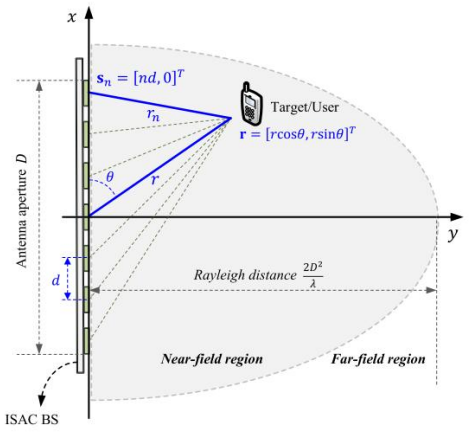

Fig. 2.10 Near field ISAC system[37]

2.4 Wireless Positioning

In traditional far-field communication systems, the angle and distance information of the target relative to the receiving point is mainly obtained by estimating the arrival angle and time of the signal at the target based on the assumption of plane waves [55]. The far-field communication system needs to deploy multiple receiving points as positioning anchors to estimate the three-dimensional coordinates of the target based on the angle and distance information of multiple anchors. In order to obtain more accurate angle and distance information, far-field communication systems usually need to configure measurement signals with larger bandwidth. In addition to the use of distance and angle, the use of the characteristics of the received signal as a fingerprint for localization is also a common method of localization and has been studied in far-field communications [56]. In the near field, based on the spherical wave model, the arrival angles of signals from antenna units in different regions of the antenna array at the target are different. By utilizing the signal transmission characteristics of beam convergence, near-field communication systems locate targets through the differences in channel angles in different areas of the antenna array, thereby reducing the demand for measurement signal bandwidth [56]. Meanwhile, the deployment of large-scale antenna arrays is beneficial for further enhancing angular resolution and providing additional distance resolution in the near-field region, which is conducive to achieving high-precision positioning in 6G mobile communication [57].

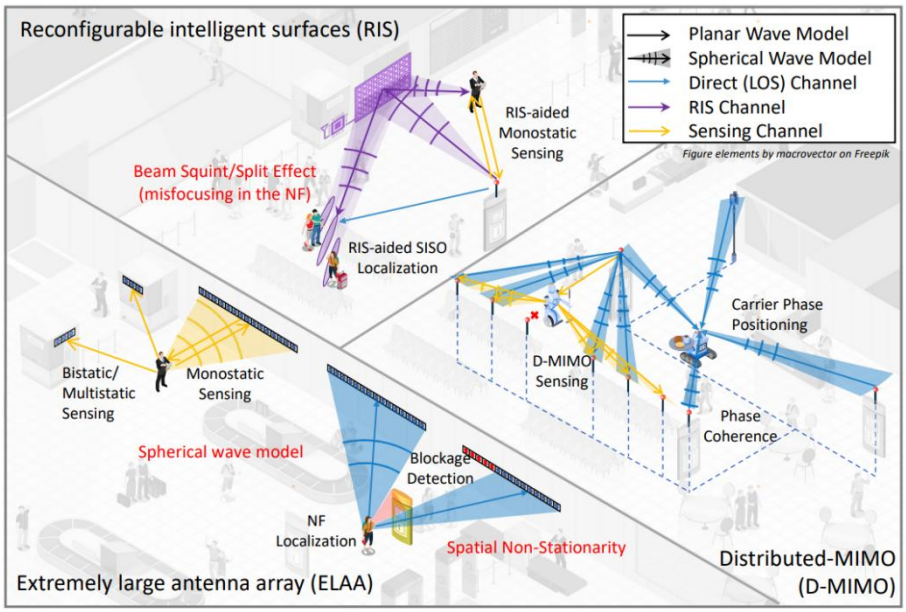

Fig. 2.11 High precision positioning based on near-field effects

High precision positioning services can be provided in the near-field through various forms such as Extremely Large Aperture Array (ELAA), Reconfigurable Intelligent Surface (RIS), and distributed MIMO (D-MIMO).

The positioning process of near-field communication systems is different from traditional far-field communication systems in terms of signal system, channel model, and positioning principle. The two belong to heterogeneous positioning networks. Therefore, heterogeneous positioning network fusion algorithms are needed between far-field and near-field communication systems to ensure seamless positioning services [59][60]. The fusion of heterogeneous positioning networks relies on the implementation of positioning accuracy estimation algorithms [61][62]. For regional positioning

systems, including near-field communication systems, positioning accuracy algorithms can evolve into availability estimation [63] to support two different modes of interoperability between heterogeneous positioning systems: "soft fusion" and "hard switching" [64].

2.5 Simultaneous Wireless Information and Power Transfer

In near-field communication, a highly directional point beam can be achieved, which concentrates the target area of the beam near the target device, thereby concentrating the energy of the RF signal to the energy collection node of the Internet of Things device. By utilizing the large number of antennas and high-precision position information, the efficiency of wireless energy transmission can be significantly improved, reducing energy waste during the transmission process. The near-field beam focusing characteristics limit the spread of energy to undesired location, but does not affect the efficiency on its own. In indoor scenarios or scenarios where the size of base station antennas is limited, wireless communication systems can use intelligent meta-surfaces to construct near-field channels and gather signal energy from home base stations to energy harvesting nodes. In addition, in the near-field communication system, the super large antenna array can obtain higher spatial resolution in the near-field range based on the wireless channel of spherical wave model, so that the base station can support higher density simultaneous wireless information and power transfer (SWIPT) terminals. SWIPT allows devices to harvest energy from RF waves and convert it to electrical energy, storing that energy into the device's battery, maximizing the device's lifespan and representing a new solution to limited energy[65][66].

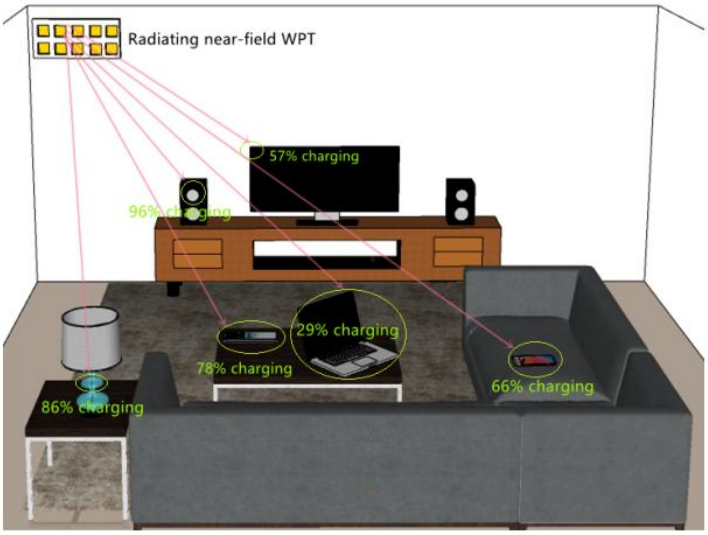

Fig. 2.12 Schematic diagram of near-field wireless energy transmission

2.6 Physical Layer Security

Due to the natural broadcasting and mobile characteristics of wireless communication, the communication of legitimate users in the network is easily eavesdropped and attacked by illegal users, and secure transmission has always been an important issue in wireless communication. In far-field communication, if the eavesdropper is in the same direction as the legitimate user, especially when the eavesdropper is closer to the base station, secure transmission will be difficult to achieve. Unlike the directional focusing of beamforming in far-field communication, in near-field communication assisted

by ultra large arrays, the beams formed by base stations have strong positional focusing [67]. This property allows the energy of the transmitted signal to concentrate at the location of legitimate users rather than just in their direction, effectively reducing information leakage at the location of eavesdropping users and improving the system's secure channel capacity. By optimizing the beam focusing design of the base station, the potential of near-field communication in enhancing physical layer security can be fully explored.

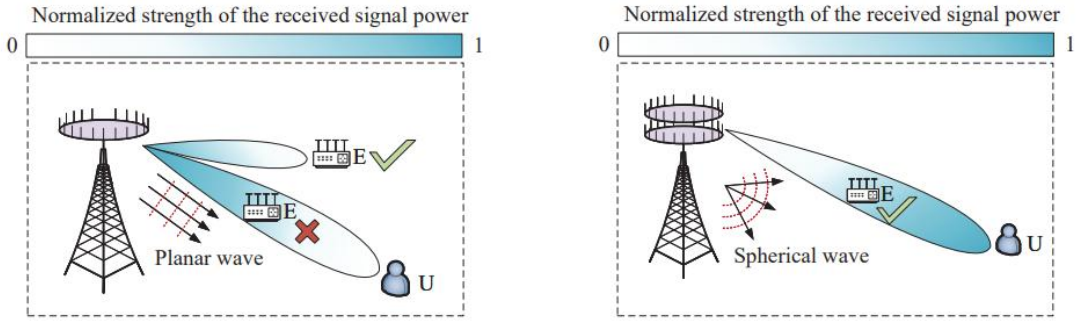

Fig. 2.13 Left: Far field secure communication using beam steering. Right: Near field secure communication using beam focusing.

2.7 Multiple Access

Multiple access technologies leverage time, frequency, code, and space domains in order to achieve the efficient utilization of transmission resources, which is the key to improving the transmission rate of the next-generation wireless network. In the current 5G massive MIMO system, spatial division multiple access (SDMA) utilizes orthogonal resources in the angular domain to distinguish different users; non-orthogonal multiple access (NOMA) further allows multiple users to reuse the same resource block and mitigate the inter-user interference through the power or code domain; unsourced random access introduces a competition mechanism of access resources (such as codewords), which saves the resource overhead intended for random access with short data packages in the scenario of massive machine-type communications (mMTC).

Compared with the far-field transmission model applied in multiple access technologies such as SDMA, the near-field transmission model reveals the two-dimensional beam focusing characteristics in the angle-distance domain and yields a larger spatial degree of freedom, indicating a great increase in available spatial resources. Therefore, integrating near-field characteristics into the design of multi-access technologies would be more conducive to serving the access requirements of massive users and further improving the system spectrum efficiency.

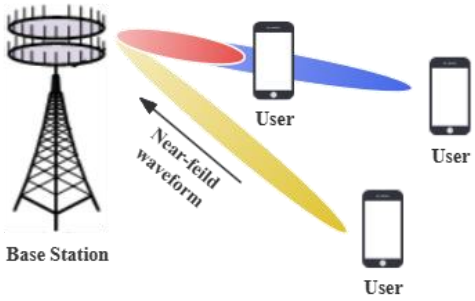

Fig. 2.14 Schematic diagram of near-field multiple access

2.8 Massive IoT Communications

Massive Internet of things (IoT) communications refer to the networking infrastructure and protocols required to support the connectivity needs of a large number of IoT devices. These devices typically generate and transmit small amounts of data intermittently, often with low power consumption requirements. In such a scenario, massive control type interactions are the dominant communication scenario. These control type communications are mostly with short packet that is even shorter than the signaling data length, but of a massive number. The communication infrastructure must be capable of supporting a massive number of IoT devices, potentially numbering in the millions or even billions. This requires scalable network architectures, protocols, and management systems that can efficiently handle the increased traffic and device density. On the other hand, some high concurrent communications might happen with even faster transmission speed requirements, for instance, while working together to deliver a real-time industrial situation awareness to the control center in the industrial IoT applications. By addressing these requirements, communication infrastructure needs to effectively support the connectivity needs of massive IoT deployments, enabling a wide range of applications and unlocking the full potential of IoT technology.

ELAA-based Near-field technology is a potential player for massive IoT communications in 6G, especially for the massive connectivity and high-speed concurrent communication requirements. By incorporating the ELAA, the base station can connect more IoT devices within the range of the Rayleigh distance. Moreover, the ELAA system working on the near-field range will be an ideal solution to the high-speed concurrent communications. According to a prior study [68], arbitrary signal to noise ratio (SNR) can be achieved simply by increasing the transceiver number, which yields faster transmission speed while deployed.

2.9 On-chip Wireless Communications

On-chip Wireless Communications refers to the utilization of on-chip antennas or near-field coupling, among other wireless interconnect methods, to facilitate data exchange and wireless communication between different modules within or among chips. The transmission distance of on-chip wireless communication typically falls below 1cm, offering advantages such as low loss, high transmission rates, and high integration. The applications of on-chip communication are widespread, notably in the Internet of Things (IoT) domain, enabling seamless interconnection among smart chips, devices, and wearables, thereby significantly enhancing communication efficiency and reducing wiring

complexity. However, this technology faces limitations including increased chip area costs, security and privacy concerns, and increased power consumption. Nevertheless, as the operating frequency rises to the millimeter-wave/terahertz frequency bands, the size of on-chip antennas significantly reduces, leading to a substantial decrease in chip area [69][70] Moreover, the proximity between transceiver chips reduces, thereby relaxing the signal power requirements for wireless communication. Additionally, the high frequency signals exhibit good directionality, enhancing the security and reliability of information transmission. These factors substantially alleviate the design complexity of on-chip wireless communication systems[71].

Simultaneously, compared to traditional wired communication method between chips, utilizing wireless communication can avoid the drawbacks introduced by transmission lines, such as high latency, high crosstalk, limited bandwidth, and parasitic effects. As illustrated in Fig. 2.15, by integrating on-chip antennas into the chip, the signal transmission mode shifts from traditional wired transmission to on-chip and inter-chip wireless communication, forming a flexible architecture of on-chip networks, thereby avoiding the limitations of wired interconnection layouts[72].

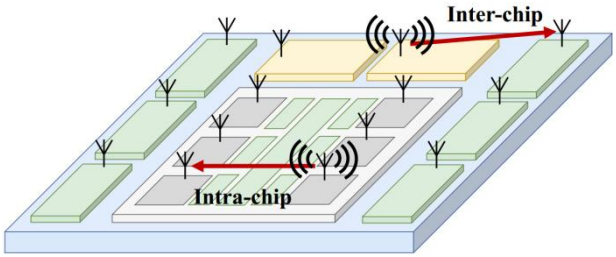

Fig. 2.15 Utilizing on-chip and inter-chip communication with antennas

Additionally, on-chip wireless communication plays a significant role in signal transmission between different system-level chiplets. As illustrated in Fig. 2.16, when forming a System-on-a-Chip (SoC) through heterogeneous integration, the difficulty of high-frequency interconnection between chiplets arises due to different structures and semiconductor materials. Traditional wire bonding methods severely degrade signal integrity. By utilizing on-chip wireless communication, high-speed, high-bandwidth heterogeneous integration between chiplets can be achieved, effectively enhancing the versatility of large-scale heterogeneous systems[73].

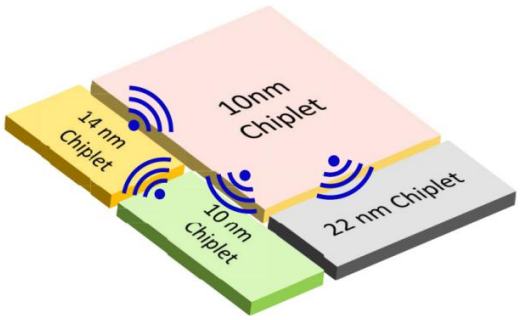

Fig. 2.16 Wireless interconnection between chips with different semiconductor materials

Furthermore, as on-chip wireless communication exploits the radiation effects of on-chip antennas or near-field coupling, it is no longer constrained by the one-to-one data transmission mode of traditional wired interconnection. In terms of data transmission, it offers higher flexibility and adaptability, enabling one-to-many transmission to support high-density device connections and data

exchanges among massive devices, thus providing more feasibility for the design of single-chip multi-core processors, as illustrated in Fig. 2.17 [74].

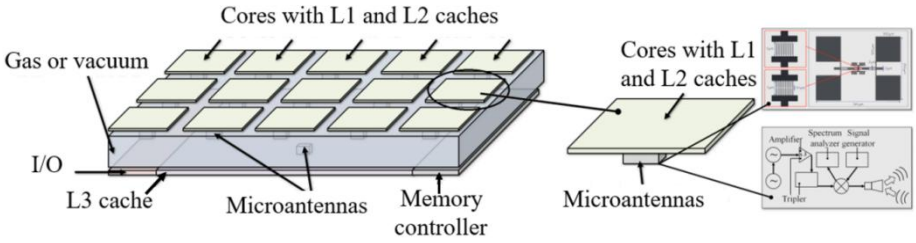

Fig. 2.17 Single-chip multi-core processors utilizing on-chip wireless communication technology

In conclusion, on-chip wireless communication can be widely applied in various mobile devices and embedded systems, such as smartphones, tablets, smartwatches, IoT devices, etc., to enhance the performance of communication devices. The application of on-chip wireless communication in 6G can reduce communication latency, provide faster data transmission capabilities, and enhance the real-time performance and energy efficiency of communication systems. High-speed and efficient on-chip communication provide feasible solutions for future 6G wireless communication systems, terahertz integrated circuits, and chip-to-chip communication interconnections.

3 Fundamental Theories of Near-field

With the technological evolution from 5G to 6G communication, in order to further improve beamforming performance and communication rate, larger antenna array apertures and higher communication frequencies are being employed. However, larger arrays also bring many traditionally far-field communication scenarios into the electromagnetic-defined near-field communication range. In near-field communication, the electromagnetic waves used for information transmission can only be regarded as spherical waves instead of plane waves. This new physical characteristic is inevitable and introduces many new electromagnetic effects, such as spatial non-stationarity, polarization, and evanescent waves. As a result, many traditional communication algorithms that were explicitly designed for far-field operation suffer from severe performance degradation or fail to leverage the new features for optimal performance in 6G near-field scenarios. In this chapter, starting from the definition of near-field provided by electromagnetic theory, we analyze the near-field electromagnetic effects, explaining their sources and impacts on existing systems. Furthermore, based on the existing literature on near-field communication, we summarize the changes in communication system design and performance caused by the emergence of near-field effects, focusing primarily on communication degrees of freedom and communication capacity.

The basic theory of near-field includes four main parts: electromagnetic near-field definition, near-field electromagnetic properties and physical effects, theoretical analysis of near-field communication degrees of freedom and near-field performance analysis.

3.1 Near-field Range Partitioning

In this section, we first introduce the differences between far-field and near-field communications. Then, we establish principles for determining the boundaries of far-field and near-field regions in several typical application scenarios.

As shown in **Fig. 3.1**, based on electromagnetic theory and antenna theory, the fields around a transmitter can be divided into the near-field and far-field regions, with the near-field further classified into the reactive near-field region and the radiative near-field region [75]. The reactive near-field region is limited to the space close to the antenna (within the Fresnel distance), where evanescent waves dominate, and the electromagnetic field does not propagate from the antenna in the form of radiative waves. The radiative near-field region extends several wavelengths away from the antenna (between the Fresnel distance and the Rayleigh distance). The Rayleigh distance is also known as Fraunhofer distance. In this region, the amplitude differences between electromagnetic waves on different antennas within the array are not significant, but the phase changes exponentially with the index of the antennas. The signal propagation model in this region must be modeled using a spherical wave model. The far-field region surrounds the radiative near-field region, and in the far-field, electromagnetic waves can be approximated as plane waves. Since the reactive near-field region is usually small and evanescent waves decay exponentially with distance, practical near-field communication systems primarily focus on wireless communication within the radiative near-field region, where "near-field" generally refers to the radiative near-field region.

In existing research, there are multiple perspectives and empirical rules to characterize the boundaries between the near-field and far-field regions, mainly including phase difference, power difference, channel capacity, and localization error.

(1) Phase difference perspective

From the perspective of phase difference, the classic boundary between near-field and far-field is referred to as the Fraunhofer distance or Rayleigh distance [76] (considering a maximum phase difference between spherical wave and plane wave model not exceeding $\frac{\pi}{8}$), expressed as $\frac{2D^2}{\lambda}$, where D represents the maximum aperture of the antenna, and λ represents the wavelength of the carrier. If the distance between the user and the base station is greater than the Rayleigh distance, the user can be considered to be in the far-field region. In this region, the signal propagation can be approximated as plane waves. On the other hand, if the distance between the user and the base station is smaller than the Rayleigh distance, the user can be considered to be in the near-field region.

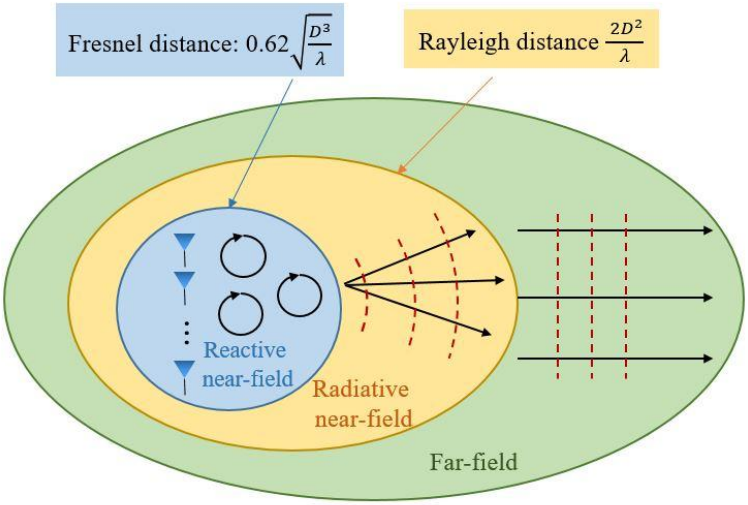

Fig. 3.1 Far-field plane wavefront and near-field spherical wavefront and corresponding physical space normalized received energy

Plane waves differ from spherical waves in their ability to adjust to radiant energy from space. More precisely, plane waves are far-field approximations of spherical waves. In the far-field region, the phase of an electromagnetic wave can be approximated by a Taylor expansion in terms of a linear function of the antenna exponent. This clean linear phase forms a plane wavefront that is only related to the angle of incidence. Thus, using the plane wavefront, far-field beamforming can steer the beam energy to specific angles at different distances, which is also known as beam steering. Unfortunately, this clean linear phase does not completely reveal information about the spherical wave. In the near-field region, the phase of a spherical wave should be derived accurately based on the physical geometry, which is a nonlinear function of the antenna index. The information on the angle of incidence and the distance for each path between the BS and the UE is contained in this nonlinear phase. By utilizing the additional distance information of the spherical wavefront, near-field beamforming can focus the beam energy at a specific location and achieve energy focusing in both the angle and distance domains. Based on this property, near-field beamforming is also known as beam focusing.

The primary concept behind the derivation of the Rayleigh distance is as follows [75]. The true phase of an electromagnetic wave must be calculated based on an accurate spherical wavefront model and the BS antenna position. In the far-field case, this phase is usually approximated by a first-order Taylor expansion based on a planar wavefront model. This approximation results in a phase difference which increases with decreasing distance. The distance between the center of the BS array and the center of the UE array is defined as the Rayleigh distance when the maximum phase difference between all BS and UE antennas reaches $\pi/8$. Therefore, if the communication distance is shorter than the Rayleigh distance, the maximum phase difference will be greater than $\pi/8$. In this case, the far-field approximation becomes inaccurate, so it is necessary to utilize the near-field propagation model.

Based on this definition, the near-field ranges of single-input-multiple-output (SIMO), multiple-input-single-output (MISO), and multiple-input-multiple-output (MIMO) communication systems can be obtained. As shown in **Fig. 3.2**, the near-field range for SIMO/MISO scenarios is accurately determined by the classical Rayleigh distance, which is proportional to the square of the aperture of the BS array. For the MIMO scenario, both the BS array aperture and the UE array aperture contribute to the Rayleigh distance since ELAA is employed on both sides of the BS-UE link; i.e., the near-field range is proportional to the square of the sum of the BS array aperture and the UE array aperture. For RIS systems, the cascaded BS-RIS-UE channel consists of BS-RIS and RIS-UE links. Therefore, the $\pi/8$ maximum phase difference needs to be calculated by summing the BS-RIS distances and the RIS-UE distances when calculating the phase difference, and the near-field range of the RIS system is determined by the harmonic mean of the BS-RIS distances and the RIS-UE distances, as shown in Fig. 2. It can be further seen from Fig. 2 that RIS-assisted communication operates in the near-field region as long as either of these two distances is shorter than the Rayleigh distance. Therefore, near-field propagation is more likely to occur in RIS systems [32].

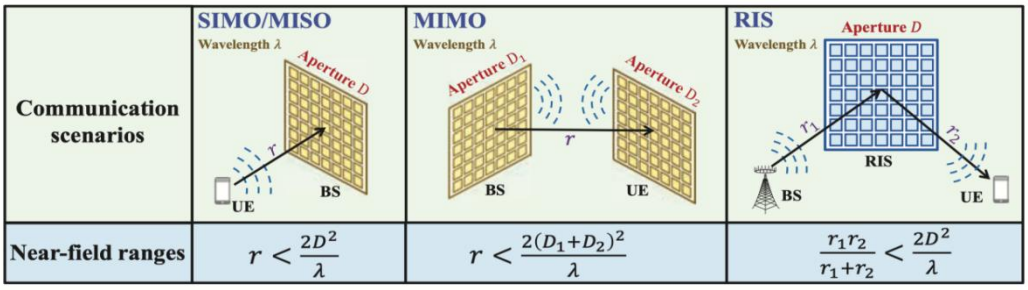

Fig. 3.2 Near-field range for typical communication scenarios

(2) Power difference perspective

When using the optimal Maximum Ratio Combining (MRC), signals from different antenna elements can be completely aligned in phase, thus eliminating the impact of phase differences on received power. However, due to imperfect channel estimation, MRC may struggle to fully neutralize phase differences. Therefore, considering power losses in practical systems, reference [77] modified the traditional Rayleigh distance and proposed the effective Rayleigh distance to characterize the boundary of the near-field range.

After eliminating the effect of signal phase on received power through MRC, the received power is only determined by the amplitude response differences of the antenna elements at the receiver. Considering the amplitude response differences of different antenna elements on the same transmitter

antenna array, the *Critical Distance* and *Uniform Energy Distance* is proposed [78][79], which characterize the near-field range from the perspective of power differences between different antenna elements. That is, the power ratio between the weakest and strongest antenna elements detected at the receiver exceeds a specified threshold beyond this distance. The *Critical Distance* is determined by the antenna aperture, primarily characterizing the boundary of the field near the antenna aperture axis. The *Uniform Energy Distance* further considers factors such as array structure and the projected aperture of the antenna array, providing a more accurate description of the near-field boundary in off-axis regions.

Looking at the differences in received power between the plane wave channel model and the spherical wave channel model from another perspective, reference [80] has derived the equal-power lines and equal-power surface for the near-field region based on the uniform linear array (ULA) and the uniform circular planar array (UCPA) structures respectively, characterizing the near-field range.

(3) Capacity perspective:

From the perspective of capacity, the near-field range can be described by combining the channel capacity [81], eigenvalues [82], rank [80], multi-stream transmission characteristics [83], or effective degrees of freedom [84], to evaluate the applicable area of far-field plane waves and near-field spherical waves. Reference [80] proposes the boundary of the near-field region through equip-rank surface. It shows that the near-field range increases with the number of scatterers in both line-of-sight (LoS) and non-line-of-sight (NLoS) environments, with is more apparent in the NLoS environment. Considering spatial reuse, reference [83] introduces the effective reuse distance metric $D_{max}^{(m)}$, representing the maximum distance at which the channel can efficiently accommodate m independent spatial streams at a specific signal-to-noise ratio (SNR). The near-field boundary from the perspective of multi-stream transmission is discussed by combining the channel's effective degrees of freedom [84], which demonstrates that the near-field range is not only related to the antenna array aperture but also influenced by the number of antenna elements.

(4) Localization error perspective

The Fraunhofer distance serves merely as a rough estimate to delineate between the far-field and near-field regions. However, for localization applications, it is not an appropriate boundary between near and far fields, as it does not consider several essential parameters for localization, such as AoA, beam squint, or transmit power. In fact, it has been shown in [85] that this distance is insufficient to suggest when the mismatched far-field model can be used in practice, instead of the more accurate near-field, without significant performance degradation due to the model mismatch. Therefore, a metric based on the mismatched Cramer-Rao lower bound is proposed, such that the boundary between the far-field and the near-field is the -3 dB contour of the model mismatch positioning error between the two regimes.

3.2 Near-field Electromagnetic Physical Effects

In the near-field region, the electromagnetic physical effects of wireless signals will become non-negligible. Specifically, electromagnetic physical effects include tri-polarization effects, energy mapping effects, etc. Next, we will start with Maxwell's equations to establish electromagnetic near-field channels and reveal these electromagnetic near-field effects.

3.2.1 Near-field Electromagnetic Signal Model

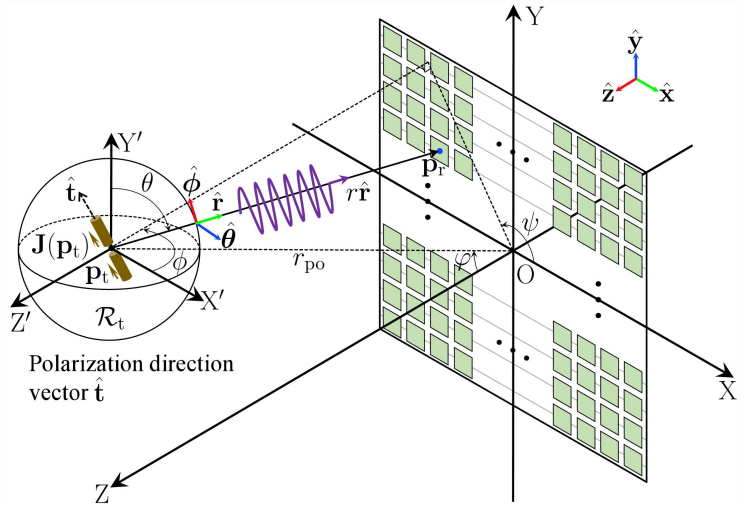

Fig. 3.3 Near-field electromagnetic radiation system diagram

As shown in **Fig. 3.3**, in the Cartesian coordinate system $OXYZ$, we consider that the transmitter is located at point $\mathbf{p}_t=(x_t,y_t,z_t)$ inside the source region $\mathcal{R}_t\subseteq\mathbb{R}^3$ and equipped with a current density $\mathbf{J}(\mathbf{p}_t)$. The transmitter is a common low-cost single-polarized antenna with a normalized polarization direction vector $\hat{\mathbf{t}}=t_x\hat{\mathbf{x}}+t_y\hat{\mathbf{y}}+t_z\hat{\mathbf{z}}$ ($\hat{\mathbf{x}}$、$\hat{\mathbf{y}}$、$\hat{\mathbf{z}}$ are three basis vectors). The coordinates of each point on the receiving array are $\mathbf{p}_r=(x_r,y_r,0)$.

Further, we consider the scalar electric field defined from the power point of view. Specifically, we exploit the scalar electric field that is a component of the *Poynting vector* perpendicular to the *observation region:* $\mathcal{E}_s(\mathbf{r})=|\mathcal{E}_s(\mathbf{r})|\exp(\mathrm{j}k_0r)$, where

$$\begin{aligned}|\mathcal{E}_s(\mathbf{r})|^2 &= \overbrace{\|\mathbf{E}(\mathbf{r})\|^2}^{\text{Transmitting energy}}\overbrace{\left(-\frac{\mathbf{p}_r-\mathbf{p}_t}{\|\mathbf{p}_r-\mathbf{p}_t\|}\cdot\hat{\mathbf{z}}\right)}^{\text{Energy mapping effects along the } Z\text{-direction}}\\ &=\mathcal{E}_{in}^2\underbrace{\frac{1}{4\pi r^2}}_{\text{Free space attenuation}}\underbrace{\frac{z_t}{r}}_{\text{Energy mapping factor}}\underbrace{\frac{1}{r^2}\left[\left(t_yx_{r,t}-t_xy_{r,t}\right)^2+\sum_{(\alpha,\beta)\in\mathbb{M}}\left(t_\alpha\ell_\beta+t_\beta\ell_\alpha\right)^2\right]}_{\text{General polarization loss}},\end{aligned}\tag{3.1}$$

where $\mathbb{M}=\{(z,x),(z,y)\}$, $\ell_x=x_{r,t}$, $\ell_y=y_{r,t}$, $\ell_z=z_t$, $x_{r,t}=x_r-x_t$, $y_{r,t}=y_r-y_t$. $\mathcal{E}_{in}=\dfrac{\eta_0 I_{in}}{2}$ is the initial electric intensity measured in volts.

In particular, when the transmitter is polarized toward the positive Y axis, i.e., $\hat{\mathbf{t}}=\hat{\mathbf{y}}$. (3.1) can be simplified to

$$\left|\mathrm{E}_{\mathrm{s,Y}}(\mathbf{r})\right|^2=\mathrm{E}_{\mathrm{in}}^2\frac{1}{4\pi r^2}\frac{z_{\mathrm{t}}}{r}\frac{x_{\mathrm{r,t}}^2+z_{\mathrm{t}}^2}{r^2}. \tag{3.2}$$

When the signal is incident perpendicularly to the receiving surface, i.e., $x_{\mathrm{t}}=y_{\mathrm{t}}=0$ and $\frac{z_{\mathrm{t}}}{r}=1$. (3.2) can be simplified to

$$\left|\mathrm{E}_{\mathrm{s,Y,v}}(\mathbf{r})\right|^2=\mathrm{E}_{\mathrm{in}}^2\frac{1}{4\pi r^2}\frac{x_{\mathrm{r,t}}^2+z_{\mathrm{t}}^2}{r^2}. \tag{3.3}$$

When $y_{\mathrm{t}}=y_{\mathrm{r}}$, i.e., $\frac{x_{\mathrm{r,t}}^2+z_{\mathrm{t}}^2}{r^2}=1$, there is no polarization loss, and (3.3) is simplified to

$$\left|\mathrm{E}_{\mathrm{s,Y,v}}(\mathbf{r})\right|^2=\mathrm{E}_{\mathrm{in}}^2\frac{1}{4\pi r^2}. \tag{3.4}$$

(3.4) is the classic Friis formula.

Next, we give the classic far-field signal formula:

$$\mathrm{E}_{far}(\mathbf{r})=\frac{\mathrm{E}_{\mathrm{in}}}{2\sqrt{\pi}r_{\mathrm{po}}}\exp\left[\mathrm{j}k_0\left(r_{\mathrm{po}}-\frac{x_{\mathrm{r}}x_{\mathrm{t}}+y_{\mathrm{r}}y_{\mathrm{t}}}{r_{\mathrm{po}}}\right)\right], \tag{3.5}$$

where $r_{\mathrm{po}}=\sqrt{x_{\mathrm{t}}^2+y_{\mathrm{t}}^2+z_{\mathrm{t}}^2}$, and the phase term uses a second-order Taylor expansion. Further, (3.5) can be simplified to

$$\mathrm{E}_{far}(\mathbf{r})=\frac{\mathrm{E}_{\mathrm{in}}}{2\sqrt{\pi}r_{\mathrm{po}}}\exp\left(\mathrm{j}k_0r_{\mathrm{po}}\right)。 \tag{3.6}$$

From the near-field signal models (3.1) - (3.4) and far-field signal models (3.5) and (3.6), we can see:

- For a near-field signal model, the amplitude term will include the polarization loss of the antenna, the energy mapping coefficient, and the point-to-point free space loss factor, and the phase term will be determined by the exact point-to-point distance.
- The far-field signal model is an approximation of the near-field signal model. For the far-field signal model, the amplitude term only has a fixed free space loss factor, and the distance of the phase term is also a fixed distance from the transmitter to the receiver reference point.

3.2.2 Near-field Electromagnetic Effects

Tri-polarization effect arises naturally for near field communication since the solution to the Maxwell's equation for a dipole antenna has a rapid-decaying radial component. Considering the tri-polarization effect, in [86] the authors considered both the near-field spherical wave channel and the multi-polarization effect using a vector Green's function, and based on this the multi-polarized

near-field spherical wave channel as well as the proposed polarization and channel oriented dual precoding are considered, and the considered systematic diagram is shown as follows.

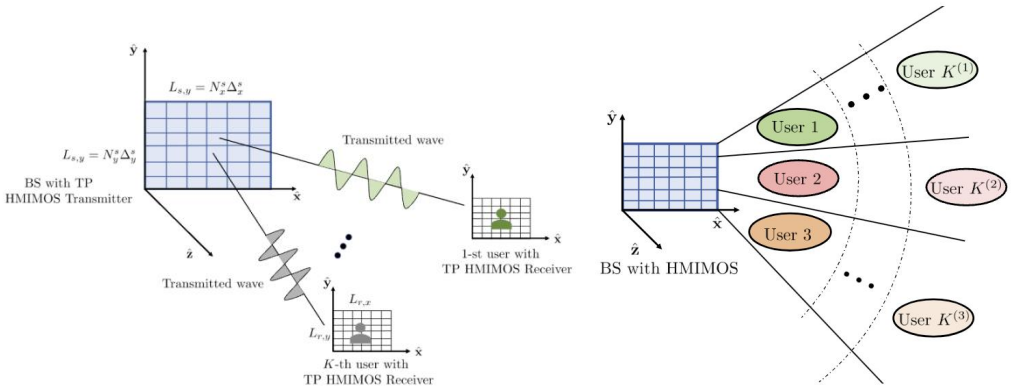

Fig. 3.4 Near-field multi-polarized spherical waves model

Simulation results demonstrate that the multi-polarization effect in near-field communication can significantly increase the system capacity in a specific range.

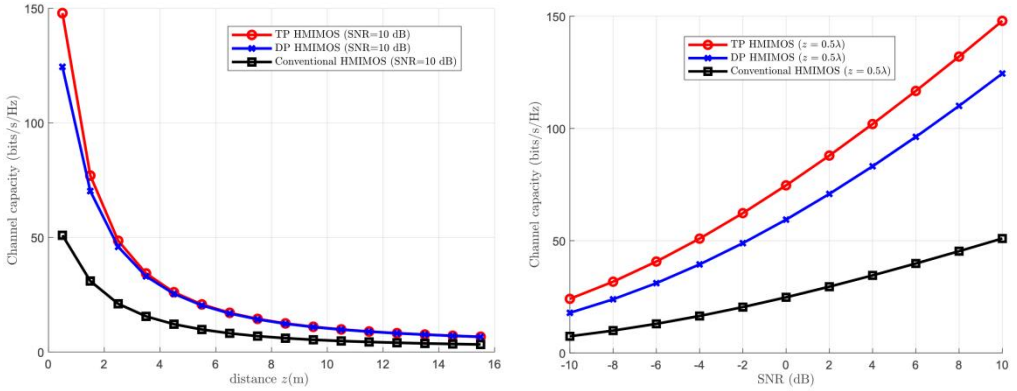

(b) Channel capacity v.s. distance z (a) Channel capacity v.s. SNR

Fig. 3.5 Near-field tri-polarized channel capacity

The near-field evanescent wave effect mainly affects the communication degrees of freedom and capacity of the reactive near-field, which we will describe in the next subsection. For the near-field beam splitting effect, in a near-field RIS, a phase shifter-based beamformer can produce a focused beam aligned to a specific location, thus providing beam focusing gain. Such beamformers work well in narrowband systems. However, for broadband systems, due to the use of an almost frequency-independent phase shifter, spherical beams of different frequencies are focused at different physical locations, which is known as the near-field beam splitting effect. This effect can lead to severe array gain loss because beams of different frequencies cannot be aligned with the target user at a specific location, which needs to be carefully considered in the design of broadband systems.

Although the beam splitting effect makes it more difficult to align the energy of a broadband system to the user, resulting in a degradation of the beam focusing performance, it has a corresponding benefit: since the same guiding frequency corresponds to the generation of spatially multiple beams, it is possible to control the angular range of the beam coverage at different frequencies by designing the system parameters. With this benefit, very fast CSI acquisition can be realized in the far-field for fast beam training or beam tracking. The research on this problem in traditional far-field communication is mainly divided into two types of work: the first type of technique hopes to mitigate the array gain loss

caused by far-field beam splitting, and introduces time-delay circuits in the beamforming structure to mitigate the far-field beam-splitting effect; the second type of technique realizes the fast acquisition of far-field CSI in a large-scale multiple-input-multiple-output system by controlling the time-delay parameter and the multiple beams.

The effect of near-field beam splitting effect is shown in **Fig. 3.6**, where it can be seen that there are multiple energy focusing points spatially during near-field broadband communication.

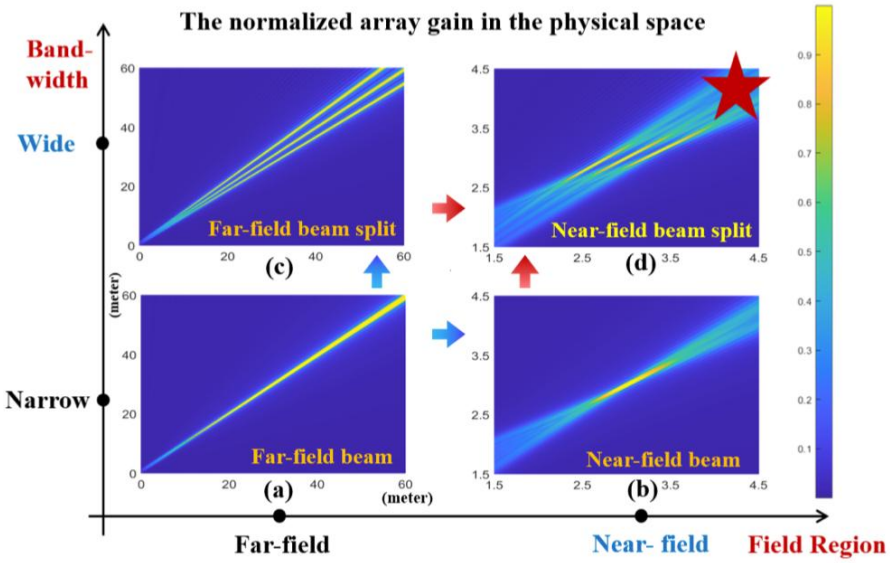

Fig. 3.6 Near-field beam splitting effect schematic

The near-field beam splitting effect is defined and analyzed in the paper [87], and a time delay (TD) based beamformer is utilized to overcome this effect. We propose to divide the whole array into subarrays and then assume that the user is located in the near-field range of the whole array but in the far-field range of each subarray. On this basis, delay circuits can also be utilized to compensate for the group delay between different subarrays caused by the near-field spherical wavefront. As a result, the beam over the entire bandwidth can be focused at the desired spatial angle and distance, and the near-field beam splitting effect is mitigated accordingly.

3.2.3 Near-field Beam Characteristics

After studying the near-field characteristics, the properties of the near-field beam can be analysed and summarized in the following three points: near-field distance-domain focusing, distance-domain asymptotic orthogonality, and distance-domain focusing properties of rectangular and circular array.

First, for the near-field distance-domain focusing characteristics, the depth-of-focus (DF) was calculated in [88] When a transmitter with distance F is focused using matched filtering, the DF is:

$$z \in \left[\frac{d_{FA}F}{d_{FA}+10F}, \frac{d_{FA}F}{d_{FA}-10F}\right] \tag{3.8}$$

where d_{FA} is the array Rayleigh distance, and the depth of the beam depends on where the matched filter is focused as shown in **Fig. 3.7**. When the focus is less than $d_{FA}/10$, the depth of the near-field beam assignment is finite.

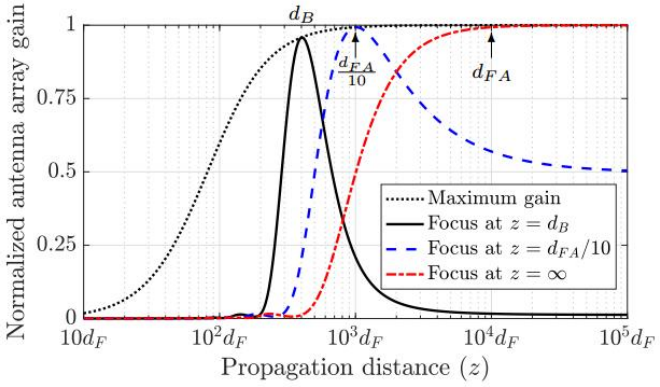

Fig. 3.7 Trend of beam gain with distance

Near-field beam focusing concentrates the beam energy at a specific location determined by angle and distance. In order to utilize the additional spatial distance domain resources to improve the spectral efficiency, researchers in [89] demonstrated the asymptotic orthogonality of the near-field array response vectors, and the channel correlation can be expressed as:

$$f^{near} \approx \left|\frac{C(\beta)+jS(\beta)}{\beta}\right| \tag{3.9}$$

where $\beta = \sqrt{\frac{N^2 d^2(1-\theta^2)}{2\lambda}\left|\frac{1}{r}-\frac{1}{\bar{r}}\right|}$. This means that as the number of array antennas N tends to infinity, β also tends to infinity and f^{near} tends to 0. As shown in **Fig. 3.8**, as the number of antennas increases, the correlation between two array response vectors at different distances at the same angle tends to 0.

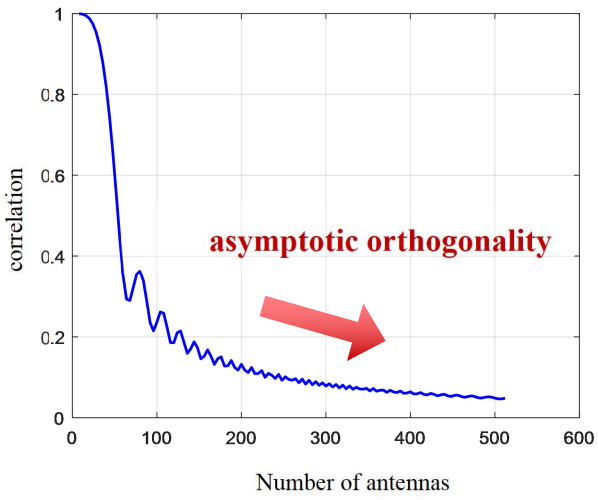

Fig. 3.8 Channel correlation versus antenna curve

The above two beam characteristics are for the Uniform planar array (UPA) and Uniform linear array (ULA) scenario, respectively. Moreover, the distance-domain focusing characteristics are elaborated next for the uniform circular array (UCA) [90]. The beam focusing gain in the UCA scenario is approximated as a zeroth-order first-type Bessel function. From **Fig. 3.9**, it can be seen that the ULA beam focusing gain decreases smoothly with decreasing distance, while the beam focusing gain of UCA decreases faster, which indicates that UCA is able to focus the signal power in a smaller range and mitigate the power leakage.

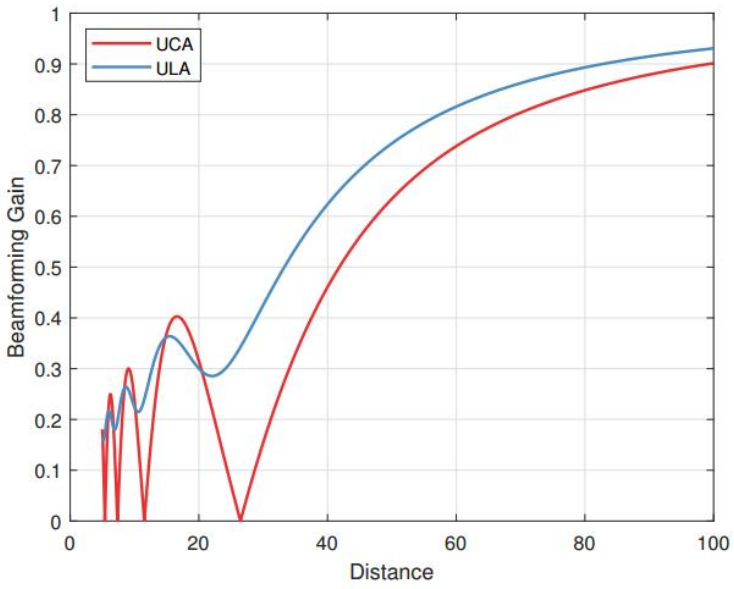

Fig. 3.9 Comparison of beamforming gain between UCA and ULA

3.3 Near-field Degree-of-freedom Theoretical Analysis

Based on the Fourier plane wave unfolding channel modelling, the authors in [91] conducted detailed research on the wave number domain modelling of near-field large-scale antenna arrays, especially investigating the degree of freedom and the communication capacity gain that can be brought about by the evanescent wave effect in the near-field communication, of which the degree of freedom gain is shown as follows, and there can be a gain of 30% in the typical reactive near-field region. In the left side figure of **Fig. 3.10**, the white wave number points correspond to the plane waves available for far-field communication, the green wave number points correspond to the additional evanescent wave numbers available for near-field communication, and the red points are the evanescent wave numbers that are not available because of too much attenuation. Since 6G systems will mostly operate in the radiative near-field, we cannot expect to get more wave number points (spatial degrees of freedom), but we can still make use of them for beamforming in both angle and depth, which was previously not possible.

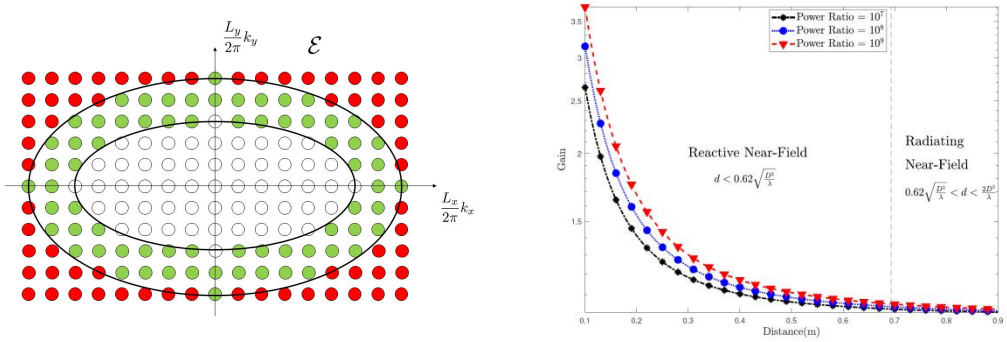

Fig. 3.10 Extra degrees of freedom in the reactive near-field

Reference [92] proposed a signal space approach to study the number of degrees of freedom of the electromagnetic field under arbitrary scattering conditions from the point of view of Nyquist sampling. It considers antenna elements in space as spatial sampling points and uses the sampling points required

to recover the electromagnetic field as communication degrees of freedom. Under isotropic propagation conditions, sampling per square meter is reduced by 13% compared to classical half-wavelength sampling. This gap increases as the angular selectivity of the scattering increases, resulting in a significant reduction in spatial sampling complexity.

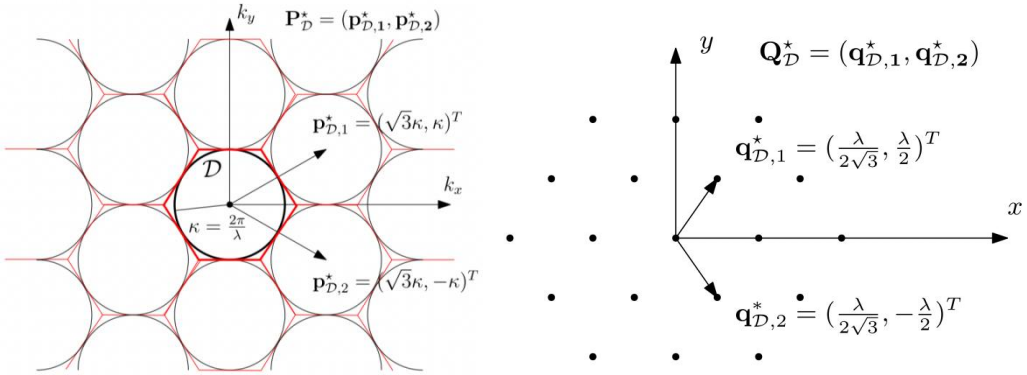

(a) Circle packing in the wavenumber domain. **(b)** Hexagonal sampling in the spatial domain.

Fig. 3.11 Nyquist sampling under isotropic scattering conditions

In the context of spatially discrete (SPD)-MIMO, the comprehensive channel response in the narrowband case is represented as a matrix H. In this case, the number of spatial degrees of freedom (DoFs) of the channel is determined by the number of positive singular values of H or the rank of the correlation matrix HH^{H}. In a far-field MIMO LoS channel, the presence of only a single incident angle at all points across the array corresponds to plane-wave propagation. In such cases, the channel has a rank of 1, corresponding to only a single DoF. In contrast, within the near-field region, spherical waves manifest non-linearly varying phase shifts and power levels for each link. This inherent diversity increases the rank of the channel matrix. This implies that, by reducing the antenna spacing within a fixed aperture, the number of spatial DoFs can be significantly increased [93].

However, it is essential to note that when two antennas are in close proximity to each other, the waves they generate at the receiver become nearly indistinguishable. This limitation should be considered, as it could potentially restrict the achievable increase in channel capacity when incorporating a large number of antennas within a fixed aperture. For a given aperture, the singular values of matrix H presents a two-slope property. We denote the ordered positive singular values of matrix H as $\sigma_1 \geq \sigma_2 \geq \cdots \sigma_{\mathrm{N}}$. Extensive simulations and measurements have consistently shown that, for small values of n, the σ_{n} values exhibit a slow decay until they reach a critical threshold, beyond which rapid decay occurs. This critical threshold is termed the number of effective DoFs (EDoFs), and is illustrated in **Fig. 3.12** [93]. This phenomenon becomes more pronounced as the number of transceiver antennas increase. By assuming that $\sigma_1 \approx \sigma_2 \approx \cdots \approx \sigma_{\mathrm{e}} \gg \sigma_{\mathrm{e}+1} \approx \cdots \sigma_{\mathrm{N}} \approx 0$, we approximate the number of EDoFs as $\mathrm{e} \approx \mathrm{tr}^2(\mathrm{HH}^{\mathrm{H}})/\|\mathrm{HH}^{\mathrm{H}}\|_{\mathrm{F}}^2$[94]. Besides, we note that the number of EDoFs of near-field channels decreases with the propagation distance. We note that $\mathrm{tr}^2(\mathrm{HH}^{\mathrm{H}})/\|\mathrm{HH}^{\mathrm{H}}\|_{\mathrm{F}}^2$ was originally introduced by Verdú to evaluate the slope of the capacity curve in the low bit SNR regime [95]. In recent years, some researchers have noticed that this expression can be also used to approximate the number of EDoFs of near-field channels.

Next, we examine the scenario where both transceivers are equipped with continuous-aperture (CAP) arrays, denoted as CAP-MIMO. In contrast to an SPD antenna array, which provides finite-dimensional signal vectors, the CAP array supports a continuous distribution of source currents

within the transmit aperture. In this context, CAP-MIMO can be regarded as a limiting case of SPD-MIMO with an infinite number of antennas in a fixed aperture area, but this is achieved through spatial oversampling, so the number of EDoFs remains the same. For example, the singular values of the CAP-MIMO channel exhibit a "two-slope" trend, as depicted in **Fig. 3.12** [96]. Therefore, for the near-field CAP-MIMO channel, the performance is still limited by the number of EDoFs. Unlike SPD-MIMO, CAP-MIMO channels cannot be characterized by a finite-dimensional matrix. Typically, it is necessary to use Green's functions to characterize the electromagnetic propagation environment between any two points on the transceiver apertures. Obtaining parallel subchannels requires performing eigenvalue decomposition on the kernel function of Green's functions, resulting in high computational complexity [96]. To estimate the number of EDoFs of near-field CAP-MIMO, one can replace the channel matrix H in the formula $e \approx \mathrm{tr}^2(\mathbf{H}\mathbf{H}^{\mathrm{H}})/\|\mathbf{H}\mathbf{H}^{\mathrm{H}}\|_{\mathrm{F}}^2$ with Green's functions [94]. Additionally, based on existing simulation results, the following conclusion can be drawn: the number of near-field EDoFs is proportional to the product of the transmitter-receiver aperture area and inversely proportional to the transmission distance between the transmitter and receiver [93].

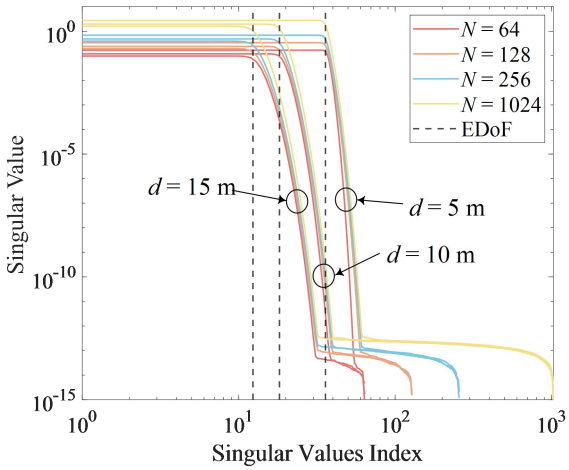

Fig. 3.12 Singular Values of Near-Field SPD-MIMO. D denotes the transmission distance and N is the number of transmit and receive antennas.

3.4 Near-field Performance Analysis and Measurement

3.4.1 Near-field Performance Analysis

The evolution from 5G massive MIMO communication to 6G ultra-massive MIMO communication involves more than just a simple increase in the number of antennas or array size. It fundamentally changes the channel characteristics, such as transitioning from the traditional far-field uniform plane waves to near-field non-uniform spherical waves and from spatial stationarity to spatial non-stationarity [79][97][98]. As a result, most performance analyses based on the traditional far-field uniform plane wave model, such as asymptotic channel gains, need to be re-evaluated within the context of the new near-field models. Moreover, the authors in [99] investigated a cooperative relaying NFC and FFC coexisting system with XL-array, raising an interest question: does the capacity improvement from NFC compensate the performance loss suffered from more time slots? To provide the solution to this question, [99] analyzed the achievable capacity for the proposed NFC schemes

compared with FFC, confirming that the capacity improvement from NFC compensates the performance loss from the half-duplex principle.

In the traditional far-field model, the equivalent channel gain of a uniform planar array increases linearly/quadratically (squared) with the array size until it approaches infinity. This conclusion clearly contradicts the laws of physics. To obtain more general conclusions, references [79][97][98] and references [100][101] have proposed new near-field spherical wave propagation models for massive MIMO active arrays and massive MIMO passive arrays, respectively. These models consider the asymptotic performance when the size of the active/passive array tends to infinity. In the spherical wave model based on near-field communications, the equivalent channel gain exhibits nonlinear growth with an increasing number of active antennas/passive elements, governed by the new parameter of angular span [102]. As the number of active antennas/passive elements tends to infinity, the equivalent channel gain converges to a constant value [79][97]-[101].

Compared to co-located massive MIMO arrays, sparse massive antenna arrays have a larger physical aperture, making their near-field characteristics more prominent. [103] studies the performance of uniform sparse antenna array. By exploiting the non-uniform distribution of the spatial angle difference, it is shown that sparse antenna arrays may achieve better interference suppression and super-resolution spatial localization capabilities. **Fig. 3.13** shows the cumulative distribution function of communication rates for co-located and uniform sparse antenna arrays, and sparse array can achieve more than four-times data rate than co-located ULA.

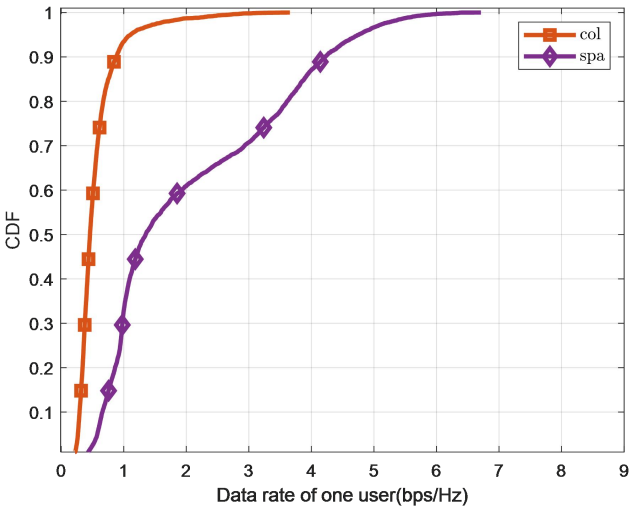

Fig. 3.13 CDF of data rate for co-located and sparse array[103]

Furthermore, [104]-[107] studied a novel modular array architecture to accommodate extremely large arrays, termed modular XL-array. All array elements in modular XL-array are regularly deployed in a modular manner on a common platform. Each module is comprised of a moderate/flexible number of array antennas with the inter-element spacing typically in order of half-wavelength, while different modules are separated by the relatively large inter-module spacing, so as to enable conformal capability with the deployment environment in practice. [104][105] proposed the near-field non-uniform spherical wave (NUSW) model for modular XL-array. Under this model, the authors derived the closed-form expression for near-field SNR, which reveals the SNR scaling law and asymptotic performance, as well as the difference from the conventional far-field uniform plane wave (UPW) model. **Fig. 3.14** shows

that the SNR result under UPW model grows linearly unboundedly, while the SNR result under NUSW model approaches to a constant value. According to the characteristics of modular array architecture, [106] proposed sub-array based uniform spherical wave (USW) models under different angles/common angle, and analysed its near-field beam focusing patterns. It can be seen from **Fig. 3.15** that compared to co-located counterpart with the same number of antennas, modular XL-array can significantly enhance spatial resolution from angular and distance dimensions, while at the cost of more severe grating lobes. To further alleviate the issue of grating lobes, [107] proposed a user grouping strategy based on greedy algorithm for the multi-user modular XL-MIMO communication system. As a result, users located within the grating lobes of each other are not allocated to the same time-frequency resource block (RB), which greatly mitigates inter-user interference (IUI) in multi-user scenarios. As can be seen in **Fig. 3.16**, in contrast to co-located counterpart, modular XL-MIMO can significantly enhance the communication performance.

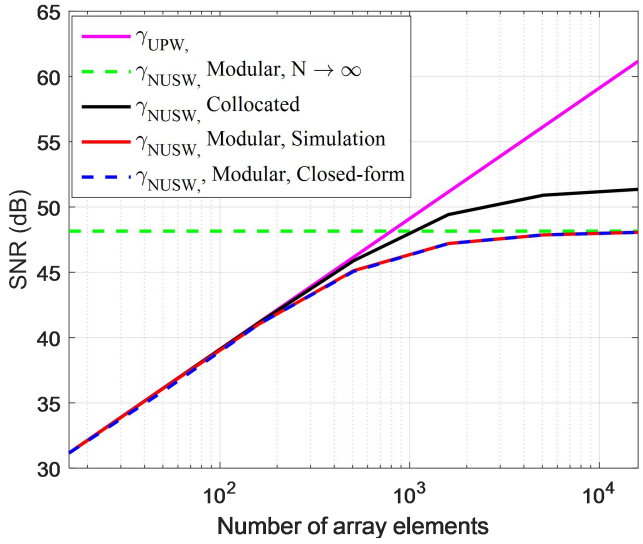

Fig. 3.14 SNRs versus the number of array elements for different models[104].

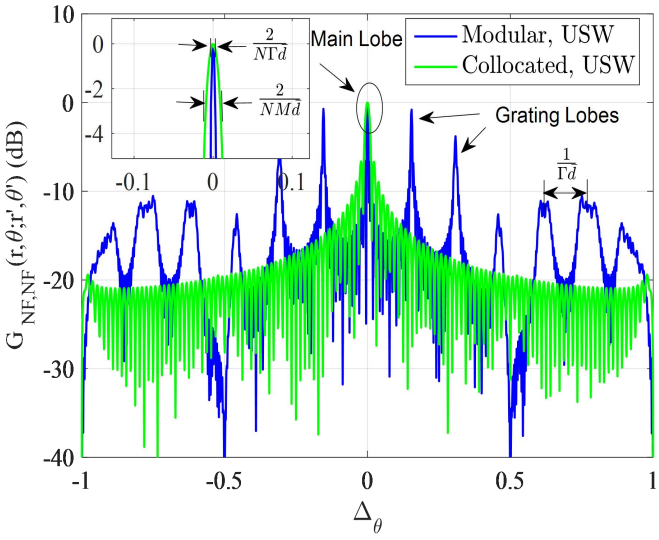

(a) Near-field beam focusing patterns versus spatial frequency differences.

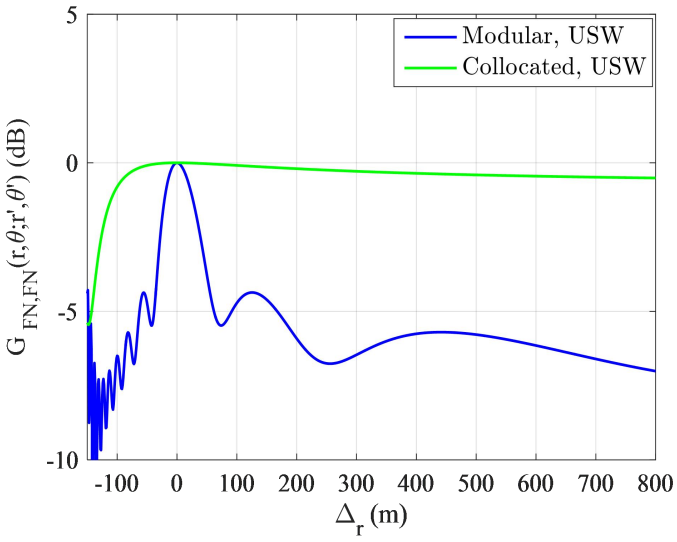

(b) Near-field beam focusing patterns versus distance differences.

Fig. 3.15 Near-field beam focusing patterns under different array architectures[106][107].

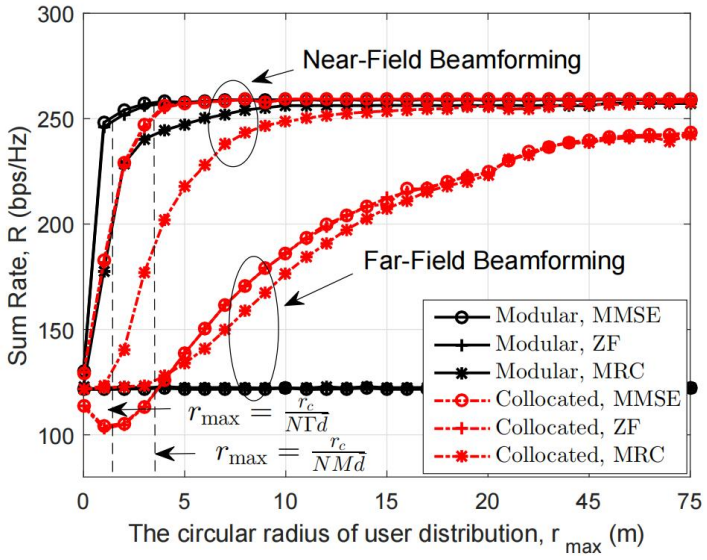

Fig. 3.16 Achievable sum rates for modular and co-located arrays versus the circular radius of user distribution, under far-field and near-field linear beamforming [107].

Compared to large-scale active antenna arrays, the passive RIS is more likely to achieve extremely large-scale configurations in practice due to its appealing advantages, such as low cost and low energy consumption. In communication systems where an extremely large-scale RIS(XL-RIS) is deployed near the base station (BS) side, as illustrated in **Fig. 3.17**, the distances from users to the RIS and the BS are nearly the same. Moreover, when the IRS is sufficiently large, the effective propagation path loss of the reflected link is comparable to that of the direct link. Due to the half-space reflection nature of the RIS, a BS equipped with omnidirectional antennas will have at most half of its transmitted power reflected by the RIS. Therefore, a desired transmit diversity gain can be further achieved through deliberate design of the reflected link[100][101].

If we consider passive beamforming design with intelligent reflective surfaces, the beamforming gain of massive intelligent reflector arrays in the near-field model no longer strictly follows the

traditional "square-law growth"[108]. Instead, it converges to a constant value as the number of reflective units tends to infinity [101] [109].

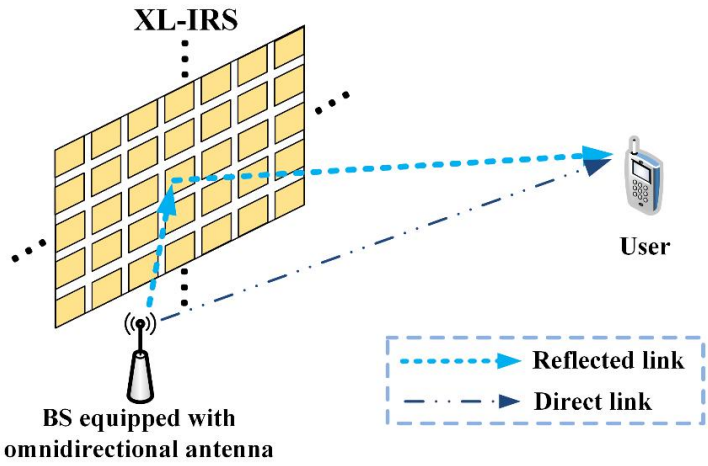

Fig. 3.17 XL-IRS aided communication system

Generally, the path loss increases with distance following a minimum loss exponent α of 2 (i.e., free-space loss model). In other words, the path loss exhibits a square decay with respect to the distance. However, reference [101] first unveiled that under near-field conditions, when the size of IRS goes infinity, the equivalent path loss of the reflected link with passive beamforming only decays with the absolute value of the distance, i.e., the equivalent minimum loss exponent α is 1 (the simulation results in **Fig. 3.18** verified this conclusion).

For multi-path XL-MIMO communications, the spatial correlation is of paramount importance for the second-order statistical channel characterization. The far-field uniform plane wave (UPW) based spatial correlation only depends on the power angular spectrum (PAS), which exhibits spatial wide-sense stationarity (SWSS). By contrast, the near-field non-uniform spherical wave based spatial correlation depends on both the scatterers' angles and distances, i.e., power location spectrum (PLS), and SWSS is no longer valid [110][111].

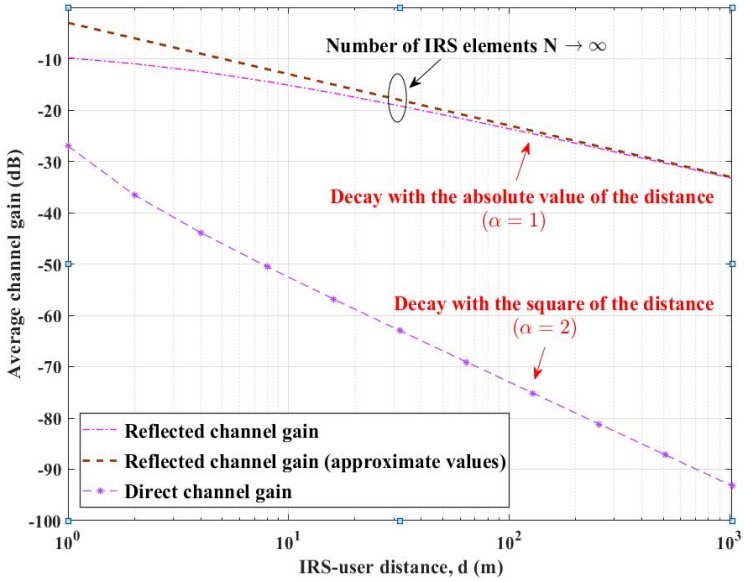

Fig. 3.18 Channel power gain versus the IRS-user distance

In addition to near-field communication, the extremely large-scale multiple-input-multiple-output (XL-MIMO) also provides new opportunities for high-precision sensing due to its ultra-high spatial resolution. In this context, the near-field sensing exhibits more practical scaling laws compared to far-field models [112]. Moreover, when the number of antennas in the XL-array goes infinity, the Cramer-Rao Bounds (CRBs) for angle estimations in XL-MIMO radar no longer decrease without limit, but converge to a constant value [113]. To investigate the fundamental limit of the proposed system's positioning accuracy, the authors in 133 obtained the Fisher Information Matrix (FIM) and CRLB while considering the antenna radiation pattern. The analysis results indicate that the Fisher Information Matrix grows quadratically with the size of the RIS (see **Fig. 3.19**).

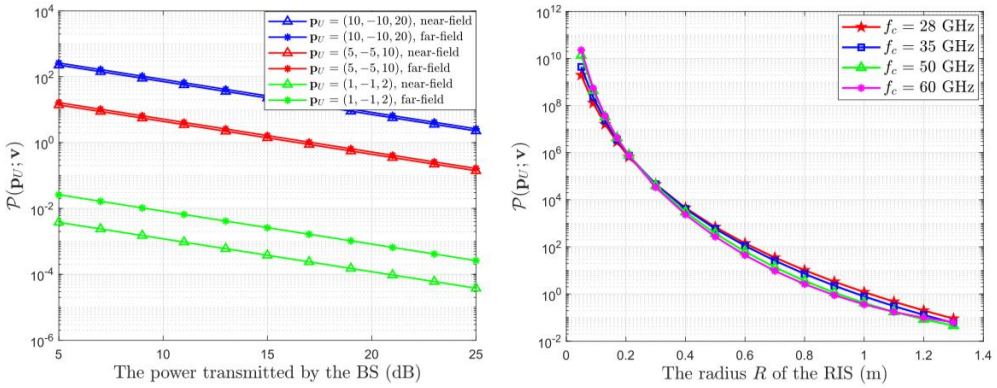

Fig. 3.19 RIS-assisted Localization Performance

Pizzo, Marzetta and other scholars have proposed to model the communication channel corresponding to a near-field massive antenna array in the wave number domain in the papers[115]-[117]. The main idea is to reconstruct the HMIMO channel based on Fourier expansion using a finite number of sampling points of the channel in the wave number domain, as shown in **Fig. 3.20**. Similar to the Fourier transform between the time and frequency domains, the relationship between the spatial and wave number domains is also described by the Fourier transform, and the spatial domain channel can be characterized by the Fourier transform of the wave number domain channel, which is denoted by:

$$h(\boldsymbol{r}, \boldsymbol{s}) = \frac{1}{(2\pi)^2} \iiint a_r(\boldsymbol{k}, \boldsymbol{r}) H_a(k_x, k_y, \kappa_x, \kappa_y) a_s(\kappa, \boldsymbol{s}) dk_x\, dk_y d\kappa_x d\kappa_y \tag{3.10}$$

where $\mathrm{H_a}(\mathrm{k_x}, \mathrm{k_y}, \kappa_\mathrm{x}, \kappa_\mathrm{y})$ denotes the wave number domain channel, $\mathrm{a_r}(\mathrm{k}, \mathrm{r})$ denotes the received wave vector, $\mathrm{a_s}(\kappa, \mathrm{s})$ denotes the transmitted wave vector and $\mathrm{h}(\mathrm{r}, \mathrm{s})$ is the spatial domain channel. From the above equation, it can be seen that the channel model consists of three main components, i.e., the transmit and receive wave vectors and the wave number domain channel. Therefore, the modeling of the spatial domain channel can be equated to the alternative modeling of the wave number domain channel, which is given by the following equation:

$$H_a(k_x, k_y, \kappa_x, \kappa_y) = S^{\frac{1}{2}}(k_x, k_y, \kappa_x, \kappa_y) W(k_x, k_y, \kappa_x, \kappa_y) \tag{3.11}$$

where the wave number domain channel can be expressed in terms of the channel spectral density $\mathrm{S}(\mathrm{k_x}, \mathrm{k_y}, \kappa_\mathrm{x}, \kappa_\mathrm{y})$ related to the scattering environment and antenna arrangement. $\mathrm{W}(\mathrm{k_x}, \mathrm{k_y}, \kappa_\mathrm{x}, \kappa_\mathrm{y})$ relates to the stochastic properties of the channel. Wave number domain channels generally have a sparse structure, i.e., they are dominated by a finite number of nonzero coefficients. Based on sampling

theory, the wavelength domain channel can be approximated by uniformly sampling a finite integral region. The accuracy of the channel approximation depends on the number of points of the region being sampled. As the computational complexity increases, one can obtain a more accurate representation of the channel by generating more samples.

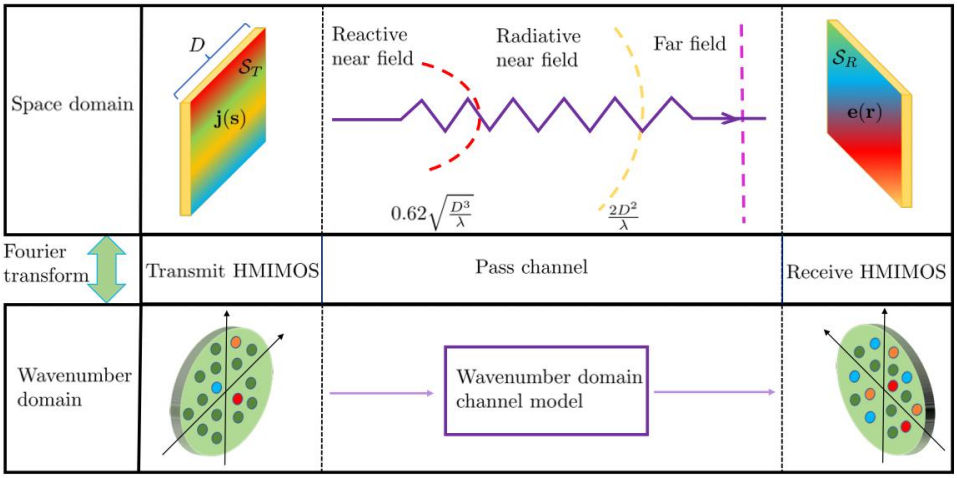

Fig. 3.20 Fourier plane wave expansion channel model

The simulation results corresponding to the spherical wave channel modelling are shown in **Fig. 3.21**, and it can be seen that the far-field Rayleigh fading model is no longer applicable at this point, while the modelled channel model coincides with the physical Clarke model.

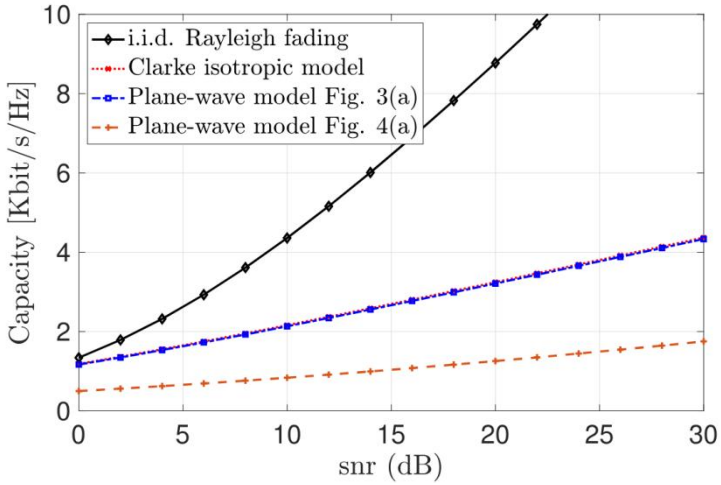

Fig. 3.21 Fourier plane wave expansion channel capacity simulation

The contribution [118] characterized the theoretical capacity limits of near-field communications based on electromagnetic propagation channels in **Fig. 3.22**. From the Maxwell's equations and the Helmholtz wave equation which describe the electromagnetic wave propagation properties, [118] used the Green's function to establish an electromagnetic near-field channel model for extremely large-scale discrete array with single-polarized antennas. Then, for the single-user scenario, the authors derived the closed-form capacity limit when the array has an extremely large aperture. They also revealed the impact of antenna polarization mismatch and discrete aperture on the system performance in the near field. Additionally, based on the proposed channel model, the authors proposed a more general expression for near-field Rayleigh distance, depicting the influence of signal incident angles and

non-stationary array power on the field boundaries. Furthermore, for the multi-user scenario, the authors exploited the non-stationary features extracted from the single-user scenario to propose two low-complexity linear precoding schemes based on the concept of visibility regions and utilizing the method from graph theory. These algorithms effectively addressed the high computational complexity challenges associated with extremely large-scale antenna arrays.

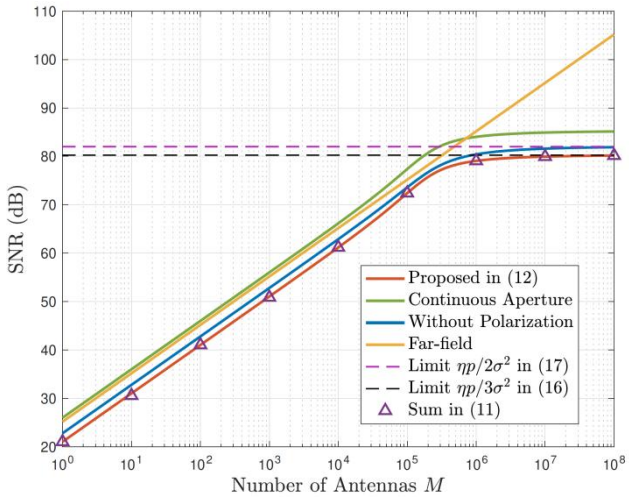

Fig. 3.22 Near-field electromagnetic channel capacity limit

The reference [119] provides a comprehensive summary overview of the current principles and technologies of HMIMO array near-field communication at the software and hardware levels, which is conducive to a full understanding of the principles, technological evolution, and development direction of HMIMO near-field communication.

Fig. 3.23 HMIMO Communication Application Scenarios

3.4.2 Near-Field Measurement and Near-Field to Far-Field Transformation

Electromagnetic scattering characteristics refer to the various information contained in the scattered waves formed by the radiation of induced currents on the surface of an object when electromagnetic waves are irradiated. Measurement of electromagnetic scattering characteristics refers to obtaining information such as the radar cross section (RCS) and its statistical characteristics, angular scintillation

and its statistical characteristics, polarization scattering matrix, and distribution of multiple scattering centers of a target through experimental instruments or professional testing equipment [120][121]. According to different testing distances, it can be classified as far-field measurement, compact-field measurement, and near-field measurement.

Far-field measurement requires a testing distance of $R \geq 2d^2/\lambda$, where d is the maximum size of the target and λ is the testing wavelength. Therefore, a larger space is required. Outdoor far-field testing sites require a large amount of land resources, and the site is also affected by natural meteorological environments such as precipitation, light, temperature, humidity, and wind speed. Although indoor far-field measurement avoids interference from the testing environment, it still requires the construction of large-scale darkroom buildings and the extensive installation of absorbing materials, which makes its construction and maintenance costs high.

Compact-field measurements occupy less space than far-field measurements. However, the contraction field requires high technical requirements and limited static area, making conducting full-scale testing for large targets impossible. Meanwhile, its higher cost makes it not an optimal choice.

Indoor near-field testing is a testing method that has developed in recent decades. Near field refers to testing distances less than the classical far-field conditions ($R<2d^2/\lambda$). Indoor near-field testing does not meet far-field conditions, and the measured data differs from the physical definition of scattering cross-sectional area, which cannot directly reflect the scattering characteristics of the target. The near-field scattering characteristics test results must be transformed into the target scattering cross-section obtained under far-field conditions through near-field and far-field transformation techniques. Therefore, high transformation accuracy, fast speed, and near-field and far-field transformation technology are the most critical factors determining the performance of indoor near-field testing fields. Indoor near-field testing can be divided into planar near-field scanning, cylindrical near-field scanning, and spherical near-field scanning according to the scanning method, and each scanning method requires corresponding near-field and far-field transformation algorithms. In recent years, near-field and far-field transformation technology has become a focus of research for scholars in target characteristic testing both domestically and internationally. The near-field and far-field transformation algorithm based on synthetic aperture imaging, studied by LaHaier, a scholar from General Dynamics in the United States, has become a hot topic of industry experts due to its simple implementation, high transformation accuracy, and good denoising function.

Early methods for measuring target characteristics were limited by testing equipment or locations and were often tested through narrowband and angle scanning. Even today, the ground plane field, which is most widely used in field testing, is more suitable for narrowband testing of targets [122]. The commonly used methods for near-far field transformation in narrowband measurements include Merlin filtering [123], equivalent aperture secondary radiation method [124], Hankel extrapolation method [125][126], etc.

Narrowband measurement conditions limit the near-field to far-field transformation technology in narrowband measurement. Traditional algorithms use certain approximations in the derivation process, which limits their applicability. Broadband measurement of targets can obtain electromagnetic scattering characteristics at multiple frequency points, and the measurement results contain more dimensional scattering information, which can improve the accuracy of single station near-field and

far-field transformation[125]. Spherical near-field to Far-Field Transformation (CNFFFT) is commonly used in broadband measurements for near-field and far-field transformation. The CNFFFT algorithm, proposed by the LaHaie team [126]-[130], is a highly accurate and widely used near-field and far-field transformation algorithm in engineering applications.

4 Channel Measurement and Modeling of Near-field

In the era of 5-th generation (5G), 3D MIMO is considered to be an important practical technology that enhances the performance of communication systems [131]. When the communication distance between base stations and users is greater than the Rayleigh distance, users are located in the far-field region of the base station. At this point, the electromagnetic waves reaching the base station array can be approximated as plane waves. Conversely, electromagnetic waves reaching the base station array need to be modeled as spherical waves when the communication distance is less than the Rayleigh distance [32]. At present, the new mid-band has attracted extensive attention from industry and academia[132]. In December 2023, the Third Generation Partnership Program (3GPP), the leading standardization organization leading the development of the global mobile communications industry, identified the first 16 RAN proposals for Rel-19, including the 7-24 GHz channel model research section, which includes near-field and spatially non-stationary channel measurement and modeling. In the next generation communication systems, the array size and frequency will continue to increase, and the near-field range of Extremely Large Aperture Array (ELAA) systems can reach several tens of meters or even hundreds of meters. In typical deployment scenarios, it is necessary to consider near-field communication[133][134]. Understanding channel characteristics and models is a prerequisite for the design and technical evaluation of communication systems. Therefore, comprehensive channel measurements and accurate channel characterization are needed. This section will introduce near-field channel research from the dimensions of channel measurement and channel modeling, including channel measurement, statistical models, deterministic models, near-field channel spatial non-stationary characteristics, continuous element channel models, discrete element channel models, and so on.

4.1 Near-field Channel Measurement

Channel measurement equipment is used to obtain the Channel Impulse Response (CIR) of the antennas at the transmission and reception ends of the link. As shown in **Fig. 4.1**, there are mainly two types of channel measurement platforms: time-domain channel measurement based on correlation and frequency-domain channel measurement. Correlation-based channel measurement platforms have the advantages of short sampling time and flexible operation at the transmission and reception ends. However, the disadvantages include limited operating bandwidth, limited system dynamic range, and complex synchronization between the transmission and reception ends [135]-[137]. Channel measurement platforms based on Vector Network Analyzers (VNAs) belong to the frequency-domain channel detection system. The advantages of this type of system include scalable working frequencies and bandwidth, high dynamic range, and ease of calibration. However, the frequency scanning time for such detection systems is typically long [138][139]. Therefore, VNA-based channel measurement platforms are usually limited to static scenarios. For the measurement of near-field MIMO channels, greater attention should be paid to the measurement capabilities in the spatial domain, as effectively utilizing the spatial dimension is a key task in near-field MIMO technology.

To achieve the measurement of near-field channels, there are currently several approaches for capturing the spatial distribution characteristics of the channels, including real antenna arrays, switchable antenna arrays, phased arrays, and virtual antenna arrays. However, when it comes to near-field channel measurements involving hundreds of antenna elements, most of these approaches face challenges. For real antenna arrays, switchable arrays, and phased arrays, the hardware cost and calibration complexity become very high due to the need for large arrays with physical dimensions. Virtual antenna arrays are formed by mechanically moving a single antenna unit (or multiple antenna elements in the case of small antenna arrays) to create a large antenna array [131][140]-[142]. This

method allows for convenient implementation of scalable array configurations and is the most commonly used in large-scale MIMO channel measurements. However, due to the slow mechanical movement, the measurement scenarios of virtual antenna arrays are limited to quasi-static environments.

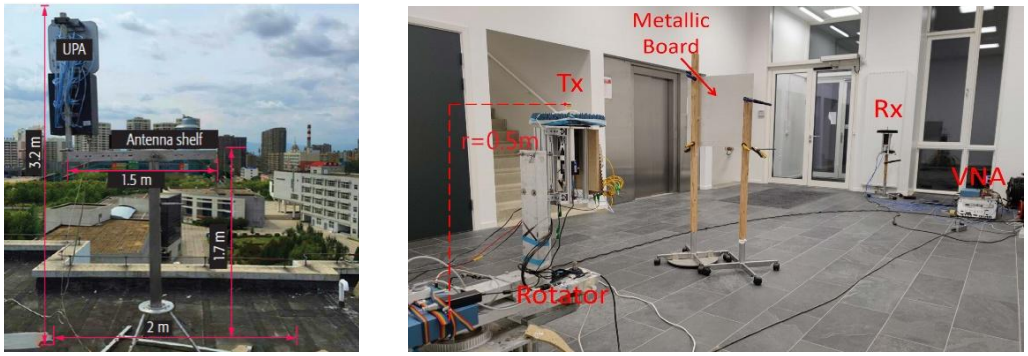

(a) **Time domain** (b) **Frequency domain**

Fig. 4.1 Channel measurement platforms in time and frequency domains[131][142]

As shown in **Fig. 4.2**, near-field channel measurements based on a virtual array with a Vector Network Analyzer (VNA). A rotator is used to achieve a uniformly circular array with different radii. For each element, the VNA performs frequency sweeping to collect the channel impulse response. In the current measurement setup, both the transmitter and receiver are equipped with omnidirectional antennas, and the line-of-sight distance is 6.5 meters. A metal plate is placed between the transmitting and receiving antennas as an obstacle. The Rx antenna forms a virtual circular array with a radius of 0.5 meters by mechanically rotating from 0° to 360° using a turntable, with a rotation step of 0.15°, forming 2400 antenna elements. The measurement frequency range is from 95 GHz to 105 GHz. From the results, several "S"-shaped curves can be observed, identified as multipath components with different delays on different array elements. This is a result of the significant variation in the propagation distance of multipath due to the near-field spherical wavefront effect. Additionally, in this scenario, most of the multipath measurements appear as incomplete "S"-shaped curves distributed across some elements, indicating the spatial non-stationarity of the channel. Partial obscuration occurs because some physically limited objects in the scene prevent the complete capture of multipath across the entire large array. The results suggest the presence of near-field and spatially non-stationary characteristics in ultra-large-scale MIMO channels. In reference[143], based on a time-domain channel measurement platform, virtual array measurements with 256 elements were conducted in the 3.5 GHz frequency band under LOS and NLOS conditions. Changes in cluster appearance and disappearance were observed, and corresponding models were established based on birth-death processes.

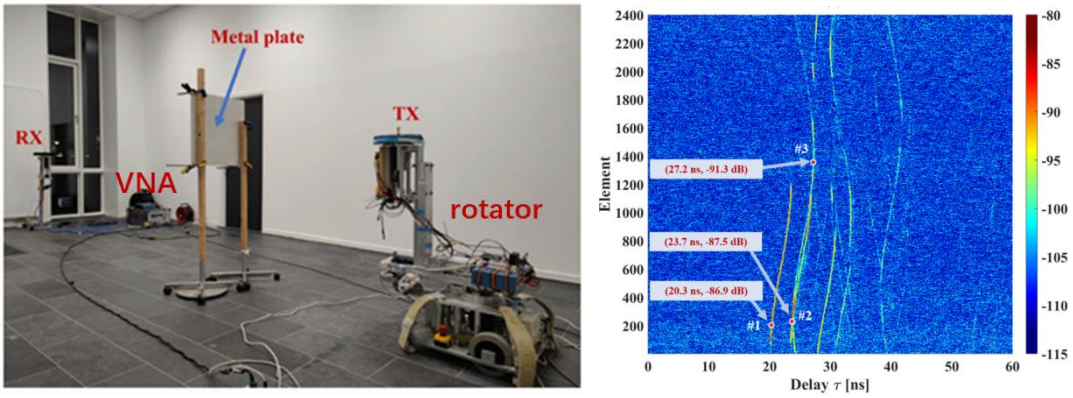

Fig. 4.2 (a) Near-field channel measurements with a virtual array based on VNA. (b) Channel impulse response on the array elements[143]

4.2 Near-field Channel Simulation

Near-field is a concept with relativity, for large-scale antenna array, based on the distance to the center of the antenna from near to far, there are three zones that can be classified, respectively: reactance near-field zone, radiation near-field zone (Fresnel zone) as well as the radiation far-field zone (Fraunhofer zone). In the reactance near-field zone, the radiation pattern is similar to flat ripples with non-significant amplitude variations; In the radiation near-field zone, the antenna pattern is smoother with a tendency to beam forming; In the radiation far-field zone, the main lobe as well as the side lobe have been completed forming. The boundary distance between the radiated near field and the radiated far field is called the Rayleigh distance. In this scenario, the far-field condition is still satisfied between the transmitting antenna element and the receiving antenna element.

For the case where the distance between the transceiver antenna elements is also near-field, the simulation results are shown as in **Fig. 4.3**.

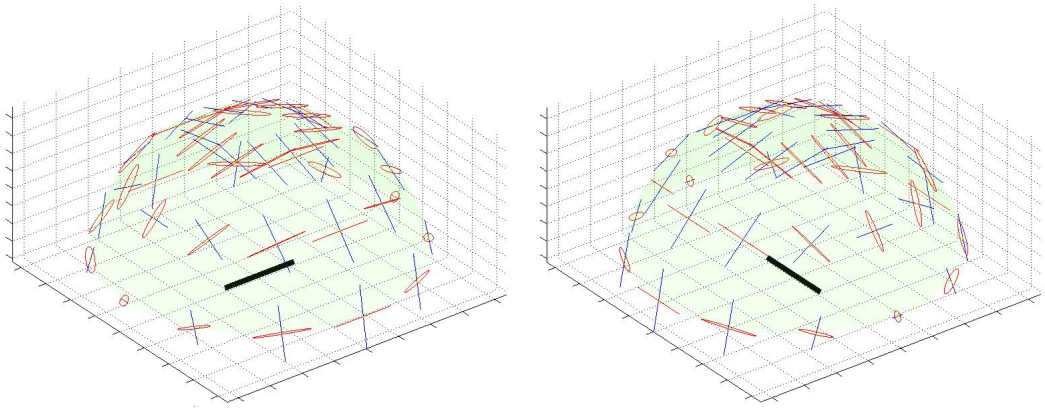

(1) The near field electromagnetic field distribution for horizontal polarization electric dipole (left).
(2) The near field electromagnetic field distribution for vertical polarization electric dipole (right).

Fig. 4.3 Near field simulation in element level

As shown in **Fig. 4.3**, the electric and magnetic field are demonstrated corresponding to horizontally and vertically polarized current sources in the near-field, respectively. The black line at the center of the hemisphere indicates the direction of the current source, the red line indicates the trace formed by the end of the electric field strength vector, and the blue line indicates the trace formed by the end of the electric field strength vector. It can be observed that the electric field strength vector exhibits elliptical polarization in the near field, and the axial ratio, major axis inclination angle, and ellipticity angle of the electric field strength at the near field points with different orientation angles are different, while the magnetic field strength exhibits stable linear polarization characteristics, which means that Poynting vector is a time-varying vector in the near field, which is a major difference between the element-level near field and the panel-level near field.

From point of view of engineering commercialization, the assumption of far-field between the transmitting element and the receiving element is generally still satisfied even for large-scale antenna arrays.

For the case where the transceiver antenna is in the near-field and the LOS/NLOS states between the elements are consistent, the channel states between the other element of the transceiver antenna need to be estimated based on the channel states of the Tx/Rx antenna's anchor elements, and the channel states between other elements of the Tx/Rx antennas can be derived based on the dual-mobility

spatial consistency model when it is assumed that the NLOS paths of the wireless channel between the anchor elements are dominated by the specular reflections, assuming there are no spatial non-stationarity between any two pairs of elements of Tx and Rx antennas, such as channel birth and death etc.

To configure the antenna array as depicted in **Fig. 4.4**, operating at 6 GHz. The simulation results of spatial consistency for the intra-element in BS antenna are shown **Fig. 4.6** - **Fig. 4.8** in near field with a frequency of 6 GHz and 1024 elements (assuming the scenario that the terminal antenna is a single element).

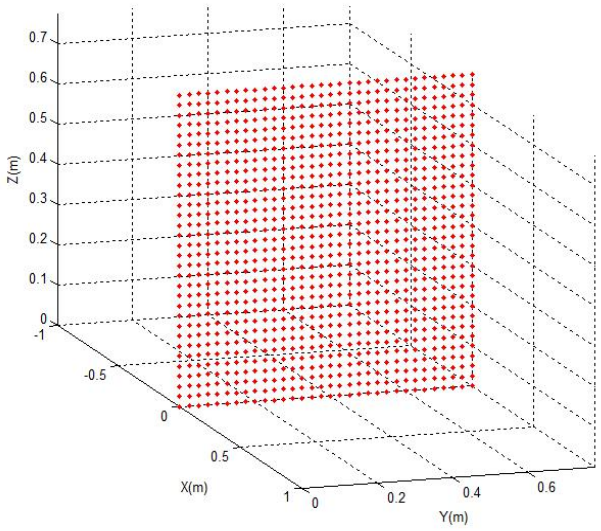

Fig. 4.4 The deployment of large antenna array (6GHz, 1024elements)

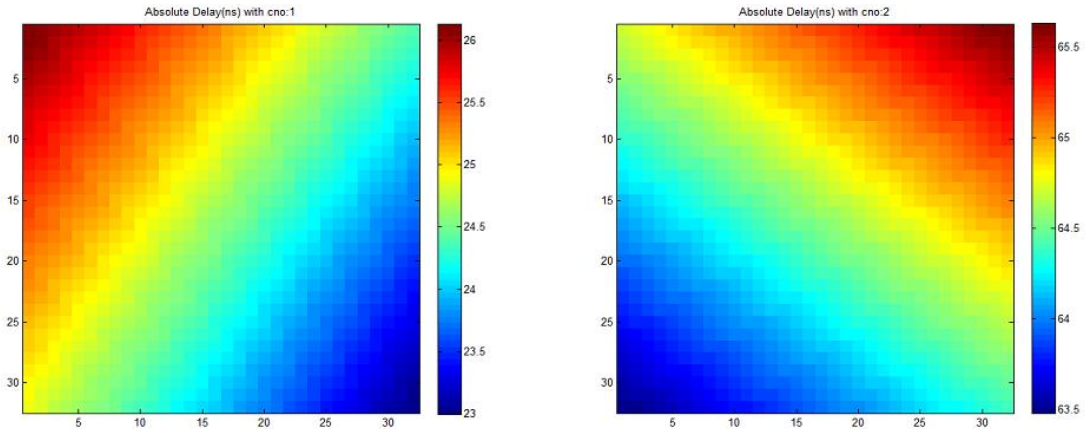

(1) Absolute delay of the 1st ray per element in BS antenna (left).
(2) Absolute delay of the 2nd ray per element in BS antenna (right).

Fig. 4.5 Absolute delay of a ray per element in BS antenna

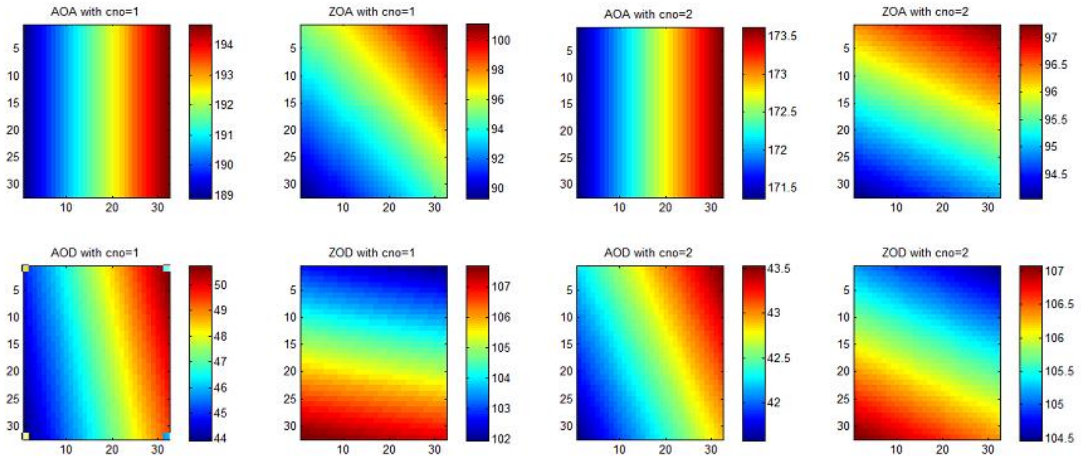

(1) AoA/AoD/ZoA/ZoD of the 1st ray per element in BS antenna (cno=1)
(2) AoA/AoD/ZoA/ZoD of the 2nd ray per element in BS antenna (cno=2)

Fig. 4.6 AoA/AoD/ZoA/ZoD of a ray per element in BS antenna

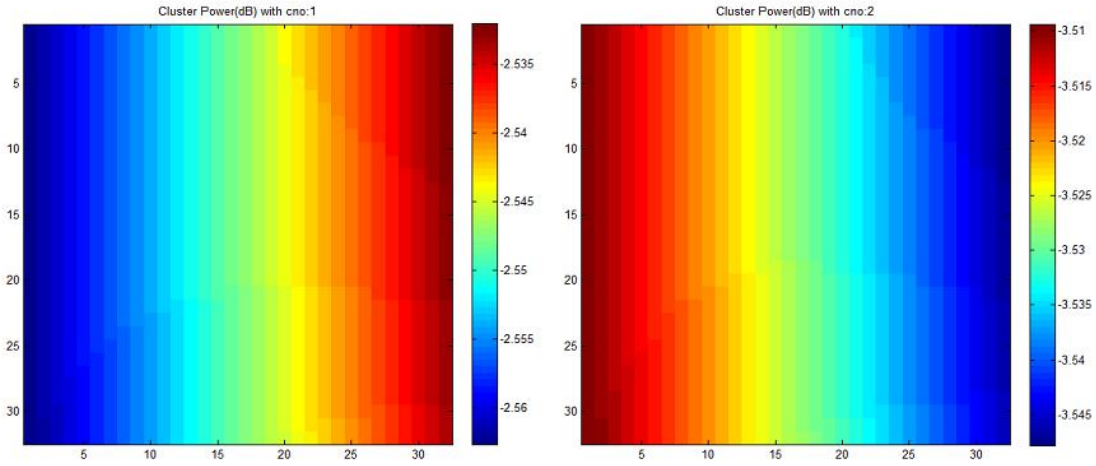

(1) Power gain of the 1st ray per element in BS antenna (cno=1)
(2) Power gain of the 2nd ray per element in BS antenna (cno=2)

Fig. 4.7 Power gain of a ray per element in BS antenna

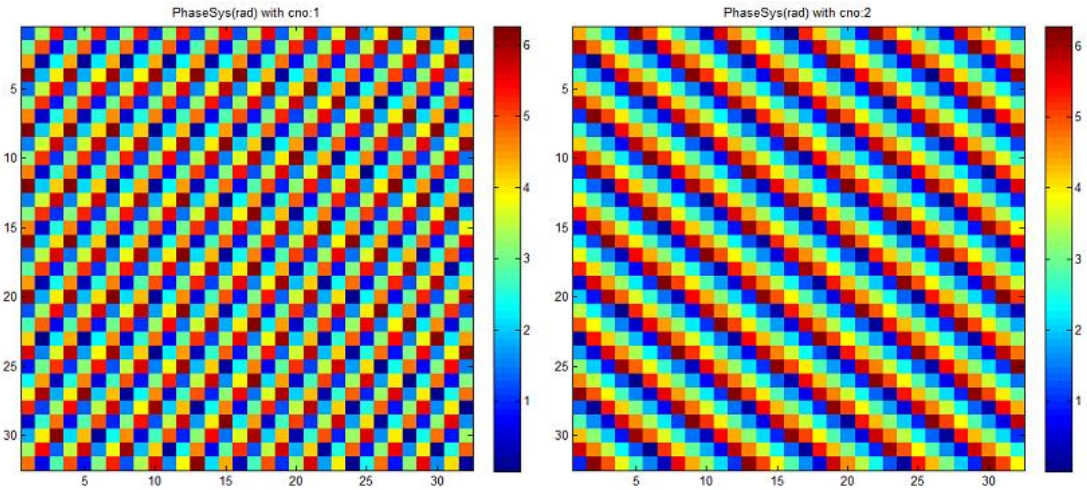

(1) Phase of the 1st ray per element in BS antenna (cno=1)
(2) Phase of the 2nd ray per element in BS antenna (cno=2)

Fig. 4.8 Phase of a ray per element in BS antenna

In the case of the presence of scatterers in the near-field of antenna arrays, it is necessary to study the correlation characteristics of the wireless channel among the elements in large antenna arrays based on the near-field scattering model (electromagnetic equations, high-frequency solution, or full-wave numerical solution).

As shown in **Fig. 4.9**, for an PEC conductor sphere near the large-scale array, the incident wave vector of the the plane wave is shown as the blue line, and the black points in the antenna array indicate the region of the incident wave vector that is blocked by the scatterer, and the red points indicate the region that is not blocked. The simulation results of the magnitude and absolute phase are shown in **Fig. 4.10** to **Fig. 4.11** per element after blocking , reflection and diffraction by scatter.

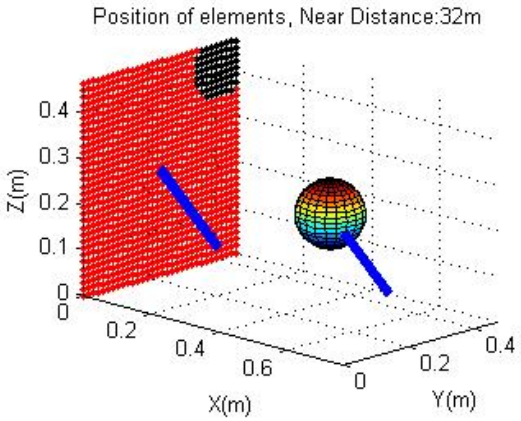

Fig. 4.9 The position of antenna array and PEC sphere as well as the incident wave vector

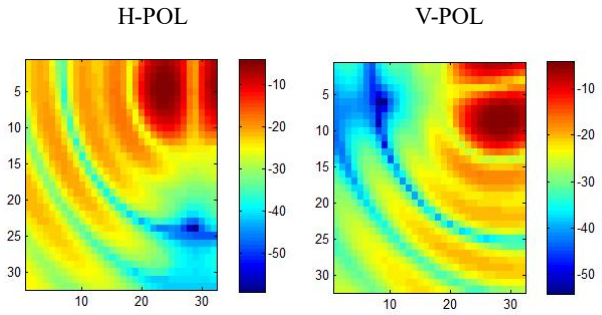

Signal Strength Gain(dB)

Fig. 4.10 The distribution of signal strength gain in antenna array due to H-pol and V-pol incident

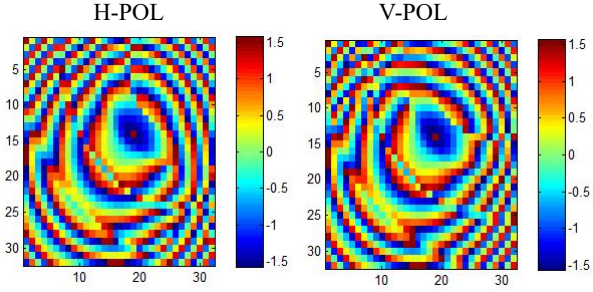

Phase (rad)

Fig. 4.11 The distribution of phase in antenna array due to H-pol and V-pol incident

As shown in **Fig. 4.12**, for a random scatter near the large-scale array, the incident wave vector of the plane wave is shown as the blue line, and the black points in the antenna array indicate the region of the incident wave vector that is blocked by the scatterer, and the red points indicate the region that is not blocked. The simulation results of the magnitude and absolute phase are shown in **Fig. 4.13** to **Fig. 4.14** per element after blocking, reflection and diffraction by scatter.

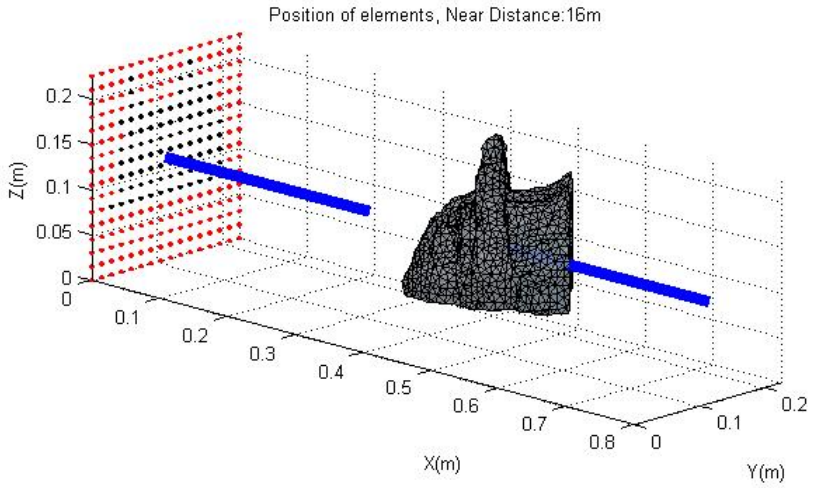

Fig. 4.12 The position of antenna array and random scatter as well as the incident wave vector

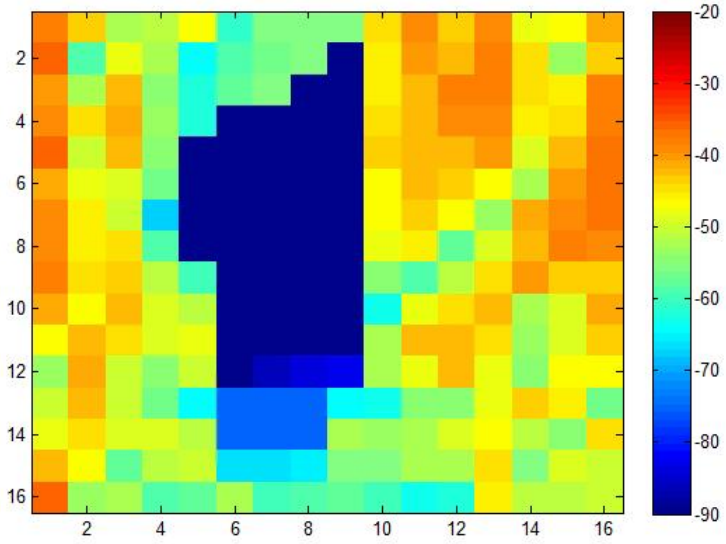

Fig. 4.13 The distribution of signal strength gain in antenna array due to V-pol incident

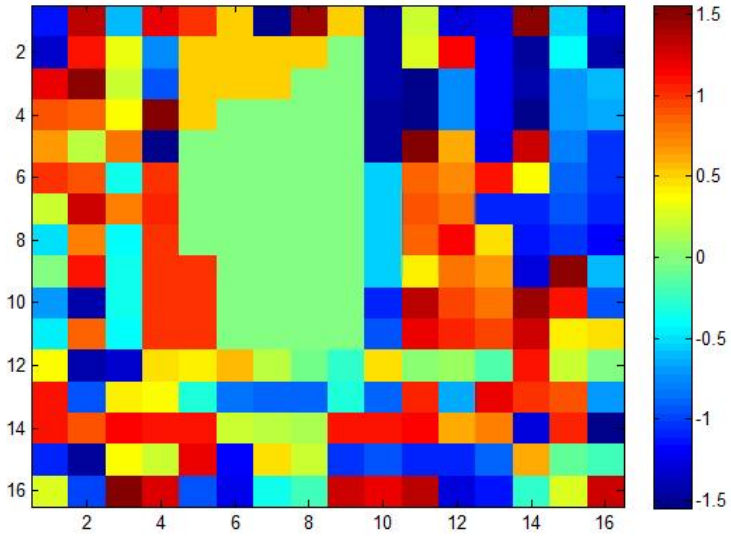

Fig. 4.14 The distribution of phase in antenna array due V-pol incident

4.3 Near-field Channel Modeling

There is a lot of work in the literature on massive MIMO channel modeling that considers near-field effects. For deterministic channel modeling, the METIS project [144] proposed a massive MIMO channel model based on ray tracing, which can represent spatial non-stationary characteristics. However, the high computational complexity and lack of detailed digital maps and material databases make this deterministic modeling method less applicable in some scenarios with complex environments. In [145], the authors proposed a deterministic ray-tracing method for THz channel model, and showed that the ray-tracing channel model captured the propagation characteristics well. For statistical channel modeling, the COST 2100 model [146] proposed the concept of the visible region for the first time to represent the spatially non-stationary channels of MIMO antennas, confining the cluster of mobile terminals to a limited region. In [147], the concept of the visible region is further extended to massive MIMO antenna arrays. Specifically, only the array elements in the visible region can see the cluster, while the array elements outside the visible region cannot. Based on the concept of the visible region, the birth and death processes on the array axis were used in [148] for statistical characterization of spatial non-stationary properties. To verify the model, statistical properties such as correlation and average lifetime of clusters on the matrix are analyzed numerically. In [149], based on channel characteristics, a stationary interval partitioning method on XL-MIMO arrays is studied. In [150], an efficient channel simulation method applied to ray tracing was proposed to realize the simulation of near-field and spatially non-stationary channels under the deployment of very large-scale antennas with guaranteed accuracy.

In [151], a new massive MIMO channel model framework is proposed, which accounts for near-field and spatial non-stationarity properties. Massive MIMO channels with near-field and spatially non-stationary properties are captured by spherical wave propagation and physical multipath propagation mechanisms. The validation based on channel measurement and model proves its effectiveness, which is briefly described below.

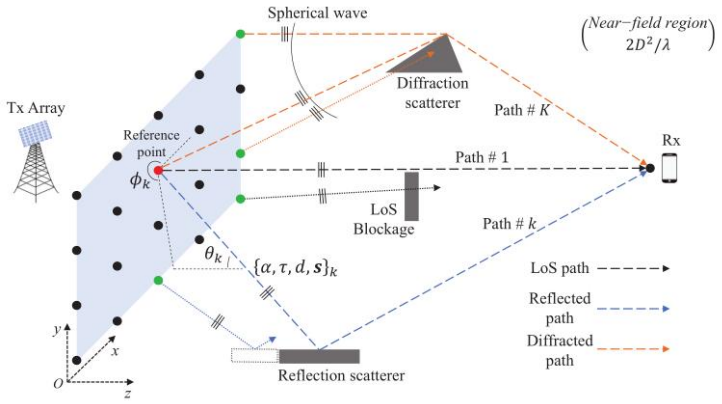

Fig. 4.15 Spherical propagation with the SnS characteristic

We assume there exist K SnS spherical-propagation paths between the Tx array and Rx. The massive MIMO channel at the frequency f can be modeled as a superposition of CFRs of the K paths on the array. It can be succinctly expressed as

$$\mathbf{H}^{sns}(f) = \mathbf{S} \odot \mathbf{A}(\boldsymbol{f}) \cdot \mathbf{H}(\boldsymbol{f}) \tag{4.1}$$

where $\mathbf{H}^{sns}(f)$ comprises M complex values, i.e., $\mathbf{H}^{sns}(f) \in \mathrm{C}^{\mathrm{M}\times 1}$, f $\in [f_L, f_U]$ denotes the frequency within the designed range, and represents elementwise product operation. A novel matrix **S** is introduced in the proposed modeling framework for the SnS property, which represents a non-stationary parameter matrix reflecting the non-stationary characteristics of the channel. **H**(f) $\in \mathrm{C}^{\mathrm{K}\times 1}$ denote CFRs at f of the K paths at the reference point.

$$\mathbf{H}(f) = [a_1 e^{-j2\pi f\tau_1}, \cdots, a_k e^{-j2\pi f\tau_k}, \cdots, a_K e^{-j2\pi f\tau_K}]^T \tag{4.2}$$

where $\{\alpha_k, \tau_k\}$ represent the complex amplitude and propagation delay of the kth path, respectively. $(\cdot)^{\mathrm{T}}$ denotes the transpose operation. **A**(f) $\in \mathrm{C}^{\mathrm{M}\times\mathrm{K}}$ is the array manifold matrix. The manifold projected on the *m*th antenna element by the kth path, i.e., A's (m, k)th entry $a_{m,k}$, can be represented by the transfer difference of the *m*th element with respect to the reference point, i.e.,

$$a_{m,k}(f) = \frac{\|\mathbf{d}_k\|}{\|\mathbf{d}_{m,k}\|} e^{-j2\pi f \frac{\|d_{m,k}\| - \|d_k\|}{c}} \tag{4.3}$$

where c is the light speed and $\|\cdot\|$ represents the Euclidean norm of the argument. $\boldsymbol{d}_{\mathrm{k}}$ denotes the vector pointing from the reference point to the first scattering source of the *k*th path propagation route. $\boldsymbol{d}_{\mathrm{m,k}}$ denotes the vector pointing from the *m*th antenna element to the source point.

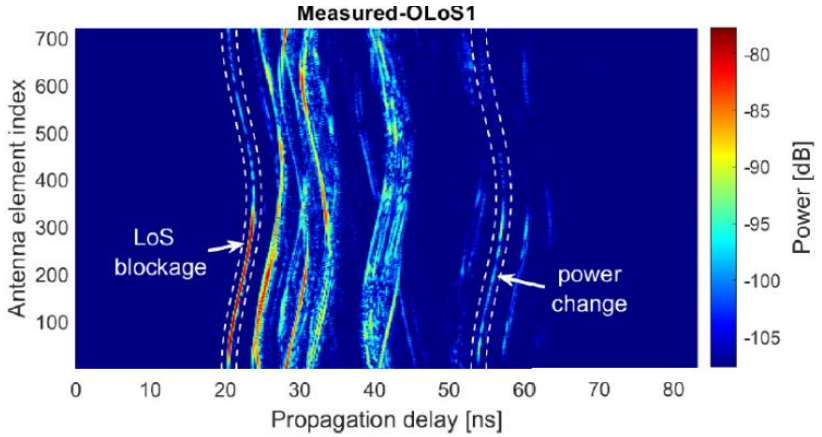

(a)

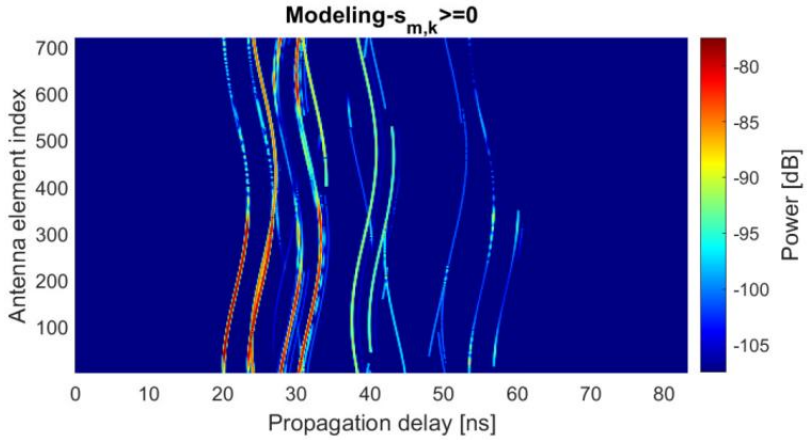

(b)

Fig. 4.16 (a) measurement result, (b) generation of channel model.

Fig. 4.16 shows the verification results. The generated channel by the model is shown in Fig. 3-4, where all SnS phenomena observed in the measurements are captured well. Besides the stationary paths, all SnS paths that have responses on the partial array with/without power change, are accurately generated.

Focusing on the modeling and simulation of ultra-large MIMO channels, [152] proposes an innovative simulation framework based on the 3GPP channel model, which adds support for the spatial non-stationary characteristics of massive MIMO channels and the simulation of near-field characteristics, and realizes the accurate generation of massive MIMO channel coefficients with near-field spatial non-stationary characteristics. The work on 6G channel emulator BUPTCMCCCMG - IMT2030 finish[1].

Because of the larger size of the XL-MIMO array, when the user approaches the array, the channel energy is only concentrated on part of the antennas, which is called the visibility region (VR) [153][154] of the user. In [155][156], VR is defined as the part of the array that occupies the majority of channel energy. In the actual scene with scatterers or obstacles, the scatterers are usually divided into multiple clusters. Thus, in [157]-[159], VR is cascaded by the visibility region Φ_{UC} between the user and the scatterer and the visibility region between the scatterer and the array, which represent the scatterers visible to the user and the array antennas visible to the scatterer, respectively, as shown in **Fig. 4.17**.

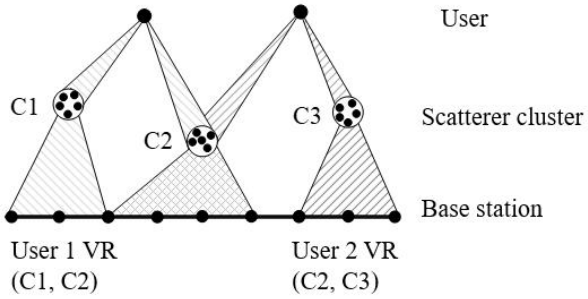

Fig. 4.17 Visibility region of the array and user

When the finite-path channel model is used, the occurrence of non-stationarity makes XL-MIMO channel model different from the traditional channel model, and the variance can be reflected by the steering vector. Firstly, in the vicinity of the array, since plane wave model is no longer accurate, the phase of each element in the steering vector should be described by the spherical wave model.

[1] https://hpc.bupt.edu.cn/dataset-public/home-page

Secondly, the amplitude of each element is no longer the same due to the uneven path loss across the array as well as the interaction caused by obstacles in the environment. Therefore, the spatially nonstationary finite-path channel model of user k is expressed by

$$\mathbf{h}_k = \sum_{c\in\Phi_{\mathrm{UC},k}} \sum_{s=1}^{S_c} \beta_{c,s}\mathbf{a}_{c,s} \tag{4.4}$$

where $\beta_{c,s}$ is the complex coefficient of the path generated by scatterer s in cluster c, which also represents the response of this path on the reference antenna, $\mathbf{a}_{c,s} \in \mathbb{C}^{N\times 1}$ is the steering vector of the path, and N is the number of antennas. By further considering VR, the finite-path channel model is transformed into

$$\mathbf{h}_k = \sum_{c\in\Phi_{\mathrm{UC},k}} \sum_{s=1}^{S_c} \beta_{c,s}\mathbf{a}_{c,s} \odot \mathbf{p}_c \tag{4.5}$$

$$[\mathbf{p}_c]_n = \begin{cases} 1, & if\ \ n \in \Phi_{\mathrm{CA,c}} \\ 0, & else \end{cases} \tag{4.6}$$

where $\odot$ takes Hadamard product, and $\mathbf{p}_c = \{0,1\}^{N\times 1}$ indicates the antennas visible from cluster c [159][160].

In addition, the XL-MIMO channel modeling can be based on the channel covariance matrix, which can also reflect VR. The channel covariance matrix illustrates the statistical covariance of the channel between different antennas and has been widely used in multi-antenna channel modeling. Let $\boldsymbol{R}_{\mathrm{A}} \in \mathbb{C}^{N\times N}$ and $\boldsymbol{R}_{\mathrm{s}} \in \mathbb{C}^{S\times S}$ denote the covariance matrices on the array side and the scatterer side, respectively, where S is the number of scatterers. In this case, the multi-antenna channel model based on channel covariance matrix is

$$\boldsymbol{h}_k = \boldsymbol{R}_{\mathrm{A}}^{\frac{1}{2}} \boldsymbol{H}_w \boldsymbol{R}_{\mathrm{s}}^{\frac{1}{2}} \boldsymbol{h}_w \tag{4.7}$$

where $\boldsymbol{H}_w \in \mathbb{C}^{N\times S}$ and $\boldsymbol{h}_w \in \mathbb{C}^{S\times 1}$ are small scale fading matrices. Since different clusters have different VRs, considering spatially non-stationary scenario, the channel between user k and the base station is represented as

$$\boldsymbol{h}_k = [\boldsymbol{G}_1, \ldots, \boldsymbol{G}_C]\, \boldsymbol{R}_{\mathrm{s}}^{\frac{1}{2}} \boldsymbol{D}_{\mathrm{UC},k} \boldsymbol{h}_{w,k} \tag{4.8}$$

$$\boldsymbol{G}_c = \boldsymbol{D}_{\mathrm{CA,c}} \boldsymbol{R}_{\mathrm{CA},c}^{\frac{1}{2}} \boldsymbol{H}_{w,c} \in \mathbb{C}^{N\times S_c} \tag{4.9}$$

where $\boldsymbol{G}_c$, C, and S_c represent the channel between the array and cluster c, the number of scatterer clusters and the number of scatterers in scatterer cluster c, respectively. S_c and C satisfy $\sum_{c=1}^{C} S_c = S$. $\boldsymbol{D}_{\mathrm{UC},k} = \{0,1\}^{S\times|\Phi_{\mathrm{UC},k}|}$ and $\boldsymbol{D}_{\mathrm{CA,c}} = \{0,1\}^{N\times|\Phi_{\mathrm{CA},c}|}$ denote the cluster visible to user k and the antenna visible to cluster c, respectively. $\boldsymbol{R}_{\mathrm{CA},c} \in \mathbb{C}^{|\Phi_{\mathrm{CA},c}|\times|\Phi_{\mathrm{CA},c}|}$ is the covariance matrix

across antennas within $\Phi_{\mathrm{CA},c}$, while $\boldsymbol{H}_{w} \in \mathbb{C}^{|\Phi_{\mathrm{CA},c}| \times S_c}$ and $\boldsymbol{h}_{w,k} \in \mathbb{C}^{|\Phi_{\mathrm{UC},k}| \times 1}$ are small scale fading matrices.

As shown in **Fig. 4.18**, for antenna arrays or intelligent reflecting surfaces (RIS) based on discrete elements, the resulting near-field channel can be modeled as the complex-valued sum of all far-field channels between each individual transmit antenna (TA) and the receive antennas (RA). This type of channel model is referred to as the Non-Uniform Spherical Wave (NUSW) model [161]. Consequently, the near-field channels between antenna arrays can be characterized by a channel matrix with dimensions corresponding to the numbers of receive and transmit antennas. The degrees of freedom in the near-field channels are determined by the rank of this channel matrix, achieving full rank even in the absence of scatterers. Regarding channel state information (CSI) acquisition, near-field channels demand higher precision than far-field channels to effectively utilize their enhanced degrees of freedom. For extremely large-scale MIMO systems, subarray-based estimation methods might be employed. For spatially discrete antennas, NUSW channel models strike an appropriate balance between accuracy and complexity in most scenarios.

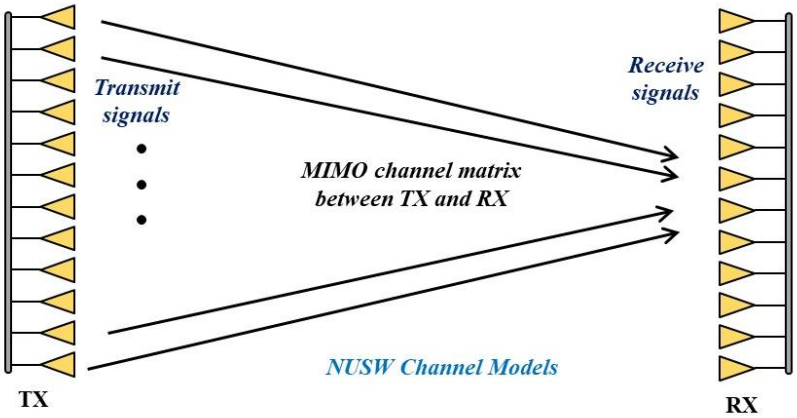

Fig. 4.18 NUSW channel model for spatially discrete antennas

In recent years, meta-materials have been used to realize (approximate) continuous transmit and receive apertures, thus facilitating holographic beamforming. Compared to traditional beamforming techniques, holographic beamforming achieved through continuous-aperture (CAP) antennas provides ultra-high spatial resolution [161]. In the case of continuous-aperture antennas, near-field channel modeling can rely on the Green's function method [162]. In this model, the Green's function can be regarded as the spatial impulse response function between the continuous-element transmitter and the near-field receiver. As depicted in **Fig. 4.19**, employing the Green's function method allows for computing the electromagnetic field distribution in a given area for a specified transmitter current distribution. Consequently, based on the specific properties of the receiving antennas, the received field strength or induced current distribution can be obtained. This model yields an accurate volume-to-volume model (i.e., transmitter effective volume to receiver effective volume) compared to the traditional point-to-point model, enabling full utilization of the higher degrees of freedom in the near-field channel. Similar to discrete antennas, continuous-element antennas also require more precise channel state information due to their channel modeling reliance on Green's functions and spatial integration. Channel state information acquisition for continuous-element antennas remains a challenging subject for future research.

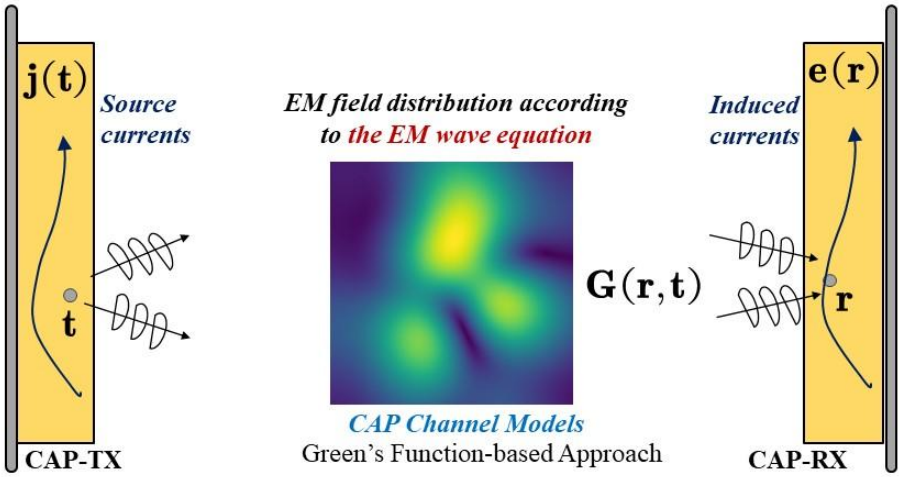

Fig. 4.19 Green's function-based channel model for CAP antennas

The aforementioned use of metamaterial-based aperture antennas, also referred to as holographic MIMO (HMIMO), enables breakthroughs in uncontrollable factors of traditional wireless channels, reshaping the wireless propagation environment and introducing new degrees of freedom, particularly in near-field scenarios. Research has indicated that traditional channel modeling approaches are no longer applicable in near-field channel scenarios [163]. Currently, the most effective near-field modeling approaches are derived from electromagnetic field theory and utilize tools such as computational electromagnetics to characterize wave propagation channels. By combining the advantages of information theory, an electromagnetic field information theory mathematical analysis framework has been established, leading to the development of field propagation models for massive MIMO communications.

The multi-polarized free-space channel, as shown in **Fig. 4.20**, considers both the near-field spherical wave channel and the multi-polarization effects through the vectorial Green's function. Based on this, a model for the multi-polarized near-field spherical wave channel is established.

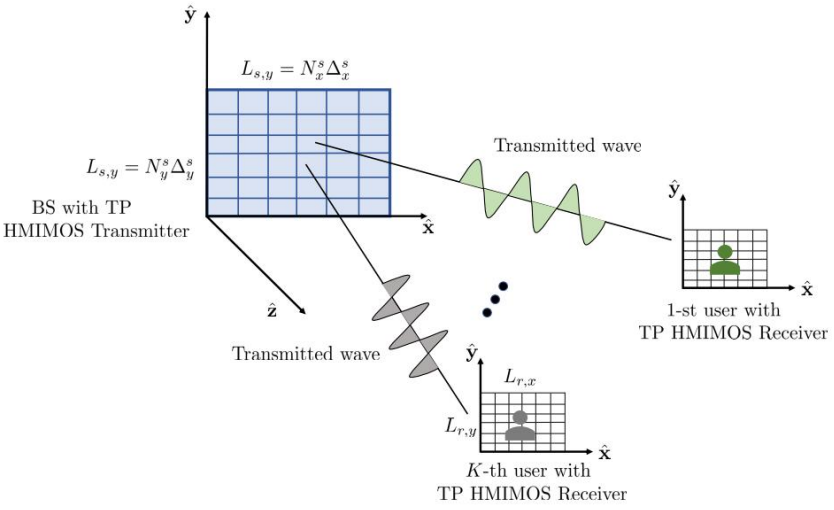

Fig. 4.20 Modeling of near-field multi-polarized spherical waves

The received electric field in the transmitting HMIMO system can be represented as:

$$\mathbf{E}(\mathbf{r}) = \sum_{n=1}^{N_s} \int_{\Delta^s} d\mathbf{r}_n' \bar{\mathbf{G}}\left(\mathbf{r}, \mathbf{r}_n'\right) \cdot \mathbf{J}\left(\mathbf{r}_n'\right) = \sum_{n=1}^{N_s} \int_{-\Delta_x^s/2}^{\Delta_x^s/2} \int_{-\Delta_y^s/2}^{\Delta_y^s/2} dx_0' dy_0' \left[\bar{\mathbf{I}} + \frac{\nabla\nabla}{k_0^2}\right] \frac{e^{ik_0 r_n}}{4\pi r_n} \mathbf{J}\left(\mathbf{r}_n'\right),$$

(4.10)

The channel from the *n*-th transmitting antenna of the HMIMO system to a specific receiving point can be represented as:

$$\mathbf{H}_n = \mathcal{E}(\tilde{R}_n)\mathbf{C}_n = \mathcal{E}(\tilde{R}_n)\left(c_1(\tilde{R}_n)\mathbf{I} + c_2(\tilde{R}_n)\vec{\mathbf{r}}_n\vec{\mathbf{r}}_n\right), \tag{4.11}$$

$$c_1(\tilde{R}_n)=\left(1+\frac{i}{k_0\tilde{R}_n}-\frac{1}{k_0^2\tilde{R}_n^2}\right), c_2(\tilde{R}_n)=\left(\frac{3}{k_0^2\tilde{R}_n^2}-\frac{3i}{k_0\tilde{R}_n}-1\right), \tag{4.12}$$

The size of the receiving HMIMO at the receiver end is typically smaller than that of the transmitting HMIMO at the sender end. Therefore, it is reasonable to assume that the power of each receiving HMIMO antenna is proportional to its size: $\Delta^r = \Delta_x^r\Delta_y^r$. Consequently, the channel between the *n*-th transmitting HMIMO antenna and the *m*-th receiving HMIMO antenna can be expressed as:

$$\mathbf{H}_{mn}=\Delta^s\Delta^r\frac{e^{(ik_0\tilde{R}_{mn})}}{4\pi\tilde{R}_{mn}}\operatorname{sinc}\frac{k_0(x_m-x_n')\Delta_x^s}{2\tilde{R}_{mn}}\operatorname{sinc}\frac{k_0(y_m-y_n')\Delta_y^s}{2\tilde{R}_{mn}}\mathbf{C}_{mn}=\begin{bmatrix}H_{mn}^{xx}, H_{mn}^{xy}, H_{mn}^{xz}\\ H_{mn}^{yx}, H_{mn}^{yy}, H_{mn}^{yz}\\ H_{mn}^{zx}, H_{mn}^{zy}, H_{mn}^{zz}\end{bmatrix}, \tag{4.13}$$

where $\mathbf{C}_{mn} \triangleq c_1(\tilde{R}_{mn})\mathbf{I} + c_2(\tilde{R}_{mn})\vec{\mathbf{r}}_{mn}\vec{\mathbf{r}}_{mn} \in \mathbb{C}^{3\times3}$. Thus the entire channel matrix can be expressed as:

$$\mathbf{H} = \begin{bmatrix}\mathbf{H}_{xx} & \mathbf{H}_{xy} & \mathbf{H}_{xz}\\ \mathbf{H}_{yx} & \mathbf{H}_{yy} & \mathbf{H}_{yz}\\ \mathbf{H}_{zx} & \mathbf{H}_{zy} & \mathbf{H}_{zz}\end{bmatrix} \in \mathbb{C}^{3N_r\times3N_s}, \tag{4.14}$$

where the channel submatrix $\mathbf{H}_{pq} \in \mathbb{C}^{N_r\times N_s}, p, q \in \{x, y, z\}$ represents the channel between the transmitter component in the *p*-polarization direction to the receiver component in the *q*-polarization direction.

The channel capacity of tri-polarized HMIMO is higher compared to dual-polarized HMIMO and conventional unpolarized HMIMO as in **Fig. 4.21** [164].

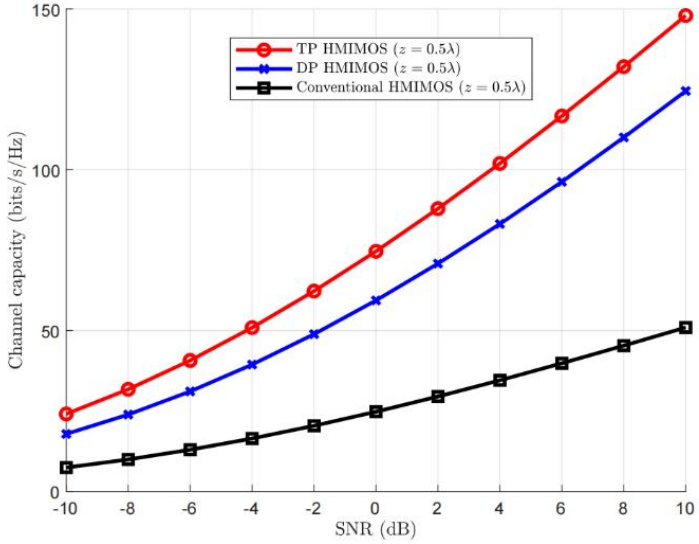

Fig. 4.21 Multi-polarized channel capacity

The existing channel models usually assume that the scattering clusters are located in the near field or the far field. However, in reality, there are mixed near and far fields in the medium and ultra-massive MIMO systems, that is, some scattering clusters are located in the near field and some scattering clusters are located in the far field. In other words, very large MIMO channels usually consist of both far field and near field path components. The existing near-field or far-field channel

models cannot match the characteristics of the hybrid near-field channel, so a channel model considering both the far field and the near field will be established next.

The boundary division between near field and far field has an impact on many aspects of wireless communication systems, such as array antenna characterization, propagation channel, perception, etc. [84]. In order to build a hybrid near and far field channel model, we first discuss the boundary division between far field and near field. According to whether the transceiver is configured with multiple antennas, the system can be divided into MISO/SIMO and MIMO. The far-field and near-field boundaries of these two types of systems are described below.

MISO/SIMO system: The classical antenna near and far field boundary is the Rayleigh distance, $2D^2/\lambda$,where D represents the array aperture and λ represents the carrier wavelength.

MIMO systems: For MIMO systems, an extended form of Rayleigh distance is widely accepted, i.e,$2(D_R + D_T)^2/\lambda$, where D_R, D_T represent the maximum array aperture of receiver and transmitter respectively.

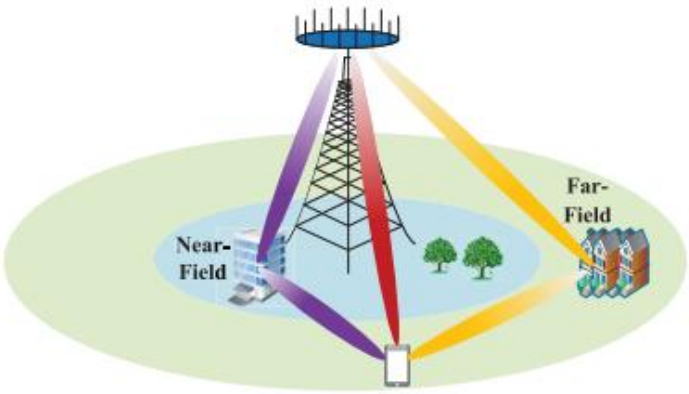

Fig. 4.22 XL-MIMO hybrid near and far field propagation environment

As shown in **Fig. 4.22**, there are two different scattering clusters in the ultra-large MIMO system. The cluster away from the base station is located in the far field region and generates the far field component, while the cluster near the base station is located in the near field region and generates the near field component. In this case, the base station serves a distant user. Although the direct connection path belongs to the far field component, the near field component generated by the near field cluster may also exist in the channel, so the mixed channel of the far field and the near field must be considered.

In order to describe the characteristics of the mixing of near and far fields in the channel, the formula of the mixed field channel model is as follows:

$$\mathbf{h}_{hybrid-fie1d} = \sqrt{\frac{N}{L}}\left(\sum_{l_f=1}^{\gamma L}\alpha_{l_f}\mathbf{a}\left(\theta_{l_f}\right)+\sum_{l_n=1}^{(1-\gamma)L}\alpha_{l_n}\mathbf{b}\left(\theta_{l_n},r_{l_n}\right)\right) \tag{4.15}$$

Where, L represents the number of paths, $\gamma \in [0,1]$ is an adjustable parameter, used to control the ratio of near field cluster and far field cluster, α_{l_f} and θ_{l_f} respectively represents the l_f path gain and arrival Angle of the first far field path, $\mathbf{a}(\theta_{l_f})$ and θ_{l_f} is related to the far field array guide vector, α_{l_n} , θ_{l_n} ,and r_{l_n} respectively represents the path gain, angle and distance of the first near field path, $b(\theta_{l_n}, r_{l_n})$ is θ_{l_n} and r_{l_n} related to the near field array guide vector. When $\gamma = 1$, the mixed field model becomes a far field model, when $\gamma = 0$, the model becomes a near field model.

Therefore, the mixed-field model is a more general channel model, and the existing near-field and far-field models can be regarded as its special cases.

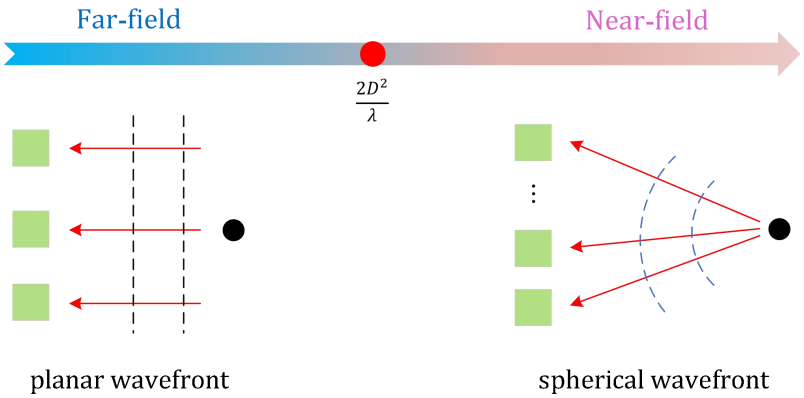

Fig. 4.23 Illustration of the planar and spherical wavefronts in the RIS-enabled channel model

Existing studies have shown that there are obvious differences in investigating RIS-enabled channel statistics based on the assumption that transmitter and receiver are in far-field regions of each other, compared to the assumption that the transceivers are in near-field regions[165][166]. Therefore, the Rayleigh distance criterion must be derived to determine the boundary of the far-field and near-field propagation scenarios for measuring the channel propagation statistics, as shown in **Fig. 4.23**. In the existing literature, the planar wavefront assumption has been adopted to simplify the channel modeling process in MIMO systems under far-field condition. In practice, the far-field condition is not always satisfied in RIS-assisted wireless communications. This is mainly because that the dimension of RIS becomes comparable to the propagation distance and no longer negligible when the RIS units number is large [167][168]. To address this issue, it is important to propose a sub-array partitioning scheme to divide the entire RIS array evenly into several smaller sub-arrays, where each sub-array consists of several RIS units. For each sub-array, the far-field condition holds, meaning that the dimension of each sub-array is much smaller and negligible as compared to the propagation distances. Consequently, we can apply planar wavefront assumption to each sub-array, as shown in **Fig. 4.24**. In each sub-array, once the distance/angle parameters of any one RIS unit are calculated, the distance/angle parameters of the remaining RIS units can be obtained accordingly. This significantly reduces the channel modeling complexity [169]. In the proposed dynamic sub-array partitioning scheme, the sub-array Rayleigh distances are adopted as the boundary of far-field and near-field to perform dynamic sub-array partition, which establishes a dynamic mapping relationship between sub-arrays and physical propagation environments.

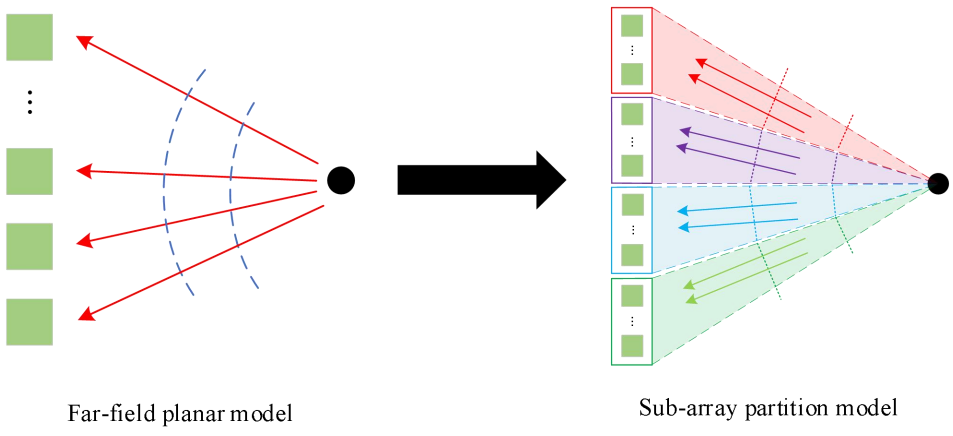

Fig. 4.24 Illustration of the sub-array partition model.

In RIS-enabled channel scenarios, the Fraunhofer distance, which distinguishes between the far-field and near-field ranges, can be expressed as

$$L_{\mathrm{RIS}}=\frac{2d_M^2\left((M_x-1)^2+(M_z-1)^2\right)}{\lambda} \tag{4.16}$$

with λ being the wavelength. Due to the dynamic features of the transceivers, the distance between the transceivers and the RIS continually vary in the real-time motion stage [170][171]. This will result in the alternating presence of near-field and far-field ranges, making the conventional methods that rely solely on spherical or planar-wave-based channel models inadequate for assessing the communication system performance for RIS-enabled scenarios [172]. To tackle this challenge, it is important to divide the entire RIS array into $M_x^{\mathrm{sub}}(t)\times M_z^{\mathrm{sub}}(t)$ sub-arrays in an evenly distributed manner. The largest sub-array contains $M_x^{\mathrm{sub}}(t)\times M_z^{\mathrm{sub}}(t)$ RIS reflecting elements. For the convenience of the subsequent derivations, assume that the largest sub-array is square under the premise of acceptable computational complexity, i.e., $M_{x,\max}^{\mathrm{sub}}(t)=M_{z,\max}^{\mathrm{sub}}(t)$. In order to ensure that the planar-wave model can be applied to each sub-array, the distances $\xi_{T,\mathrm{RIS}}(t)$ and $\xi_{R,\mathrm{RIS}}(t)$ are required to meet the following constraint condition:

$$\xi_{T,\mathrm{RIS}}(t)\geq\frac{2\left(P\delta_T+\sqrt{2}d_M\left(M_{x/z,\max}^{\mathrm{sub}}(t)-1\right)\right)^2}{\lambda} \tag{4.17}$$

$$\xi_{R,\mathrm{RIS}}(t)\geq\frac{2\left(Q\delta_R+\sqrt{2}d_M\left(M_{x/z,\max}^{\mathrm{sub}}(t)-1\right)\right)^2}{\lambda} \tag{4.18}$$

In light of this, we can obtain the constraint of the largest sub-array $M_{x/z,\max}^{\mathrm{sub}}(t)$ as follows:

$$M_{x/z,\max}^{\mathrm{sub}}(t)\leq min\left\{\underbrace{\frac{\sqrt{\lambda\xi_{T,\mathrm{RIS}}(t)}}{2d_M}-\frac{P\delta_T}{\sqrt{2}d_M}+1}_{g_1},\underbrace{\frac{\sqrt{\lambda\xi_{R,\mathrm{RIS}}(t)}}{2d_M}-\frac{Q\delta_R}{\sqrt{2}d_M}+1}_{g_2}\right\} \tag{4.20}$$

In addition to the above constraint conditions, it is crucial to ensure that the dimension of the RIS panel in each sub-array remains smaller than that of the entire RIS array, that is, $M_{x/z,\max}^{\mathrm{sub}}(t)\leq M$. Therefore, the $M_{x/z,\max}^{\mathrm{sub}}(t)$ also needs to satisfy the following constraint:

$$M_{x/z,\max}^{\mathrm{sub}}(t)=\begin{cases}\min\left\{\lfloor g_1\rfloor,\ \lfloor g_2\rfloor,\ M\right\}, & \text{if } \min\left\{g_1,g_2\right\}>1\\ 1, & \text{if } \min\left\{g_1,g_2\right\}\leq 1\end{cases} \tag{4.21}$$

where $\lfloor x\rfloor$ denotes the operation of the largest integer not greater than x. Here, we have

$$M_{x/z}^{\mathrm{sub}}(t)=\begin{cases}\dfrac{M_{x/z}-\mathrm{mod}\left(M_{x/z},M_{x/z,\max}^{\mathrm{sub}}(t)\right)}{M_{x/z,\max}^{\mathrm{sub}}(t)}+1,\\ \qquad\text{if mod}\left(M_{x/z},M_{x/z,\max}^{\mathrm{sub}}(t)\right)\neq 0\\ M_{x/z}/M_{x/z,\max}^{\mathrm{sub}}(t),\\ \qquad\text{if mod}\left(M_{x/z},M_{x/z,\max}^{\mathrm{sub}}(t)\right)=0\end{cases} \tag{4.22}$$

Consequently, for the $(m_x^{\mathrm{sub}},m_z^{\mathrm{sub}})-\mathrm{th}$ sub-array, i.e., $m_x^{\mathrm{sub}}=1,2,...,M_x^{\mathrm{sub}}(t)$ and $m_z^{\mathrm{sub}}=1,2,...,M_z^{\mathrm{sub}}(t)$, their numbers of RIS reflecting elements are represented by

$$M_{m_{x/z}^{\mathrm{sub}}}(t)=\begin{cases}M_{x/z}^{\mathrm{sub}}(t), & \text{if } 1\leq m_{x/z}^{\mathrm{sub}}<M_{x/z}^{\mathrm{sub}}(t)\\ M_{x/z}-\left(M_{x/z}^{\mathrm{sub}}(t)-1\right)M_{x/z}^{\mathrm{sub}}(t), & \text{if } m_{x/z}^{\mathrm{sub}}=M_{x/z}^{\mathrm{sub}}(t)\end{cases} \tag{4.23}$$

For the convenience of subsequent expressions, define the $m_{x,z}^{\text{sub}}$ as the $(m_x^{\text{sub}}, m_z^{\text{sub}})$. It is worth noting that the proposed sub-array partitioning scheme is a software-level method, which implies that the sub-arrays can be repartitioned dynamically to accommodate the motion of the transmitter and receiver. Therefore, the proposed sub-array partitioning scheme can be extended to divide the large antenna arrays at the transmitter and receiver in ultra massive MIMO systems into small sub-arrays to reduce the modeling complexity.

As shown in **Fig. 4.25**, when the dimension of the RIS array is relatively small, which causes the propagation distance from the RIS to the transceivers to exceed the Rayleigh distance of the RIS-enabled channels; therefore, the planar wavefront assumption will hold for accurately characterizing the channel statistics in this context. The results in the RIS-enabled channel models based on the near-field scenarios provide the same performance as those based on the far-field scenarios. However, when the RIS array dimension continually increases, the length of the Rayleigh distance can be larger values. This results in the transmitter and receiver within the near-field scenarios of the RIS-enabled channels, which leads to different performance characteristics regarding modeling errors.

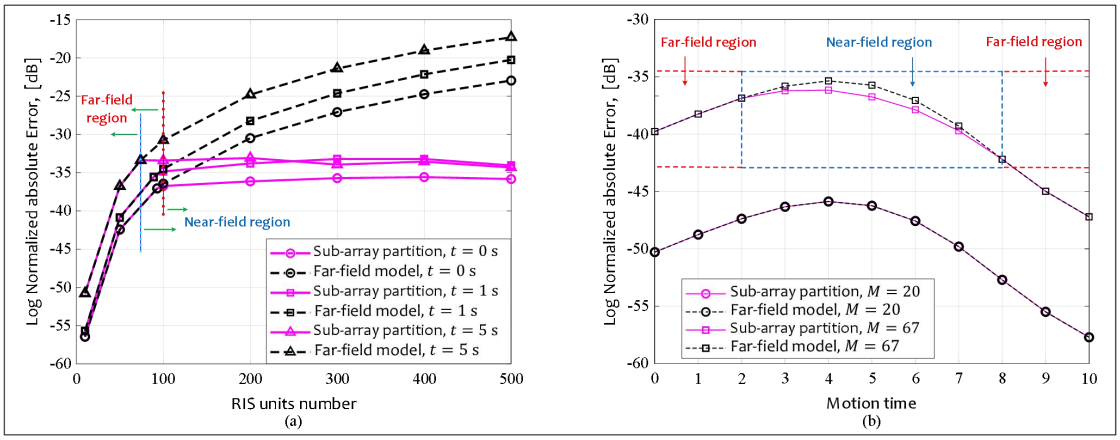

Fig. 4.25 Comparisons of the channel modeling accuracy based on the sub-array partition-based algorithm and that based on the far-field planar wavefront model under different motion time instants and different RIS units.

4.4 Bridging the Gap between Near and Far-Field Models

With the increasing importance of near-field considerations alongside the established significance of far-field characterizations, there is a growing necessity to bridge the gap between these two domains. Here, we summarize some recent findings by drawing parallels between conventional channel modeling methods and those based on the fundamental wave propagation modeling approach via Maxwell's equations (Green's function). Our objective is to offer engineers and researchers fresh perspectives, enabling them to leverage techniques developed for standard far-field models in the exploration of near-field scenarios. Specifically, we concentrate on environments devoid of scattering, where communication relies solely on the line-of-sight (LOS) link.

To elucidate the characteristics of near and far-field models, we examine a multiple-input single-output (MISO) system setup, focusing on beamforming applications at various distances from the transmitter [173]. This system comprises a rectangular grid of $N = N_x N_y$ small antenna elements, uniformly spaced at half of the wavelength at the transmitter. In our simulations, we utilize a carrier frequency of 30GHz corresponding to a wavelength of $\lambda = 0.01m$. The transmitter configuration

comprises a rectangular grid of antenna elements, with $N_x = 20$ antennas along the X-axis and $N_y = 200$ antennas along the Y-axis. Each antenna element has a square shape with a side length $a = 0.5\lambda$.

In **Fig. 4.26** (a), (b), and (c), we examine the performance of a matched filter beamformer designed to maximize the received power at the receiver positioned at $(0,0,\mathrm{d})$ with $d = 10\lambda = 0.1m$, $d = 250\lambda = 2.5m$, and $d = 5000\lambda = 50m$, respectively. From plots (a) and (b), the discrepancy between the near and far-field models becomes evident. In the near-field scenario, the near-field model allows for power concentration at the specific receiver position, and for $d' = d \pm \delta,\ \delta > 0$, the power decreases. In contrast, in the far-field, the transmitter can only concentrate power towards an angular orientation of the receiver. As illustrated in **Fig. 4.26** (c), when the distance between the transmitter and the receiver is sufficiently large, the near and far-field models almost coincide, indicating that the far-field model serves as an approximation of the near-field model. It is noteworthy that for the given transmitter antenna configuration, the Fraunhofer distance is approximately 200m. However, this distance provides a highly conservative estimate for the reliable employment of far-field models. This discussion underscores the accuracy of the near-field model in describing wireless propagation and highlights its utility in leveraging an additional degree of freedom (the distance d) to enhance performance in various applications. Notably, in **Fig. 4.26** (a) with d=0.1m, the far-field model tends to overestimate the received power. Further elaboration and analysis can be found in [173].

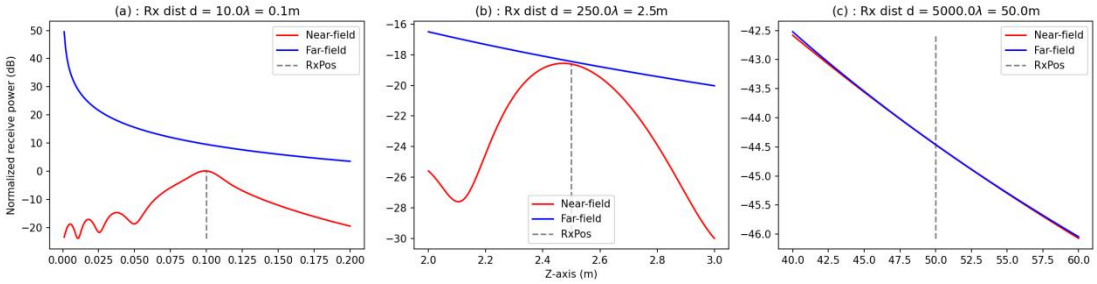

Fig. 4.26 Comparison of near and far-field models for different Tx-Rx distances [173].

5 Transmission Technologies of Near-field

Due to the mismatch between near-field propagation models and existing far-field communication technologies, existing far-field technologies will experience significant performance degradation in the near-field region. This chapter will introduce near-field communication technologies from the aspects of channel estimation, beamforming, codebook design, beam training, multiple access technology, non-coherent detection, system architecture and deployment, and standardization.

5.1 Near-Field Channel Estimation

Accurate channel state information (CSI) is fundamental for designing accurate beamforming in 6G communications, which is a key factor in achieving ultra-high-speed transmission. The Massive MIMO 5G technology was designed around the use of model-agnostic channel estimation, using uplink pilots, uplink-downlink duality, and the use of non-parametric channel estimation methods. These methods can be used for near-field estimation without any modifications. Nevertheless, there are good reasons for considering parametric estimation methods in 6G: the increased carrier frequency reduces the available pilot resources per coherence block and increased number of antennas calls for more pilot resources. This issue can be resolved by shifting to parametric methods, where channels are described with a number of parameters that is independent of the number of antennas. However, the new characteristics introduced by near-field communications pose challenges when applying such methods.

Previous parametric estimation methods designed for mmWave bands often utilize the sparsity of far-field channels in the angle domain and employ compressive sensing (CS) algorithms to recover sparse channels with low pilot overhead. To achieve this goal, the Fourier transformation is first performed in the antenna domain of the channel, converting it to the sparse angle domain. Then, the sparse signal reconstruction methods such as Orthogonal Matching Pursuit (OMP) are utilized to accurately reconstruct the sparse angular-domain channel. The far-field channel estimation scheme heavily relies on the sparsity of the angular-domain channel, which originates from the far-field planar-wave model. Due to the fact that the near-field channel of extremely large-scale antenna array (ELAA) is composed of spherical waves, the propagation characteristics of near-field spherical waves will lead to energy spread effects in the near-field angular-domain channel, where the energy of each near-field path spread to multiple angles in the angle domain. The energy spread effect disrupts the sparsity of near-field channels in the angle domain (ref. **Fig. 5.1**). Therefore, existing channel estimation schemes will suffer from a serious performance decrease in near-field communications.

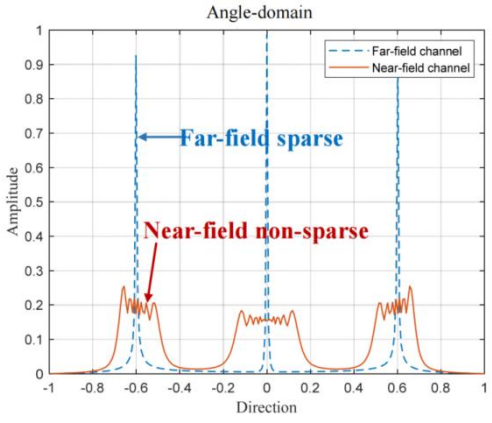

Fig. 5.1 The energy spread effect in the angle-domain

To overcome the energy spread problem in near-field communications, a near-field codebook dictionary matrix can be constructed based on the characteristics of near-field spherical waves, where the sparsity of near-field codebooks can be restored and thereby compressive sensing methods could be leveraged in near-field communications. Specifically, the existing angular-domain dictionary matrix of far-field Fourier transformation is a uniform sampling of spatial angles, ensuring the sparsity of far-field channels in the angle domain. To adapt to the propagation characteristics of spherical waves, an additional non-uniform sampling of spatial distance can be added on the basis of uniformly sampled spatial angles, while ensuring that the coherence of codewords is as small as possible in the distance domain dimension for the uniform linear array (ULA). This allows for the simultaneous extraction of channel information in the two dimensions, i.e. “angular-distance" (polar) domain with the near-field polar domain codebooks. Based on the Fresnel approximation, it can be proven that the proposed polar domain representation method can adapt to the near-field propagation environment, ensuring the sparsity of the near-field channel in the polar domain [174]. By transforming the channel from the spatial domain to the polar domain and utilizing the sparsity of the near-field channel in the polar domain, compressive sensing could be utilized to achieve low-overhead channel estimation.

In [175], by exploiting the fact that with given observations, the angle and distance are coupled, a distance-parameterized angular-domain sparse near-field channel representation dictionary is proposed, followed by joint dictionary learning and sparse recovery channel estimation algorithm. The proposed algorithm iteratively estimates the angle and distance parameters, which are then used for the reconstruction of the near-field channel. Specifically, the proposed near-field channel representation dictionary takes the distance as an unknown parameter while only the sampling at the angle domain is performed, which well addresses the high storage and high coherence issues brought by the polar-domain method, as illustrated in **Fig. 5.2**. To reduce the dictionary construction difficulty of the polar-domain method, a model-based deep learning approach was proposed for the near-field channel estimation in [176]. In this work, a small-sized dictionary was learned from the received observations to represent the near-field channel, and the channel parameters are recovered by virtue of a learning-based iterative shrinkage thresholding algorithm.

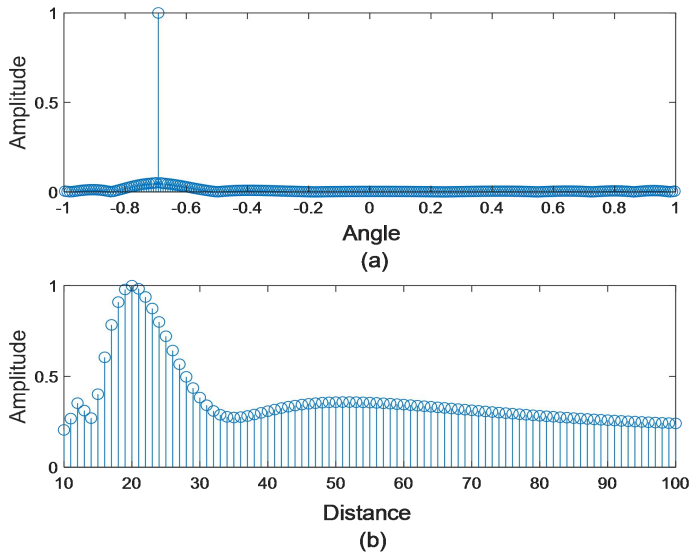

(a) The distance-parameterized angular-domain dictionary. (b) The Polar-domain dictionary.

Fig. 5.2 Dictionary coherence comparison

In addition to constructing codes in the near-field polar domain to ensure the sparsity of the near-field channel, in [177], a wavefront transformation-based matrix is constructed to transform the near-field channel into an approximation of the far-field channel, or even a far-field channel. Then, a discrete Fourier transform (DFT) matrix is used to project the channel onto the angle domain, ensuring the sparsity of the channel. Unlike the structure of far-field channels, existing near-field channels include an additional distance matrix, which is the phase deviation of different antenna array units. To alleviate the impact of phase deviation, a row full rank matrix perpendicular to the space where the far-field steering vector matrix is located can be constructed based on the structural characteristics of the near-field channel and far-field channel. A full rank matrix can be obtained through matrix operation, and the diagonal elements of the full rank matrix can be extracted and normalized as the constructed wavefront transformation matrix. When the number of antennas is large enough, the wavefront transformation matrix is related to angles and distance, and the estimation error of the channel will approach zero [177].

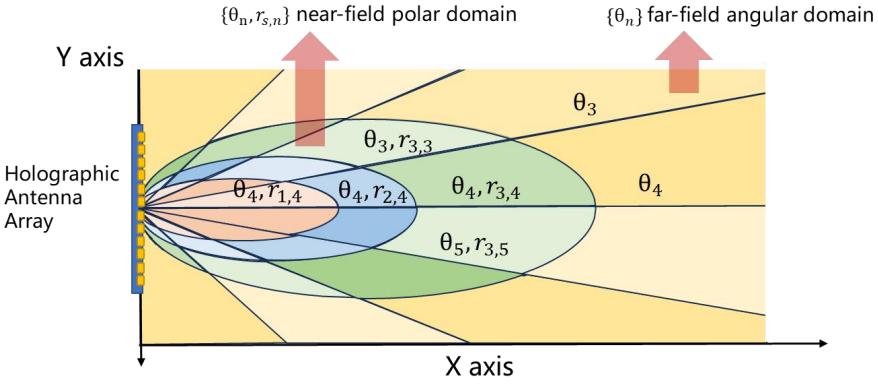

Fig. 5.3 Space Partition Based on Joint Angular-Polar Domain Transform

To mitigate the accuracy, decrease of far-field methods in near-field communications, [178] proposes a power-diffusion-aware orthogonal matching pursuit algorithm (PD-OMP) for hybrid-field channel estimation. Different from other hybrid-field channel estimation methods, PD-OMP transforms the spatial-domain channel to the joint angular-polar domain, where both the near-field and the far-field steering vectors are included in the compressed sensing dictionary. As shown in **Fig. 5.3**, the space covered by the holographic antenna array is divided into the near-field region and the far-field region. In the joint angular-polar domain, the near-field region is partitioned two-dimensionally in both direction and distance with near-field steering vectors, and the far-field region is partitioned one-dimensionally in direction with far-field steering vectors.

Based on the transform result in the joint angular-polar domain, PD-OMP estimates all path components of the hybrid-field channel in iteration. In each iteration, a peak representing a path is detected in the transform result and PD-OMP calculates this path's power diffusion range, which quantifies the range of power diffusion in the joint angular-polar domain. The power diffusion effect of this path is therefore identified and then eliminated so that the estimation of the remaining path components is not affected by the power diffusion effect. It is noticed that the amplitude of the highest peak, which represents the path with the strongest power gain, is larger than the interference of the power diffusion effect of the other paths. Therefore, in the first iteration, this peak can be detected and

the corresponding power diffusion range can be identified, which ensures that each path component can be detected successfully in the following iteration.

Due to the energy spread effect, the near-field channel exhibits block structure in angular domain, i.e., the significant angle ingredients of the channel are continuous. Moreover, as polar-domain representation contains the angle ingredients, the near-field channel in the polar domain also exhibits block structure. The authors in [179] reformulated the near-field channel as a block-sparse model by exploiting this structural characteristic. They further proposed an enhanced compressed sensing technique, called block-dominant compressed sensing, to perform reliable near-field channel estimation in both angular and polar domain. Benefiting from the exploitation of the subspace information among various channel blocks, channel estimation by the way of block-dominant compressed sensing offers fertile advantages in terms of both accuracy and complexity.

By further considering the dual-band deployment of practical communication systems, [180] proposed various dual-band near-field channel estimation schemes based on the block-sparse model in [179]. The authors present several theoretical results, revealing that the reliability high-band channel estimation with minimum estimation error can be guaranteed with the assistance of the low-band channel state information. The single subcarrier and multiple subcarrier systems are analyzed separately to achieve the optimal solution of the corresponding system. Furthermore, both on- and off-grid scenarios are verified to substantiate the feasibility of the dual-band channel estimation schemes, which results in a significant reduction in pilot overhead.

Apart from the works on ULA, [181] and [182] propose parametric deconstruction techniques for a more general uniform planar array (UPA) scenario that incorporates both two-dimensional azimuth-elevation angles and distance parameters. In particular, these coupled geometry parameters, consisting of a pair of elevation-azimuth angles and the distance, are decomposed independently by employing a carefully designed mapping strategy from the original channel matrix to the three covariance matrices, each of which is associated exclusively with a single geometry parameter. This results in three independent one-dimensional (1D) parameter recovery problems that can be solved using compressive sensing techniques. Furthermore, benefiting from independent parametric estimates, the multiplicative complexity order can be relaxed to its additive counterpart. This implies that the proposed Triple Parametric Decomposition (TPD) enables practical implementation due to the beneficially reduced gridding and computational complexity as well as viable pilot overhead savings.

By exploiting the near-field channel sparsity in the polar domain and the high-performance capabilities of deep learning (DL)-based algorithms in channel estimation (CE), the authors in [183] proposed two channel estimation schemes, i.e., the polar-domain multiple residual dense network (P-MRDN) and the polar-domain multi-scale residual dense network (P-MSRDN) based CE schemes. Moreover, the proposed schemes were compared with the polar-domain orthogonal matching pursuit (P-OMP) algorithm[174] to reveal the impact of channel sparsity on the performance of both traditional and DL-based algorithms.

To mitigate the influence of additional Tx/Rx-coupled LoS component in the double-sided near-field MIMO, which cannot be decomposed into the multiplication of transmitter-side and receiver-side array response vectors, the authors in [184] proposed a unified LoS/NLoS-mixed compressive-sensing-based estimation method. The Tx/Rx-coupled LoS component and

Tx/Rx-decomposed NLoS paths, far-field and near-field cases, and near-field MIMO/MISO scenarios, are uniformly considered under this estimation scheme.

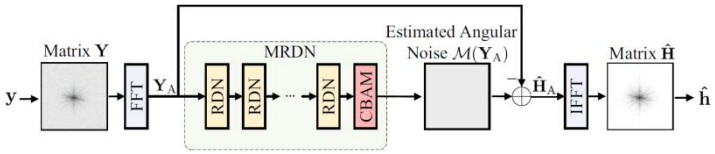

Fig. 5.4 MRDN-based channel estimation scheme

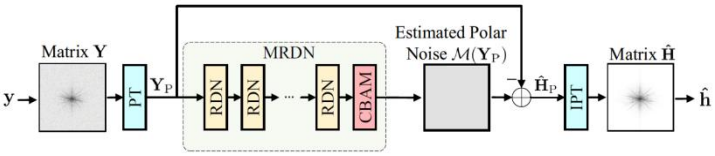

Fig. 5.5 P-MRDN-based channel estimation scheme

Fig. 5.4 illustrates the conventional MRDN-based channel estimation scheme [185]. The MRDN aims to transform the received signal into the angular domain using Fast Fourier Transform (FFT), thereby fully utilizing the sparsity of the channel in the angular domain. Subsequently, the MRDN is employed to recover the sparse far-field channel in the angular domain. However, the sparsity of the near-field channel in the angular domain is not significant. Instead, similar to the sparsity of the far-field channel in the angular domain, the radiation near-field channel exhibits certain sparsity in the polar domain.

As shown in **Fig. 5.5**, to leverage the polar-domain channel sparsity in near-field systems, the proposed P-MRDN-based channel estimation scheme adopts the polar-domain transform (PT) to transform the received signal into the polar domain counterpart, similar to the angular domain transformation. The key distinction between the MRDN and PMRDN lies in their approach to exploit the inherent channel sparsity. The MRDN-based CE scheme transforms the channel to the angular domain, exploiting the angular-domain sparsity in the far-field. In contrast, the P-MRDN-based CE scheme transforms the channel to the polar domain, leveraging the polar-domain sparsity in the near-field. To further improve the channel estimation accuracy, the authors in [185] define a parallel part of the atrous spatial pyramid pooling (ASPP) and residual dense network (RDN), named ASPP-RDN, as shown in **Fig. 5.6**. By incorporating the notion of ASPP into the proposed P-MRDN, the new CE scheme can achieve lower normalized mean-square error (NMSE) performance as the ASPP can integrate multi-scale features of its input.

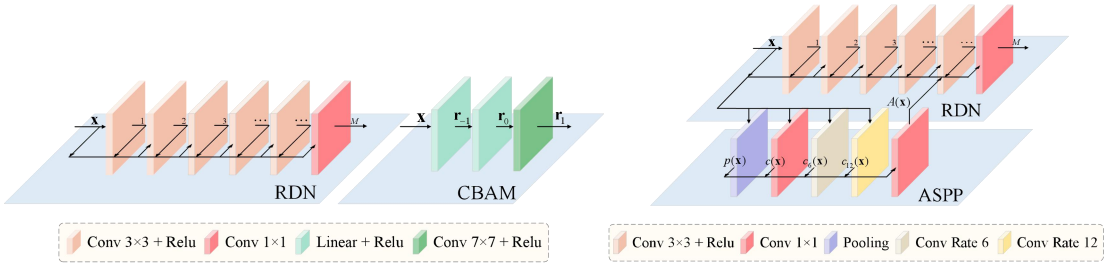

Fig. 5.6 RDN、CMAM and ASPP-RDN system models

Moreover, another key characteristic of the near-field channel is the spatial non-stationarity, i.e., different visibility regions (VRs) for different antenna subarrays. which hinders the application of traditional beamforming schemes. As indicated in [186], this phenomenon results in performance

degradation for conventional beamforming schemes that neglect the non-stationarities. The formation of spatial non-stationary effects can be attributed to several factors, including unequal pathloss between the user and different array elements. As a consequence of extended array size, when the distance between users and the array is less than the Fresnel distance, the spherical wave propagation characteristics lead to weaker energy reception by antennas farther away from the user. From another perspective, the unequal channel power arises from the signal blockage caused by obstacles. Different from the far-field situation the total channel is more likely to be blocked, and the channel of a user in the near field or the Fresnel region may usually be obstructed partially, which leads to unequal distribution of channel power among the array elements. It can be anticipated that when users communicate with the BS equipped with an extra large-scale array, only partial array elements perceiving a favorable channel environment receive the majority of signal power. Conversely, a significant portion of array elements, owing to factors such as unideal distance and angle relative to the user, may only capture low signal power.

To obtain the channel state information regarding the non-stationary and near-field characteristics, it is imperative to carry out VR identification from both the array side and the user side. When the fully-digital RF-front is equipped with the BS and a single-antenna user is served, the VR identification at the array side can be realized based on the uplink pilot [160][187]. However, the near-field and non-stationary characteristics are especially obvious for extra large-scale arrays with hybrid beamforming structures, the direct acquisition of received signal power corresponding to each antenna element poses significant challenges. Therefore, the authors in [188] consider the VR identification problem when a subarray-based hybrid beamforming structure is equipped with the BS. The near-field channel parameters are first extracted through the parameterized channel estimation schemes, afterwards the VR is identified by comparing the received signal and the reconstructed channel. The extra large-scale RIS also stands as one of the implementation approaches for extra large-scale MIMO systems, therefore the deployment of an extra large-scale RIS similarly introduces near-field and spatial non-stationary characteristics. Specifically, [189] considers the VR identification of extra large-scale RIS systems. The UE-RIS-BS cascaded channel is first estimated, and the VR is then identified by detecting the inequality power of the reconstructed channel. As for the VR identification at the UE side, the VR is defined as geometric areas associated with certain sets of antennas. That is, when a user is situated within the VR, the signal can be received by specific array elements. As the user transitions into another VR, the signal can be received by a different set of array elements. In [190], the VRs of some beacon users are assumed to be known as a priori, and then a neural network-based approach termed VR-Net is designed to detect the correspondence between the VRs and the sets of array elements, which realizes accurate VR identification with low complexity.

5.2 Near-Field Beamforming

Beamforming is a signal processing technique that uses antenna arrays to direct a wireless signal towards a specific receiver, rather than broadcasting it in all directions. It can be achieved by adjusting the weights and phases of the antenna elements to create constructive and destructive interference patterns in the desired directions or locations. Beamforming can improve the quality, capacity, and reliability of wireless communication by enhancing the desired signal and reducing interference. In the existing far-field wireless communication system, since the electromagnetic wave front is planar,

beamforming can only control signal propagation in one dimension of angle. Unlike the far-field, in the near-field communications, the near-field beamforming (beam focusing) technique is able to focus the signal energy at a specific location by exploiting the propagation characteristics of spherical waves to achieve the control of signal propagation in both angular and distance domains [191][192]. Near-field beamforming (beamfocusing) provides a novel multi-user interference control mechanism.

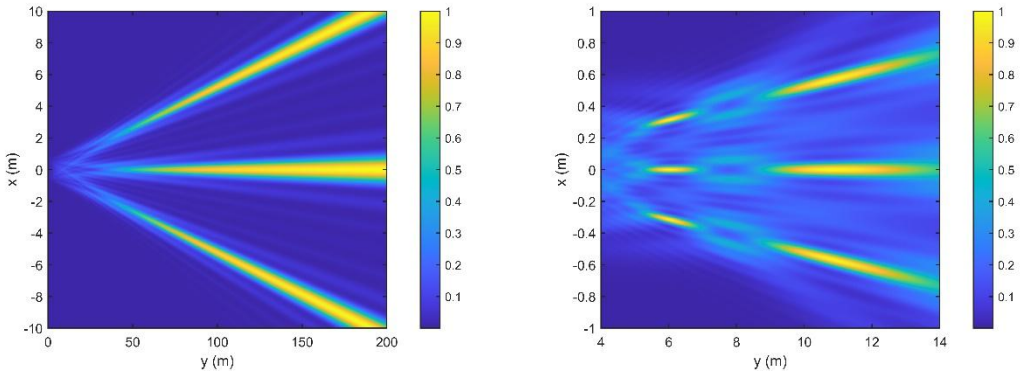

Fig. 5.7 Far-field beamforming and Near-field beamforming

With known CSI, the near-field beamforming design can still adopt the traditional MIMO beamforming design methods, such as Maximum Ratio, Zero-Forcing and Minimum-Mean Square Error, to achieve spatial multiplexing. Compared with far-field plane wave propagation, near-field spherical wave propagation can substantially enhance the spatial multiplexing capability. Specifically, as shown in **Fig. 5.7**, in far-field communications, the channels of different users converge to orthogonality only gradually in the angular domain as the antenna array size increases. This orthogonality is determined by the beam width. However, when the users are located in the near field, the asymptotic orthogonality of the user channels exists not only in the angular domain but also in the distance domain. This orthogonality is determined by both beam width and beam depth [193]. Therefore, in the near-field communications, beamforming is able to focus the beam on a specific angle and distance at the same time, achieving a higher degrees-of-freedom (DoFs) of spatial multiplexing, effectively suppressing inter-user interference, and facilitating multiple access. To exploit the multiple DoFs more effectively in near-field LoS MIMO channels with limited RF chain constraint, spatial path index modulation (SPIM) is also a promising beamforming architecture for higher energy efficiency in near-field communication [194].

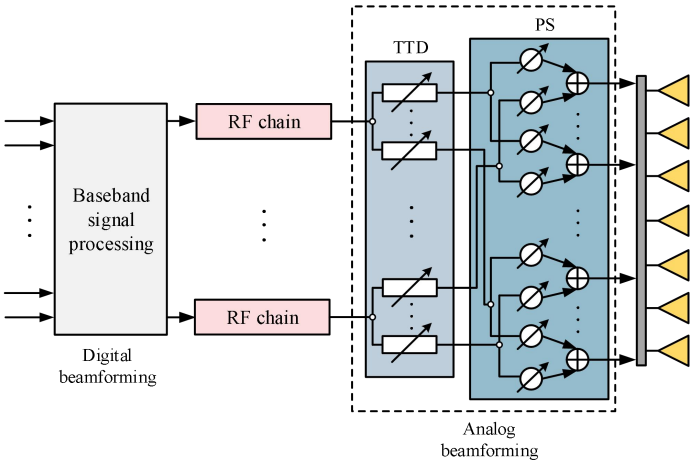

Fig. 5.8 Fully-Connected Delay-Phase Hybrid Beamforming

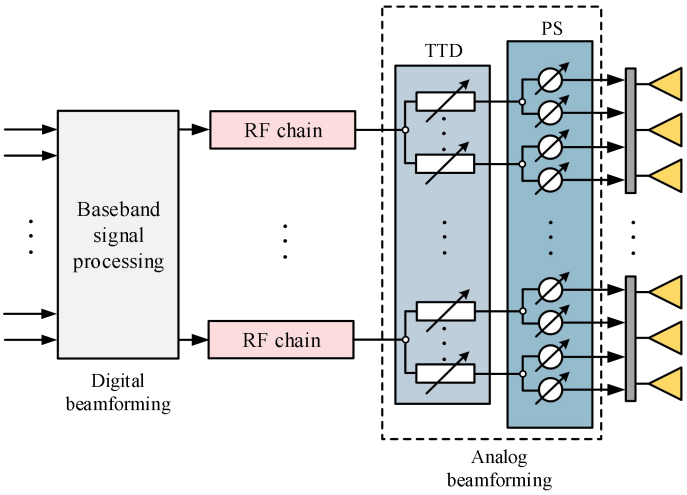

Fig. 5.9 Partially-Connected Delay-Phase Hybrid Beamforming

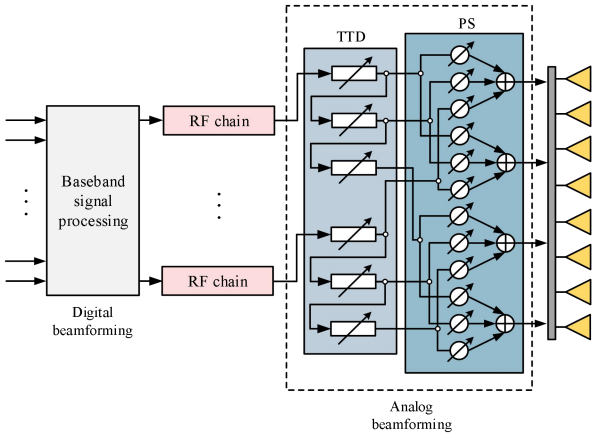

Fig. 5.10 Serially-Connected Delay-Phase Hybrid Beamforming

There is a dual wideband effect in multi-antenna wideband systems, namely a frequency wideband effect caused by multipath effects and a spatial wideband effect due to large antenna apertures. The frequency wideband effect results in frequency selectivity of the near-field channel, causing serious inter-symbol interference (ISI) problems. Such challenges can be effectively addressed by various existing techniques, such as Orthogonal Frequency Division Multiplexing (OFDM) with cyclic prefixes. The spatial wideband effect allows different subcarriers to “see" the user position at different angles and distances. The problem of beam squinting or beam splitting can occur when transceivers use energy-efficient hybrid digital-analog beamforming architectures. Specifically, conventional analogue beamforming uses phase shifters (PSs) that are not frequency-selective to generate beams. PSs are unable to generate different beams for different subcarriers, and therefore are not able to accurately focus the beams at the user for different subcarriers. To cope with these challenges, [195] and [196] proposed a fully-connected delay-phase hybrid beamforming architecture, as shown in **Fig. 5.8**. This architecture effectively overcomes the beam squinting or beam splitting problems by introducing an appropriate amount of true time delayers (TTDs) to realize frequency-dependent analog beamforming.

However, in near-field communications, in order to ensure a certain scale of near-field range, antenna arrays are usually required to have a large aperture, which puts stringent requirements on the

achievable maximum delay of individual TTDs. To address this issue, [197] and [198] proposed partially-connected and serially-connected delay-phase beamforming architectures (as shown in **Fig. 5.9** and **Fig. 5.10**), respectively, in order to reduce the maximum delay requirement, and hence the hardware cost and complexity, as follows:

- Partially-Connected Delay-Phase Beamforming [197]: In this architecture, each RF chain is connected to an antenna subarray through TTDs and PSs. Therefore, each set of TTDs only needs to overcome the beam squinting or beam splitting issue of each subarray. Since each subarray has a smaller aperture, the maximum delay requirement of individual TTDs can be greatly reduced. However, there may be an unavoidable performance loss with this architecture as each RF chain cannot fully exploit the entire antenna array.
- Serially-Connected Delay-Phase Beamforming [198]: In this architecture, each RF chain is still connected to the entire antenna array. However, the TTDs no longer work independently in parallel, but are connected in serial. As a result, the architecture is able to utilize multiple short-range TTDs to accumulate a large delay and effectively overcome the beam squinting or beam splitting issue. However, the serial connection of TTDs introduces cumulative insertion loss at the same time, and therefore new TTDs with low insertion loss need to be designed.

In addition, under near-field non-stationary conditions, precoding can be designed using VR in the visible area of the antenna that dominates the user's received power. Considering that antenna VR has a significantly lower number of antennas compared to the entire extremely large antenna array (ELAA), precoding based on VR design can significantly reduce the complexity of matrix inversion and other operations.

The authors of [118] proposes that the closed form expression for the received power of each sub-array can be calculated based on the near-field channel expression, in order to find the set of subarrays that play a dominant role in the signal reception process. Subsequently, based on the obtained VR information, the channels corresponding to each user in VR can be reconstructed to design low complexity precoding based on VR. Meanwhile, due to the fact that array VR can receive the vast majority of signal energy, this algorithm can achieve performance similar to precoding based on full array received signals. Extremely large-scale antenna arrays have the ability to serve a large number of users, and considering the dispersed distribution of users in space, each user may have different antenna VR.

Therefore, based on the graph theory maximum independent set algorithm, users with similar VR can be divided into groups, and intra group interference can be eliminated using partial interference zero forcing algorithm. Compared to performing zero forcing interference cancellation on a large number of users, the partial interference zero forcing algorithm based on user grouping can further reduce the precoding complexity. Due to the small inter group interference between user groups with small VR overlap, the intra group interference cancellation algorithm can achieve system performance that is very close to full user interference cancellation [118].

Meanwhile, a beamforming design scheme was also proposed in [199], which utilizes the user visible area distribution information obtained through channel estimation from base stations for beamforming. As shown in **Fig. 5.11**, an extremely large-scale MIMO system with CPU and LPU collaborative processing is considered. By using distributed precoding based on subarrays at the base station, the non-stationary characteristics of the channel can be effectively utilized to achieve good

spectral efficiency (SE), and low complexity receivers designed based on the randomized Kaczmarz (rKA) algorithm can achieve a balance between performance and complexity.

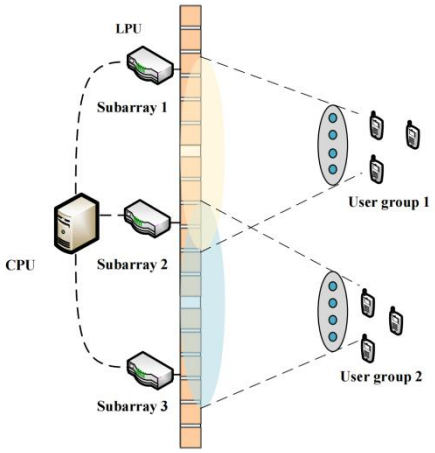

Fig. 5.11 Extremely large-scale MIMO system with CPU and LPU collaborative processing.

In [200], a dual beamforming scheme is designed based on a two-layer antenna architecture composed of an active layer of phased array antenna (PAA) and a passive layer of reconfigurable intelligent surface (RIS), as illustrated in **Fig. 5.12**. The PAA acts as the feed antenna for the RIS, and the RIS forwards the incident signals to the user equipment (UE) equipped with conventional antenna arrays. Specifically, precoded signal streams are emitted by the PAA subarrays and beamformed towards the respective RIS subarrays. When the RIS size is sufficiently large, the incident power distribution on the RIS can be manipulated by steering the PAA beams so that a particular subset of RIS elements at desired locations can be illuminated. Next, the phases of the illuminated RIS elements are adjusted to steer the RIS beams towards the UE to achieve coherent transmission. The above system effectively realizes aperture adaptation with fixed physical antennas such that the effective line-of-sight (LoS) MIMO channel can be orthogonalized in order to achieve higher spatial multiplexing gain. Furthermore, this scheme helps to reduce the cost and power consumption of the base station (BS) and is also able to simplify the baseband spatial processing of both BS and UE.

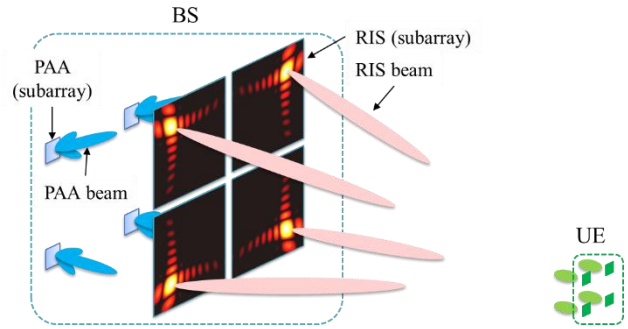

Fig. 5.12 PAA-RIS dual beamforming scheme

In addition to beam focusing that could result in a narrow beam given a large aperture and a high frequency, variable beamwidth near field beamforming is proposed to illuminate a larger region so that it's robust to user location errors. In [201], the authors used a technique that maps the RIS elements to a tunable spherical surface. By tuning the size and center of the surface, variable width beams and illuminated areas can be achieved. In addition, unlike the wider beam design in [202], the proposed spherical-mapping-based beamforming remains a good illumination shape when the BS and UE are far

from the RIS boresight direction. The rate heatmap comparison using near field beam focusing, far field beamforming, and the proposed variable beamwidth design is provided in **Fig. 5.13.** The desired illumination region is marked in red. The system operates under 30 GHz and the number of RIS is 200×200. It can be seen that the proposed beamforming can illuminate the desired coverage region at the cost of decreased highest rate but a higher average rate.

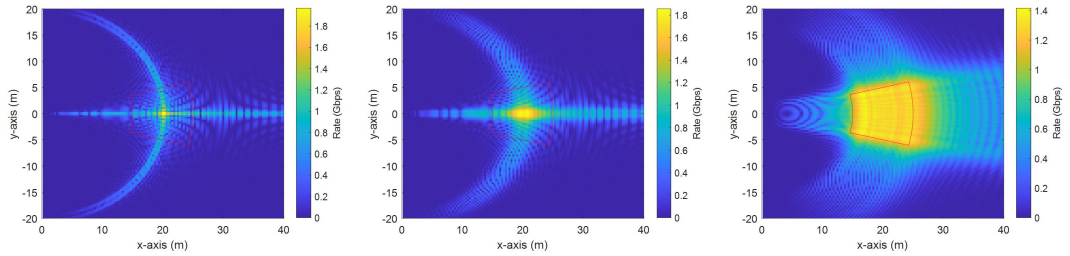

Fig. 5.13 Rate heatmap comparison (from left to right: near field beam focusing, far field beamforming, the proposed variable beamwidth near field beamforming).

5.3 Near-Field Codebook Design

At present, the design of near-field codebooks mainly faces three major challenges. The first is that in practical applications, near-field phenomena often occur with extremely large-scale antenna arrays. The extremely large-scale antenna array has a higher spatial resolution, resulting in the need for more codewords to cover the entire near-field space. This makes the near-field codebook design bulky and time-consuming for beam training. The second issue is that near-field codebooks need to distinguish space from direction and distance variables, resulting in multiplicative time complexity and further expanding the volume of near-field codebooks. The third issue is that near-field space is difficult to orthogonally decompose. Due to the irregular shape of the near-field beam, the designed codebook may be unable to cover the entire near-field space, leading to near-field blind spots. In addition, if the orthogonality between codewords is not satisfied, it will cause some space to be covered by multiple codewords, resulting in redundancy in the codebook.

In the existing 5G NR standard, the PMI codebook used to indicate CSI information uses DFT vectors as the basic unit of constructing codewords, which can be regarded as uniform quantization of the angle domain. When considering the scenario where the user is located in the near field, the fractional Fourier Transform (FRFT) vectors can be used as the basic codeword construction unit [203]. Specifically, as shown in **Fig. 5.14** in the ULA scenario, the codewords are the FRFT vectors obtained by sampling the $\left(\sin\theta, \cos^2\theta / r\right)$ domains; while the UPA scenario corresponds to the sampling of the $\left(\sin\theta\cos\phi, \sin\theta\sin\phi, 1/r\right)$ domain. When the transformed distance domain information feedback value is 0, the FRFT codeword degenerates into a DFT codeword, maintaining compatibility with the existing PMI codebook scheme.

By analyzing the correlation between the near-field steering vector and the codeword, it can be found that the uniform sampling of the transform domain at equal intervals ensures the uniform, symmetrical, and monotonic characteristics of the correlation function distribution. From this, the maximum quantization error of the mixed field including near field and far field can be obtained. At

the same time, the correlation function can be expressed by a quadratic polynomial, that is, the correlation contour is an ellipse. Based on this, the optimal sampling interval of the transform domain can be obtained analytically. Theoretical analysis shows that when the codebook size is limited, the angle domain should be quantized first. The distance domain introduced by the near field only requires a small number of samples, adding an additional 1 to 3 bits of feedback overhead[203]. In addition to sampling at equal intervals in the transform domain to obtain the near-field codebook, “angle-displaced" sampling can also be performed in the distance domain as shown in **Fig. 5.15**. Theoretical analysis shows that this new codebook design method can ensure the same quantization performance as uniform sampling, but the codebook size is only 77% of the comparison scheme.

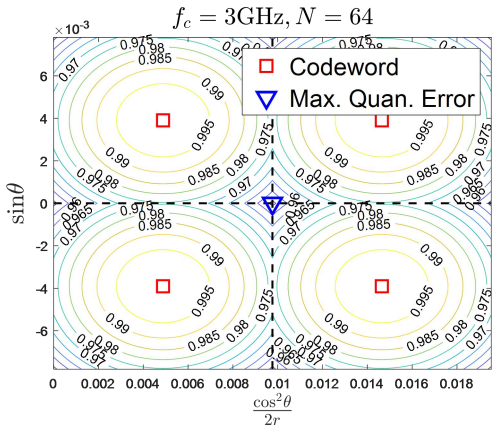

Fig. 5.14 Illustration of FRFT codeword quantization performance

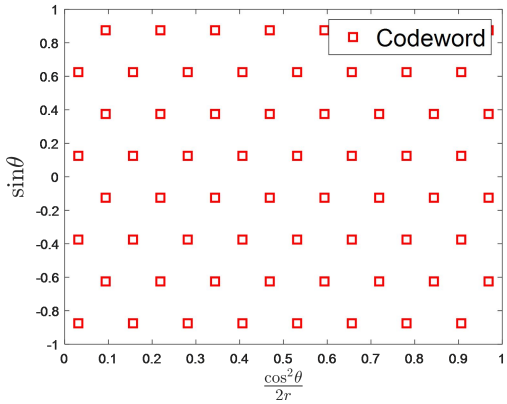

Fig. 5.15 Angle-displaced near-field codebook design method

The codebooks in 5G NR are based on discrete Fourier transform (DFT) vectors, as shown in **Fig. 5.16**(a). But reusing DFT-codebooks for near-field beamforming causes severe SNR loss due to mismatch with the near-field channel. In contrast, beamfocusing based on the spherical wavefront assumption forms the optimum coherent beamformer for the near-field channel, as shown in **Fig. 5.16** (d). However, ideal beamfocusing codewords are difficult to be expressed parametrically, and cannot be decomposed with Kronecker product for widely used uniform rectangular antenna arrays. Therefore, near-field codebooks shall be considered for large aperture MIMO antenna arrays.

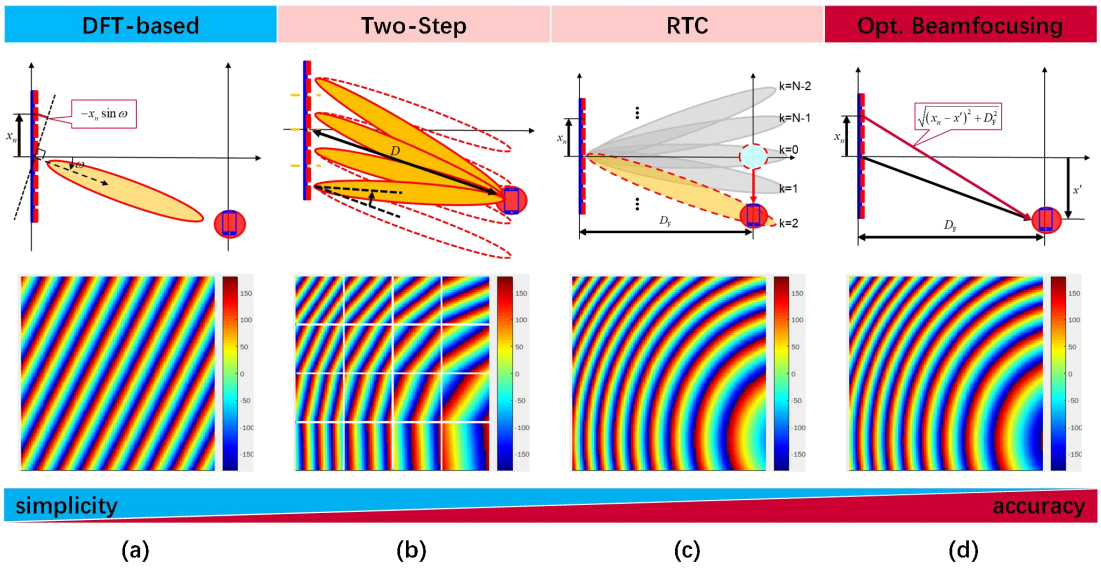

Fig. 5.16 Principle and phase distribution of far- and near-field codebooks

Two near-field codebooks are proposed by industry. One is referred to as two-step beamforming [204]. The idea is to divide a large aperture MIMO antenna array into multiple smaller subarrays such that the user is located in the far-field of each individual subarray and, thus, DFT-beams can be employed. The codewords are constructed as follows. In the first step, choose the DFT-beam pointing in the user direction for the entire array. In the second step, let the sub-beam of each subarray be steered by a small angle according to the relative position of the respective subarray w.r.t. the reference point of the entire array, and configure an initial phase for the subarray to compensate for the phase shift caused by the spherical wavefront. This codebook can be easily implemented accommodating the multi-panel antenna architecture. The other is referred to as ring-type codebook (RTC) [205]. The RTC is composed of two layers of codewords corresponding to the distance and the direction information of the user, respectively. The first layer of RTC is designed based on the Fresnel principle to form a focal point in the axial direction such that the user is located within the focal plane. The second layer is compatible with DFT-codebooks and meant to steer the focused beam generated by the first layer into the user direction. As compared to the two-step beamforming, the RTC is more accurate. Furthermore, the RTC still performs well with coarse phase quantization.

Traditional codebooks are usually designed only for far-field areas. However, the enlargement in the physical dimension of antenna array causes the expansion of the near--field region, resulting in users being distributed across both near- and far-field regions [206]. Due to the different propagation characteristics of electromagnetic wave in different regions, traditional pure near- or far-field codebooks are no longer applicable to such a near-far field communication [207]. By combining propagation characteristics of the spherical wave for near field and plane wave for far field, a near-far codebook is constructed to perform beamforming without prior knowledge of user distribution [208].

1) **Codeword coverage discretization:** As shown in **Fig. 5.17**, the coverage of the transmitter is divided into the near- and far-field regions according to the radiation characteristics of electromagnetic waves, and then further discretized into P areas corresponding to P codewords.
2) **Equivalent channel modeling:** Given the codeword coverage discretization, the equivalent channel from the transmitter to each area is constructed according to the electromagnetic wave

propagation characteristics of each area.

3) **Codeword design:** The codeword design principle is that users receive no signal if they are outside the coverage area of the codeword, otherwise the received power is a constant *C*. Based on this principle and the equivalent channel models, each codeword design problem can be modeled as a quadratic problem and solved by a closed-form solution.

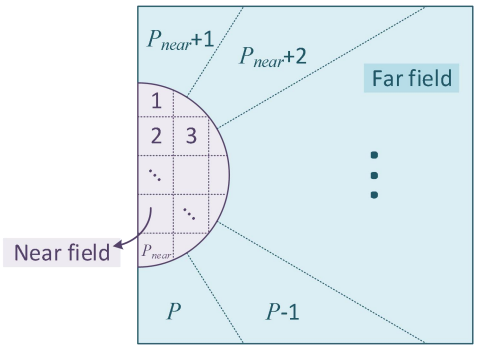

Fig. 5.17 Codeword coverage discretization in the near-far field codebook

In the future, near-field characteristics can be analyzed from two perspectives: signal processing and matrix theory, and near-field characteristics can be used to remodel near-field channels and codebook design rules. The near-field problem essentially belongs to the spatial filtering problem of non-stationary spatial signals. Its characteristics are similar to the frequency domain filtering problem of non-stationary time signals. By comparing the two, the near-field problem can be modeled as a spatial Doppler problem. The traditional estimation algorithm for Doppler frequency shift can be transferred to the near-field problem to estimate the directional shift of the near-field channel seen by antennas at different positions, thereby further deriving key near-field parameters such as user distance and direction. The future near-field codebook design can capture the non-stationary characteristics of near-field signals for design.

From the perspective of matrix theory, codebook design is based on the principle of compressive sensing. However, the signal space in the near-field is significantly different from that in the far-field. The far-field signal space exhibits linear characteristics, that is, the signal space is a low dimensional hyperplane; The near-field signal space is nonlinear and low dimensional. In addition, in multipath scenarios, the straight lines in far-field signal space have an orthogonal relationship, while the curves in near-field signal space do not have an orthogonal relationship. However, the near-field signal space is not any form of low dimensional manifold, and it has shape invariance. Cut two sub arrays of any size on the array, with the same spatial shape of the signals on them. If a codebook is designed based on this characteristic to estimate the spatial shape of the near-field signal, and then the low dimensional trend is projected onto a hyperplane, the problem of determining the near-field signal space will degenerate into a far-field problem.

Based on the above analysis, future near-field codebook design can be developed from the following ideas:

- No longer confined to the codebook design concept of cross-correlation forms. The traditional codebook design framework uses the designed and channel for cross-correlation, and then selects the codeword with the highest cross-correlation value as the final configuration of the array. However, the cross-correlation function is only applicable for estimating the direction of the

wavefront and not for estimating the curvature of the wavefront. Due to the spherical wave characteristics of near-field electromagnetic waves, codebook design work needs to consider both the direction and curvature of the electromagnetic waves. Therefore, a single cross-correlation method can no longer perfectly meet the requirements. Autocorrelation methods and other methods can be used to assist in forming near-field codebooks.

- A “layered" codebook can be designed based on the principle of electromagnetic radiation. On a half wavelength antenna array, the near-field beam shape is mainly influenced by three factors. The first factor is the interference phenomenon caused by different antenna phases; The second is the diffraction phenomenon caused by the limited space of the array; The third one is the influence of the geometric relationship formed between the position and size of the array and the user's position. The coupling of these three factors leads to the irregular characteristics of near-field beams. Therefore, when designing codebooks, the three factors can be decoupled and considered separately, rather than directly designing near-field codebooks based on the results of the coupling of the three factors.
- Codebook design can be based on the analysis of the wave source position, without being limited to Fourier angle spectrum theory. The Fourier angle spectrum theory decomposes any form of wavefront into the sum of plane waves. The near-field wavefront is a spherical wave, so using angular spectrum theory for analysis and codebook design may introduce additional issues. Based on the analysis of the solution to the Helmholtz equation, we know that the solution of the angular spectrum theory is equivalent to the solution in the form of the Green's function, which is based on the analysis of the wave source position and is in the form of spherical waves. Using a solution in the form of spherical waves to represent near-field spherical waves is more concise and clearer than using the angular spectrum theory in the form of plane waves to represent near-field spherical waves. Therefore, designing near-field codebooks based on models such as Green's function is one of the future entry points.

5.4 Near-Field Beam Training

For XL-MIMO array communications in high-frequency bands with hybrid precoding architectures, near-field beam training becomes particularly important. The near-field beam training, can establish an initial high SNR link between the BS and the user before channel estimation and data transmission. Moreover, the XL-MIMO near-field wireless communication system has larger beam gain, narrower beam width, and stronger directivity regardless of whether one operates in the far-field or near-field, but it also poses new challenges to beam training. Existing research shows that directly using DFT-based far-field codebooks for near-field beam training will greatly reduce its achievable rate performance. It is because that the energy of a far-field directional beam aimed at a specific direction will be spread to multiple angles, and the true user angle cannot be found through the maximum received signal power. Different from far-field beam training, XL-MIMO near-field beam training requires beam search in two dimensions in the angle and distance domains.

In [174], the authors proposed a new polar-domain codebook, in which each beam codeword points to a specific position with a target angle and distance. In terms of angle and distance sampling, this work suggests a strategy of uniform sampling of angles and non-uniform sampling of distances. Moreover, the sampling density of distance should decrease as the distance increases, so as to minimize

the column coherence of adjacent codewords. Based on the near-field polar-domain codebook, a straightforward beam training method is to conduct a two-dimensional exhaustive search of all possible beam codewords.

However, this method leads to excessive beam training overhead. In order to reduce the training pilot overhead of exhaustive search, the authors in [209] proposed an effective two-phase fast near-field beam training method. Specifically, when far-field DFT beam codebook scanning is used, users can receive relatively high beam power within a certain angle domain (called the dominant angle region). This work revealed that the user's true angle is approximately in the middle of this dominant angle region. Therefore, by leveraging this important phenomenon, this method first estimates the user angle using angle domain DFT codebook scanning, and then use the polar-domain codebook to further estimate the user distance. The total beam training pilot overhead of this scheme is significantly lower than that of the two-dimensional exhaustive search scheme. A joint angle and distance estimation-based beam training scheme with DFT codebook was innovatively proposed in [210] The traditional beam training method determines the user angle based on the user's maximum received power. However, this does not make full use of the power pattern received at the user. The innovation of this scheme is to revisit the near-field beam training design based on the DFT codebook scanning. For the first time, this work proposes a new effective scheme to jointly estimate user angle and range. Specifically, this work first analyzes the received beam pattern at the user when far-field beamforming vectors are used for beam scanning. It shows an interesting observation that the received beam pattern contains useful user angle and range information. Then, based on this observation, two effective schemes are proposed to jointly estimate user angle and range. This scheme reduces near-field training pilot overhead while obtaining more accurate user distance information, which is useful for applications such as near-field user positioning.

In order to design an efficient beam training scheme from the perspective of hierarchical beam training, the authors in [212] proposed a near-field two-dimensional (2D) hierarchical beam training scheme. This scheme involves the design of a multi-resolution codebook that takes inspiration from hierarchical beam training methods used in far-field scenarios. Contrary to the far-field case, the optimal beam pattern for a near-field codeword should not only span a specific range of angles but also encompass a specific range of distances. It employs a full-digital framework to design the theoretical near-field codewords. Subsequently, based on these codewords, a practical codeword problem was formulated taking into account practical constraints such as digital-analog hybrid structure and quantized phase shift. Inspired by the Gerchberg-Saxton (GS) algorithm for digital holographic imaging phase recovery problems, the authors propose a full-digital architecture theoretical codeword design algorithm based on GS. Since a high-energy full-digital architecture is not achievable in an actual XL-MIMO system, practical codewords are designed using a digital-analog hybrid architecture. Finally, the authors develop a multi-resolution codebook using practical codewords, and proposed a near-field two-dimensional hierarchical beam training scheme. In addition, the authors in [211]. proposed an efficient near-field hierarchical beam training scheme. Specifically, in the first stage, the central sub-array of the XL-array is used to search the coarse user direction in the angular domain through a traditional far-field hierarchical codebook. Then, in the second stage, given a coarse user direction, a specially designed near-field codebook is used to progressively search for fine-grained user direction and distance in the polar-domain. The total beam training pilot overhead of this scheme is

proportional to the number of antennas N, which further reduces the beam training pilot overhead. To adapt to the property near-field beams, the authors in [213] proposed the spatial-chirp codebook-based hierarchical near-field beam training method. All near-field beams are unified with the same beam pattern based on spatial-chirp codebook. It provided the hierarchical codeword update policy for angular and surrogate distance joint binary searching, and manifold-optimization-based training codebook enhancement was further designed. The scheme requires only on RF chain with analog structure, and can be simply extended to the multi-RF digital-analog hybrid structure. Most overheads can be reduced with comparable beam training accuracy to exhaustive searching. Additionally, authors in [214] utilized the near-field beam split to retrieve multiple beam training results simultaneously, increasing the beam training speed and reducing significantly the beam training overhead.

Benefiting from the powerful nonlinear relationship learning capability of neural networks, deep learning has received widespread attention as a branch of machine learning, and studies have shown that deep learning methods applied to near-field beam training can significantly reduce the pilot overhead [215][216]. The received signals corresponding to the far-field wide beam are used to estimate the optimal near-field beam, and two training schemes are specifically proposed, i.e., the original scheme and the improved scheme. The original scheme estimates the optimal near-field codeword directly from the output of the neural network. In contrast, the improved scheme performs additional beam testing, which can significantly improve the performance of beam training. The structure of the neural network proposed by this method for beam training is shown in **Fig. 5.18**.

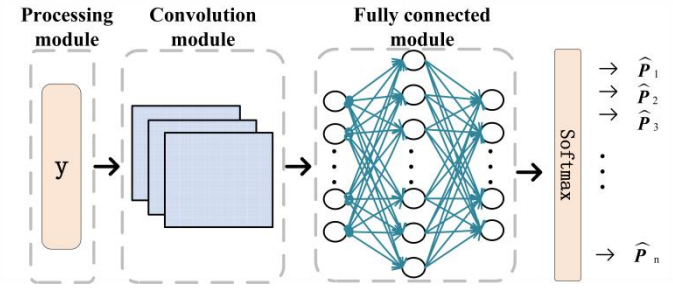

Fig. 5.18 Neural network structure for near-field beam training

In addition to performing near-field beam training in angle domain and distance domain, the location information of UEs can be used to further reduce the complexity of near-field beam training: divide the coverage area of BS into several initial grids, where the size of each grid is about equal to the coverage area of one near-field beam focus. In order to avoid the performance deterioration at the grid edge, the initial grid is shifted so that the terminal at the edge of the grid is in the center of the shifted grid. Based on whether UE is in the center or the edge of the initial grid, UE can determine to use the initial set of grids or one set of the shifted grids. Then, based on the specific grid in the selected set of grids, UE can determine the specific transmitting and receiving beam pair.

5.5 Near-Field Multiple Access

5.5.1 LDMA

One of the main goals of wireless communication system design is to continuously improve transmission rates. Under certain bandwidth resource conditions, the improvement of transmission rate mainly depends on a significant increase in spectral efficiency. The improvement of spectral efficiency

in 5G massive MIMO systems is mainly achieved through spatial division multiple access (SDMA) technology, which excavates spatial resources beyond the time and frequency domains, and utilizes different spatial beams to simultaneously serve multiple users on the same frequency. To achieve SDMA in pure LoS scenarios, existing 5G massive MIMO systems mainly generate high gain directional beams through large-scale array antennas. By using directional beams, wireless signals can be converged at specific angles. Different users are divided according to their angles, and different beams cover users at different angles. While improving the signal-to-noise ratio at the receiving end, the asymptotic orthogonality of different beams in the angle domain is utilized to effectively suppress inter user interference, thus achieving a multiplier increase in spectral efficiency.

By utilizing the new feature of the two-dimensional angle-distance focusing ability of near-field beams, SDMA turns into a location division multiple access (LDMA) technology with angle distance two-dimensional orthogonal resources, providing a new technological path for improving spectral efficiency [217]. Specifically, as shown in **Fig. 5.19**, unlike far-field beams that only have one-dimensional convergence characteristics in the angle domain, near-field beams have two-dimensional focusing characteristics in the “angular-distance" domain, that is, near-field beams can focus wireless signals at specific angles and distances (i.e., a certain position). Based on the two-dimensional focusing characteristics of near-field beams, similar to the angle domain asymptotic orthogonality of far-field beams, [217] first prove the distance domain asymptotic orthogonality of near-field beams, that is, as the antenna size expands, near-field beams focused at the same angle but different distances will tend to be orthogonal. Based on this, in 6G the MIMO technology can achieve a leap from distinguishing multiple users in the angle domain to distinguishing multiple users in the angle distance domain. By mining and utilizing undeveloped orthogonal resources in the distance domain, near-field MIMO provides a new technological approach to improve the spectrum efficiency of wireless communication systems.

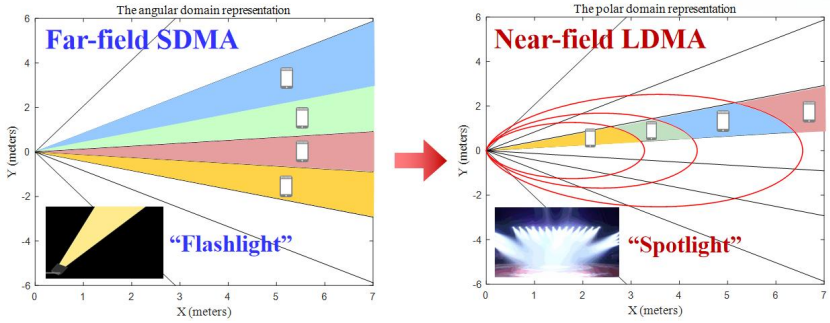

Fig. 5.19 Comparison between far-field SDMA and near-field LDMA

In numerous scenarios involving multiple-access systems, a primary goal is to concurrently serve numerous users while ensuring that the signals they receive adhere to a minimum signal-to-interference ratio (SIR) criterion. When users are roughly aligned at similar angles relative to the transmitter, their simultaneous service feasibility depends on both their distances from the transmitter and their inter-user separations. Consequently, the task evolves into identifying the subset of users for whom reliable simultaneous service is feasible. Because the selection of users is interdependent based on each other's SIR, solving the problem necessitates a joint approach encompassing all users. A graph-theoretic method utilizing the near-field channel model is outlined in [218], where the problem is cast as the maximum clique problem in an undirected graph and tackled using a heuristic algorithm. **Fig. 5.20**

illustrates the outcome of applying this algorithm to the system delineated in Section 4.3. From a pool of 100 users oriented similarly relative to the transmitter, five users are chosen, each requiring a minimum SIR of 18 dB. The graph demonstrates that closer to the transmitter, more users can be accommodated, while as the receiver moves farther away, concentrating the signal at a specific location becomes more challenging.

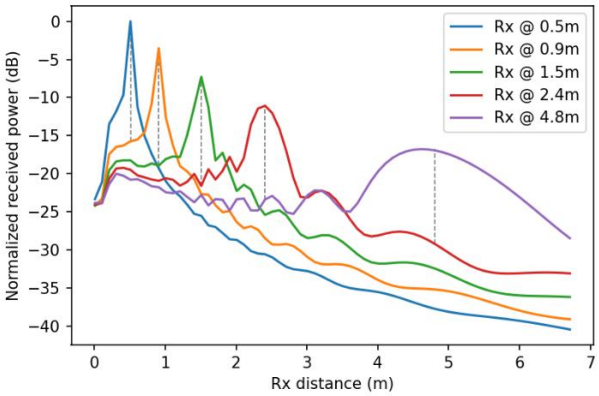

Fig. 5.20 Multiple-access in near-field for users with same angular orientation [218]

5.5.2 NOMA

Although near-field communications provide higher spatial resolution, it is still difficult to meet the demand for massive user access in wireless networks by only utilizing the degrees of freedom in the direction of range and angle. This is because, on the one hand, the resolution of beam focusing in near-field communication cannot achieve perfect accuracy except in the case where users are very close to the base station [219]; on the other hand, the large-scale antenna arrays at the base station normally employ hybrid analog-digital antenna structures in near-field communications. In this case, for Orthogonal Multiple Access (OMA) technology, the maximum number of connected users is limited by the number of RF chains. By contrast, Non-Orthogonal Multiple Access (NOMA) technology allows multiple users to be multiplexed over the same block of radio resources (e.g., time slots, subcarriers, spatial beams, etc.) and to be distinguished in the power domain or code domain, thus further enhancing the network spectral efficiency and user access capability. Therefore, near-field NOMA communications are conceived to be a promising solution. It is worth mentioning that the beam focusing capability of near-field communications also brings a series of new design opportunities for NOMA as shown in **Fig. 5.21**, which are discussed as follows:

- **"Far-to-Near" Successive Interference Cancellation (SIC):** Compared to far-field NOMA communications, the near-field beam focusing capability enables users far located from the base station (termed as far users) to achieve a higher equivalent channel gain than users close to the base station (termed as near users) with a single beam focused on the far users. Based on this feature, near-field NOMA enables a "far-to-near" SIC decoding operation [220]. The far user can act as a strong NOMA user to first decode and cancel the interference from the near user (weak NOMA user) before decoding its own signal. This is almost impossible to achieve in conventional far-field NOMA communications.

- **Range-domain NOMA User Clustering:** Compared to the angle-domain user clustering in conventional far-field NOMA, exploiting the range-domain degrees of freedom provided by near-field beam focusing, users at the same angle can be further divided into several user clusters in near-field NOMA, which can significantly reduce inter-user interference [220].
- **Hybrid Near/Far NOMA Communication:** Due to the non-perfect accuracy of the near-field beam focusing, the signal strengths of the beams serving near-field users may be superimposed at the far field. Based on this property, additional far-field users can be served using NOMA technology without changing the legacy beamforming design of the near-field communications but further enhance the user access capability of the network [221].

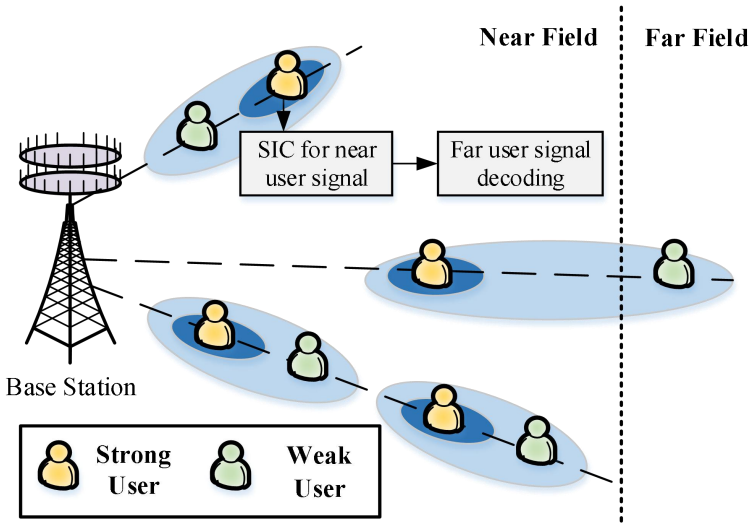

Fig. 5.21 Illustration of near-field NOMA designs

5.5.3 URA

In addition, next generation multiple access techniques aim to support the access of massive Internet of Things devices such as sensors. These users generally have a very low active probability and establish the uplink transmission via short packets. Unsourced random access (URA) is an efficient massive random-access scheme which assigns a common codebook for all potential users [222][223]. URA users select the transmitted codeword from the common codebook relying on their messages, with no obligation to identify themselves. Accordingly, the receiver reconstructs a list of messages without user identification. With the increasingly dense distribution of devices in the Internet of Things and the increase in the near-field distance caused by XL-MIMO deployments, a significant number of users are expected to locate in the near-field region. Therefore, URA schemes in the near-field condition are worthy of further exploration.

Considering that the number of codewords in the common codebook increases exponentially with the message length, multi-stage coding schemes are usually adopted for URA to reduce the system complexity. As the crucial step of decoding, the receiver requires to detect the transmitted codeword and reconstruct the corresponding channel. The near-field channel estimation technology provides a novel solution to this problem. First, codeword detection can be cast as a multiple measurement vector problem by capturing the coherent support structure of MIMO channel elements in the spatial domain, by which way the range of possible active codewords can be reduced. Then, the restricted common

codebook along with the near-field channel codebook are employed to perform enhanced channel estimation in the polar domain. The above steps are performed alternately in a turbo manner to fully exploit the sparse structure of the near-field polar domain channel, which decreases the number of parameters required for reconstruction and reduces the codeword length.

On the other hand, the features of the near field channel in the dimensions of angle and distance can be regarded as the implicit “identity" of a specific user, which assist the codeword reorganization from multiple segments without the help of user identification [224]. The concatenation process can be performed by channel clustering without adding redundant check bits, which helps to improve the coding rate and the spectral efficiency.

5.6 Non-Coherent Communication Schemes

The challenges of channel estimation for near-field communications have been detailed in section 5.1. Given the difficulties in obtaining channel information, the use of non-coherent communication techniques is proposed where Channel State Information (CSI) is not required. Traditionally, non-coherent detection entailed a well-known 3dB loss in system performance compared to its coherent counterpart employing CSI. However, with the emergence of massive MIMO, this degradation has disappeared, equalizing both forms of transmission. Several proposed schemes for future communication systems, where non-coherent detection becomes relevant for near-field communications due to its properties, are presented in [225].

Non-coherent communications can offer several benefits and improvements to near-field communications (NFC) systems as follows:

- **Resilience to Multipath Fading**: In near-field environments, multipath fading can occur due to signal reflections from nearby objects. Non-coherent communication techniques using modulation schemes based on DPSK as presented in [225]-[227] are less susceptible to multipath fading compared to coherent schemes. This resilience helps maintain communication integrity in NFC systems, especially in environments with complex signal propagation characteristics.
- **Robustness to Interference:** Non-coherent communication schemes are often more robust to interference and noise compared to coherent schemes. In near-field communication scenarios where there may be significant interference from surrounding electronic devices or environmental factors, non-coherent techniques can help maintain communication reliability.
- **Reduced Complexity**: Non-coherent communication schemes typically involve simpler modulation and demodulation processes compared to coherent schemes. This reduction in complexity can lead to lower-power and more cost-effective NFC transceivers, making them suitable for small, battery-powered devices like NFC-enabled smartphones, wearables, and IoT devices.
- **Simplicity:** Non-coherent communication techniques tend to be simpler to implement and require fewer resources compared to coherent schemes. This simplicity can be advantageous in NFC applications where low-power, low-cost, and efficient communication protocols are desirable.
- **Lower Complexity Transceivers:** Non-coherent communication systems typically require fewer complex transceivers compared to coherent systems. This can lead to smaller and more cost-effective NFC devices, making them more accessible for widespread deployment in various applications.

- **Improved Range:** Non-coherent techniques may offer improved range performance in certain near-field communication scenarios, especially when dealing with obstacles or attenuating materials. By optimizing the modulation and demodulation processes, non-coherent schemes can enhance communication range without significantly increasing power consumption.
- **Improved Signal Detection:** Non-coherent receivers do not require precise phase synchronization with the transmitted signal, making them more tolerant to timing offsets and phase distortions. As a result, non-coherent receivers can reliably detect signals even in the presence of frequency drift, phase noise, and other impairments commonly encountered in NFC environments.
- **Enhanced Security:** Non-coherent modulation techniques, such as frequency-shift keying (FSK), can provide inherent security benefits for NFC systems. By modulating the carrier frequency based on the data to be transmitted, FSK inherently spreads the signal energy across a wider frequency spectrum, making it less susceptible to interception or eavesdropping attacks.
- **Compatibility with Low-Cost Hardware:** Non-coherent communication techniques are well-suited for implementation on low-cost, low-power hardware platforms commonly used in NFC devices. By leveraging simple modulation schemes and efficient signal processing algorithms, non-coherent NFC transceivers can be deployed in a wide range of applications without significant hardware or computational overhead.
- **Adaptability to Dynamic Environments:** Non-coherent communication systems can adapt more effectively to dynamic NFC environments where signal conditions may vary rapidly. By employing adaptive modulation and error correction techniques, non-coherent NFC systems can maintain reliable communication links even in the presence of changing interference levels or channel conditions.

Overall, the use of non-coherent communication techniques in near-field communication systems offers a practical and efficient solution for achieving reliable, low-power, and cost-effective wireless connectivity in a variety of applications.

5.7 Deployment of Near-Field Communication System

According to **Chapter 3.1**, the classic criterion for distinguishing the near-field and far-field region is the Rayleigh/Fraunhofer distance, which increases with the physical size of the array and/or the carrier frequency. However, to attain significant performance enhancement in future 6G communication systems, promising technologies such as RIS, massive multiple-input multiple-output (MIMO), and terahertz (THz) communication need to substantially increase the number of active antennas/passive elements, or mitigate the carrier frequency to higher bands. This thus leads to an increase in the originally negligible Rayleigh/Fraunhofer distance to tens or even hundreds of meters. Therefore, the traditional deployment strategies based on far-field models are no longer applicable to the extremely large-scale arrays (XL-arrays) for 6G, including both XL active arrays and XL passive arrays. Additionally, the deployment of XL active/passive arrays has a significant impact on key technologies for near-field communication, such as beamforming, channel estimation, wireless power transfer, and integrated sensing and communications (ISAC). These technologies exhibit distinct implementations and effects under various deployment strategies. In the following, we will introduce

different deployment strategies from the perspectives of node placement, network deployment and optimization objectives.

(1) **Node placement:** The deployment scenarios of XL-arrays [228] can be classified into four main types: the base station (BS) side deployment [79], the relay side deployment [229], the user side deployment [230], and multiple sides deployment [231], as illustrated in **Fig. 5.22**. In practice, deploying XL-arrays at the BS or relay side is easier to implement. For the XL active arrays, deploying them directly at the BS/relay significantly enhances the capacity and coverage range of communication systems. However, this strategy faces challenges as some users are located in the near-field region of the BS/relay, necessitating the considerations of the mixed near- and far-field effects as well as the interference management between far-field and near-field users. For the XL passive arrays such as RISs, deploying them near the BS/relay not only improves the communication coverage but also substantially reduces the required number of (active) antennas at the BS/relay. Additionally, the multiplicative path loss induced by passive arrays decreases as the distance between the XL passive arrays and BS/relay reduces. In this context, besides the aforementioned mixed near- and far-field effects and interference issues among users, system design should also account for the near-field effects between the BS/relay and the XL passive arrays. Considering the device constraints in terms of the cost and energy consumption, it is impractical to deploy XL active arrays at the user side. On the contrary, with advantages of low cost and low power consumption, passive arrays (e.g., RISs) are more likely to be implemented in extremely large scale at the user side. Especially in scenarios involving a large number of randomly distributed users, XL passive arrays can be flexibly deployed as signal hotspots at the user side, significantly improving the probability of establishing virtual line-of-sight (LoS) links and enhancing user communication performance. In this context, the system design must also consider the near-field effects as the distance between the XL-arrays and users is within the Rayleigh/Fraunhofer distance.

(2) **Network deployment:** The deployment of XL-arrays (including XL active/passive arrays) can be classified into centralized deployment and distributed deployment. For a given number of active antennas/passive elements, these two deployment strategies exhibit distinct performance, as discussed below. First, the centralized and distributed deployment have different equivalent channel states, leading to variations in communication rates and transmission delays. Second, for the distributed deployment, each served user can only benefit from the beamforming gain provided by its nearby array. In contrast, centralized deployment involves an array with a larger physical size, enabling multi-user sharing where all antennas/elements in the array can serve any user and thus achieving enhanced beamforming gains. Third, distributed deployment entails more nodes, thus requiring more round-trip links for information exchange compared to centralized deployment. The larger number of nodes renders higher network overhead and network complexity. Last, the flexibility of distributed deployment facilitates the establishment of virtual line-of-sight (LoS) links with users, thereby increasing the probability of establishing LoS links compared to centralized deployment.

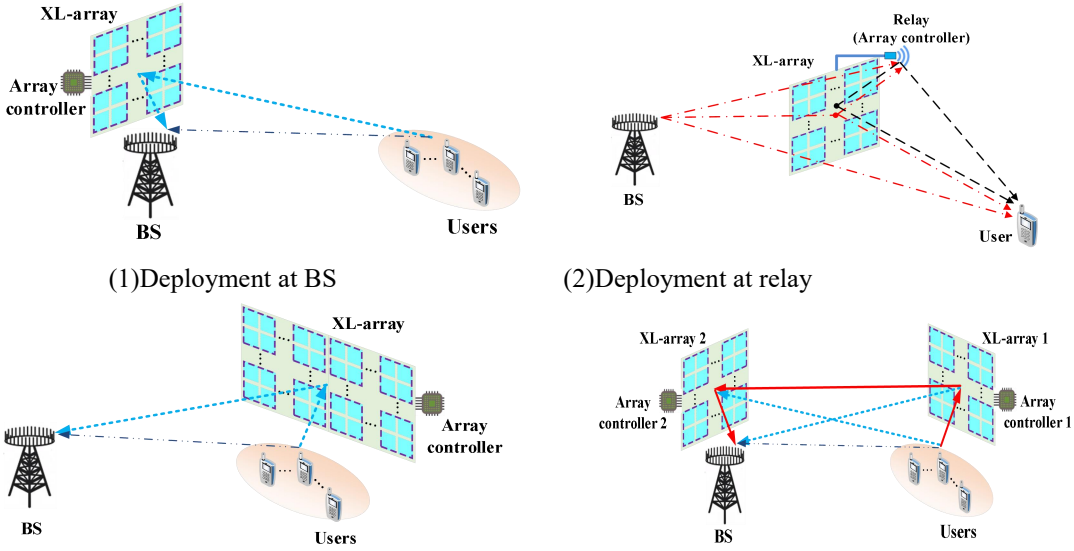

(1)Deployment at BS (2)Deployment at relay

(3)Deployment at users (4)Deployment at both BS and users

Fig. 5.22 Deployment scenarios of XL-arrays (taking RIS as an example)

(3) **Optimization objectives[231]**: For traditional far-field assumption-based cellular network deployment, the main optimization objective is the signal strength distribution of network coverage, also known as link budget. However, for near-field assumption-based network deployment, the optimization objective will not only include the signal strength distribution of coverage but also consider the changes in spatial freedom caused by near-field propagation characteristics. Therefore, when optimizing the deployment of near-field networks, factors such as near-field distance conditions, RIS size, deployment density, and angles relative to the coverage area must be considered.

Notably, most of the current research on near-field communication tends to study the performance of the near field and far field systems separately under the assumption that the propagation distance conforms to the constraints of near-field/far-field distances. Considering the distributed deployment of users and exploiting the characteristics of the near field, a hybrid communication architecture based on near-field relays can be envisioned, as depicted in **Fig. 5.23**. In this architecture, relays are deployed in proximity to the users, ensuring near-field communication conditions between the relays and users. Meanwhile, since the distances between the BS and relays are relatively remote, the communication between the BS and relays is considered as far-field communication. In the proposed hybrid communication architecture based on near-field relays, the deployment of relays and the corresponding strategies for different relays serving different groups of near-field users should be taken into account.

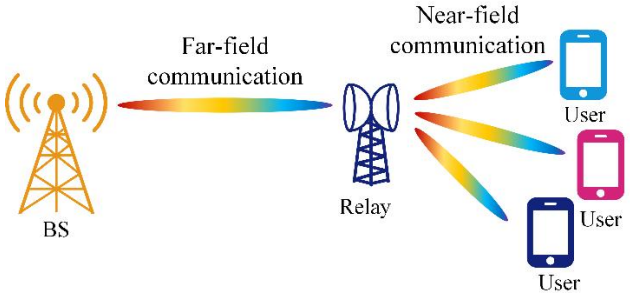

Fig. 5.23 A hybrid communication architecture based on near-field relays

5.8 Standardization

Near-field communication standardization covers a series of standards and protocols, including channel model standards, communications protocols, data exchange formats, etc. Relevant standards include NFC Forum designed protocol, ISO/IEC 18092, ISO/IEC 14443, FeliCa, etc. This subsection mainly discusses the standardization of channel models. From a standardization perspective, existing channel models are based on far-field assumptions and cannot be applied to near-field regions. In terms of channel estimation, beamforming, codebook design, and beamforming training, the current standard techniques are also difficult to apply to near-field regions. In addition, the application of extremely large-scale MIMO and high-frequency technology makes it possible for synesthesia technology to work in the near-field. The application of large panels in RIS technology also increases the probability of users being in the near-field. Therefore, in the standardization process of synesthesia and RIS technology, near-field effects also need to be considered. The potential standardization directions in the near-field include:

To standardize near-field channel models, it is imperative to assess various channel modeling schemes. Several viable solutions have been proposed in existing research. For instance, one approach involves adopting the channel model outlined in TR38.901 [232] and making necessary adjustments, such as modifying the channel parameter generation module to align with near-field requirements. Additionally, leveraging statistical models to establish the physical positions of clusters can aid in near-field channel modeling. While standardizing near-field channel models, the issue of continuity between near-field and far-field also needs to be studied and standardized. It is necessary to conduct research on the modeling of occlusions, the correlation of channel parameters between antenna subsets or large-scale antennas, in response to the non-stationary characteristics of space. The number of paths, path strength, cluster structure characteristics, spatial continuity, and other aspects in the near-field are different from those in the far-field, and need to be modeled, characterized, and included in the channel modeling standards. In terms of modeling methodology, the Geometry based Stochastic Channel Model (GBSM) architecture is concise, easy to implement, has low computational complexity, but also has low accuracy. The Map Based Hybrid Channel Model (MHCM) contains certain deterministic information components and random statistical components, which have certain accuracy and low computational complexity. Deterministic channel models (such as ray tracing methods) provide detailed descriptions of transmission environments, transmitter and receiver positions, etc., with high accuracy but high computational complexity. In standardization work, it is necessary to measure and evaluate the advantages and disadvantages of various channel modeling methods, and construct a channel model that balances accuracy and computational complexity. In December 2023, the Third Generation Partnership Project (3GPP) approved a project to enhance the 7-24GHz channel model at the RAN#102 plenary session [233]. This project will be based on the channel model standard in TR38.901, adding modeling for new frequency bands, near-field propagation, and spatial non-stationary characteristics to compensate for the limitations of existing 5G channel model standards, in order to cover existing and potential near-field application evaluation needs in the future.

In terms of channel estimation, beamforming, codebook design, beam training, and other aspects, the current standards use technologies based on the assumption that users are located in the far field, treating electromagnetic waves as plane waves. Directly applying existing technical solutions to the near field will lead to a decrease in system performance, so it is necessary to design technical solutions

that adapt to spherical wave channels. In terms of beamforming technology, unlike far-field communication where beamforming is limited to the angular domain, near-field communication, based on the assumption of spherical waves, allows for beam focusing. In near-field communication, beams can be designed not only in the angular domain but also in the distance domain, utilizing polar coordinates. Consequently, beam training and codebook design necessitate tailored schemes suitable for near-field regions.

During the standardization process of ISAC and RIS technologies, near-field effects must also be taken into account. This includes establishing channel models for ISAC and RIS technology in the near-field region. Additionally, considering the characteristics of RIS cascaded links, technical solutions such as beamforming, channel estimation, and codebook design need to be devised specifically for the near-field region of RIS.

6 Integration of Near-field Technology with Other Technologies

6.1 Near-field Based Positioning

In conventional far-field communications, the phase difference of the receiving antenna array is mainly determined by the angle of arrival of the signal, so the process of channel localization can easily calculate the angle of arrival of the signal to obtain the orientation information of the target. In contrast, efficient near-field communications require a more accurate modelling of the electromagnetic channel using a spherical wavefront. In the spherical wavefront-based channel model, both distance and bearing information are included in the phase delay, which has the potential to accurately locate the target. Moreover, adopting the far-field model for near-field sources leads to a model mismatch problem that can deteriorate the positioning performance [235]. Therefore, along with the research and development of near-field communications, near-field positioning will be an important technology in the future 6G.

6.1.1 Near-Field and Positioning

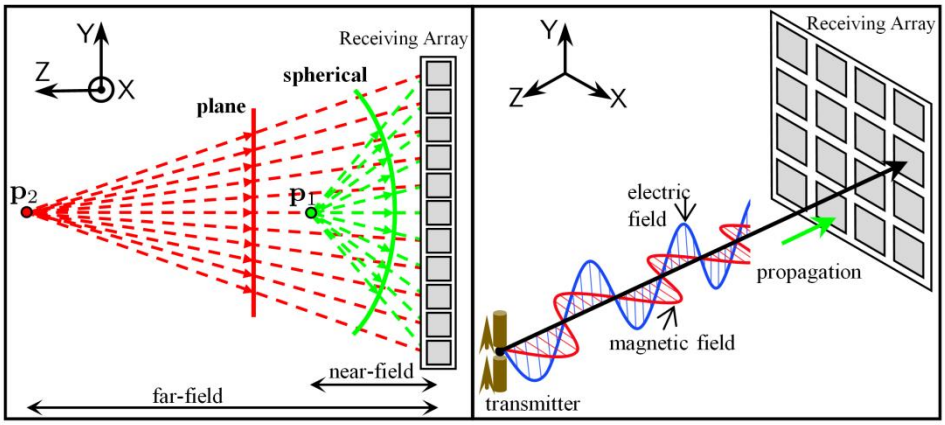

Fig. 6.1 Near-field signal model and far-field signal model.

(The transmitter $\mathbf{P}_2$ is in the far field of the receiving array, and its signal model is represented by a plane wavefront. The transmitter $\mathbf{P}_1$ is in the near field of the receiving array, and its signal model is represented by a spherical wavefront. The subfigure on the right gives a more accurate near-field signal model that considers the electromagnetic physical effects of the near field.)

Fig. 6.1 shows the near-field signal model and far-field signal model. From **Fig. 6.1**, we can explain the reasons why the spherical wavefront characteristics of near-field propagation are conducive to improving positioning accuracy:

(1) The plane wavefront modeling of the far-field signal causes the angle of arrival (AoA) obtained by different receiving antenna elements to be the same, so plane wavefront modeling in the far field can only estimate the angle of arrival. To obtain the position parameter, one feasible approach is to deploy multiple spatially distributed arrays with known positions for the estimation of AoAs. Alternatively, the clock synchronization between the transmitter and the receiver can be employed to measure the time of arrival (ToA).

(2) However, the amplitude term and phase term of the near-field signal based on spherical wavefront modeling contain the precise distance from the transmitter to each receiving antenna. This allows us to directly obtain the position information of the transmitter, thereby improving positioning accuracy.

In addition, the electromagnetic physical effects of near-field signals also make it possible to sense the attitude of the transmitter. From **Fig. 6.2**, the attitude of the transmitter is related to its physical shape. For a basic linear antenna, its attitude is represented by its orientation in three-dimensional space. Different spatial orientations will lead to different source current distributions, resulting in different excited electric fields. Therefore, the near-field electromagnetic signal and the attitude of the transmitter have a one-to-one mapping relationship, which allows us to estimate the attitude of the transmitter.

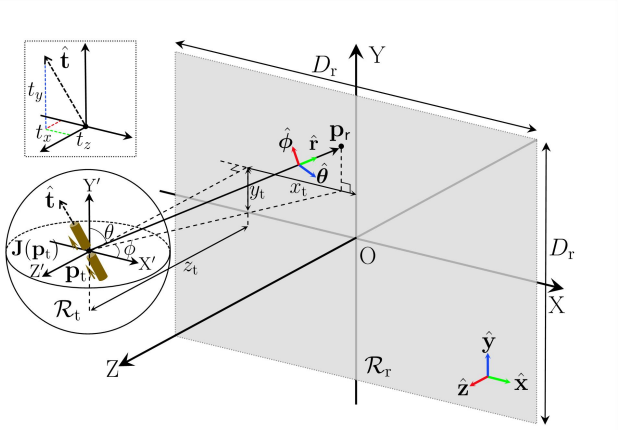

Fig. 6.2 Near-field positioning and attitude sensing.

In the literature [236], for the noise-free case, the author proposed the phase ambiguity distance and the spacing constraint distance to accurately divide the position domain of the transmitter. For each position domain, the author provided a feasible decoupling scheme and gave solutions to nonlinear electromagnetic equations.

Secondly, for the noisy case, joint positioning and attitude estimation needs to use signal estimation theory. Literature [237] pointed out that using the electromagnetic near-field model, in the millimeter wave frequency band or sub-terahertz frequency band and the size of the observation surface is at the meter level, the position estimation accuracy can reach the millimeter level. In [238], the authors developed Ziv-Zakai lower bounds for joint positioning and attitude estimation. Compared with the locally tight Cramér-Rao lower bound, the Ziv-Zakai lower bound can also provide accurate performance predictions in low signal-to-noise ratio regions. Through the Ziv-Zakai lower bound, the authors show that the attitude estimation can reach the 0.1 level (the estimation error range is ± 0.1).

It is noteworthy that source localization primarily estimates two positional parameters of the user: the angle and distance of the source relative to the base station. In far-field scenarios, source localization is usually a joint estimation problem: angle estimates are obtained through the AoA, and distance estimates are acquired through the ToA. However, this joint estimation requires precise synchronization and/or the participation of multiple access points, and its performance is usually suboptimal compared to direct positioning.

When wireless positioning shifts from far-field to near-field, the received signals exhibit a spherical wavefront rather than a planar wave. This enables the use of near-field spherical wave characteristics to enhance wireless positioning, achieving direct positioning. Specifically, the user's location can be directly calculated based on the curvature of arrival (CoA) of the spherical wavefront, allowing a single array to determine both distance and direction simultaneously [238]. This contrasts with far-field methods, where complicated two-step AoA and ToA estimation is required. By leveraging these near-field techniques, positioning estimation accuracy is significantly improved while also substantially reducing implementation complexity [239]. However, when it comes to near-field sources, it's necessary to jointly search over both the angle and range due to the angle-range coupling inherent in the spherical wavefront. This may introduce some additional complexity. In this regard, some studies focus on proposing algorithms to decouple the angle and range, then divide the 2D search into two consecutive 1D searches over the range and angle, aiming to mitigate this complexity.

Another approach to positioning in the near field is to partition the large antenna array into multiple subarrays and approximate the signal received on each subarray as a planar wave, and combine the information from multiple subarrays to estimate the position of the user. By partitioning a large array of into N subarrays of equal size, the Rayleigh distance shrinks by $\frac{1}{N^2}$. This pushes a user close to the base station into the far field of the subarrays. This allows us to apply traditional array signal processing algorithms, such as MUSIC or ESPRIT, to each subarray to find the individual AoA from the user. By combining the multiple estimated AoAs from the subarrays, one can estimate the position of the user $(\vec{r})$ with respect to the center of the array can be estimated as follows:

$$\vec{r} = argmin\left(\sum_{k=1}^{N} \gamma_k \left|(\vec{r} + \vec{r}_k) - \hat{a}_k\left((\vec{r} + \vec{r}_k) \cdot \hat{a}_k\right)\right|^2\right) \quad (6.1)$$

where $\hat{a}_k$ is the unit length direction vector at subarray k pointing towards the UE based on the estimated AoA, γ_k is the received SNR at subarray k, and $\vec{r}_k$ is the center of subarray k relative to the center of the entire array.

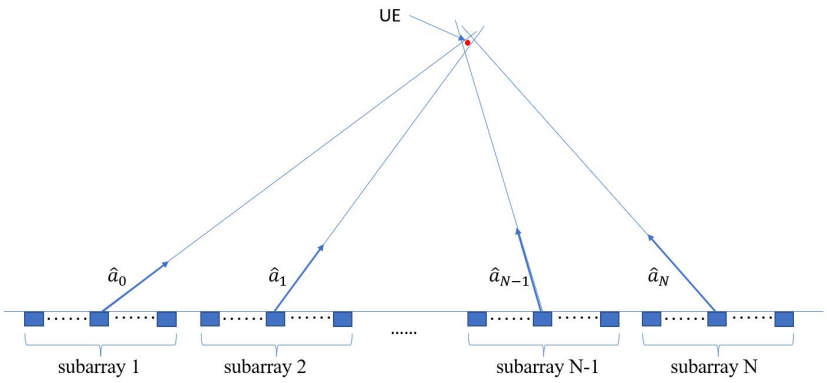

Fig. 6.3 User positioning with sub-arrays.

This approach is equivalent to approximate the nonlinear phase vector corresponding to spherical wave on a large array with NK elements with a set of N linear phase vectors of length K, each collected from a subarray of with K elements and corresponds to planar waves of slightly different AoAs. **Fig. 6.4**

shows this approximation works very well. The estimated user position $\vec{r}$ can be used to update the estimated AoAs ($\hat{a}_n$) for the sub-arrays, and further updates the channel estimation to the user. The estimated channel takes the form of a set of DFT-like vectors for the sub-arrays (and the phase offset between adjacent sub-arrays). By flipping the sign of the estimated phase, we have a beamforming vector closely approximating maximal ratio combining to focus the downlink signal to the user.

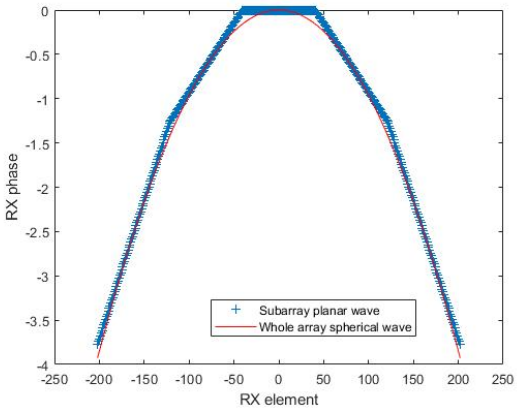

Fig. 6.4 The received phase of a spherical wave on a large array and its approximation with planar waves on 5 subarrays.

6.1.2 Near-Field Positioning Technology Based on RIS

Near field communication and positioning based on massive MIMO technology require a large number of antenna elements and RF channels, including phase shifters, mixers, ADCs, etc., resulting in high hardware costs. In contrast, RIS-based near-field positioning can take full advantage of its flexible beam switching and channel reconstruction capabilities to achieve reliable communication and perception performance. Abundant time of flight (ToF) and spatial spectrum information can be obtained by a large number of period arrangement elements in the RIS array, which is expected to accurately estimate the source position. When the source incident on the RIS, the phase delay to different elements is a function of the distance d between the source and the center of the meta-surface and the orientation (θ, φ) of each element, which means that the source can be pinpointed effectively using spatial spectrum classification or maximum likelihood estimation [240][241].

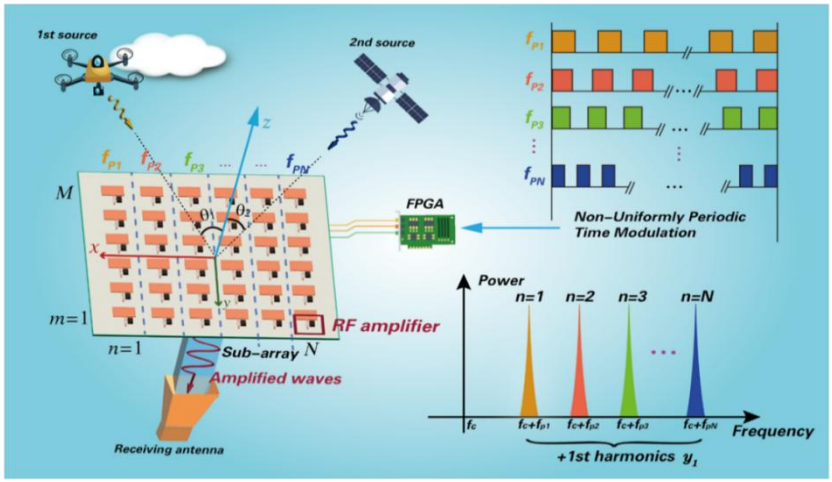

Fig. 6.5 Schematic diagram of two-dimensional DoA estimation based on RIS and non-uniform time modulation [242].

The basic theory and algorithms of information source's spatial positioning parameter estimation have been relatively mature, but many algorithms require multidimensional spatial spectrum search or high-complexity computations, which restricts the practical application because of hardware requirements, so there are still many problems to be solved. Therefore, based on the parameter estimation method of rank reduction or dimension reduction [243], the multi-dimensional spectral peak search algorithm can be transformed into several one-dimensional searches, and the angle and distance parameter estimation can be matched automatically. However, the process of splitting the 2D search into two 1D searches is not straightforward. Initially, it requires the decoupling of bearing angles and distances or electrical angles. For example, by carefully selecting specific antenna elements to compute the channel covariance matrix, one of the electrical angles can be effectively eliminated from the problem, enabling 1D-compressive sensing for the AoA [244].

In addition, RIS-based positioning can significantly reduce hardware complexity, reducing DoA estimates that traditionally require multiple RF channels to just one. The spatial phase information can be stored in the spectrum through the space-time coding strategy, as shown in **Fig. 6.5**, which uses non-uniform time modulation to realize full-duplex multi-target positioning and adaptive beam scanning. The spatial spectrum information can also be contained in the received signal of multiple time slots by radiative multiple random beams, where holographic RIS and spherical wavefronts could be applicable[245][246].

Furthermore, the users may locate in the near field of the RIS in the XL-RIS-assisted THz localization systems. Since different RIS elements no longer share the same AoA according to the spherical wavefront of near-field channel model, the modeling and estimation of near-field channels become a more challenging task. Consequently, traditional channel estimation and localization methods will suffer severe degradation when applied in near-field scenarios.

Recently, the authors of [38] have proposed an algorithm of RIS-aided near field joint channel estimation and localization (NF-JCEL) in THz systems. As shown in **Fig. 6.6**, the authors considered the near-field channel model based on the spherical wavefront, and estimated the AoAs and distances from the central reflecting element to UEs as well as the cascaded channel gains to locate the UEs by utilizing the geometric relationship. Based on the second-order Fresnel distance approximation, the researchers designed a RIS phase-shift training method to increase the rank of the channel matrix and avoid the noise amplification caused by LS estimation. Then, by utilizing the near-field channel characteristics, the researchers designed a sampling Toeplitz covariance matrix to decouple the distances and angles, and estimated the horizontal and vertical AoAs of the UEs respectively. Finally, they estimated the distances of the UEs with one-dimensional searching and obtained the estimated position by utilizing the estimated parameters and geometric relationship.

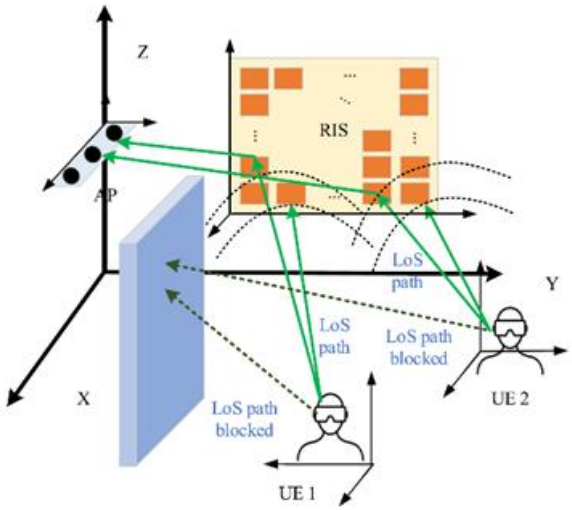

Fig. 6.6 RIS-assisted THz multi-user positioning systems.

As depicted in **Fig. 6.7**, the proposed algorithm prevails over the traditional far-field methods in the root mean square error (RMSE) of UE locations by utilizing the near-field AoA information. In addition, the RMSE will decrease with more RIS elements as well as more AoA information. Therefore, it is promising to deploy XL-RIS with more elements to enhance the localization accuracy.

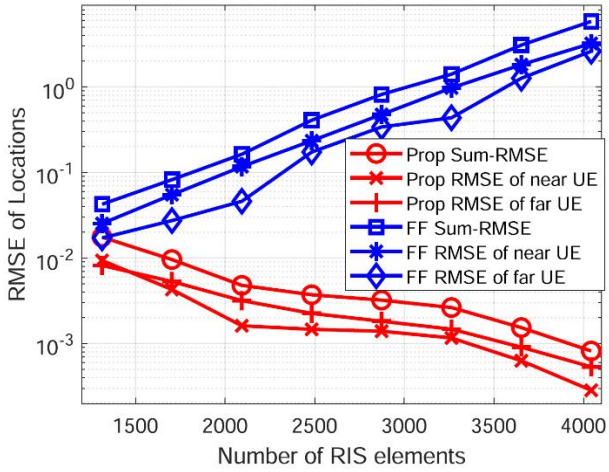

Fig. 6.7 RMSE versus the number of RIS elements.

In the following, another example of RIS-aided localization is introduced. First, the system model employed for three-dimensional (3D) localization using the RIS is presented. Furthermore, we introduce the near-field channel and a realistic amplitude-dependent phase RIS model to assess the performance metrics including positioning error bound (PEB), RMSE for localization, and achievable data rate for communication. We examine a wireless setup comprising of a single user transmitting from position $\mathrm{p} = [\mathrm{x}, \mathrm{y}, \mathrm{z}]^{\mathrm{T}}$, and an N-element RIS lens positioned in the XY plane with reference point $[0,0,0]^{\mathrm{T}}$. The RIS is placed near a single antenna equipped with a corresponding RF chain for reception, located at $\mathrm{p}_{\mathrm{ant}} \in \mathbb{R}^3$ as per **Fig. 6.8**. The figure illustrates the 3D coordinate system that shows the positional and angular information of the user and RIS. The spacing between the horizontal and vertical elements is set to $\lambda/2$ where λ is the wavelength at the carrier frequency. The n-th

element of the RIS is located at $\zeta_n = [x_n, y_n, 0]^T = l_n[\cos\Psi_n, \sin\Psi_n, 0]^T \in \mathbb{R}^3$ where l_n refer to the element's distance from the RIS origin to the element and Ψ_n is the n-th element azimuth angle.

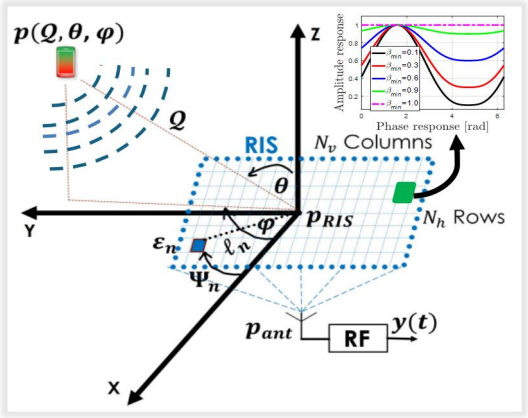

Fig. 6.8 Localization system coordinate.

The RIS is composed of N =2500 elements arranged in a $N_v \times N_h$ grid, where $N_v = N_h = 50$, at a frequency of 28 GHz with $\lambda^2/4$ element area. A single receive antenna is positioned behind it at coordinates $[0,0,-\lambda]^T$. The transmit power is 1 mW, the noise power spectral density is -174 dBm/Hz, and the reception noise figure is set to 8 dB. We choose the number of time instances to be T = 200 and the bandwidth to be 1 MHz. In our analysis, we focus on a user who possesses a wavevector k oriented in the direction $[1,1,1]^T$. The channel gains to and from the RIS are set in the near-field regime [247]. The prior knowledge about the user's location is represented by a (pdf) denoted as $p(p) = N(p; m_p, c_p)$, where $c_p = \sigma^2 I_3$. This prior information is solely employed for designing the directional beams of the (RIS), and it is not utilized during the localization process or in the calculation of the (PEB). The standard deviation in each dimension (XYZ) of the prior covariance of the user position is set to $\sigma \in \{0.1,1\}$ m to evaluate the localization performance in the random, directional, and positional phase profiles.

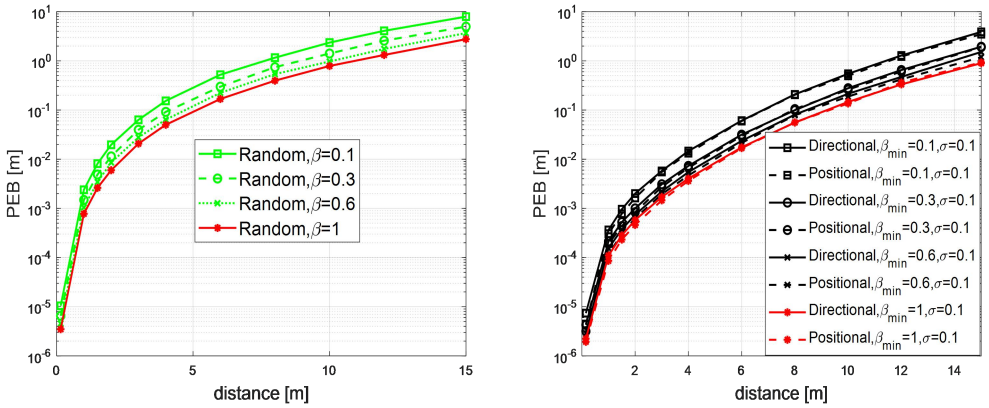

Fig. 6.9 PEB as a function of distance to the RIS using random, directional and positional RIS phase profiles.

In **Fig. 6.9** we notice that by using a basic random phase configuration, we can achieve relatively low PEB, specifically below 1 meter, for user positions within a 10-meter distance from the RIS and at different values of β_{min}. By employing directional or positional phase profiles ($\sigma = 1$ and $\beta_{min} \in$

[0,1]), it is possible to significantly decrease the Position Error Bound (PEB). The positional phase profile exhibits slightly superior performance compared to the directional phase profile, although the disparity between the two is negligible. Similarly, we observe that employing directional or positional phase profile allows us to achieve relatively enhanced (PEB), specifically below 1 meter, for user positioned within a 10-meter range from the RIS, regardless of the value of $\beta_{\min}$.

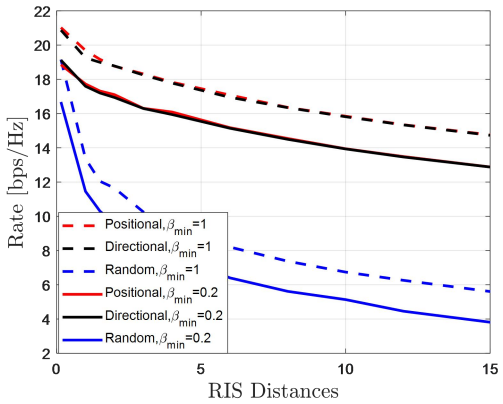

Fig. 6.10 Data Rate versus RIS distance

Fig. 6.10 shows the data rate against the distance to the RIS. Generally, the data rate is inversely proportional with the distance, and this is due the decrease in (SNR) in the reflected path, which is inversely proportional to the distance from the RIS. The realistic RIS phase shift model is adopted, and the data rate performance gap is evident when β_{min} is changed from the ideal case which is $\beta_{min} = 1$ to the actual case which is $\beta_{min} = 0.2$.

6.1.3 Near-field Localization Based on Controllable Beam Squint

For wideband massive MIMO systems using OFDM modulation, beamforming based on phase shifter (PS) structure will lead to beam squint effect. Far-field beam squint effect causes the beams of subcarriers with different frequencies to focus into different angular directions [248][249], while near-field beam squint effect causes the beams of subcarriers with different frequencies to focus at different positions. **Fig. 6.11** shows an example of near-field beam squint, where a total of M+1 subcarriers are enabled. As the frequency of subcarriers increases, the beamforming of different subcarriers will focus at different positions and can be connected into a trajectory. The starting point of the trajectory is determined by the 0-th subcarrier, while the ending point of the trajectory is determined by the M-th subcarrier. In **Fig. 6.12**, the lowest frequency of subcarrier is 30 GHz, and its near-field beamforming is focused at position $(10\text{m}, 60°)$. The highest frequency is 36 GHz, and its near-field beamforming squints to position $(22.99\text{m}, 46.19°)$. It can be seen that near-field beam squint phenomenon cannot be ignored in wideband systems.

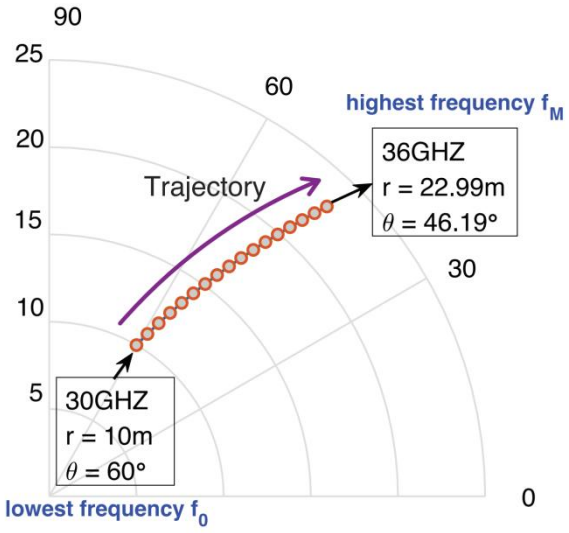

Fig. 6.11 Schematic diagram of near-field beam squint.

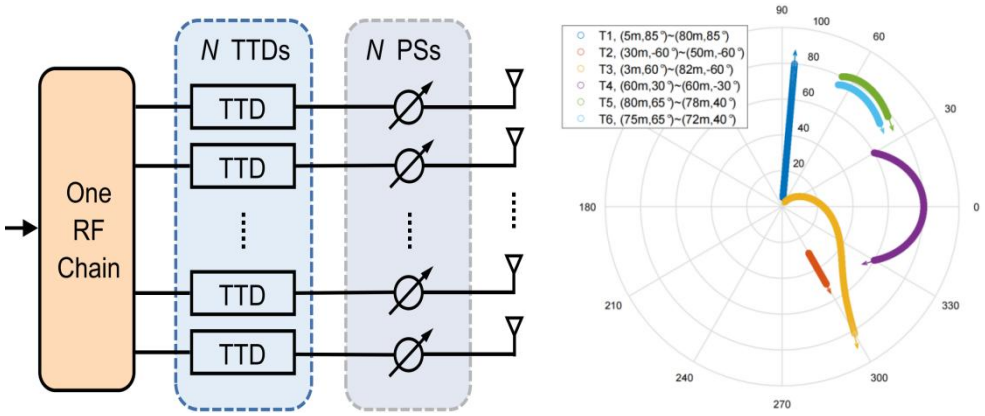

Fig. 6.12 Schematic diagram of near-field controllable beam squint.

As shown in **Fig. 6.12**, it is considered to cascade a true time delay (TTD) line for each PS in the base station (BS). By carefully setting the values of PSs and TTDs, the starting point and ending point of the near-field beam squint trajectory can be reversely controlled, which is beneficial for BS to realize user localization with low pilot overhead. Specifically, **Fig. 6.12** shows examples of several near-field controllable beam squint trajectories, where a total of 2048 subcarriers are enabled. Trajectories T1 and T2 are two radial straight lines. If the angle of user or target has already been obtained, using radial trajectories like T1 and T2 can quickly sense the distance of the user or target. Trajectory T3 spans the entire range of angle and distance, providing full area sensing. Trajectory T4 exhibits a symmetrical trend in angle, which is more conducive to obtaining the angle of user or target. Trajectories T5 and T6 are squinting in a smaller area, which facilitates beam scanning in a known and narrow area, such as a bus stop [250].

To realize fast near-field user localization, BS uses the beamforming scheme based on TTDs assisted near-field controllable beam squint for sensing pilot signal transmission. A low-complexity near-field user localization method is proposed, which includes the first angle sensing stage and the second distance sensing stage.

In first angle sensing stage, it is planned to use one time beam sweeping to obtain the angle estimates for all near-field users. Let the beamforming of subcarrier f_0 point to the starting point $(r_{mid1}, \theta_{start})$ by adjusting PSs, and let the beamforming of subcarrier f_M point to the ending point (r_{mid2}, θ_{end}) by adjusting TTDs, where r_{mid1} and r_{mid2} are two appropriate values between r_{min} and r_{max}, r_{min} and r_{max} are the minimum and maximum distances required for the near-field sensing range, θ_{start} and θ_{end} are the maximum and minimum angles of the near-field sensing range. Then BS uses near-field controllable beam squint strategy to transmit pilot signals, and the beamforming focusing angles of all subcarriers gradually squints from θ_{start} to θ_{end}, covering the entire angle sensing space. The beamforming focusing distance gradually squints from r_{mid1} to r_{mid2}, and the near-field beam squint trajectory of subcarriers is similar to trajectory T4 in **Fig. 6.12**. All near-field users receive all subcarriers and feedback the frequencies of the maximum power subcarriers to BS. The BS can calculate the angle of each user using the frequency of these maximum power subcarriers and the formula for near-field controllable beam squint angle.

After obtaining the angle sensing result, we can enter the second distance sensing stage. Assuming there are some near-field user in the angle direction of $\hat{\theta}_u^{near}$, the users' distances will be sensed in the q-th beam sweeping of distance sensing. Let the beamforming of subcarrier f_0 point to the starting point $(r_{min}, \hat{\theta}_u^{near})$ by adjusting PSs, and let the beamforming at subcarrier f_M point to the ending point $(r_{max}, \hat{\theta}_u^{near})$ by adjusting TTDs. Then BS uses near-field controllable beam squint strategy to transmit pilot signals. The beamforming focusing angle of all subcarriers is always $\hat{\theta}_u^{near}$, and the beamforming focusing distance gradually squints from r_{min} to r_{max}. The near-field beam squint trajectory of the subcarriers is similar to trajectory T1 in **Fig. 6.12**. The near-field users receive subcarriers and feedback the frequencies of the maximum power subcarriers to BS. The BS uses the frequency of the maximum power subcarrier and the formula for near-field controllable beam squint distance to calculate the distance estimates of the user, thereby achieving near-field localization.

The proposed near-field localization method based on controllable beam squint cleverly utilizes the frequency-domain beam sweeping of beam squint instead of the traditional time-domain beam sweeping, greatly reducing the time overhead compared to traditional near-field localization algorithms.

6.2 Integrated Sensing and Communication in Near Field

6.2.1 From Far-field Sensing to Near-field Sensing

The angle, distance and velocity of the sensing target relative to the sensing node are three important metrics in wireless sensing. In traditional far-field sensing, the sensing performance of these three metrics depends on the size of the antenna array, the bandwidth of the sensed signal, and the sensing duration, respectively. However, when the sensing target is located in the near-field, the spherical wave propagation of the signal brings revolutionary changes to the sensing of these three metrics, as follows.

- **Joint angle and distance sensing in the spatial domain**

In far-field sensing systems, angle and distance sensing usually need to be processed in the spatial and frequency domains, respectively. This implies that far-field sensing systems usually require a larger bandwidth or the collaborative support of multiple sensing nodes to achieve precise target localization.

However, in near-field sensing systems, the employment of large aperture antenna arrays is able to capture both angle and distance information, which makes accurate target localization possible only through spatial domain signal processing techniques [251], no longer requiring large bandwidth or the support of multiple sensing nodes, which greatly reduces the cost and complexity of the system. Additionally, the performance limits in near-field sensing scenarios are different from the traditional uniform planar wave model. In [252], a closed-form expression for the received SNR in near-field sensing is derived. Different from the conventional UPW model where the SNR scales linearly and unboundedly with the number of antennas, the SNR increases with diminishing returns in near-field sensing. Furthermore, in [253], considering XL-MIMO radar and XL-phased array radar, closed-form expressions for the Cramér-Rao bounds on angle and distance parameters are derived for monostatic and bistatic sensing systems, respectively.

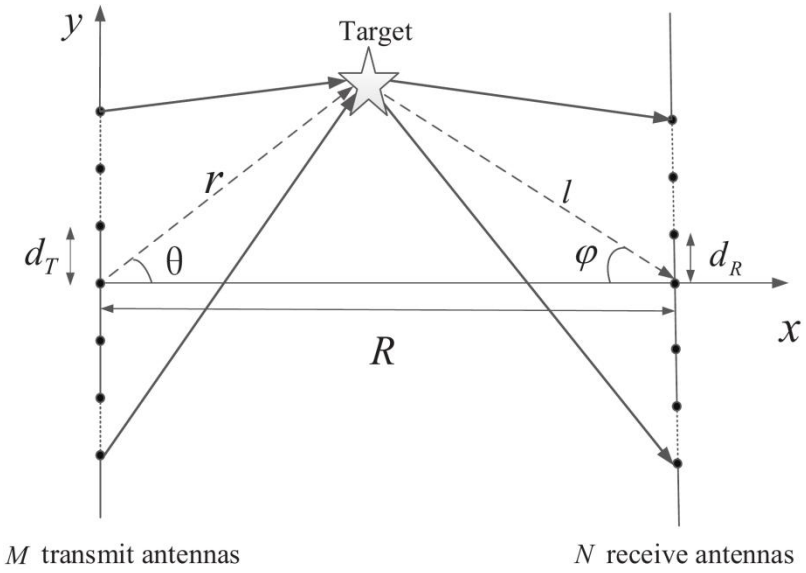

Fig. 6.13 Near-field radar sensing with XL-MIMO.

Specifically, the near-field radar sensing system with XL-MIMO is shown in **Fig. 6.13**. Let M and N denote the number of transmit and receive antenna elements, respectively, with inter-element spacing denoted by d_T and d_R. The distance between the transmit and receive ULAs is R. In the single-target scenario, the angles and distances from the target to the centers of the transmit and receive antenna arrays are denoted as (θ, r, φ, l) .When R is known, the receiver side range and angle parameters can be expressed in terms of the transmitter side parameters to reduce the number of parameters to be estimated, i.e.,

$$\begin{aligned} l(r,\theta) &= \sqrt{R^2 + r^2 - 2Rr\cos\theta}, \\ \varphi(r,\theta) &= \arcsin\left\{\frac{r\sin\theta}{\sqrt{R^2 + r^2 - 2Rr\cos\theta}}\right\}. \end{aligned} \tag{6.1}$$

The Fisher's information matrix (FIM) can be expressed as

$$\mathbf{F} = \frac{2}{N_0}\Re\left\{\left(\frac{\partial \mathbf{w}}{\partial \mathbf{z}}\right)\left(\frac{\partial \mathbf{w}}{\partial \mathbf{z}}\right)^H\right\}, \tag{6.2}$$

Where $\mathbf{w}$ is the output of matched filter, $\mathbf{z}$ is the parameters to be estimated, and N_0 is the power spectral density of noise. Therefore, the CRB of angle and range can be expressed as $\mathbf{F}_{1,1}^{-1}$ and $\mathbf{F}_{2,2}^{-1}$. It can be shown that the CRBs of angle and range in near-field sensing decrease with diminishing return and approach to certain limits as the number of antennas increases [253].

$$\begin{aligned}\lim_{\frac{D_T}{r\cos\theta}\to\infty} CRB_\theta &= \frac{1}{2\gamma L}\frac{\lambda^2 d_T \sin^2\theta}{8\pi^3 r^3\cos\theta},\\ \lim_{\frac{D_T}{r\cos\theta}\to\infty} CRB_r &= \frac{1}{2\gamma L}\frac{\lambda^2 d_T \cos\theta}{8\pi^3 r},\end{aligned} \tag{6.3}$$

Where γ is the receive SNR, d_T is the element-spacing of transmit antenna, λ is the signal wavelength. As a comparison, the CRB for angle with the conventional far-field UPW model can be derived based on [254].

$$C_\theta = \frac{1}{2\gamma L}\frac{3\lambda^2}{2\pi^2 d_T^2 M(M^2-1)\cos^2\theta}, \tag{6.4}$$

Fig. 6.14 shows the CRB of angle for monostatic XL-MIMO and XL-phased array radar, which that with the increasing of antenna number, using inappropriate far-field model to analyze near-field sensing with extremely large-scale arrays may cause severe errors. Besides, the CRBs for angle of phased array radar mode is smaller than that of MIMO radar mode, since the former usually benefits from an additional transmit beamforming gain. **Fig. 6.15** shows bistatic near-field sensing CRBs, and compared with near-field 2-D MUSIC algorithm and Capon algorithm.

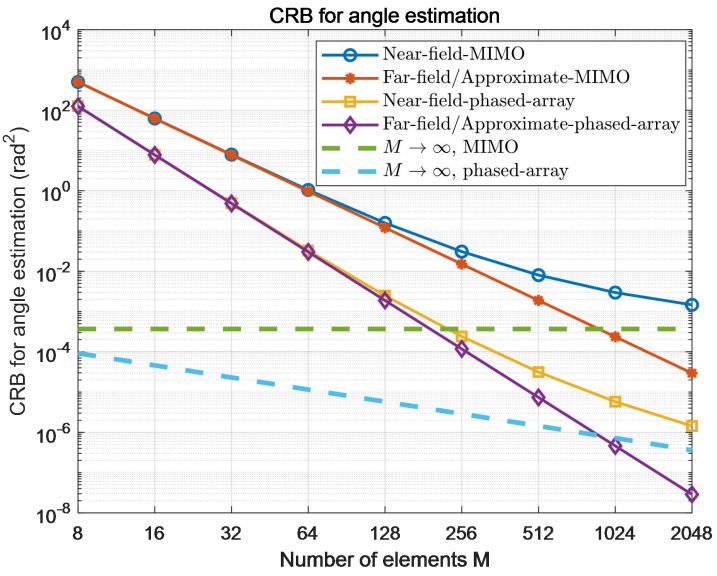

Fig. 6.14 CRB of angle for monostatic sensing.

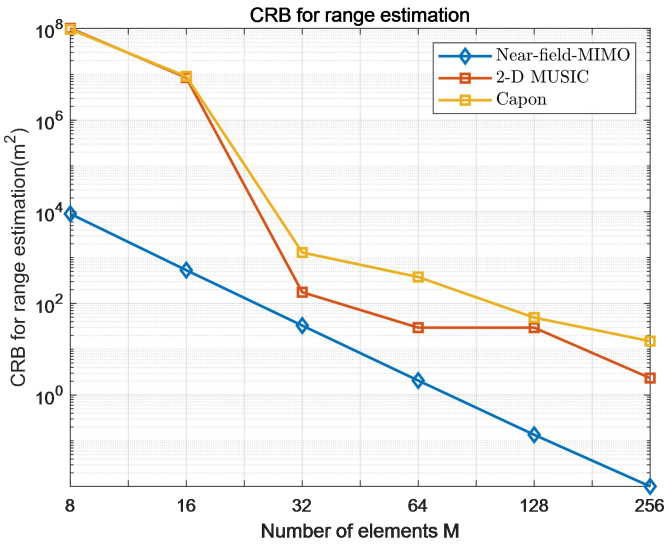

Fig. 6.15 CRB of range for bistatic sensing.

- **Multi-dimensional velocity sensing [229]**

As shown in **Fig. 6.16**, in a far-field sensing system, all antennas in an antenna array "see" the sensing target at almost the same angle. Consequently, the Doppler shift in the sensing signal arises solely due to the target's velocity projected in one direction, denoted as the radial velocity. As a result, far-field sensing systems cannot fully capture the complete motion of the sensing target. However, in near-field sensing, different antennas "see" the sensing target from different angles, which enables the capture of the projected component of the target velocity at different directions, as shown in **Fig. 6.17**. Therefore, near-field sensing is able to simultaneously sense the radial and transverse velocities of the target, obtaining complete motion state information. This complete motion state information makes it possible to accurately predict the target position at the next time interval. In communication systems, this approach can be used to design beamforming for the next communication period in advance, significantly reducing the need for channel estimation and beam training.

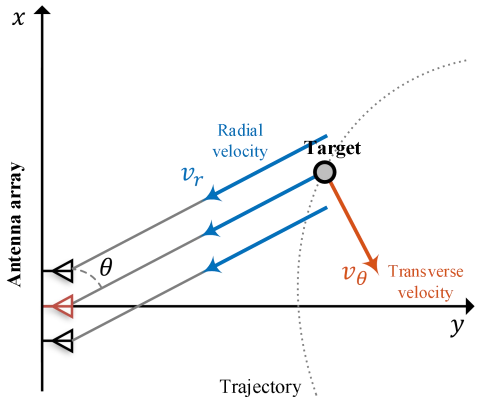

Fig. 6.16 Far-field Velocity Sensing.

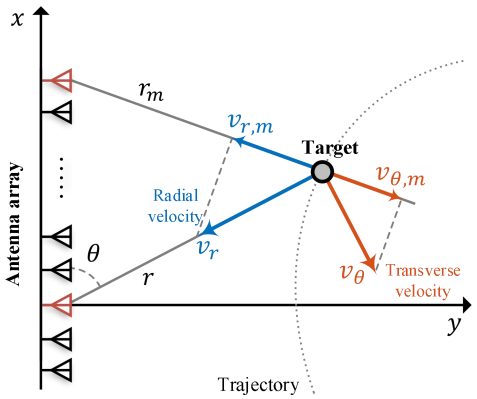

Fig. 6.17 Near-field Velocity Sensing.

6.2.2 Near-Field Integrated Sensing and Communications

Integrated sensing and communication (ISAC) represents a revolution at the intersection of sensing technology and wireless communication[255]. The core of ISAC is to optimize resource allocation and create harmonious synergies between communication and sensing (C&S) by sharing the same spectrum and hardware facilities. With the extremely large-scale array (XL-array) deployed in future wireless systems, wireless communication and sensing are expected to operate in the radiative near-field region, shifting from the traditional far-field channel modeling to near-field channel modeling [229][257]. This region needs to be considered characterized by spherical waves rather than planar waves, a new channel property that will reshape near-field communication and sensing.

In terms of wireless communications, unlike the far-field beamforming steering the beam energy along a specific direction, near-field beamforming based on spherical wavefronts achieves a new function of beam-focusing, which concentrates the beam energy in a given region. This not only enhances the received signal power at the desired user, but also eliminates interference to undesired users. Furthermore, in the far field, users in the same or similar angle cannot be distinguished, and interference between these users is inevitable. In the near field, the base station (BS) can focus the beams at different distances, thus reducing interference between users. This effectively improves the degree of freedom of the channel and further increases the system capacity.

In terms of wireless/radar sensing, the spherical wavefront at the XL-array aperture can be utilized to estimate both the target angle and range, thereby reducing the need for distributed arrays and their synchronization. Besides, the enlarged array aperture provides finer-grained spatial resolution in both the angular and range domains. In addition, the near field beam-focusing effect can be exploited to enhance the sensing SNR of echo signals for achieving more accurate estimation. While for other near-field sensing applications such as human-activity recognition, the spherical wavefront provides additional features in the range domain, hence potentially improving the recognition accuracy.

We will introduce the new opportunities and challenges brought by near-field ISAC from three perspectives: sensing-assisted near-field communication, communication-assisted near-field sensing, and joint near-field communication and sensing (JC&S) [231].

6.2.2.1. Sensing-assisted Near-field Communication

For near-field communication, beam training is an efficient approach in practice to acquire necessary channel state information (CSI) for establishing initial high-SNR links. However, they

generally require much higher training overhead than in the far-field region, due to the required two-dimensional (2D) beam search over both the angular and range domains. For example, one promising approach is to exploit environmental sensing information to reduce the near-field beam search space [231]. Specifically, one can deploy a number of environment sensors in the user zone or along the user trajectory, whose position information is known a priori at the BS and thus can be used as reference location information, as shown in **Fig. 6.18**. As such, at the beginning of near-field beam training, the sensors around the user notify the BS that the user is present within their sensing range. Then, the BS performs low-cost beam training in a small space to obtain the optimal beamforming. Especially in high mobility scenarios, fully utilizing sensing information to assist near-field beam tracking can effectively reduce communication overhead and improve communication reliability. Then, wireless sensing can also assist in the effective allocation of wireless resources, designing resource allocation based on the sensing of vehicle motion status, and geometric relationships, while considering both communication and sensing performance, so as to provide high-quality services with almost no handover overheads [236].

Compared with the far-field case, the near-field sensing-assisted beam tracking is more challenging, since it tends to cause faster phase variations change over the XL-array. Furthermore, robust radar sensing-assisted beam tracking needs to be designed for near-field scenarios, since near-field beams achieved by XL-arrays have very narrow beamwidths and are susceptible to beam misalignment.

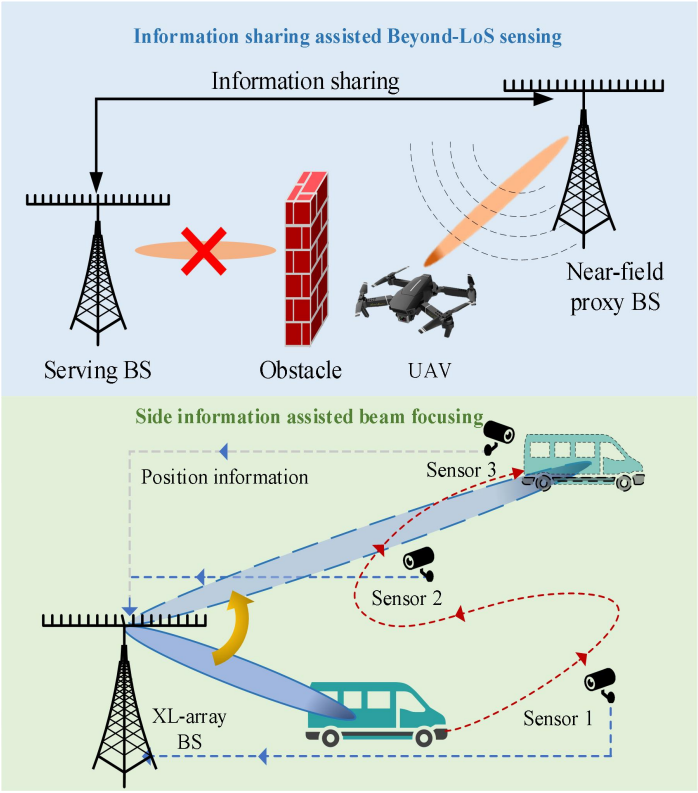

Fig. 6.18 Communication-assisted near-field sensing and sensing-assisted near-field communication.

6.2.2.2. Communication-assisted Near-field Sensing

Besides sensing-assisted near-field communication, communication functionalities in cellular networks can also be used to assist near-field sensing to improve the sensing range, resolution,

accuracy, and reliability. Near-field radar sensing typically relies on the LoS channels between the XL-array and targets, which, however, may not always exist due to random obstacles and environmental scatterers. To tackle this issue, a promising approach is leveraging wireless network architectures to achieve near-field networked sensing through information fusion [237]. First, consider a challenging scenario where the XL-array BS needs to sense a target located beyond its LoS due to obstacles in between, as shown in **Fig. 6.18**. An effective solution is to delegate the sensing task to a proxy XL-array BS, which is capable of establishing an LoS link to the target in its near-field. By exploiting spherical wavefront propagation, the proxy BS can efficiently estimate the target range and angle without the need of additional anchors as in the far-field case. Then, the proxy BS sends its estimated information to the serving BS, which then can estimate the target location based on the relative positions. In addition, in the near-field sensing system, the fusion of single sensing data collected by multiple BSs can achieve better sensing performance than single-node sensing. The 6G communication architecture is expected to provide a reconfigurable framework to support the need for the transfer of large amounts of sensing data from multiple units to converged centers with powerful computing capabilities.

Next, to further improve the radar sensing performance, an effective approach is to use widely deployed BSs to achieve mixed-field networked sensing for which the target may be located in the far-field or near-field of different BSs. In this scenario BSs can share their obtained angle and range information with each other for jointly estimating the locations and velocities of targets. Among others, an important design issue is how to effectively fuse all information to achieve accurate and high-resolution localization by taking into account various factors such as sensing SNR, number of XL-array antennas, spatial correlation of proxy BSs.

6.2.2.3. Joint Near-field Communication and Sensing

For near-field ISAC, one design paradigm is to jointly optimize both C&S performance in a shared system architecture and hardware platform. Therefore, several new near-field effects have to be considered in balancing C&S performance trade-off for both narrow-band and wide-band systems[258]. Consider a narrow-band near-field wireless system, where an ISAC BS equipped with an XL-array simultaneously serves multiple communication users and senses surrounding targets in its near-field region[259]. For JC&S, efficient beamforming designs need to be devised to compensate for severe path-loss in high-frequency bands. Specifically, to enhance near-field communication performance, communication beams should be tuned towards the communication users at fixed locations by exploiting the near-field beam-focusing effect. On the other hand, the beam control for near-field radar sensing generally depends on its estimation aim. For target parameter estimation such as angle and distance, the sensing beams should dynamically scan the region of interest in both the angular and range domains. To balance the C&S performance, one simple yet effective method is to apply the multi-beam design based on array-partition, which divides the entire XL-array into multiple sub-arrays, each responsible for controlling a sub-beam. However, this method reduces the number of antennas allocated per sub-array; thus, communication users/sensing targets may be located in the far-field of the sub-array, thereby reducing the beam-focusing effect. Therefore, it is necessary to properly determine the number of sub-arrays for C&S services, as well as optimize the antenna allocation for these sub-arrays to strike the C&S performance trade-off.

The spherical wave channel model assumption in the near-field can enhance the measurement accuracy of positioning and sensing. In far-field scenarios, classical positioning depends on the estimation of the received signal strength (RSS) based positioning schemes, time of arrival (ToA) and time difference of arrival (TDoA) based positioning estimation methods, and angle of arrival (AoA) based positioning estimation. Positioning estimation methods based on RSS and ToA are not limited by the transmission and reception beams, and thus, these methods cannot leverage the hardware advantages of massive MIMO in the near-field scenarios. The positioning and sensing techniques based on the AoA are more suitable for the near-field communication systems, where the spherical wave channel model is assumed between the transmitter and receiver. According to the near-field spherical wave channel model, the AoAs of the reflected electromagnetic waves of the sensing target or the positioning signals of the target are different for each antenna. The nonlinear phase characteristics introduced by the spherical wave model are used to obtain the positioning and sensing results. Moreover, the positioning and sensing in the near-field scenarios reduce the requirement for signal bandwidth. References [260] and [261] validate the feasibility of sensing and positioning techniques in near-field scenarios. The experimental results further reveal that the weak correlation between different signal bandwidths and near-field positioning accuracy (ref. **Fig. 6.19**). Reference [260] further validate the impact of increasing the antenna scale on the sensing accuracy.

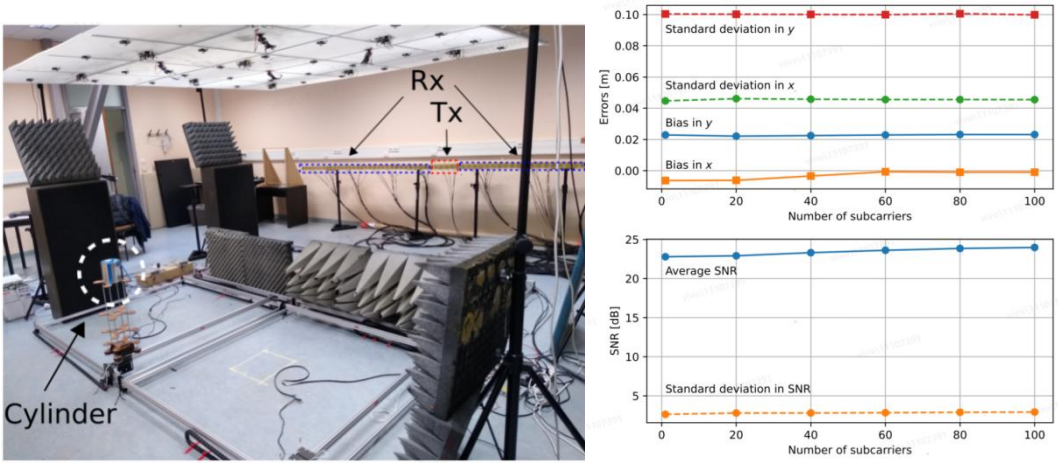

Fig. 6.19 Experimental environment for near-field sensing, and measurement results for sensing accuracy in terms of signal bandwidth [260].

6.3 Wireless Power Transfer in Near Field

Wireless power transfer (WPT) technology, capable of wirelessly charging low-power devices, holds significant promise in the 6G era of the Internet of Things (IoT). Existing WPT technologies primarily focus on far-field scenarios, leading to lower energy transfer efficiency. In 6G near-field scenarios, the use of near-field spherical wave propagation characteristics enables beam focusing techniques to concentrate the energy of radio frequency signals around the energy receiver, thereby significantly enhancing the efficiency of energy transfer [262]. Meanwhile, beam focusing technology can effectively reduce electromagnetic pollution and limit human exposure to radiated energy. This capability opens up broader prospects for the future development of wireless energy transfer technology for 6G IoT applications.

6.3.1 Electromagnetic Radiation-Based WPT

With the rapid development of the 5G/6G information age, more and more wireless smart devices (such as mobile phones, laptops, and smart sensors, etc.) bring convenience to people's lives, and these devices are widely distributed in different scenarios, so their energy supply is full of challenges. WPT technology provides a new solution to the charging problem of these mobile devices, as it can avoid complex wires while ensuring efficient and sustainable operation, so that has obvious advantages in security and flexibility, which is an indispensable technology for the future society. The existing near-field WPT mainly adopts electromagnetic induction, electromagnetic resonance, electromagnetic radiation, and other forms [263], among which electromagnetic radiation form can flexibly modulate electromagnetic waves, and carry out the ability of beamforming for different functions, so that is suitable for long transmission distance, multiple targets and different application scenarios. In the WPT system, the receiver of the electromagnetic radiation system can be designed with a smaller aperture, so that it can be fully integrated with different devices and scenarios. As electromagnetic waves can carry both information and energy, WPT technology can be combined with mobile communications and construct the simultaneous wireless information and power transmission (SWIPT) system to greatly improve the utilization of electromagnetic waves [264].

6.3.1.1. Transmitter Design

The electromagnetic radiation-based WPT can generally reach the transmission distance of a meter level, among which the microwave power transfer (MPT) is not affected by weather conditions so that it can work all the time. The transmitter of the system can be the antenna and its array, such as parabolic antenna and microstrip array [265] to improve system performance through advantages such as high gain and low profile. Electromagnetic meta-surface, as a two-dimensional planar structure of electromagnetic metamaterials, is composed of sub-wavelength units, exhibiting electromagnetic characteristics that natural materials do not possess, to achieve flexible modulation of electromagnetic wave's amplitude, phase, polarization, and other dimensions [266], which can be achieved by reflective, transmissive, holographic and other types. By loading the diode or other active adjustable devices on the meta-surface unit, the function of the meta-surface unit can be reconstructed by adjusting the state of the active adjustable device, and the digitally encoded reconfigurable meta-surface can be formed to realize the real-time modulation according to the requirements of specific scenes. To meet the demand for high power levels in the WPT scenario, amplifiers can also be loaded on the meta-surface unit to realize different power level applications. **Fig. 6.20** shows the schematic diagram of the adaptive intelligent near-field charging system using a programmable meta-surface [267].

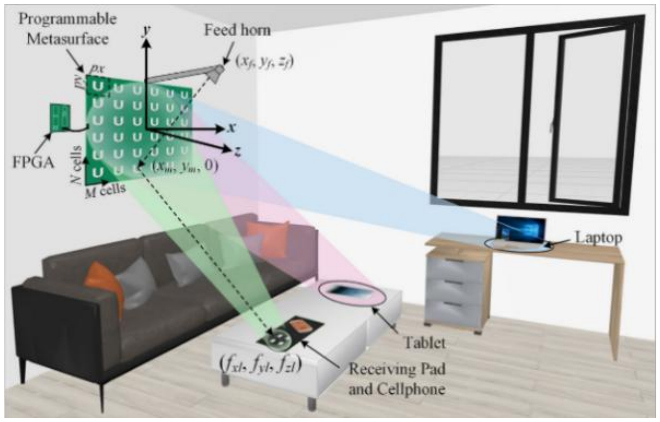

Fig. 6.20 Adaptive intelligent near-field charging system based on programmable metasurface [267].

6.3.1.2. Design of the Energy Transmission Beams

The beamforming technology can be used to distribute the electromagnetic energy at a specific region where the targets are located in the near-field range. Compared with the beams suitable for far-field range such as directional high-gain beams, the focused beam can concentrate the energy into the focal spot, which will significantly improve the receiving efficiency and reduce the aperture of the receiver. If it is necessary to charge multiple targets at the same time, multiple focused beams can be carried out and algorithm optimization can be used to improve beam performance [268]. In addition, the non-diffraction beams can be used to obtain a larger WPT range and a richer beam trajectory than the focused beam based on suppressing divergence. As shown in **Fig. 6.21**, since the Bessel beam has both non-diffraction and self-reconstruction characteristics, multiple targets can be charged at the same time in the beam's propagation path, thus expanding the multi-target WPT from the 2D range to the 3D range [269]. In addition, Airy beam, Pearcy beam, and other special beams with self-bending characteristics can also be included by non-diffraction beams, they have further self-bending characteristics, reflecting the ability to avoid obstacles to achieve WPT with higher performance [270].

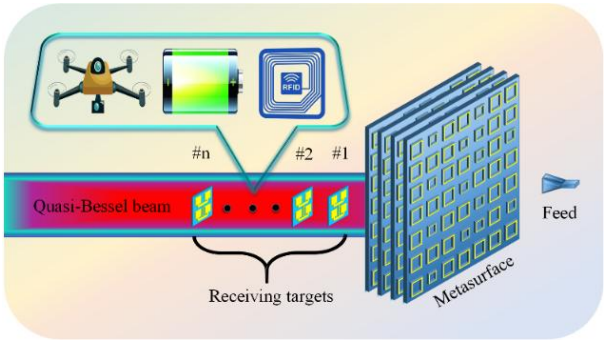

Fig. 6.21 Schematic diagram of multi-target WPT system based on quasi-Bessel beams [269].

6.3.1.3. Receiver Design

The receiver of the WPT system needs to use the antenna and its array or the meta-surface to receive the transmitted electromagnetic energy [271], which is similar to the transmitter. In addition to the installation of a specific power transmitter at the transmitting end, wireless energy harvesting (WEH) can also be performed on energy in the natural environment. With the continuous implementation of concepts such as the IoE [272], the construction of smart cities has increased the electromagnetic energy in the environment, and WEH technology has attracted wide attention because it can avoid the battery replacement of electrical devices such as sensors. After receiving the electromagnetic energy, it also needs to be converted into direct current (DC) energy by a rectifier circuit, and then the energy is stored or supplied to electrical devices. The block diagram of the whole system is shown in **Fig. 6.22**. Considering that there are also a large number of natural energy sources such as solar, wind, and heat in the natural environment, mixing electromagnetic energy with other forms for energy harvesting will also provide more possibilities for WEH.

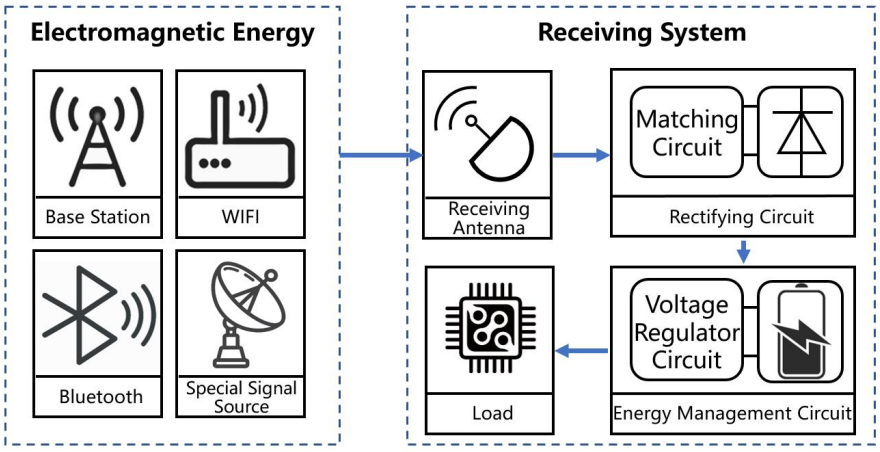

Fig. 6.22 Block diagram of wireless energy harvesting system.

To obtain more abundant electromagnetic energy, the receiving antenna should work in multi-band or wide-band and can receive or transform electromagnetic waves with different polarization. When the subwavelength unit of the electromagnetic meta-surface is used, the stability of the incoming wave's incidence angle and polarization insensitivity characteristic can be further expanded, to comprehensively harvest electromagnetic energy of different frequencies, polarizations, and directions [273]. The corresponding rectifier circuit also needs to be designed in multi-band and should have high efficiency over a large input power range [274][275]. Combining the receiving meta-surface with the rectifying circuit can further form the rectifying meta-surface. As shown in **Fig. 6.23**, the rectifying meta-surface achieves miniaturization, dual frequency bands, wide incidence angle, polarization insensitivity, and high rectifying efficiency, showing high performance based on removing complex circuit design [276].

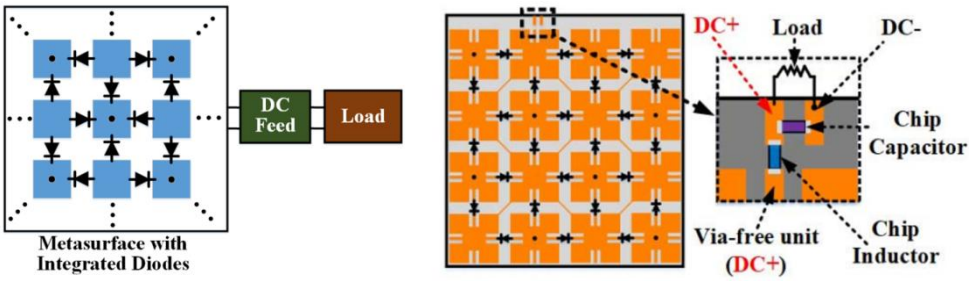

Fig. 6.23 Schematic diagram of the rectifying metasurface.

6.3.1.4. Function Expansion - SWIPT

In addition to carrying energy, electromagnetic waves can also load information, and the combination of the above two functions can form a simultaneous wireless information and power transfer (SWIPT) system, which is of great significance for the future scenario of the IoE. In the applications of SWIPT, energy, and information transmission are required to achieve their functions and do not interfere with each other, which has high requirements for the transmitter design, receiver design, and system framework. For this reason, there are systems such as SWIPT systems, wireless-powered communication networks (WPCN), wireless-powered backscatter communication (WPBC) systems [275], and other forms, which divide electromagnetic energy through different dimensions such as time, space, frequency, polarization, etc., to achieve energy transmission and communication functions respectively. **Fig. 6.24** shows the SWIPT system based on frequency

diversity [277] and polarization diversity [278] respectively. Through the modulation of the energy ratio of different functions, the application of different beams, and the design of holographic meta-surface and amplifying programmable meta-surface, the energy allocation of energy transfer and information transfer can be balanced to optimize the overall performance of the system.

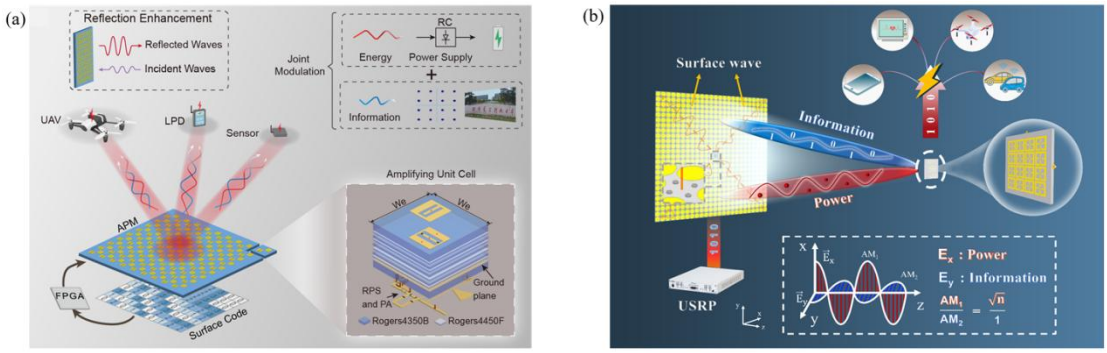

Fig. 6.24 SWIPT systems based on (a) frequency diversity and (b) polarization diversity

6.3.2 Wireless Power Transfer through Power Amplifier

In advanced transmitter systems, the PA has become an increasingly important part of sending data to faraway places by amplifying the RF signal. The PA is a crucial component in the WPT system for 6G communication because it provides outstanding power transfer. The drain efficiency (DE), power added efficiency (PAE), and output power (Pout) of the PA could have a tremendous impact on the efficacy of WPT systems.

In the WPT system, it is challenging to transmit the power efficiently from one end to the other end. While transmitting the power wirelessly from one antenna (at the transmitting end) to the other antenna (at the receiving end), there is a leakage of power. This leakage power generally depends on the input power fed to the transmitting antenna through PA and the received power received at the receiving antenna, as given in (6.6).

$$Leakagepower = P_{input} - P_{Received} \tag{6.6}$$

The leakage power can also be formulated as given in (6.7)

$$Leakagepower = (1 - \Gamma^2) * P_{input} \tag{6.7}$$

where the reflection coefficient (Γ) is expressed as

$$\Gamma = \left(\frac{Z_{in} - Z_o}{Z_{in} + Z_o}\right) \tag{6.8}$$

by putting the values from (6.7) and (6.8) in (6.6), we get

$$\left(1 - \left(\frac{Z_{in} - Z_o}{Z_{in} + Z_o}\right)^2\right) * P_{input} = P_{input} - P_{Received} \tag{6.9}$$

So, it is essential to find the amount of power transmitted from the transmitting side to the receiving side after the impact of leakage power. To formulate the expression for power transmitted to the receiver, we need to define the equation of other factors on which the WPT depends [280]. These factors are propagation loss (PLoss), absorption loss (ALoss), reflection loss (RLoss), transmission loss

(TrLoss), mismatch loss (MisLoss), transmitter loss (TLoss), medium loss (MLoss), and receiver loss (ReLoss). In the above equations, the values of the transmission coefficient (Tcoefficient), medium attenuation (Mattenuation), and receiver attenuation (Rattenuation) can be preassigned by the user. Then the power received by the receiving antenna can be obtained [281].

- Need of PA for WPT

WPT can be classified as either near-field (operating range Hz to MHz) or far-field (operating range MHz to THz) transmission. In general, near-field power transmission methods are more efficient than their far-field counterparts.

In [281], A switched-capacitor-based stimulator integrated circuit that enables efficient harvesting of RF power for applications involving neuro-stimulation is given. A radiating near-field (RNF) RF harvester containing a rectenna and source/transmitter with a 47.7\% efficiency at 2.4 GHz was developed and produced [282]. A class E amplifier is developed for systems that utilize capacitive coupled wireless power transfer (CCWPT) in the MHz band [283]. Also, Casanova suggested the design and optimization of a Class E PA that utilizes inductive coupling for wireless power technology [284]]. In [285], gallium nitride (GaN) -based class F PA designed at 3 GHz for wireless applications is discussed. A hybrid class E/F3 PA is analyzed and discussed in [286]. On reviewing some of the articles, it is suggested that there is a need for an efficient, high-power PA to perform WPT from the transmitter to the receiver associated with a bio-implant device.

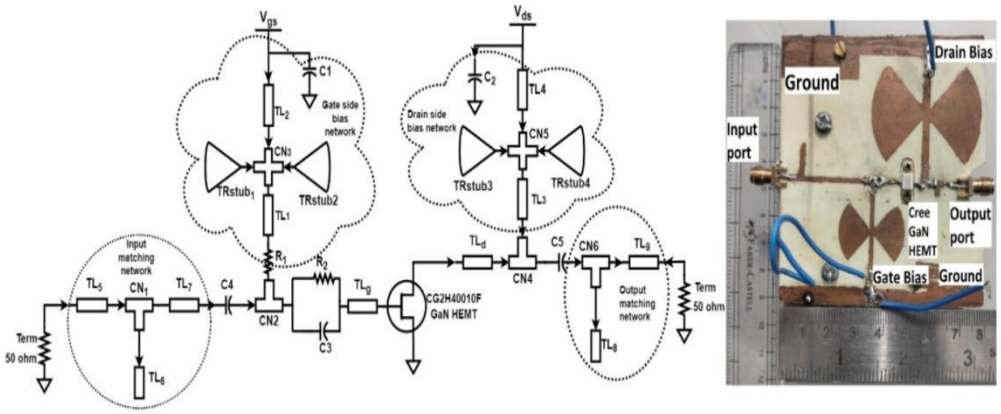

Fig. 6.25 Representation of schematic with the fabricated view of the developed PA.

A Class F^{-1} PA is designed by keeping load impedance with the even harmonics as open-circuited and odd harmonics as short-circuited [287]. Following the optimization of the transmission lines (TL) dimensions, a 10-W Cree CG2H40010F [288] GaN-based class F^{-1} PA is designed at 4.6 GHz with the operating point (Vgs = -2.7 V and Vds = 28 V). The schematic of GaN-based class F^{-1} PA with the utilization of optimized values of design parameters of microstrip TLs is shown in **Fig. 6.25**. The harmonic balance simulation is performed to check the small and large signal parameters of the proposed PA. The transient response of current-voltage (I-V) waveforms of the developed class F^{-1} PA is represented in **Fig. 6.26**, having voltage as half sinusoidal and current as a square waveform in nature.

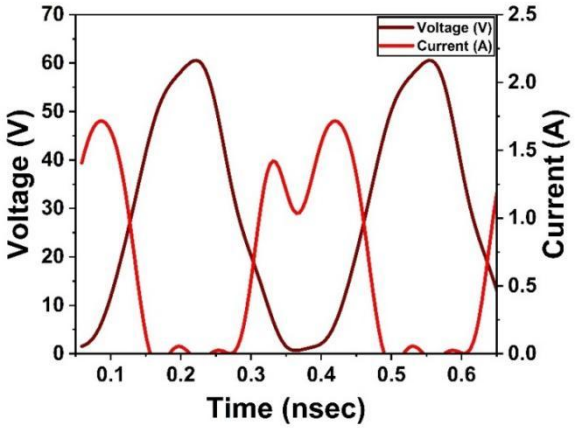

Fig. 6.26 Simulated IV curve of 10-W PA at 28 dBm input power.

The actual area of the whole PA is 88 mm × 80 mm. We have utilized a driver amplifier [287] of 17 dB gain, a signal generator (N5172B), a spectrum analyzer (N9020A), an attenuator (BW-S40W20+) from mini-circuits, a 3 dB coupler, a power sensor, and a direct current (DC) power source. The measured results of the suggested PA show that both DE and Pout have an effective value (in **Fig. 6.27** (a) and **Fig. 6.27** (b). All other parameters are compatible with the requirements of such a type of PA for WPT. Also, this proposed PA follows the safety and regulatory guidelines required for performing WPT for 6G communications.

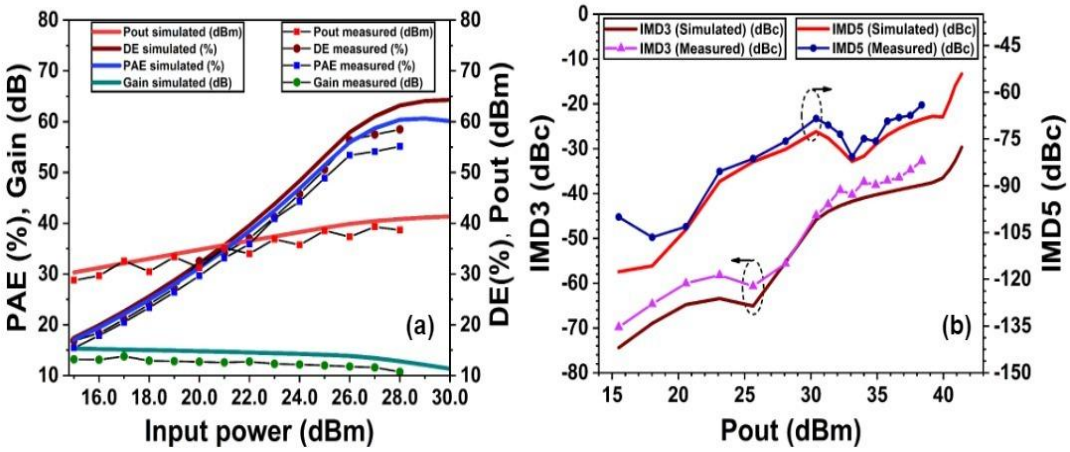

Fig. 6.27 Obtained results of (a) PAE, Pout, DE, and Gain (b) IMD3 and IMD5 w.r.t Pout of PA

6.3.3 Far/Near-Field SWIPT

Apart from serving as information carriers, wireless signals can also facilitate energy WPT employs microwave signals for energy transmission which enables the capability to charge low-power devices. WPT has found extensive application as a cable-free alternative for charging devices in diverse environments, including mobile edge computing, rapid data aggregation, mobile crowd sensing, and ISAC. As shown in **Fig. 6.28**, near-field simultaneous wireless information and power transfer (SWIPT) emerges as a promising technology capable of wirelessly transmitting both data and power simultaneously. In this scenario, the reception of both information and power can be carried out through either time switching or power allocation [291]. The integration of information and energy transmission eliminates the requirement for separate power or wired connections, enhancing the

flexibility, mobility, and convenience of devices. Thus, SWIPT has the potential to bring about a revolutionary impact on various industries and applications.

Although most of the existing work considers either near-field or far-field communication, it is probable that a hybrid communication model will arise, incorporating both near-field and far-field users within the system [292]. This indicates that in typical communication scenarios, users may be located in near-field and far-field regions at a distance from the BS, leading to more complex interference problems. Specifically, in [292], due to the energy diffusion effect, the authors reveal a noteworthy phenomenon that when the spatial angle of the far-field beam based on the Discrete Fourier Transform (DFT) is in the vicinity of the far-field user's angle, the near-field user may suffer from strong interference from the far-field beam. On the other hand, this power leakage phenomenon can also be used to benefit the near-field users, leading to new application scenarios for SWIPT with mixed fields.

In [291], a new practical scenario i.e., hybrid near-field and far-field SWIPT is considered, where the energy harvesting (EH) and information decoding (ID) receivers are located in the near-field and far-field regions of the BS that is equipped with an ultra-large-scale array, respectively. Specifically, a weighted sum power harvesting maximization problem subject to ID sum rate and BS transmit power was formulated by jointly designing the BS beamforming scheduling and power allocation. To efficiently solve this non-convex optimization problem, binary variable elimination and successive convex approximation methods were proposed to obtain a suboptimal solution.

In terahertz-based SWIPT system or RIS-assisted SWIPT system supported by multi-base station/multi-RIS fitted with ultra-large scale antenna arrays, the introduction of distinct channel models and beam splitting gives rise to the presence of mixed near/far fields. In this case, it is necessary to collaborative scheduling of beamforming along all BSs during the power allocation design [293]. Most studies on terahertz-based or RIS-aided SWIPT systems have primarily concentrated on optimizing the beam design of either the base station or RIS to fulfill the system's performance requirements. With the application of ultra-large scale array antennas, the terahertz channel model and beam splitting characteristics will change, resulting in traditional beam design/transmission schemes no longer being practical. Therefore, under the hybrid near/far field model, it is necessary to design a low-power and high-performance SWIPT system, in terms of transceiver structure/RIS structure, power allocation method and energy/information transfer protocol design.

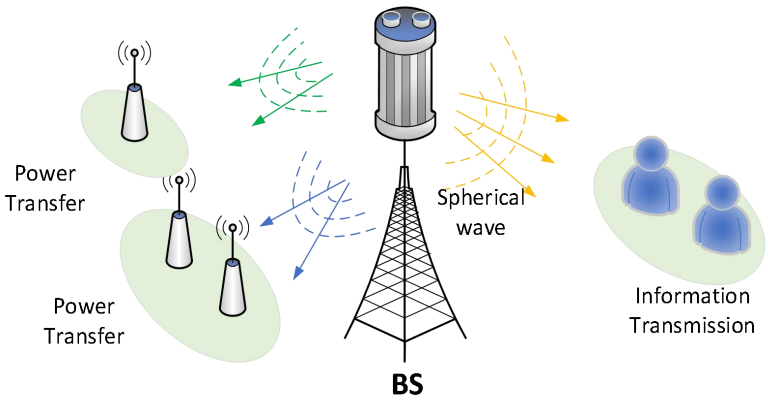

Fig. 6.28 Near-Field SWIPT.

6.3.4 Holographic SWIPT

With the development of metamaterials, holographic meta-surfaces with subwavelength spacing antenna elements can achieve nearly continuous antenna apertures and thus have powerful electromagnetic manipulation capabilities [294]. Imagine a SWIPT system that makes full use of the propagation characteristics of electromagnetic channels to achieve maximum energy aggregation for energy users and maximum interference cancellation for information users, so as to infinitely approach the performance limit of SWIPT. This is the concept of holographic SWIPT [295].

For near-field communication scenarios, the information user is still in a position relatively far from the transmitter, and its distance to the base station is usually considered to be much larger than the aperture of the antenna array. Based on the Fresnel approximation, the near-field channel model is usually simplified by using the Taylor series expansion of the first or second order $\sqrt{1+x}=1+x/2-x^2/8+0\ (x^2)$ [296]. However, for SWIPT, the energy user has a high probability of being located in the area very close to the transmitter, and the error of the near-field channel based on the Taylor series expansion will degrade the performance of SWIPT. Therefore, it is necessary to adopt a more accurate electromagnetic channel model [297]:

$$\mathbf{G}(\mathbf{r},\mathbf{s})=\frac{\mathrm{i}\kappa Z_0}{4\pi}\frac{e^{\mathrm{i}\kappa\|\mathbf{p}\|}}{\|\mathbf{p}\|}\left[\left(\mathbf{I}_3-\hat{\mathbf{p}}\hat{\mathbf{p}}^H\right)+\frac{\mathrm{i}}{\kappa\|\mathbf{p}\|}\left(\mathbf{I}_3-3\hat{\mathbf{p}}\hat{\mathbf{p}}^H\right)+\frac{1}{(\kappa\|\mathbf{p}\|)^2}\left(\mathbf{I}_3-3\hat{\mathbf{p}}\hat{\mathbf{p}}^H\right)\right]. \tag{6.10}$$

Where $\mathbf{r}$、$\mathbf{s}$ are the position coordinates of the points in the transmitting region and receiving region, respectively. $\mathbf{p}=\mathbf{r}-\mathbf{s}$. The latter two terms correspond to evanescent waves that propagate only over the metamaterial surface and become negligible at distances of a few wavelengths. The former term corresponds to the radiation field, and the well-known Fresnel zone is further divided in the first term based on the Fresnel approximation.

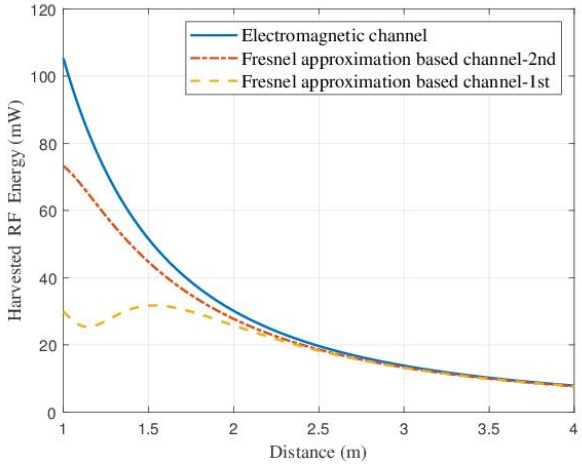

Fig. 6.29 Holographic WPT [295]

A holographic meta-surface with a length of 1.5m and a width of 0.5m is considered in reference [295], and the single-energy user is located on the central axis of the continuous meta-surface. It can be seen from **Fig. 6.30** that the energy user can harvest more energy under the electromagnetic channel model. As the distance from the transmitter increases, the error of the near-field channel model under

the Fresnel approximation decreases gradually, so as to obtain the same WPT performance as the electromagnetic channel.

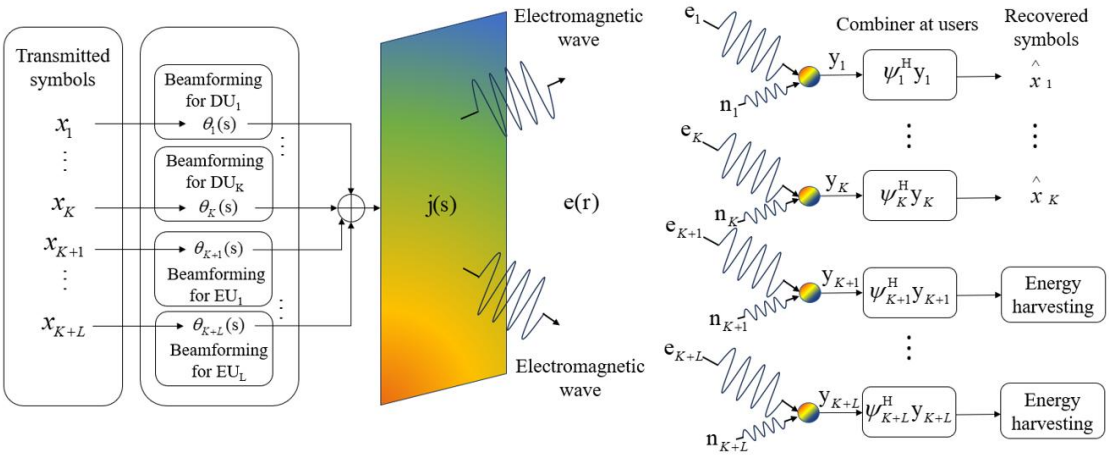

Fig. 6.30 Holographic SWIPT [295]

For the multiuser SWIPT scenario, a careful design of the current on the transceiver holographic hypersurface is required to implement holographic SWIPT, including the amplitude, phase, and polarization direction of the current. In order to meet the trade-off between communication and WPT, the electromagnetic waves carrying information of different users are focused at the energy user and orthogonal at the information user as much as possible. A holographic SWIPT system is considered in [295], where the transmitter and multiple information users and energy users are equipped with holographic meta-surfaces. Specifically, an optimization problem is designed to maximize the sum-rate of the information users while satisfying the energy harvesting requirements of the energy users. To solve this non-convex optimization problem, holographic beamforming schemes are proposed based on block coordinate descent and successive convex approximation.

6.4 Physical Layer Security in Near-Field

6.4.1 Design of Near-Field Physical Layer Security

The broadcast nature of wireless channels exposes wireless signals to free space and makes them susceptible to eavesdropping by malicious eavesdroppers. To solve this problem, researchers have proposed the concept of physical layer security (PLS). PLS is able to utilize the physical characteristics of the wireless channel (e.g., interference, fading, noise, directionality, and discreteness) to enhance the security of the communication, thus avoiding the complexity of the generation and management of the secret key and compensating for the shortcomings of cryptography.

In order to meet the demand for dramatically increasing data rates in 6G networks and beyond, emerging technologies such as mmWave, THz, and ultra-massive multiple-input-multiple-output (UM-MIMO) are being researched incessantly. The realization of most of these techniques relies on extremely large-scale antenna arrays and tremendously high frequencies. However, deploying extensive antenna arrays and utilizing very small wavelengths substantially extends the Rayleigh distance. This extension leads to a noteworthy expansion of the near-field range, highlighting the imminent need for research in the near-field region of wireless communications.

The Rayleigh distance functions as a vital metric for distinguishing between far-field and near-field transmissions, generally, transmissions ranges beyond the Rayleigh distance are assumed to be conventional far-field plane waves. When the wireless transmission occurs within the Rayleigh distance, the conventional assumption of far-field plane waves becomes obsolete, instead, near-field effects come into play, prompting a shift in the transmission model towards a more accurate representation using spherical waves. Conventional far-field wireless communication scenarios typically use plane-wave channel propagation models [298], which limit the security gains offered by spatial beamforming for near-field communication. As shown in **Fig. 6.31**, in near-field communication scenarios, when the eavesdropper is located between the base station and the legitimate user, its channel is highly correlated with the legitimate channel in terms of angle and is difficult to distinguish. Therefore, in near-field secure communication, the crucial factor is the substantial difference in distance between the legitimate user and any potential eavesdropper. The electromagnetic (EM) propagation in near-field communication is explained by the spherical wave channel model [299]. In contrast to the plane wave model, this model incorporates both direction and distance information of the receiver. This feature enables the antenna array to concentrate its beam on a specific point in free space, a phenomenon known as beam focusing. Therefore, near-field communication can leverage the additional dimension of distance to achieve more precise signal enhancement and effective interference management in wireless networks.

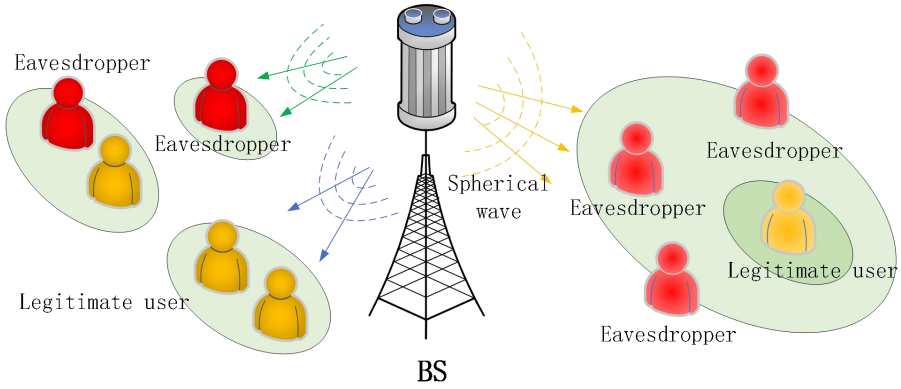

Fig. 6.31 Near-Field PLS.

Currently, studies have initiated to utilize the distance dimension in the spherical wave channel model to enhance communication security[300], however there is still a lack of research on secure beam focusing schemes for MIMO networks. In addition, the large-scale antenna arrays and full-digital beamforming structures commonly used in near-field MIMO communications result in a substantial hardware cost, so exploring cost-effective beam-focusing schemes for secrecy MIMO networks has become a current research priority. In this background, a novel near-field secure transmission framework can be used to securely transmit information to a user via a base station in response to the presence of a potential eavesdropper. When the eavesdropper is located between the user and the base station, a secure beam focusing technique based on a hybrid beamforming architecture can be used to effectively reduce the RF link overhead. It has been shown that the security rate can be further improved even the eavesdropping user is closer to the base station compared to legitimate user in near-field communication[301]. Therefore, in near-field PLS communication, its secure

communication performance mainly depends on the distance between the eavesdropping user and the legitimate user, rather than the distance between the eavesdropping user and the base station.

6.4.2 RIS Empowered Near-field Physical Layer Security Transmission Design

Due to the characteristics of the double-fading effect in reflective cascaded channels and high path loss in the high-frequency band, the performance improvement of traditional RIS-assisted wireless communication is limited. Considering that the RIS array gain is proportional to the square of the number of reflection elements, increasing the number of RIS elements can effectively compensate for the severe double-fading effect in cascaded channels. Therefore, traditional RIS is evolving towards extremely XL-RIS. XL-RIS-assisted communication systems are more likely to establish near-field communication, where the distance between the transmitter and XL-RIS, or XL-RIS and the receiver, is less than the Rayleigh distance, allowing XL-RIS-assisted wireless communication systems to operate in the near-field region [32].

In far-field covert communication systems, positive covert communication rates cannot be achieved when the warden and the legitimate receiver are at the same direction and the warden is closer to the XL-RIS. Near-field communication systems have degrees of freedom in both angle and distance, whereas distance freedom allows covert communication systems to achieve positive covert rates in the above scenario. The authors in [302] studied an XL-RIS-assisted near-field covert communication system. In this study, the achievable covert rate is maximized by optimizing the base station's hybrid precoding and the reflection coefficient matrix of the XL-RIS. A beam diffraction pattern is also revealed in this study, i.e., a transitional state between beam steering and beam focusing. **Fig. 6.29** shows the normalized heatmap of beam diffraction, with XL-RIS located at coordinates (0,0). It can be observed that the beam first splits and creates a null region at the warden and then converges at the legitimate receiver, Bob. The beam diffraction phenomenon can be extended to XL-RIS-assisted multi-user systems, NOMA systems, and enhance near-field physical layer security.

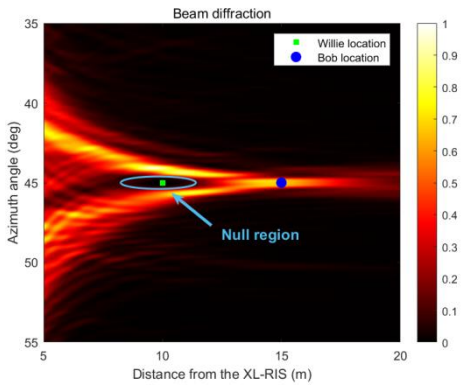

Fig. 6.32 Beam diffraction in near-field.

6.5 Near-Field Based OAM

Wireless communication technology carries information through the frequency, amplitude, phase, polarization, and other dimensions of electromagnetic waves, but the linear momentum and its combined application are limited by the existing dimensions, and it is difficult to achieve significant efficiency improvement. As a new technology for next-generation mobile communication, orbital angular momentum (OAM) has the property different from that of electromagnetic wave radiative

linear momentum and is expected to be used to expand the communication dimension, which can be used to transmit data or as a new degree of freedom to control beam, to increase communication capacity and improve system performance.

6.5.1 OAM and Vortex Waves

OAM is an inherent physical quantity of electromagnetic wave belonging to angular momentum, and electromagnetic wave carrying OAM can be called electromagnetic vortex wave (also known as vortex wave or vortex beam) [303]. Compared with conventional plane waves, vortex waves have helically distributed phase wavefronts and can be distinguished by the periodicity of the helical phase, which is also embodied as their intrinsic modes. In theory, the OAM carried by vortex waves has an infinite variety of mutually orthogonal modes, which can be used as a new physical dimension independent of time, frequency, polarization, and other degrees of freedom. As spectrum resources are increasingly scarce and the communication rate is close to the limit of Shannon's theorem, OAM shows important research and application value in wireless communication, imaging, detection, and other fields.

OAM differentiates the space resources in the same direction, provides a new dimension, and realizes the high degree of freedom spatial multiplexing transmission under LOS channel without multipath, so that can solve the problem of limited multiplexing layer number of single users in high-frequency LOS channel. OAM greatly improves channel capacity and spectral efficiency by expanding new dimensions, its mode orthogonality can be used for interference elimination (such as inter-cell interference, upstream and downstream interference, full-duplex self-interference, etc.), and can be used to enhance communication security and avoid eavesdropping.

The technology based on OAM has a wider application prospect in the future of wireless communication. The characteristics of OAM apply to microwave wireless backhaul links, achieving more efficient and high-speed wireless self-backhaul, effectively reducing the construction cost and laying difficulty of optical fiber, and improving the flexibility of network deployment. OAM has high spectral efficiency, realizes high-speed data interaction, and can support 6G new scenarios such as digital twin domain and intelligent interaction. In addition, OAM can be used for point-to-point high-speed communication and short-distance single-user ultra-high-rate data transmission. OAM technology in near-field transmission can make full use of the high degree of freedom of the LOS channel and reduce OAM mode crosstalk caused by multipath. The application of OAM is more suitable for high-frequency communication, as the probability of near-field transmission is significantly increased at this time, the combination with high-frequency architecture is a development trend of OAM technology in the future.

The generation, modulation, reception, and detection of vortex waves are the basis of its practical application. To realize the phase factor of $e^{jl\Phi}$ corresponding to the spiral phase of vortex waves (where j is the imaginary unit, l is the OAM mode of the vortex wave, and Φ is the spatial azimuth angle), the uniform circular array (UCA) or a reasonably optimized UCA model should be formed using generation devices. The existing methods can be used in the form of spiral phase plates, antenna arrays, single antenna, electromagnetic meta-surface, etc. At the receiving end, the beam can be received by the receiving device corresponding to the transmitting end. If the OAM mode needs to be detected, the Fourier transform relationship between the spatial azimuth domain and the OAM mode domain can be

used to analyze the OAM mode spectrum of the vortex wave based on the Fourier transform principle and sampling theorem.

6.5.2 Near-Field Modulation of Vortex Beams

The propagation environment is usually uncontrollable, and the reflection, scattering, and refraction caused by obstacles will affect the LOS channel and destroy the orthogonality of modes. The multipath effect is significantly reduced in near-field transmission, which better guarantees the orthogonality between OAM modes, reduces beam diffusion, realizes the expansion from SU to MU, and supports the simultaneous transmission of multiple users.

The traditional vortex beam has obvious divergence characteristics, so the application of long distance is often limited, and it is easier to make use of its advantages in the modulation of vortex beams in the near field region. The modulation for vortex beams in the near-field has also become a key technology in the research and application of OAM. In particular, the non-diffraction beam can be combined with the vortex beam by using the diffractive suppression characteristic embodied in transmission, to realize the non-diffraction vortex beam within a certain propagation distance. Because the modulation of the non-diffraction beam and vortex beam is very complicated, it is often necessary to use the array with many elements such as antenna array or meta-surface.

Typical non-diffraction beams include the Bessel Beam, Airy Beam, Mathieu Beam, etc., of which the high-order Bessel beam itself has vortex characteristics, and other non-diffraction beams can often form non-diffraction vortex beams by combining the non-diffraction beam with the spiral phase. **Fig. 6.33** shows the design of a transmissive electromagnetic meta-surface to generate a quasi-Bessel vortex beam through simultaneous modulation of amplitude and phase [304]. It can be seen that combining the non-diffraction beam with the traditional OAM beam can effectively suppress the divergence in the near field region, to achieve better application.

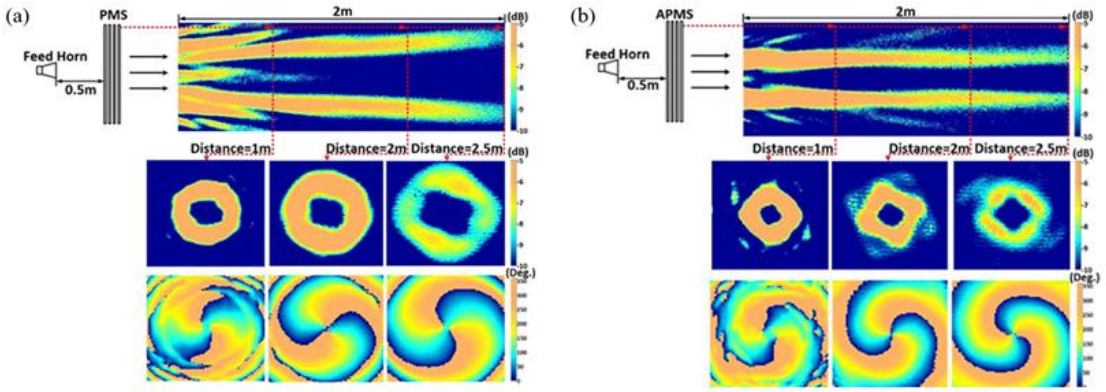

Fig. 6.33 Comparison of the electric field between (a) conventional OAM beam and (b) non-diffraction Bessel vortex beam [291].

6.5.3 The Reception of Vortex Beam and the Detection of OAM

Effective reception and OAM detection of vortex beams are important topics in theory and application research. Typical reception methods of vortex beam are aperture sampling, which can be divided into full aperture sampling and partial aperture sampling according to the type of sampling aperture, as shown in **Fig. 6.34**. The full aperture sampling and receiving method can effectively ensure the orthogonality between different OAM modes, while the OAM modes that can be received by partial

aperture need to differ by a certain multiple. In addition, the receiving and demodulation of OAM can be realized under the condition of minimal sampling receiving aperture based on the analysis of the sampling matrix [306]. This method abstracts the receiving of OAM mode as a matrix equation-solving problem, so that the relevant matrix equation-solving methods (such as singular value decomposition, least square method), or some signal processing methods can be used, which greatly expands the research idea and realization means of OAM reception and detection.

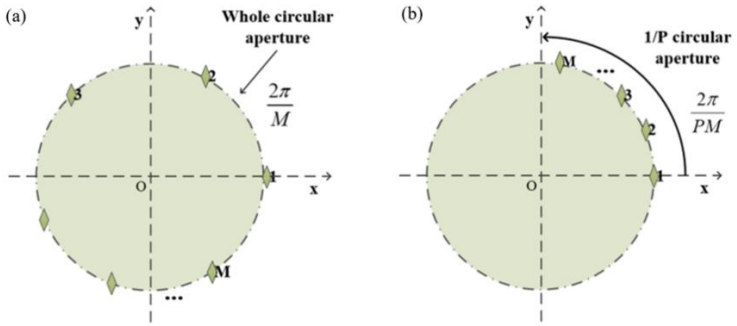

Fig. 6.34 Schematic diagram of (a) full aperture sampling and receiving method and (b) partial aperture sampling and receiving method [305].

6.6 Near-Field Based Intelligent Communication

6.6.1 Near-Field Based Semantic Communication System

In order to further improve the transmission efficiency of wireless communication and make full use of the computation power of the device, the original data is first subjected to feature extraction to obtain relevant semantic information, and then the lightweight semantic information is transmitted through the near field communication architecture to achieve high efficiency transmission. The difference from traditional communication is that the semantic communication architecture based on near-field communication needs to take the near-field channel into account in the joint training of semantic proposing at the joint transmitter and semantic recovery at the receiver, as shown in **Fig. 6.35**.

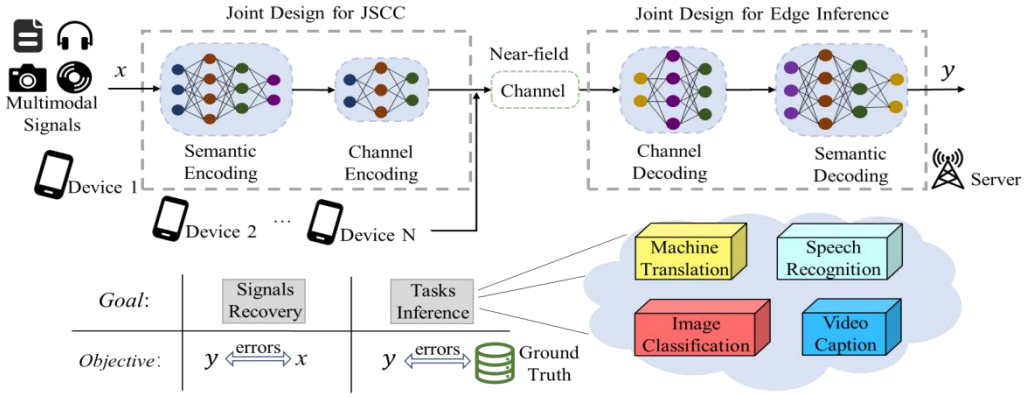

Fig. 6.35 An illustration of the near-field based semantic communication system.

6.6.2 Near-Field Based Federated Learning Framework

Consider a federated learning system over the wireless communication network. In order to protect the privacy of user data, each user will transmit the calculated local federated learning model through the wireless channel and retain local privacy data. The base station will collect the local

federated learning model to further perform model aggregation. Considering that the channel between the user and the base station is a near-field channel, it is necessary to re-derive the convergence model of the federated learning system based on near-field channels to establish the energy and delay model of the federated learning system based on near-field communication. Jointly optimizing communication and learning parameters in the near-field communication obtains the optimal resource allocation.

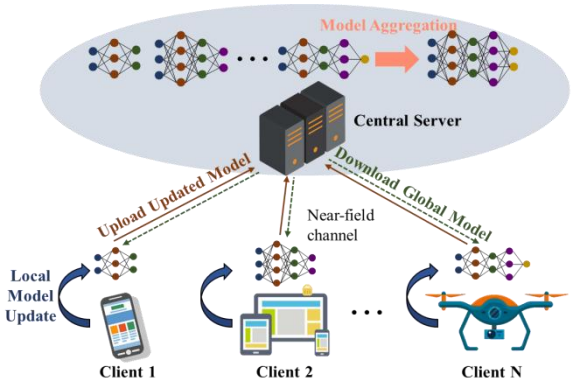

Fig. 6.36 An illustration of the near-field based federated learning framework.

6.6.3 AI-based Near-field Wideband Beamforming Design

The sixth-generation mobile communication (6G) system exhibits significant trends in the development of extremely large-scale antenna arrays and tremendously high frequencies, thus is more likely to operate in the near-field region. In wideband communication, traditional phase shifter-based analog beamforming methods experience beam splitting phenomenon, resulting in a reduction in beamforming gain. To enhance near-field beam focusing and alleviate wideband beam splitting, a hybrid beamforming architecture based on true-time delay is designed at the transmitter. The true-time delay can apply different phase shifts to different frequency components, thereby achieves beam focusing in wideband large-scale antenna communication systems. For the design of true-time delay-based hybrid beamforming, traditional approaches employ fully digital approximate optimization to jointly solve the digital beamforming matrix, analog beamforming matrix, and delay matrix. For instance, one can utilize the weighted minimum mean square error (WMMSE) method to find the optimal fully digital beamformer, then use block coordinate descent to approximate the delay-based hybrid beamforming to the fully-digital beamformer. However, the near-field wideband beamforming design based on fully-digital approximate optimization methods faces challenges such as high computational complexity and susceptibility to changes in channel environments. In this regard, the near-field wideband intelligent beamforming, as illustrated in **Fig. 6.37 (left)**, is proposed. For example, deep reinforcement learning (DRL) algorithms can interact with the environment in real-time to obtain channel capacity information as rewards for updating the network, addressing issues associated with traditional optimization methods. As shown in **Fig. 6.37 (right)**, DRL methods can significantly reduce optimization iteration time and achieve 90% performance compared to the WMMSE-based optimization method [307].

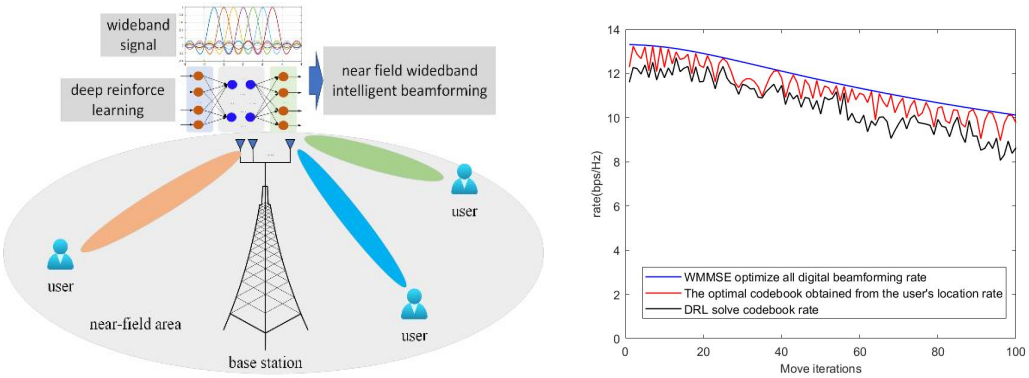

Fig. 6.37 Near-field intelligent beamforming (left) and performance comparison (right).

6.7 Near-field On-chip Wireless Communications

6.7.1 On-chip Wireless Communication Based on On-chip Antenna

With the continuous development of the field of mobile communication, the demand for miniaturization of communication systems has become increasingly urgent. On-chip antennas refer to the antenna structures integrated within the chip. It has the characteristics of miniaturization, low cost, collaborative design with the circuit, high integration and suitability for large-scale mass production. They serve as a feasible alternative within chips to wired signal interconnection. For the future 6G communication systems operating in the terahertz frequency range (100 GHz to 10 THz), the physical size of antennas is significantly reduced. This provides feasibility for utilizing on-chip antennas to achieve high-frequency interconnectivity with chips, enabling the realization of fully integrated on-chip wireless communication systems. Compared to traditional communication systems, this not only significantly improves data transmission rates but also greatly enhances system integration. Therefore, on-chip antenna technology emerges as a highly attractive research direction in the field of 6G communication.

On-chip communication typically adopts the system architecture illustrated in **Fig. 6.38**[308]. At the transmitter, the modulated signal is amplified by a power amplifier (PA) and then transmitted by the on-chip antenna. The on-chip antenna at the receiver transmits the received signal to the low noise amplifier (LNA) for low noise amplification, enhancing the sensitivity of the entire receiver. The signal is filtered, frequency-shifted, amplified, and then demodulated to extract the baseband signal. The distance between the transceivers in on-chip communication systems is small, and the required output power is low. The most commonly used on-chip antennas for on-chip communication are monopole and dipole antennas.

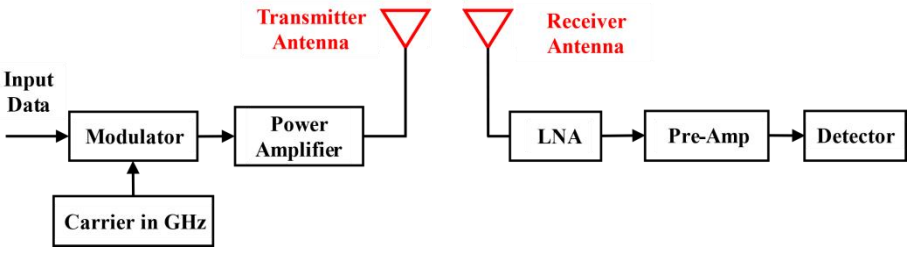

Fig. 6.38 Commonly used on-chip communication system block diagram[296]

In reference [309], researchers developed two planar on-chip antenna topologies on a SiPh platform, as illustrated in **Fig. 6.39**, for intra-chip RF transmission and network-on-chip (NOC) communication. Furthermore, by suppressing electromagnetic radiation, Electromagnetic bandgap (EBG) structures have been used to package open microstrip line baluns to enhance the overall wireless inter-chip link budget [310]. Previous research has integrated Substrate Integrated Waveguide with Metamaterials technologies and present a terahertz planar on-chip antenna for intra-chip wireless communications. This antenna operates in a single thin substrate layer, resulting in significantly reduced losses introduced by the antenna substrate[311].

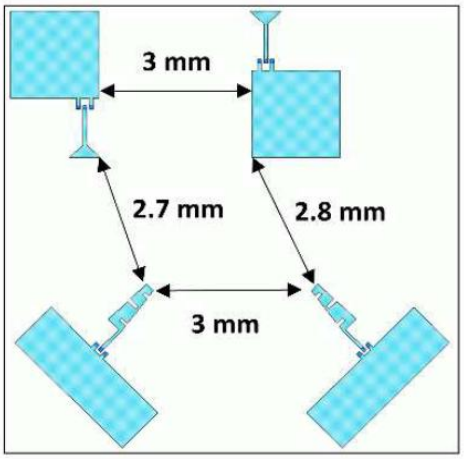

Fig. 6.39 Layout representation for the intra-chip communication arrangement[309].

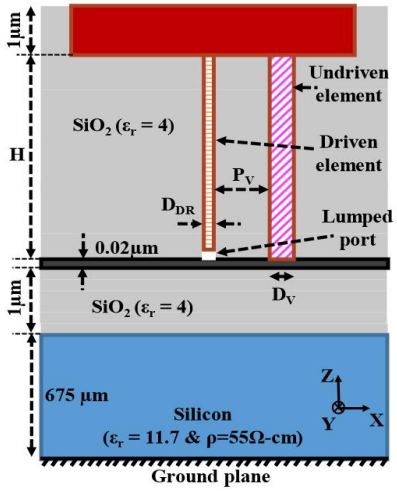

Fig. 6.40 Cross-section of the on-chip top-hat antenna [313].

The majority of on-chip antennas currently available for wireless communication systems are based on silicon technology[312]. In standard silicon-based processes, the silicon substrate has a high relative dielectric constant and a substantial substrate thickness, leading to a significant increase in antenna radiation losses. To address the above issue, researchers have proposed several methods to enhance the radiation efficiency of on-chip antennas. For instance, a novel interconnection device utilizing an on-chip vertical top-hat monopole antennas instead of horizontally placed antennas, as shown in **Fig. 6.40**, is used in 225 GHz on-chip wireless communication. This approach mitigates the challenges associated with the low transmittance in the plane of the chip and the limited radiation resistance of the silicon substrate when the radiation orthogonal to the plane of the chip[313].

Researchers have also proposed manufacturing terahertz on-chip antennas on SiC substrates based on GaN technology, as illustrated in **Fig. 6.41**. This approach enables on-chip full integration with GaN MMIC chips, further enhancing the radiation efficiency and gain of the antennas[314].

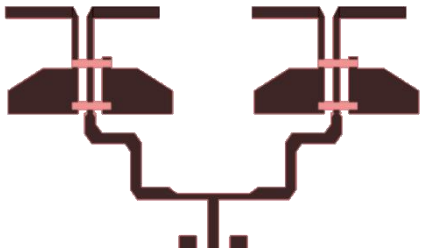

Fig. 6.41 On-chip antenna based on GaN technology [302].

On-chip antennas can be utilized as implantable devices for military, medical and commercial applications. For example, implanted antennas for biomedical therapy and diagnostics, have been designed to monitor various physiological parameters. Furthermore, in conjunction with various kinds of sensors, on-chip antennas can be implanted as part of a biomedical telemetry system, facilitating wireless communication between implantable devices and external instruments. The integration of on-chip antenna technology within wireless transmission systems holds the potential to provide an array of possibilities for the advancement of wireless communication in the 6G era.

6.7.2 On-chip Wireless Communication Based on 3D Stacking Chips

The development of integrated circuits has driven the emergence of system-on-chip (SoC) technology, enabling more functions to be implemented on the same chip. However, the design and manufacturing of SoCs still face challenges, such as increased size due to complex functionalities and difficulties in integrating heterogeneous functional modules with existing process technologies. To address these challenges and meet the demands of 6G communication, researchers have proposed three-dimensional (3D) stacking chips technology, which involves stacking different chips together to form a 3D structure, thereby further enhancing system integration.

However, 3D stacking technology needs to address the interconnection issues between stacked chips, which are crucial for the overall performance of the system[315]. Currently, interconnection technologies used in 3D stacking chips can be classified into two main categories: wired and wireless. Wired interconnection technologies include multi-chip packaging (MCP) and through silicon via (TSV)[316]. MCP involves vertically stacking several chips, with the signals and power pads of each chip connected to a Printed Circuit Board (PCB) through solder joints for communication. TSV technology utilizes vertical silicon vias to achieve interconnection between chips. While these two communication methods can solve interconnection and packaging issues between stacked chips, they also have drawbacks. For example, MCP technology suffers from issues like long solder wires and different resonant frequencies, while TSV technology faces problems like high development costs and low yield rates. At the same time, both of these technologies need to introduce additional electrostatic protection devices. Wireless interconnection technologies applied to 3D stacking chips eliminate the need for wires and silicon vias for communication between chips, effectively overcoming the aforementioned issues. This represents an important direction for future chip design and system integration technologies. Wireless interconnection technologies for chip-to-chip communication in 3D

stacking chips mainly include coupled wireless interconnection technologies and on-chip antenna interconnection technologies as mentioned in section 6.7.1.

Utilizing coupling wireless interconnection technologies: In chip-to-chip near-field communication within stacked chips, coupled interconnection technologies are commonly employed in the mid to low-frequency bands of 6G communication, primarily achieved through capacitive coupling or inductive coupling. Capacitive coupling requires the two plates of the capacitive structure to be placed as close as possible, necessitating face-to-face stacking of chips. As a result, capacitive coupling is not only limited by the number of communicating chips (applicable only to 2-chip configurations) but also constrained by communication distances. Furthermore, capacitive coupling has a larger area and is susceptible to interference from other channels. In contrast, inductive coupling has more advantages than capacitive coupling. Inductively coupled interconnect is not only an efficient and low-cost way of interconnecting chips, but also can reduce power consumption and parasitic effects of complex circuits. **Fig. 6.42(a)** illustrates the traditional inductive coil array structure used for wireless chip-to-chip communication[317]. By inserting a shielding structure between adjacent coils, as shown in **Fig. 6.42(b)**, crosstalk can be reduced. Additionally, to address crosstalk issues and minimize chip area, researchers have further proposed a zigzag structure, depicted in **Fig. 6.42(c)**.

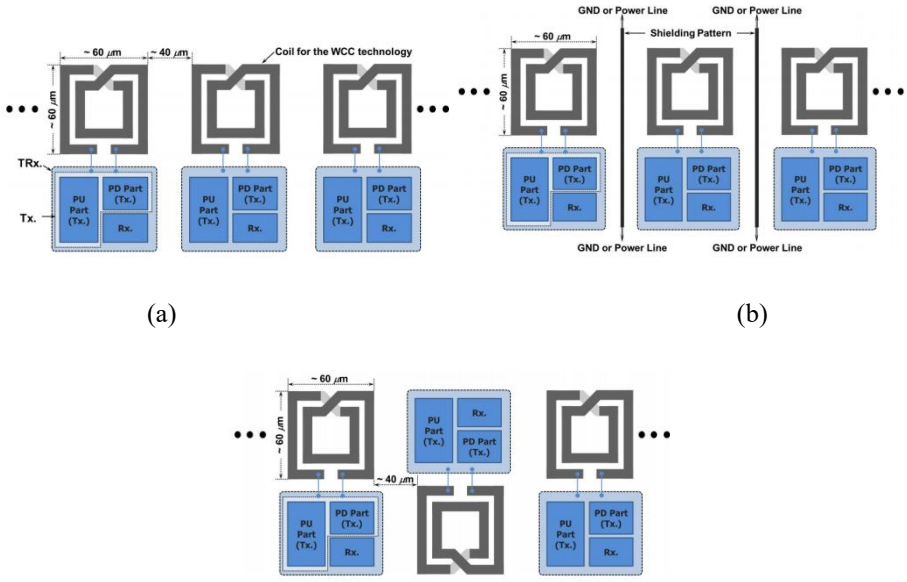

(a) (b)

(c)

Fig. 6.42 (a)Typical coil array structure, (b)Coil array structure with a shielding pattern, (c)Proposed zigzag-shaped coil array for wireless chip-to-chip communication.

On-chip antenna wireless interconnection technology: In chip-to-chip near-field communication within stacked chips, on-chip antenna technology is predominantly employed in the mid to high-frequency bands of 6G communication. While 3D integrated circuits boast high integration density, the flexibility of communication between these circuits is constrained by internal and external links. Wireless data communication between on-chip antennas can alleviate issues such as high latency, low flexibility, and poor scalability associated with wired communication. It can also address the challenge of lower signal frequencies when transmitting wireless communication through coupling. Wireless interconnection systems consist of transmitters and receivers integrated with on-chip antennas.

The most commonly used on-chip antennas for chip-to-chip communication in 3D stacking chips are monopole and dipole antennas, zigzag antennas, linear antennas, curved antennas and through glass via (TGV)-integrated antennas[318].

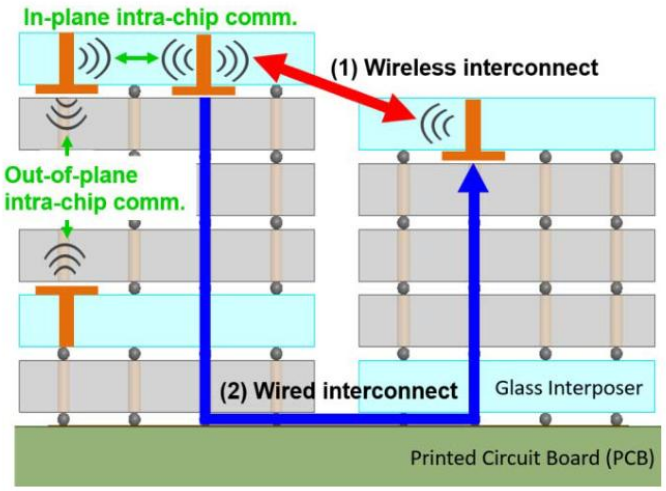

Fig. 6.43 Illustration of wireless in-plane/out-of-plane intra-/interchip communications utilizing TGV-integrated antennas in 3D System-in-Packaging (SiP).

With the advancement of 6G wireless communication, there is a growing demand for higher circuit integration density to exponentially increase the number of transistors per unit area. To meet this current requirement, researchers have proposed three-dimensional stacking chips technology. Traditional wired interconnections such as MCP and TSV face numerous challenges in integration and packaging, including increased power consumption, significant delays, high crosstalk, and complex manufacturing processes associated with wiring across multiple in-plane and out-of-plane dimensions. In comparison to wired methods, wireless interconnection can reduce signal delays, increase communication distances, and decrease chip size. The utilization of wireless interconnection technology employing inductive/capacitive coupling and on-chip antennas provides a solution for on-chip communication and chip interconnection.

6.8 Near-field and Material Sensing

Material sensing technology is playing an increasingly important role in intelligent manufacturing, environmental monitoring and other fields. Traditional material perception technology mainly relies on visual image analysis, which has many limitations in low light, line-of-sight occlusion, bad weather and other scenes. Recent studies have shown that base station massive MIMO arrays have the potential to estimate the electromagnetic coefficient of near-field objects by using OFDM communication signals, and then realize near-field-based object material perception[319]. The near-field material perception problem belongs to one of electromagnetic inverse scattering problems, so the electromagnetic inverse scattering model should be established first.

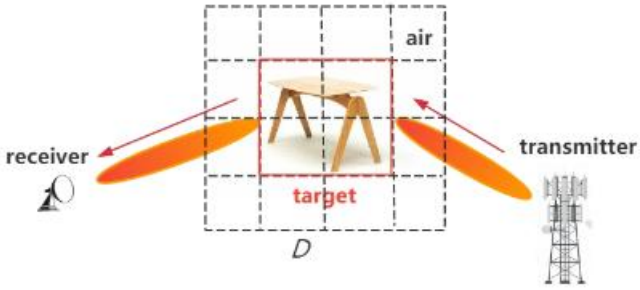

Fig. 6.44 Sensing scenario.

As shown in **Fig. 6.44**, consider a system model consisting of a multi-antenna transmitter, a target, and a multi-antenna receiver. For the system shown in **Fig. 6.44,** the forward scattering channel model is built using the Lippman-Schwinger equation. Because OFDM signal contains many sub-carrier signals of different frequencies, it is necessary to establish a forward channel at each frequency. Due to the fact that objects occupy only a small part of the sensing domain, the electromagnetic coefficient vector to be sensed can be estimated by combining the compressed sensing method. In particular, it can be solved by using the optimization method of mixed norm minimization. Because permittivity contrast and conductivity contrast have the same support set, a model based on generalized multiple measurement vectors (GMMV), the key is to use the joint sparsity structure to improve perception.

Suppose that the known object is made of one of several possible materials whose permittivity and conductivity have been accurately measured in advance. It should be noted that only materials with significant differences in dielectric constant or conductivity can be distinguished. The material identification method consists of two steps: first, clustering, and then classification.

In order to determine the material of the target, we first need to distinguish between the part of D occupied by air and the part occupied by the target. To achieve this, we use the K-means clustering algorithm to divide the sampling points in D into two categories. K-means is an unsupervised algorithm with strong generalization ability for clusters of different shapes and sizes, and convergence is guaranteed regardless of the target. Since the relative permittivity and conductivity have different dimensions, we use dimensionless and scale-invariant Mahalanobis distances in the K-means clustering algorithm. The number of clusters is predetermined at 2, representing air and target respectively. The cluster centroid of air, representing the average permittivity and conductivity values of air, is expected to approach the point (1,0). On the other hand, the centroid of the target cluster, which represents its average permittivity and conductivity, is expected to be significantly farther away from the (1,0) point.

After the clustering is complete, the next step is to determine the material category of the target. This is done by calculating the Mahalanobis distance between the cluster centroid of the target material and the true values of the permittivity and conductivity of each possible material. The target is then classified into the material category with the shortest Mahalanobis distance, which indicates the closest match between the measured electromagnetic properties of the target and the known properties of the material.

7 Summarization and Prospects

In conclusion, the exploration of near-field propagation characteristics has garnered extensive attention and achieved considerable advances. This article represents a pioneering endeavor in the industry, serving as the first comprehensive and systematic white paper on the subject. It meticulously compiles and summarizes the research findings in near-field technology across various dimensions, including application scenarios, foundational theories, channel measurement and modeling, transmission technologies, and its integration with other technological domains. The intention behind this compilation is to lay a robust theoretical foundation and provide practical directives for the future trajectory of near-field technology research.

However, the journey of near-field technology research and its practical engineering applications is not without challenges. These challenges are multifaceted and include, but are not limited to, the need for deeper theoretical exploration to establish a more robust framework. Additionally, there is a discernible deficiency in the measurement data pertaining to near-field channels, and the methodologies for channel modeling require significant enhancement. While strides have been made in near-field transmission technology research, many of the underlying assumptions remain overly simplistic and idealistic, necessitating rigorous investigation into more complex and realistic scenarios and their solutions.

Furthermore, the confluence of near-field technology with other technological fields presents itself as a novel research paradigm. Delving deeper into the unique characteristics of near-field propagation and how to optimally harness these attributes warrants further study. A pivotal aspect of the journey towards practical application is standardization. The initiation of a standardization research project on near-field channel models by 3GPP marks a commendable beginning in this direction. Balancing academic inquiry with proactive efforts in engineering and standardization research is crucial to advance the effective implementation of near-field technology in the forthcoming 6G network landscape.

Looking ahead, near-field technology is poised to introduce to new electromagnetic spatial dimensions to future wireless communication systems. It is increasingly recognized as a cornerstone technology, pivotal for realizing higher data rates, precise sensing capabilities, and efficient wireless power transfer in the 6G network framework. Its potential as a key technology for the future 6G wireless air interface is particularly noteworthy. As such, the anticipation for more groundbreaking research outcomes in near-field technology is high, and there is a keen expectation for its augmented role in shaping the future of wireless networks.

Reference

[1] ITU-R WP 5D, "M.2160-0 (11/2023), Framework and overall objectives of the future development of IMT for 2030 and beyond", Nov., 2023. https://www.itu.int/rec/R-REC-M.2160/en

[2] Tiejun Cui, Shi Jin, Jiayi Zhang, Yajun Zhao, Yifei Yuan, Huan Sun, et al., Research Report on Intelligent Metasurface Technology [R], IMT-2030 (6G) Promotion Group, 2021.

[3] RIS TECH Alliance, Reconfigurable Intelligent Surface White Paper (2023), March 2023, Hangzhou, China, (doi: 10.12142/RISTA.202302002). Available: http://www.risalliance.com/en/riswp2023.html

[4] IMT-2030 (6G) Promotion Group, White Paper on Typical Scenarios and Key Capabilities of 6G, July 2022

[5] L. Zhu, W. Ma, and R. Zhang, “Movable antennas for wireless communication: opportunities and challenges," IEEE Communications Magazine, DOI: 10.1109/MCOM.001.2300212, early access, 2023.

[6] Jiayi Zhang, Jiying Xiang, Bo Ai, Mengnan Jian, Yajun Zhao. 6G Multi Antennas and Reconfigurable Intelligent Surface, Electronic Industry Press, 2023.

[7] Z. Zhou, X. Gao, J. Fang, and Z. Chen. “Spherical wave channel and analysis for large linear array in LoS conditions," in Proc. IEEE Globecom Workshops2015, pp. 1–6.

[8] R. Liu, H. Lin, H. Lee, F. Chaves, H. Lim and J. Sköld, "Beginning of the Journey Toward 6G: Vision and Framework," in IEEE Communications Magazine, vol. 61, no. 10, pp. 8-9, October 2023.

[9] R. Liu, R. Yu-Ngok Li, M. Di Renzo, and L. Hanzo, “A Vision and An Evolutionary Framework for 6G: Scenarios, Capabilities and Enablers,"arXiv e-prints, p. arXiv:2305.13887, May 2023.

[10] R. Liu et al., "6G Enabled Advanced Transportation Systems," in IEEE Transactions on Intelligent Transportation Systems, early access.

[11] H. Zhang, N. Shlezinger, F. Guidi, D. Dardari and Y. C. Eldar, "6G Wireless Communications: From Far-Field Beam Steering to Near-Field Beam Focusing," in IEEE Communications Magazine, vol. 61, no. 4, pp. 72-77, April 2023, doi: 10.1109/MCOM.001.2200259.

[12] "Regulations on the Allocation of Radio Frequencies in the People's Republic of China," Order No. 62 of the Ministry of Industry and Information Technology of the People's Republic of China, May 2023. https://www.gov.cn/govweb/gongbao/2023/issue_10646/202308/content_6898890.html.

[13] WRC-23 Booklet: Agenda and Relevant Resolutions, ITU, Dec. 2023. https://www.itu.int/wrc-23/booklet-wrc-23/

[14] 3GPP. RP-234018, Channel Modelling Enhancements for 7-24 GHz. 3GPP TSG RAN Meeting #102, Edinburgh, UK, 11th -15th December, 2023.

[15] Next G Alliance Report: 6G Technologies, Jun. 2022. https://www.nextgalliance.org/wp-content/uploads/dlm_uploads/2022/07/TWG-report-6G-technologies.pdf

[16] M. Jian and R. Liu, "Baseband Signal Processing for Terahertz: Waveform Design, Modulation and Coding," 2021 International Wireless Communications and Mobile Computing (IWCMC),

Harbin City, China, 2021, pp. 1710-1715.

[17] Sarieddeen, Hadi, Mohamed-Slim Alouini, and Tareq Y. Al-Naffouri. "An overview of signal processing techniques for terahertz communications." Proceedings of the IEEE 109.10 (2021): 1628-1665.

[18] Akyildiz, Ian F., et al. "Terahertz band communication: An old problem revisited and research directions for the next decade." IEEE Transactions on Communications 70.6 (2022): 4250-4285.

[19] H. Zhang, N. Shlezinger, F. Guidi, D. Dardari, M. F. Imani and Y. C. Eldar, "Beam Focusing for Near-Field Multiuser MIMO Communications," in IEEE Transactions on Wireless Communications, vol. 21, no. 9, pp. 7476-7490, Sept. 2022, doi: 10.1109/TWC.2022.3158894.

[20] H. ZHANG, N. SHLEZINGER, F. GUIDI, et al. Beam Focusing for Near-Field Multiuser MIMO Communications[J/OL]. IEEE Transactions on Wireless Communications, 2022, 21(9): 7476-7490. DOI:10.1109/TWC.2022.3158894.

[21] Singh, Arjun, Ali J. Alqaraghuli, and Josep M. Jornet. "Wavefront engineering at terahertz frequencies through intelligent reflecting surfaces." 2022 IEEE 23rd International Workshop on Signal Processing Advances in Wireless Communication (SPAWC). IEEE, 2022.

[22] Singh, Arjun, et al. "Bessel Beams for 6G-A Performance Analysis." 2022 56th Asilomar Conference on Signals, Systems, and Computers. IEEE, 2022.

[23] Singh, Arjun, Vitaly Petrov, and Josep M. Jornet. "Utilization of Bessel beams in wideband sub Terahertz communication systems to mitigate beamsplit effects in the near-field." ICASSP 2023-2023 IEEE International Conference on Acoustics, Speech and Signal Processing (ICASSP). IEEE, 2023.

[24] Reddy, Innem VAK, et al. "Ultrabroadband terahertz-band communications with self-healing bessel beams." Communications Engineering 2.1 (2023): 70.

[25] Paschaloudis, Konstantinos D., et al. "Near-Field Links with Obstructed Line of Sight via Bessel Beams." 2023 17th European Conference on Antennas and Propagation (EuCAP). IEEE, 2023.

[26] Guerboukha, Hichem, et al. "Curving THz wireless data links around obstacles." Communications Engineering 3.1 (2024): 1-8.

[27] Singh, Arjun, Ali J. Alqaraghuli, and Josep M. Jornet. "Wavefront engineering at terahertz frequencies through intelligent reflecting surfaces." 2022 IEEE 23rd International Workshop on Signal Processing Advances in Wireless Communication (SPAWC). IEEE, 2022.

[28] Singh, Arjun, et al. "Design and operation of a graphene-based plasmonic nano-antenna array for communication in the terahertz band." IEEE Journal on Selected Areas in Communications 38.9 (2020): 2104-2117.

[29] Akyildiz, Ian F., and Josep Miquel Jornet. "Realizing ultra-massive MIMO (1024× 1024) communication in the (0.06 – 10) terahertz band." Nano Communication Networks 8 (2016): 46-54.

[30] Petrov, Vitaly, Duschia Bodet, and Arjun Singh. "Mobile near-field terahertz communications for 6G and 7G networks: Research challenges." Frontiers in Communications and Networks 4 (2023): 1151324.

[31] Bodet, Duschia, and Josep M. Jornet. "Joint Waveform & Wavefront Engineering for Terahertz Communications in 6G." 2023 IEEE International Conference on Acoustics, Speech, and Signal Processing Workshops (ICASSPW). IEEE, 2023.

[32] M. Cui, Z. Wu, Y. Lu, X. Wei and L. Dai, "Near-Field MIMO Communications for 6G: Fundamentals, Challenges, Potentials, and Future Directions," in IEEE Communications Magazine, vol. 61, no. 1, pp. 40-46, January 2023, doi: 10.1109/MCOM.004.2200136.

[33] R. Liu, Q. Wu, M. Di Renzo and Y. Yuan, "A Path to Smart Radio Environments: An Industrial Viewpoint on Reconfigurable Intelligent Surfaces," in IEEE Wireless Communications, vol. 29, no. 1, pp. 202-208, February 2022.

[34] R. Liu, J. Dou, P. Li, J. Wu and Y. Cui, "Simulation and Field Trial Results of Reconfigurable Intelligent Surfaces in 5G Networks," in IEEE Access, vol. 10, pp. 122786-122795, 2022.

[35] Z. Tang, Y. Chen, Y. Wang, T. Mao, Q. Wu, M. Di Renzo, and L. Hanzo, “Near-Field Sparse Channel Estimation for Extremely Large-Scale RIS-Aided Wireless Communications," in Proceedings of IEEE Globecom Workshops, Kuala Lumpur, Malaysia, 2023.

[36] S. Lv, Y. Liu, X. Xu, A. Nallanathan, and A. L. Swindlehurst, “RIS-aided near-field MIMO communications: Codebook and beam training design," arXiv preprint arXiv:2310.00294, 2023.

[37] Z. Wang, X. Mu, and Y. Liu, “Near-field integrated sensing and communications," IEEE Commun. Lett., vol. 27, no. 8, pp. 2048–2052, Aug. 2023.

[38] Y. Pan, C. Pan, S. Jin and J. Wang, “RIS-aided near-field localization and channel estimation for the terahertz system," IEEE J. Sel. Topics Signal Process., vol. 17, no. 4, pp. 878–892, Jul. 2023.

[39] H. Lu, Y. Zeng, C. You, et al. “A tutorial on near-field XL-MIMO communications towards 6G," arXiv preprint arXiv:2310.11044, 2023.

[40] X. Li, H. Lu, Y. Zeng, S. Jin, and R. Zhang, “Near-field modeling and performance analysis of modular extremely large-scale array communications," IEEE Commun. Lett., vol. 26, no. 7, pp. 1529–1533, Jul. 2022.

[41] X. Li, H. Lu, Y. Zeng, S. Jin, and R. Zhang, “Modular extremely large-scale array communication: Near-field modelling and performance analysis," China Commun., vol. 20, no. 4, pp. 132–152, Apr. 2023.

[42] H. Wang and Y. Zeng, "Can Sparse Arrays Outperform Collocated Arrays for Future Wireless Communications?" IEEE GLOBECOM Workshops, Kuala Lumpur, Malaysia, 2023.

[43] L. Zhu, W. Ma, and R. Zhang, “Movable antennas for wireless communication: opportunities and challenges," IEEE Communications Magazine, DOI: 10.1109/MCOM.001.2300212, early access, 2023.

[44] L. Zhu, W. Ma, and R. Zhang, “Modeling and performance analysis for movable antenna enabled wireless communications," IEEE Transactions on Wireless Communications, DOI: 10.1109/TWC.2023.3330887, early access, 2023.

[45] W. Mei, X. Wei, B. Ning, Z. Chen, and R. Zhang, “Movable antenna position optimization: A graph-based approach," arXiv preprint arXiv:2403.16886, 2024.

[46] W. Ma, L. Zhu, and R. Zhang, “MIMO capacity characterization for movable antenna systems," IEEE Transactions on Wireless Communications, DOI: 10.1109/TWC.2023.3307696, early access, 2023.

[47] L. Zhu, W. Ma, B. Ning, and R. Zhang, “Movable-antenna enhanced multiuser communication via antenna position optimization," IEEE Transactions on Wireless Communications, DOI: 10.1109/TWC.2023.3338626, early access, 2023.

[48] X. Shao, Q. Jiang, and R. Zhang, “6D movable antenna based on user distribution: Modeling and

optimization," arXiv preprint arXiv:2403.08123, 2024.

[49] L. Zhu, W. Ma, and R. Zhang, "Movable-antenna array enhanced beamforming: Achieving full array gain with null steering," IEEE Communications Letters, vol. 27, no. 12, pp. 3340 – 3344, Dec. 2023.

[50] W. Ma, L. Zhu, and R. Zhang, "Multi-beam forming with movable-antenna array," IEEE Communications Letters, vol. 28, no. 3, pp. 697 – 701, Mar. 2024.

[51] R. Liu et al., "Integrated sensing and communication based outdoor multi-target detection, tracking, and localization in practical 5G Networks," in Intelligent and Converged Networks, vol. 4, no. 3, pp. 261-272, September 2023.

[52] T. Mao, J. Chen, Q. Wang, C. Han, Z. Wang, and G. K. Karagiannidis, "Waveform Design for Joint Sensing and Communications in Millimeter-Wave and Low Terahertz Bands," IEEE Trans. Commun., vol. 70, no. 10, pp. 7023-7039, Oct. 2022.

[53] F. Zhang, T. Mao, R. Liu, Z. Han, S. Chen, and Z. Wang, "Cross-domain waveform design for 6G integrated sensing and communication," arXiv preprint arXiv:2311.04483, 2024.

[54] A. Sakhnini, S. De Bast, M. Guenach, A. Bourdoux, H. Sahli, and S. Pollin, "Near-field coherent radar sensing using a massive MIMO communication testbed," IEEE Trans. Wireless Commun., vol. 21, no. 8, pp. 6256–6270, Aug. 2022.

[55] R. Liu, C. Zhang and J. Song, "Line of Sight Component Identification and Positioning in Single Frequency Networks Under Multipath Propagation," in IEEE Transactions on Broadcasting, vol. 65, no. 2, pp. 220-233, June 2019.

[56] M. Lipka, S. Brückner, E. Sippel, and M. Vossiek, "On the Needlessness of Signal Bandwidth for Precise Holographic Wireless Localization," in 2020 17th European Radar Conference (EuRAD), 2021, pp. 202 – 205.

[57] H. Chen, M. F. Keskin, A. Sakhnini, N. Decarli, S. Pollin, D. Dardari, and H. Wymeersch, "6G localization and sensing in the near field: Fundamentals, opportunities, and challenges," arXiv preprint arXiv:2308.15799, 2023.

[58] Zhang Yuexia, Liu Chong. "5G ultra-dense network fingerprint positioning method based on matrix completion," China Communication,2023, 20 (3) , pp.105-118.

[59] Zou Deyue; Meng Weixiao; Han Shuai; He, Kai; Zhang Zhongzhao. "TOWARD UBIQUITOUS LBS: MULTI-RADIO LOCALIZATION AND SEAMLESS POSITIONING," IEEE WIRELESS COMMUNICATIONS, 2016, 23(6), pp. 107-113.

[60] Zou, Deyue; Meng, Weixiao; Han, Shuai. "Euclidean distance based handoff algorithm for fingerprint positioning of WLAN system," IEEE Wireless Communications and Networking Conference(WCNC), 2013, pp.1564-1568.

[61] Zou, Deyue; He, Liansheng. "Fusion Handover Algorithm Based on Accuracy Estimation," 2022 2nd International Conference on Frontiers of Electronics, Information and Computation Technologies (ICFEICT 2022), 2022, pp. 282-286.

[62] Zou, Deyue; Meng, Weixiao; Han, Shuai. "An accuracy estimation algorithm for fingerprint positioning system," 2014 4th International Conference on Instrumentation and Measurement, Computer, Communication and Control (IMCCC 2014), 2014, pp. 573-577.

[63] Chen, Liang; Wen, Pei; Zou, Deyue; Li, Feng; He, Liansheng. "An Innovative Accuracy Estimation Algorithm of Fingerprint Positioning," 2022 International Wireless Communications

and Mobile Computing (IWCMC 2022), 2022, pp. 201-204.

[64] He, Liansheng; Zou, Deyue. “Fusion Localization Based on Accuracy Estimation," 2022 5th International Conference on Advanced Electronic Materials, Computers and Software Engineering (AEMCSE 2022), 2022, pp. 12-18.

[65] Yuexia Zhang, Ying Zhou, Siyu Zhang, Guan Gui, Bamidele Adebisi, Haris Gacanin and Hikmet Sari. “An Efficient Caching and Offloading Resource Allocation Strategy in Vehicular Social Networks," in IEEE Transactions on Vehicular Technology, 2023,early access.

[66] Yunong Yang, Yuexia Zhang and Zhihai Zhuo. “ Adaptive Time Slot Resource Allocation in SWIPT IoT Networks," in Computer Modeling in Engineering & Sciences,2023,vol.136, no. 3, pp:2787-2813.

[67] Z. Zhang, Y. Liu, Z. Wang, X. Mu, and J. Chen, “Physical layer security in near-field communications," arXiv preprint arXiv:2302.04189, 2023.

[68] F. Rusek et al., "Scaling Up MIMO: Opportunities and Challenges with Very Large Arrays," in IEEE Signal Processing Magazine, vol. 30, no. 1, pp. 40-60, Jan. 2013.

[69] Jornet, Josep Miquel, and Amit Sangwan. "Nanonetworking in the Terahertz band and beyond." IEEE Nanotechnology Magazine (2023).

[70] Abadal, Sergi, Chong Han, and Josep Miquel Jornet. "Wave propagation and channel modeling in chip-scale wireless communications: A survey from millimeter-wave to terahertz and optics." IEEE access 8 (2019): 278-293.

[71] A. Sindgi and U. B. Mahadevaswamy, "Wavelet-Powered mm-Wave OFDM for Efficient Wireless Network-on-Chip Communication," 2023 International Conference on Network, Multimedia and Information Technology (NMITCON), Bengaluru, India, 2023, pp. 1-8.

[72] R. Medina, J. Kein, Y. Qureshi, M. Zapater, G. Ansaloni and D. Atienza, "Full System Exploration of On-Chip Wireless Communication on Many-Core Architectures," 2022 IEEE 13th Latin America Symposium on Circuits and System (LASCAS), Puerto Varas, Chile, 2022, pp. 1-4.

[73] H. -i. Kim, R. Bowrothu and Y. -K. Yoon, "Tri-axis Polarized Loop Antenna for mmWave Wireless Inter/intra Chip Communications," 2020 IEEE 70th Electronic Components and Technology Conference (ECTC), Orlando, FL, USA, 2020, pp. 1875-1880.

[74] V. Petrov et al., "Terahertz Band Intra-Chip Communications: Can Wireless Links Scale Modern x86 CPUs?," in IEEE Access, vol. 5, pp. 6095-6109, 2017.

[75] A. Yaghjian, “An overview of near-field antenna measurements," IEEE Trans. Antennas Propag., vol. 34, no. 1, pp. 30 – 45, Jan. 1986.

[76] K. T. Selvan and R. Janaswamy, “Fraunhofer and Fresnel distances: Unified derivation for aperture antennas," IEEE Antennas Propag. Mag., vol. 59, no. 4, pp. 12 – 15, Aug. 2017.

[77] M. Cui and L. Dai, “Near-field wideband beamforming for extremely large antenna array," arXiv preprint arXiv:2109.10054, 2023.

[78] H. Lu and Y. Zeng, “How does performance scale with antenna number for extremely large-scale MIMO?’’ in Proc. IEEE ICC, Jun. 2021, pp. 1-6.

[79] Lu, Haiquan, and Yong Zeng, “Communicating with extremely large-scale array/surface: Unified modeling and performance analysis," IEEE Transactions on Wireless Communications, vol. 21, no. 6, pp. 4039 – 4053, 2022.

[80] R. Li, S. Sun, and M. Tao, “Applicable regions of spherical and plane wave models for extremely large-scale array communications,"accepted by China Communications, 2023. [Online]. Available: https://arxiv.org/pdf/2301.06036.pdf.

[81] J.-S. Jiang and M. Ingram, “Spherical-wave model for short-range MIMO," IEEE Transactions on Communications, vol. 53, no. 9, pp. 1534 – 1541, Sep. 2005.

[82] F. Bohagen, P. Orten, and G. E. Oien, “On spherical vs. plane wave modeling of line-of-sight MIMO channels," IEEE Transactions on Communications, vol. 57, no. 3, pp. 841 – 849, Mar. 2009.

[83] P. Wang, Y. Li, X. Yuan, L. Song, and B. Vucetic, “Tens of gigabits wireless communications over E-Band LoS MIMO channels with uniform linear antenna arrays," IEEE Transactions on Wireless Communications, vol. 13, no. 7, pp. 3791 – 3805, Jul. 2014.

[84] S. Sun, et al. "How to Differentiate between Near Field and Far Field: Revisiting the Rayleigh Distance." arXiv preprint arXiv:2309.13238 (2023).

[85] H. Chen, A. Elzanaty, R. Ghazalian, M. F. Keskin, R. Jäntti and H. Wymeersch, "Channel Model Mismatch Analysis for XL-MIMO Systems from a Localization Perspective," GLOBECOM 2022 - 2022 IEEE Global Communications Conference, Rio de Janeiro, Brazil, 2022, pp. 1588-1593,

[86] L. Wei et al., "Tri-Polarized Holographic MIMO Surfaces for Near-Field Communications: Channel Modeling and Precoding Design," in IEEE Transactions on Wireless Communications, doi: 10.1109/TWC.2023.3266298.

[87] M. Cui, L. Dai, R. Schober, and L. Hanzo, “Near-field wideband beamforming for extremely large antenna array," arXiv preprint arXiv:2109.10054, Sep. 2021.

[88] Ramezani P, Kosasih A, Irshad A, et al, Exploiting the depth and angular domains for massive near-field spatial multiplexing[J]. IEEE BITS the Information Theory Magazine, 2023.

[89] Wu Z, Dai L. Multiple access for near-field communications: SDMA or LDMA?[J]. IEEE Journal on Selected Areas in Communications, 2023, 41(6): 1918-1935.

[90] Z. Wu, M. Cui and L. Dai, "Enabling More Users to Benefit from Near-Field Communications: From Linear to Circular Array," in IEEE Transactions on Wireless Communications, doi: 10.1109/TWC.2023.3310912.

[91] R. Ji et al., "Extra DoF of Near-Field Holographic MIMO Communications Leveraging Evanescent Waves," in IEEE Wireless Communications Letters, vol. 12, no. 4, pp. 580-584, April 2023, doi: 10.1109/LWC.2023.3234003.

[92] A. Pizzo, A. d. J. Torres, L. Sanguinetti and T. L. Marzetta, "Nyquist Sampling and Degrees of Freedom of Electromagnetic Fields," in IEEE Transactions on Signal Processing, vol. 70, pp. 3935-3947, 2022, doi: 10.1109/TSP.2022.3183445.

[93] C. Ouyang et al., “Near-field communications: A degree-of-freedom perspective," arXiv preprint arXiv:2308.00362, 2023.

[94] Z. Xie et al., “Performance analysis for near-field MIMO: Discrete and continuous aperture antennas," Early Access, IEEE Wireless Commun. Lett., 2023, doi: 10.1109/LWC.2023.3317492.

[95] S. Verdu, “Spectral efficiency in the wideband regime," IEEE Trans. Inf. theory, vol. 48, no. 6, pp. 1319–1343, Jun. 2002, 10.1109/TIT.2002.1003824.

[96] D. A. B. Miller, “Communicating with waves between volumes: Evaluating orthogonal spatial channels and limits on coupling strengths," Appl. Opt., vol. 39, no. 11, pp. 1681–1699, Apr. 2000,

doi: https://doi.org/10.1364/AO.39.001681.

[97] Dong Z, Zeng Y. Near-field spatial correlation for extremely large-scale array communications[J]. IEEE Communications Letters, 2022, 26(7): 1534-1538.

[98] Lu H, Zeng Y, You C, et al. A tutorial on near-field XL-MIMO communications towards 6G[J]. arXiv preprint arXiv:2310.11044, 2023.

[99] B. Zhuo, J. Gu, W.Duan, L. Zhang, M. Wen, and P.-H. Ho, "Extremely Large-Scale Array System: Cooperative NFC or FFC?" IEEE Wireless Communications Letters, to appear 2024. DOI: 10.1109/LWC.2024.3367132

[100]Zheng B, Ma T, Yi X, et al. Intelligent reflecting surface-aided transmit diversity and performance analysis[C]//ICC 2023-IEEE International Conference on Communications. IEEE, 2023: 2822-2827.

[101]Zheng B, Zhang R. Simultaneous transmit diversity and passive beamforming with large-scale intelligent reflecting surface[J]. IEEE Transactions on Wireless Communications, 2022, 22(2): 920-933.

[102]H. Lu and Y. Zeng, "How does performance scale with antenna number for extremely large-scale MIMO?" in Proc. IEEE Int. Conf. Commun. (ICC), Montreal, QC, Canada, Jun. 2021, pp. 1 – 6.

[103]H. Wang and Y. Zeng, "Can Sparse Arrays Outperform Collocated Arrays for Future Wireless Communications?" IEEE GLOBECOM Workshops, Kuala Lumpur, Malaysia, 2023.

[104]X. Li, H. Lu, Y. Zeng, S. Jin, and R. Zhang, "Near-field modeling and performance analysis of modular extremely large-scale array communications," IEEE Commun. Lett., vol. 26, no. 7, pp. 1529 – 1533, Jul. 2022.

[105]X. Li, H. Lu, Y. Zeng, S. Jin, and R. Zhang, "Modular extremely large-scale array communication: Near-field modelling and performance analysis," China Commun., vol. 20, no. 4, pp. 132 – 152, Apr. 2023.

[106]X. Li, Z. Dong, Y. Zeng, S. Jin, and R. Zhang,"Near-field beam focusing pattern and grating lobe characterization for modular XL-array,"Presented at IEEE Globecom, arXiv preprint arXiv:2305.05408, 2023.

[107]X. Li, Z. Dong, Y. Zeng, S. Jin, and R. Zhang, "Multi-user modular XL-MIMO communications: Near-field beam focusing pattern and user grouping," Submitted to IEEE Trans. Wireless Commun., arXiv:2308.11289, 2023.

[108]Wu Q, Zhang R. Intelligent reflecting surface enhanced wireless network via joint active and passive beamforming[J]. IEEE transactions on wireless communications, 2019, 18(11): 5394-5409.

[109]C. Feng, H. Lu, Y. Zeng, T. Li, S. Jin, and R. Zhang, "Near-field modelling and performance analysis for extremely large-scale IRS communications," IEEE Trans. Wireless Commun., 2023.

[110]Z. Dong and Y. Zeng. "Near-field spatial correlation for extremely large-scale array communications," IEEE Commun. Lett., 2022, 26(7): 1534-1538.

[111]H. Lu, Y. Zeng, C. You, et al. "A tutorial on near-field XL-MIMO communications towards 6G," arXiv preprint arXiv:2310.11044, 2023.

[112]Wang H, Zeng Y. SNR scaling laws for radio sensing with extremely large-scale MIMO[C]//2022 IEEE International Conference on Communications Workshops (ICC Workshops). IEEE, 2022: 121-126.

[113]H. Wang, Z. Xiao, and Y. Zeng. Cram\'er-Rao bounds for near-field sensing with extremely large-scale MIMO[J]. arXiv preprint arXiv:2303.05736, 2023.

[114]X. Gan, C. Huang, Z. Yang, C. Zhong and Z. Zhang, "Near-Field Localization for Holographic RIS Assisted mmWave Systems," in IEEE Communications Letters, vol. 27, no. 1, pp. 140-144, Jan. 2023, doi: 10.1109/LCOMM.2022.3209570.

[115]A. Pizzo, T. L. Marzetta, and L. Sanguinetti, "Spatially-stationary model for holographic MIMO small-scale fading," IEEE J. Sel. Areas Commun., vol. 38, no. 9, pp. 1964 – 1979, Sep. 2020.

[116]A. Pizzo, T. Marzetta, and L. Sanguinetti, "Holographic MIMO communications under spatially-stationary scattering," in Proc. 2020 54th Asilomar Conf. Signals, Sys., Comp., Nov. 2020, pp. 702 – 706.

[117]A. Pizzo, L. Sanguinetti, and T. L. Marzetta, "Fourier plane-wave series expansion for holographic MIMO communications," IEEE Trans. Wireless Commun., pp. 1 – 1, Sep. 2022.

[118]Zhi, C. Pan, H, Ren, et al. "Performance Analysis and Low-Complexity Design for XL-MIMO with Near-Field Spatial Non-Stationarities," accepted by IEEE JSAC, arXiv preprint arXiv:2304.00172, 2023.

[119]T. Gong et al., "Holographic MIMO Communications: Theoretical Foundations, Enabling Technologies, and Future Directions," in IEEE Communications Surveys & Tutorials, doi: 10.1109/COMST.2023.3309529.

[120]G. T. Ruck, D. E. Barrick, W. D. Stuart, et al., "Radar Cross Section Handbook",. Volumes 1 & 2, Plenum Press, New York, 1970.

[121]E. F. Knott, J. F. Shaeffer, M. T. Tuley. "Radar Cross Section", Institution of Engineering and Technology, 2004.

[122]IEEE Recommended Practice for Radar Cross-Section Test Procedures: IEEE Std 1502-2020 (Revision of IEEE Std 1502-2007):2020: 1-78.

[123]J. Melin, "Measuring radar cross section at short distance", IEEE Transactions on Antennas & Propagation, 1987, 35(8): 991-6.

[124]Sheng Xinqing, Essentials of Computational Electromagnetics, Beijing: Science Press, 2004.

[125]I. J. Lahaie, E. I. Lebaron, J. W. Burns. "Far field radar cross-section (RCS) predictions from planar near field measurements", proceedings of the IEEE Antennas and Propagation Society International Symposium 1992 Digest, F 18-25 June 1992.

[126]I. J. Lahaie, "Overview of an Image-Based Technique for Predicting Far-Field Radar Cross Section from Near-Field Measurements", IEEE Antennas Propagation Magazine, 2003, 45(6): 159-69.

[127]I. J. Lahaie, S. A. Rice, "antenna-pattern correction for near-field-to-far field RCS transformation of 1D linear SAR measurements", IEEE Antenn Propag M, 2004, 46(4): 177-83.

[128]C. Coleman, I. Lahaie, S. Rice, "Antenna pattern correction for the circular near field-to-far field transformation (CNFFFT)", proceedings of the Proc AMTA, F, 2005.

[129]I. J. Lahaie, "An improved version of the circular near field-to-far field transformation (CNFFFT)", Proceedings of the 27th Annual Meeting of the Antenna Measurement Techniques Association (AMTA'05), Newport, RI, F, 2005.

[130]S. A. Rice, I. J. Lahaie, "A partial rotation formulation of the circular near-field-to-far-field transformation (CNFFFT)", IEEE Antennas Propagation Magazine, 2007, 49(3): 209-14.

[131]J. Zhang, Z. Zheng, Y. Zhang et al., "3D MIMO for 5G NR: Several Observations from 32 to Massive 256 Antennas Based on Channel Measurement," IEEE Communications Magazine, vol. 56, no. 3, pp. 62-70, Mar. 2018.

[132]J. Zhang, H. Miao, P. Tang et al., "New Mid-Band for 6G: Several Considerations from Channel Propagation Characteristics Perspective." IEEE Communications Magazine, Accepted, 2024.

[133]M. Li, Z. Yuan, Y. Lyu, P. Kyösti, J. Zhang and W. Fan, "Gigantic MIMO Channel Characterization: Challenges and Enabling Solutions," in IEEE Communications Magazine, vol. 61, no. 10, pp. 140-146, Oct. 2023.

[134]E. Bjornson, L. Sanguinetti, H. Wymeersch et al., "Massive MIMO is a reality-What is next? Five promising research directions for antenna arrays" Digital Signal Process., vol. 94, pp. 320, Nov. 2019.

[135]J. Zhang, Y. Zhang, Y. Yu et al., "3-D MIMO: How Much Does It Meet Our Expectations Observed From Channel Measurements?," IEEE Journal on Selected Areas in Communications, vol. 35, no. 8, pp. 1887-1903, Aug. 2017.

[136]X. Li, E. Leitinger, M. Oskarsson et al., "Massive MIMO-Based Localization and Mapping Exploiting Phase Information of Multipath Components," IEEE Transactions on Wireless Communications, vol. 18, no. 9, pp. 4254-4267, Sept. 2019.

[137]Y. Zheng et al., "Ultra-Massive MIMO Channel Measurements at 5.3 GHz and a General 6G Channel Model," IEEE Transactions on Vehicular Technology, vol. 72, no. 1, pp. 20-34, Jan. 2023.

[138]Y. Lyu, Z. Yuan, M. Li et al., "Enabling Long-range Large-scale Channel Sounding at Sub-THz Bands: Virtual array and Radio-over-fiber Concepts," IEEE Communications Magazine, Nov. 2022.

[139]J. Medbo, H. Asplund et al., "60 GHz Channel Directional Characterization Using Extreme Size Virtual Antenna Array," in 2015 IEEE 26th Annual International Symposium on Personal, Indoor, and Mobile Radio Communications (PIMRC), 2015, pp. 176-180.

[140]X. Gao, F. Tufvesson, O. Edfors and F. Rusek, "Measured propagation characteristics for very-large MIMO at 2.6 GHz," in 2012 Conference Record of the Forty Sixth Asilomar Conference on Signals, Systems and Computers (ASILOMAR), 2012, pp. 295-299.

[141]J. Li and Y. Zhao, "Channel Characterization and Modeling for Large-scale Antenna Systems," in 2014 14th International Symposium on Communications and Information Technologies (ISCIT), 2014, pp. 559-563.

[142]B. Ai et al., "On Indoor Millimeter Wave Massive MIMO Channels: Measurement and Simulation," IEEE Journal on Selected Areas in Communications, vol. 35, no. 7, pp. 1678-1690, Jul. 2017.

[143]C. Wang, J. Zhang, L. Tian et al., "The Spatial Evolution of Clusters in Massive MIMO Mobile Measurement at 3.5 GHz," in Proc. IEEE VTC Spring., Jun. 2017, pp. 1-6.

[144]"METIS channel models," document Deliverable/ICT-317669/D1.4 V3,Tech. Rep., Mar.2017.

[145]J. Zhang, J. Lin, P. Tang et al., "Deterministic Ray Tracing: A Promising Approach to THz Channel Modeling in 6G Deployment Scenarios", IEEE Communication Magazine, 2023.

[146]L. Liu, C. Oestges, J. Poutanen et al., "The COST 2100 MIMO Channel Model," IEEE Wireless Communication, vol. 19, no. 6, pp. 92-99, 2012.

[147]X. Gao, F. Tufvesson, and O. Edfors, "Massive MIMO Channels Measurements and Models," in IEEE ASILOMAR, 2013, pp. 280-284.

[148]E. T. Michailidis, N. Nomikos, P . Trakadas et al., "Three-dimensional Modeling of mmwave Doubly Massive MIMO Aerial Fading Channels," IEEE Transactions on Vehicular Technology , vol. 69, no. 2, pp. 1190-1202, 2020.

[149]W. Zuo, P. Tang, H. Miao et al., "Analysis of Spatial Non-Stationary Characteristics for 6G XL-MIMO Communication," in 2024 Vehicular Technology Conference (VTC2024-Spring)., Accepted, Mar. 2024.

[150]Z. Yuan, J. Zhang, V. Degli-Esposti, et al., "Efficient Ray-tracing Simulation for Near-field Spatial Non-stationary mmWave Massive MIMO Channel and Its Experimental Validation, " IEEE Transactions on Wireless Communications, Jan. 2024.

[151]Z. Yuan, J. Zhang, Y. Ji et al., "Spatial Non-Stationary Near-Field Channel Modeling and Validation for Massive MIMO Systems," IEEE Transactions on Antennas and Propagation, vol. 71, no. 1, pp. 921-933, Jan. 2023.

[152]T. Gao, P. Tang, L. Tian et al., "A 3GPP-Like Channel Simulation Framework Considering Near-field Spatial Non-stationary Characteristics of Massive MIMO," in 2023 IEEE Globecom Workshops(GCWkshps)., Accepted, Dec. 2023.

[153]Carvalho E D, Ali A, Amiri A, et al. Non-Stationarities in Extra-Large-Scale Massive MIMO[J]. IEEE Wireless Communications, 2020, 27(4): 74-80.

[154]Björnson E, Sanguinetti L, Wymeersch H, et al. Massive MIMO is a reality—What is next?: Five promising research directions for antenna arrays[J]. Digital Signal Processing, 2019, 94: 3-20.

[155]Amiri A, Angjelichinoski M, Carvalho E d, et al. Extremely Large Aperture Massive MIMO: Low Complexity Receiver Architectures[C]. 2018 IEEE Globecom Workshops (GC Wkshps), 2018: 1-6.

[156]Ali A, Carvalho E D, Heath R W. Linear Receivers in Non-Stationary Massive MIMO Channels With Visibility Regions[J]. IEEE Wireless Communications Letters, 2019, 8(3): 885-888.

[157]Li X, Zhou S, Björnson E, et al. Capacity Analysis for Spatially Non-Wide Sense Stationary Uplink Massive MIMO Systems[J]. IEEE Transactions on Wireless Communications, 2015, 14(12): 7044-7056.

[158]Amiri A, Rezaie S, Manchón C N, et al. Distributed Receiver Processing for Extra-Large MIMO Arrays: A Message Passing Approach[J]. IEEE Transactions on Wireless Communications, 2022, 21(4): 2654-2667.

[159]Zhu Y, Guo H, Lau V K N. Bayesian Channel Estimation in Multi-User Massive MIMO With Extremely Large Antenna Array[J]. IEEE Transactions on Signal Processing, 2021, 69: 5463-5478.

[160]Han Y, Jin S, Wen C K, et al. Channel Estimation for Extremely Large-Scale Massive MIMO Systems[J]. IEEE Wireless Communication Letters, 2020, 9(5): 633 - 637.

[161]Liu, Z. Wang, J. Xu et al., "Near-field Communications: A Tutorial Review, " IEEE Open Journal of the Communications Society., vol. 4, pp. 1999-2049, Aug. 2023.

[162]Y. Liu, J. Xu, Z. Wang et al., "Near-field Communications: What Will Be Different? " arXiv preprint arXiv:2303.04003, 2023.

[163]L. Wei, C. Huang et al., "Multi-User Holographic MIMO Surfaces: Channel Modeling and

Spectral Efficiency Analysis," in IEEE Journal of Selected Topics in Signal Processing, vol. 16, no. 5, pp. 1112-1124, Aug. 2022.

[164]L. Wei, C. Huang et al., "Tri-Polarized Holographic MIMO Surfaces for Near-Field Communications: Channel Modeling and Precoding Design," IEEE Transactions on Wireless Communications.

[165]H. Jiang et al., `` Large-Scale RIS Enabled Air-Ground Channels: Near-Field Modeling and Analysis," IEEE Trans. Wireless Commun.,

[166]H. Jiang et al., ``Physics-based 3D end-to-end modeling for double-RISs assisted non-stationary UAV-to-ground communication channels," IEEE Trans. Commun., vol. 71, no. 7, pp. 4247-4261, July 2023.

[167]B. Xiong et al., ``A 3D non-stationary MIMO channel model for reconfigurable intelligent surface auxiliary UAV-to-ground mmWave communications," IEEE Trans. Wireless Commun., vol. 21, no. 7, pp. 5658-5672, July 2022.

[168]B. Xiong et al., ``A statistical MIMO channel model for reconfigurable intelligent surface assisted wireless communications," IEEE Trans. Commun., vol. 70, no. 2, pp. 1360-1375, Feb. 2022.

[169]H. Jiang et al., ``Hybrid far- and near-field modeling for reconfigurable intelligent surface assisted V2V channels: A sub-array partition based approach," IEEE Trans. Wireless Commun., vol. 22, no. 11, pp. 8290-8303, Nov. 2023.

[170]H. Jiang et al., ``A general wideband non-stationary stochastic channel model for intelligent reflecting surface-assisted MIMO communications," IEEE Trans. Wireless Commun., vol. 20, no. 8, pp. 5314-5328, Aug. 2021.

[171]H. Jiang et al., ``Three-dimensional geometry-based stochastic channel modeling for intelligent reflecting surface-assisted UAV MIMO communications," IEEE Wireless Commun. Lett., vol. 10, no. 12, pp. 2727-2731, Dec. 2021.

[172]B. Xiong et al., ``Reconfigurable intelligent surface auxiliary mmWave communication: What if LoS path exists?" IEEE Wireless Commun. Lett., vol. 12, no. 2, pp. 247-251, Feb. 2023.

[173]N. Agrawal, E. Tohidi, R. L. G. Cavalcante, and S. Stanczak, "Towards Bridging the Gap between Near and Far-Field Characterizations of the Wireless Channel", IEEE International Conference on Communications (ICC), Denver, USA, June 2024.

[174] Cui M, Dai L. Channel estimation for extremely large-scale MIMO: Far-field or near-field?[J]. IEEE Transactions on Communications, 2022, 70(4): 2663-2677.

[175] Zhang X, Zhang H, Eldar Y C. Near-field sparse channel representation and estimation in 6G wireless communications[J]. IEEE Transactions on Communications, 2023.

[176]Zhang X, Yang Z, Zhang H, et al. Near-field channel estimation for extremely large-scale array communications: A model-based deep learning approach [J]. IEEE Communications Letters, 2023, 27(4):1155-1159.

[177]Li W, Yin H, Qin Z, et al. Wavefront Transformation-based Near-field Channel Prediction for Extremely Large Antenna Array with Mobility[J]. arXiv preprint arXiv:2312.02175, 2023.

[178]Yue S, Zeng S, Liu L, Di B. Channel estimation for holographic communications in hybrid near-far field [C]//2023 IEEE Global Communications Conference (GLOBECOM). Kuala Lumpur, Malaysia: IEEE, 2023: 1-6.

[179]Lu L, Ma K, Wang Z. Block-dominant compressed sensing for near-field communications: Fundamentals, solutions and future directions[J]. arXiv preprint arXiv: 2403.12369, 2024.

[180]Wu H, Lu L, Wang Z. Near-field channel estimation in dual-band XL-MIMO with side information-assisted compressed sensing[J]. arXiv preprint arXiv: 2403.12620, 2024.

[181]Guo X, Chen Y, Wang Y. Compressed channel estimation for near-field XL-MIMO using triple parametric decomposition[J]. IEEE Transactions on Vehicular Technology, 2023, 72(11): 15040-15045.

[182]Chen Y, Wang Y, Wang Z, et al. Angular-Distance Based Channel Estimation for Holographic MIMO[J]. arXiv preprint arXiv:2311.15158, 2023

[183]Lei H, Zhang J, Xiao H, et al. Channel Estimation for XL-MIMO Systems with Polar-Domain Multi-Scale Residual Dense Network[J]. IEEE Transactions on Vehicular Technology, 2023.

[184]Shi X, Wang X, Tan J, Wang J. Sparse estimation for XL-MIMO with unified LoS/NLoS representation[C]// 2024 IEEE International Conference of Communication (ICC). Denver, USA: IEEE, 2024.

[185]Jin Y, Zhang J, Huang C, et al. Multiple residual dense networks for reconfigurable intelligent surfaces cascaded channel estimation[J]. IEEE Transactions on Vehicular Technology, 2021, 71(2): 2134-2139

[186]Xu B, Zhang J, Du H, et al. Resource allocation for near-field communications: Fundamentals, tools, and outlooks[J]. arXiv preprint arXiv:2310.17868, 2023.

[187]Zhang J, Zhang J, Han Y, et al. Average spectral efficiency for TDD-based non-stationary XL-MIMO with VR estimation[C]// 2022 14th International Conference on Wireless Communications and Signal Processing (WCSP). Nanjing, China: IEEE, 2022: 973-977.

[188]Tian J, Han Y, Jin S, et al. Low-overhead localization and VR identification for subarray-based ELAA systems[J]. IEEE Wireless Communications Letters, 2023, 12(5): 784-788.

[189]Han Y, Jin S, Wen C K, et al. Localization and channel reconstruction for extra large RIS-assisted massive MIMO systems[J]. IEEE Journal of Selected Topics in Signal Processing, 2022, 16(5): 1011-1025.

[190]Liu D, Wang J, Li Y, et al. Location-based visible region recognition in extra-large massive MIMO systems[J]. IEEE Transactions on Vehicular Technology, 2023, 72(6): 8186-8191.

[191]Zhang H, Shlezinger N, Guidi F, et al. Beam focusing for near-field multi-user MIMO communications[J]. IEEE Transactions on Wireless Communications, 2022, 21(9): 7476-7490.

[192]Zhang H, Shlezinger N, Guidi F, et al. 6G wireless communications: from far-field beam-steering to near-field beam-focusing[J]. IEEE Communications Magazine, 2023, 61(4): 72-77.

[193]Ramezani P, Kosasih A, Irshad A, et al, Exploiting the depth and angular domains for massive near-field spatial multiplexing[J]. IEEE BITS the Information Theory Magazine, 2023.

[194]Wang J, Zhang X, Shi X, Song J. Higher spectral efficiency for mmWave MIMO: Enabling techniques and precoder designs [J]. IEEE Communications Magazine. 2021, 59(4):116-22.

[195]Gao F, Wang B, Xing C, et al. Wideband beamforming for hybrid massive MIMO terahertz communications[J]. IEEE Journal on Selected Areas in Communications, 2021, 39(6): 1725-1740.

[196]Dai L, Tan J, Chen Z, et al. Delay-phase precoding for wideband THz massive MIMO[J]. IEEE Transactions on Wireless Communications, 2022, 21(9): 7271-7286.

[197]Wang Z, Mu X, Liu Y. Beamfocusing optimization for near-field wideband multi-user communications[J]. arXiv preprint arXiv: 2306.16861, 2023.

[198]Wang Z, Mu X, Liu Y, et al. TTD configurations for near-field beamforming: Parallel, serial, or hybrid?[J]. arXiv preprint arXiv: 2309.06861, 2023.

[199]Xu B, Zhang J, Li J, et al. Jac-PCG based low-complexity precoding for extremely large-scale MIMO systems[J]. IEEE Transactions Vehicular Technology, 2023.

[200]Li X, Wang X, Hou X, et al. RIS-aided Mega MIMO: achieving orthonormal spatial multiplexing with adaptive aperture [C]// 2022 IEEE Global Communications Conference (GLOBECOM) Workshops. Rio de Janeiro, Brazil: IEEE, 2022: 692-698.

[201]X. Tian, N. Gonzalez-Prelcic and R. W. Heath, "Variable beamwidth near field codebook design for communications aided by a large scale RIS," in Proc. IEEE GLOBECOM, Kuala Lumpur, Malaysia, Dec. 2023.

[202]V. Jamali, G. C. Alexandropoulos, R. Schober, and H. V. Poor, "Low-to-zero-overhead IRS reconfiguration: Decoupling illumination and channel estimation," IEEE Commun. Letters, vol. 26, no. 4, pp. 932-936, 2022.

[203]Zheng F, Yu H, Wang C, et al. Extremely large-scale array systems: Near-filed codebook design and performance analysis[J]. arXiv preprint arXiv:2306.01458, 2023.

[204]Li X, Wang X, Hou X, et al. Two-Step Beamforming Scheme for Large-Dimension Reconfigurable Intelligent Surface[C]//2022 IEEE 95th Vehicular Technology Conference:(VTC2022-Spring). Helsinki, Finland: IEEE, 2022: 1-5.

[205]Wang F, Wang X, Li X, et al. Ring-type codebook design for reconfigurable intelligent surface near-field beamforming[C]//2022 IEEE 33rd Annual International Symposium on Personal, Indoor and Mobile Radio Communications (PIMRC). Kyoto, Japan: IEEE, 2022: 391-396.

[206]Zhang Y, Di B, Zhang H, et al. Codebook design for large reconfigurable refractive surface enabled holographic MIMO systems[C]// 2022 IEEE Global Communications Conference (GLOBECOM). Rio de Janeiro, Brazil: IEEE, 2022: 639-644.

[207]Zhang Y, Di B, Zhang H, et al. Near-far field beamforming for holographic multiple-input multiple-output[J]. Journal of Communications and Information Networks, 2023, 8(2): 99-110.

[208]Zhang S, Zhang Y, and Di B. Near-far field codebook design for IOS-aided multi-user communications[C]// 2023 IEEE Global Communications Conference(GLOBECOM). Kuala Lumpur, Malaysia: IEEE, 2023.

[209]Zhang Y, Wu X, You C. Fast near-field beam training for extremely large-scale array[J]. IEEE Wireless Communications Letters, 2022, 11(12): 2625-2629.

[210]Wu X, You C, Li J, et al. Near-field beam training: Joint angle and range estimation with DFT codebook[J]. arXiv preprint arXiv:2309.11872, 2023.

[211]Wu C, You C, Liu Y, et al. Two-stage hierarchical beam training for near-field communications[J]. IEEE Transactions on Vehicular Technology, 2023: 1-13.

[212]Lu Y, Dai L. Hierarchical beam training for extremely large-scale MIMO: From far-field to near-field[J]. IEEE Transactions on Communications, 2023.

[213]Shi X, Wang J, Sun Z, Song J. Spatial-chirp codebook-based hierarchical beam training for extremely large-scale massive MIMO [J]. IEEE Transactions on Wireless Communications, 2023.

[214]M. Cui, L. Dai, Z. Wang, S. Zhou and N. Ge, "Near-Field Rainbow: Wideband Beam Training for XL-MIMO," in IEEE Transactions on Wireless Communications, vol. 22, no. 6, pp. 3899-3912, June 2023, doi: 10.1109/TWC.2022.3222198.

[215]Liu W, Ren H, Pan C, et al. Deep learning based beam training for extremely large-scale massive MIMO in near-field domain[J]. IEEE Communications Letters, 2022, 27(1): 170-174.

[216]Liu W, Pan C, Ren H, et al. Low-overhead beam training scheme for extremely large-scale RIS in near field[J]. IEEE Transactions on Communications, 2023, 71(8): 4924-4940.

[217]Wu Z, Dai L. Multiple access for near-field communications: SDMA or LDMA?[J]. IEEE Journal on Selected Areas in Communications, 2023, 41(6): 1918-1935.

[218] N. Agrawal, E. Tohidi, R. L. G. Cavalcante, and S. Stanczak, “Towards Bridging the Gap between Near and Far-Field Characterizations of the Wireless Channel”, IEEE International Conference on Communications (ICC), Denver, USA, June 2024.

[219]Ding Z. Resolution of near-field beamforming and its impact on NOMA[J]. arXiv preprint arXiv:2308.08159, 2023.

[220]Zuo J, et al. Non-orthogonal multiple access for near-field communications[J]. arXiv preprint arXiv:2308.08159, 2023.

[221]Ding Z, Schober R, Poor H. V. NOMA-based coexistence of near-field and far-field massive MIMO communications[J]. IEEE Wireless Communications Letters, 2023, 12(8): 1429-1433.

[222]Polyanskiy Y. A perspective on massive random-access[C]. IEEE International Symposium on Information Theory (ISIT), 2017: 2523-2527.

[223]Gao J, Wu Y, Li T, et al. Energy efficiency of MIMO massive unsourced random access with finite blocklength[J]. IEEE Wireless Communications Letters, 2023, 12(4): 743-747.

[224]Xie X, Wu Y, An J, et al. Massive unsourced random access: Exploiting angular domain sparsity[J]. IEEE Transactions on Communications, 2022, 70(4): 2480-2498.

[225]V. M. Baeza, "Multiuser non coherent massive mimo schemes based on dpsk for future communication systems," Tesis doct., Universidad Carlos III de Madrid, 2019.

[226]V. M. Baeza and A. G. Armada, "Noncoherent Massive MIMO," en Wiley 5G Ref: The Essential 5G Reference Online, Hoboken, NJ, USA: Wiley, 2019, pp. 1-28. doi: 10.1002/9781119471509.w5GRef027

[227]V. M. Baeza and A. G. Armada, "Performance and Complexity Tradeoffs of Several Constellations for Non Coherent Massive MIMO," en 2019 22nd International Symposium on Wireless Personal Multimedia Communications (WPMC), 2019, pp. 1-6. doi: 10.1109/WPMC48795.2019.9096091.

[228]You C, Zheng B, Mei D, et al. How to deploy intelligent reflecting surfaces in wireless network: BS-side, user-side, or both sides?[J]. Journal of Communications and Information Networks, 2021, 10(9): 2080-2084.

[229]Zheng B, Zhang R. IRS meets relaying: Joint resource allocation and passive beamforming optimization?[J]. IEEE Transactions on Communications, 2022, 70(4): 2663-2677.

[230]Feng J, Zheng B, You C, et al. Joint passive beamforming and deployment design for dual distributed-IRS aided communication[J]. IEEE Transactions on Vehicular Technology, 2023, 72(10): 13758-13763.

[231]Zheng B, You C, Zhang R. Double-IRS assisted multi-user MIMO: Cooperative passive

beamforming design[J]. IEEE Transactions on Wireless Communications, 2021, 20(7): 4513-4526.

[232]Zhao Y. Reconfigurable Intelligent Surface Constructing 6G Near-field Networks[J]. Authorea Preprints, 2024.

[233]3GPP(2020).Study on Channel Model for Frequencies from 0.5 to 100 GHz, V16.1.0.Tech. Rep. 38.901.

[234]3GPP. RP-234018, Channel Modelling Enhancements for 7-24 GHz. 3GPP TSG RAN Meeting #102, Edinburgh, UK, 11th – 15th December, 2023.

[235]A. Elzanaty, J. Liu, A. Guerra, F. Guidi, Y. Ma and R. Tafazolli. "Near and Far Field Model Mismatch: Implications on 6G Communications, Localization, and Sensing." ArXiv abs/2310.06604, 2023.

[236]A. Chen, L. Chen, Y. Chen, N. Zhao, and C. You, "Near-field positioning and attitude sensing based on electromagnetic propagation modeling," ArXiv, vol. abs/2310.17327, 2023. [Online]. Available: http://arxiv.org/abs/2310.17327.

[237]Chen A, Chen L, Chen Y, et al. Cramér-Rao bounds of near-field positioning based on electromagnetic propagation model[J]. in IEEE Transactions on Vehicular Technology, vol. 72, no. 11, pp. 13808-13825, Nov. 2023, doi: 10.1109/TVT.2023.3284658.

[238]Elzanaty A, Guerra A, Guidi F, et al. Towards 6G holographic localization: Enabling technologies and perspectives[J]. IEEE internet of things magazine, 2023.

[239]Q. Yang, A. Guerra, F. Guidi, et al. Near-field Localization with Dynamic Metasurface Antennas[C]. IEEE International Conference on Acoustics, Speech and Signal Processing (ICASSP). Rhodes Island, Greece: IEEE, 2023: 1-5.

[240]Abu-Shaban Z, Keykhosravi K, Keskin M F, et al. Near-field localization with a reconfigurable intelligent surface acting as lens [C]. 2021-IEEE International Conference on Communications. IEEE, 2021: 1-6.

[241]Elzanaty A, Guerra A, Guidi F, et al. Reconfigurable intelligent surfaces for localization: position and orientation error bounds [J]. IEEE Transactions on Signal Processing, 2021, 69: 5386-5402.

[242]D. X. Xia, X. Wang, J. Q. Han, et al. Accurate 2-D DoA Estimation Based on Active Metasurface With Nonuniformly Periodic Time Modulation [J]. IEEE Transactions on Microwave Theory and Techniques,2023, 71(8): 3424-3435

[243]Zhang X, Chen W, Zheng W, et al. Localization of near-field sources: a reduced-dimension MUSIC algorithm [J]. IEEE Communications Letters, 2018, 22(7): 1422-1425.

[244]O. Rinchi, A. Elzanaty and M. -S. Alouini, "Compressive Near-Field Localization for Multipath RIS-Aided Environments," in IEEE Communications Letters, vol. 26, no. 6, pp. 1268-1272, June 2022.

[245]X. Gan, C. Huang, Z. Yang, C. Zhong and Z. Zhang, "Near-Field Localization for Holographic RIS Assisted mmWave Systems," in IEEE Communications Letters, vol. 27, no. 1, pp. 140-144, Jan. 2023, doi: 10.1109/LCOMM.2022.3209570.

[246]A. Elzanaty, A. Guerra, F. Guidi, et al. Toward 6G Holographic Localization: Enabling Technologies and Perspectives[J]. IEEE Internet of Things Magazine, 2023, 6(3): 138-143.

[247]Abu-Shaban, Z. et al. Near-feld localization with a reconfgurable intelligent surface acting as lens. In ICC 2021-IEEE International Conference on Communications. 1–6 (IEEE, 2021).

[248]B. Wang, F. Gao, S. Jin, H. Lin, and G. Y. Li, "Spatial- and frequency- wideband effects in millimeter-wave massive MIMO systems," IEEE Trans. Signal Process., vol. 66, no. 13, pp. 3393 – 3406, Jul. 2018.

[249]H. Luo, F. Gao, H. Lin, S. Ma, and H. V. Poor, "YOLO: An efficient terahertz band integrated sensing and communications scheme with beam squint," IEEE Trans. Wireless Commun., pp. 1 – 1, Feb. 2024.

[250]H. Luo, F. Gao, W. Yuan, and S. Zhang, "Beam squint assisted user localization in near-field integrated sensing and communications systems," IEEE Trans. Wireless Commun., pp. 1 – 1, Oct. 2023.

[251]Z. Wang, X. Mu and Y. Liu, "Near-Field Integrated Sensing and Communications," in IEEE Communications Letters, vol. 27, no. 8, pp. 2048-2052, Aug. 2023, doi: 10.1109/LCOMM.2023.3280132.

[252]H. Wang and Y. Zeng, "SNR scaling laws for radio sensing with extremely large-scale MIMO," in Proc. ICC Workshops, Seoul, Korea, Republic of, 2022.

[253]H. Wang, Z. Xiao, Y. Zeng, "Cramer-rao bounds for near-field sensing with extremely large-scale MIMO." IEEE Trans. Signal Process, 2024, doi: 10.1109/TSP.2024.3350329.

[254]Boyer, Rémy. "Performance bounds and angular resolution limit for the moving colocated MIMO radar." IEEE Trans. Signal Process, 2010: 1539-1552.

[255]F. Liu, Y. Cui, C. Masouros, J. Xu, T. X. Han, Y. C. Eldar, and S. Buzzi, "Integrated sensing and communications: Toward dual-functional wireless networks for 6G and beyond," IEEE J. Sel. Areas Commun., vol. 40, no. 6, pp. 1728 – 1767, Jun. 2022.

[256]Z. Wang, X. Mu and Y. Liu, "Near-Field Velocity Sensing and Predictive Beamforming," arXiv:2311.09888, 2023.

[257]Feng J, Zheng B, You C, et al. Joint passive beamforming and deployment design for dual distributed-IRS aided communication[J]. IEEE Transactions on Vehicular Technology, 2023, 72(10): 13758-13763.

[258]Cong J, You C, Li J, et al. Near-field integrated sensing and communication: Opportunities and challenges[J]. arXiv preprint arXiv:2310.01342, 2023.

[259]You C, Zhang Y, Wu C, et al. Near-field beam management for extremely large-scale array communications[J]. arXiv preprint arXiv:2306.16206, 2023.

[260]A. Sakhnini, S. De Bast, M. Guenach, A. Bourdoux, H. Sahli, and S. Pollin, "Near-field coherent radar sensing using a massive MIMO communication testbed," IEEE Trans. Wireless Commun., vol. 21, no. 8, pp. 6256 – 6270, Feb. 2022.

[261]M. Lipka, S. Brückner, E. Sippel, and M. Vossiek, "On the Needlessness of Signal Bandwidth for Precise Holographic Wireless Localization," in 2020 17th European Radar Conference (EuRAD), 2021, pp. 202 – 205.

[262]Zhang H, Shlezinger N, Guidi F, et al. Near-field wireless power transfer for 6G Internet of everything mobile networks: Opportunities and challenges [J]. IEEE Communications Magazine, 2022, 60(3): 12-18.

[263]Z. Zhang, H. Pang, A. Georgiadis, C. Cecati. Wireless power transfer—An overview [J]. IEEE Trans. Ind. Electron, 2019, 66(2): 1044-1058.

[264]ZHANG R, HO C K. MIMO broadcasting for simultaneous wireless information and power

transfer [J]. IEEE Transactions on Wireless Communications, 2013, 12(5): 1989-2001.

[265]Huang Kama, Chen Xing, Liu Changjun The principle and technology of microwave wireless energy transmission [M] Beijing: Science Press, 2021.

[266]LI Long,ZHANG Pei,HAN Jiaqi,et al. Key Technologies of Microwave Wireless Power Transfer and Energy Harvesting Based on Electromagnetic Metamaterials(Invited)［J］. Acta Photonica Sinica,2021, 50(10):1016001

[267]J. Han, L. Li, T. J. Cui, et al., Adaptively smart wireless power transfer using 2-bit programmable metasurface [J]. IEEE Transactions on Industrial Electronics, 2022, 69(8): 8524-8534.

[268]X. Wu, et al. Multitarget wireless power transfer system strategy based on metasurface-holography multifocal beams [J]. IEEE Trans. Microwave Theory Tech. 2023, 71(8): 3479-3489.

[269]H. Xue, et al. Multitarget wireless power transfer system using metasurface for quasi-Bessel beams with large half power beam length [J]. IEEE Trans. Microwave Theory Tech. 2022, 70(10): 4449-4462.

[270]S. Zhang, H. Xue, S. Zhao, J. Han, L. Li, T. J. Cui. Generation and modulation of a two-dimensional Airy beam based on a holographic tensor metasurface [J]. Phys. Rev. Appl. 2022. 18(6): 064085.

[271]J. Zhou, et al. Metamaterials and metasurfaces for wireless power transfer and energy harvesting [J]. Proc. IEEE 2022, 110(1): 31-55.

[272]Atzori, Luigi, Antonio Iera, and Giacomo Morabito. The internet of things: A survey [J]. Computer networks 2010, 54(15): 2787-2805.

[273]Zhang, Xuanming, Haixia Liu, and Long Li. Tri-band miniaturized wide-angle and polarization-insensitive metasurface for ambient energy harvesting [J]. Applied physics letters, 2017, 111(7).

[274]Du, Zhi-Xia, and Xiu Yin Zhang. High-efficiency single-and dual-band rectifiers using a complex impedance compression network for wireless power transfer [J]. IEEE Transactions on industrial electronics, 2017, 65(6): 5012-5022.

[275]Chang, Mingyang, et al. Metamaterial Adaptive Frequency Switch Rectifier Circuit for Wireless Power Transfer System [J]. IEEE Transactions on Industrial Electronics 2022, 70(10): 10710-10719.

[276]Li, Long, et al. Compact dual-band, wide-angle, polarization-angle-independent rectifying metasurface for ambient energy harvesting and wireless power transfer [J]. IEEE transactions on microwave theory and techniques 2020, 69(3): 1518-1528.

[277]Wang, X., Han, J.Q., Li, G.X. et al. High-performance cost efficient simultaneous wireless information and power transfers deploying jointly modulated amplifying programmable metasurface [J]. Nat. Commun. 2023, 14, 6002.

[278]H. X. Liu, Y. C. Li, F. J. Cheng, X. Wang, M. Y. Chang, H. Xue, S. Zhang, J. Q. Han, G. X. Li, L. Li, T. J. Cui, Holographic Tensor Metasurface for Simultaneous Wireless Powers and Information Transmissions Using Polarization Diversity [J]. Advance Functional Materials, 2023, 2307806.

[279]T. S. Rappaport, Wireless communications: Principles and practice, 2/E. Pearson Education India, 2010.

[280]A. Goldsmith, Wireless communications. Cambridge university press, 2005.

[281]Le, Anh M., Linh H. Truong, Toan V. Quyen, Cuong V. Nguyen, and Minh T. Nguyen T. Nguyen. "Wireless power transfer near-field technologies for unmanned aerial vehicles (UAVs): A review." EAI Endorsed Transactions on Industrial Networks and Intelligent Systems 7, no. 22 (2020): e5-e5.

[282]H. Lyu, J. Wang, J.-H. La, J. M. Chung, and A. Babakhani, "An energy-efficient wirelessly powered millimeter-scale neurostimulator implant based on systematic codesign of an inductive loop antenna and a custom rectifier," IEEE transactions on biomedical circuits and systems, vol. 12, no. 5, pp. 1131 – 1143, 2018.

[283]B. J. DeLong, A. Kiourti, and J. L. Volakis, "A radiating near-field patch rectenna for wireless power transfer to medical implants at 2.4 ghz," IEEE Journal of Electromagnetics, RF and Microwaves in Medicine and Biology, vol. 2, no. 1, pp. 64 – 69, 2018.

[284]R. Narayanamoorthi, A. Vimala Juliet, B. Chokkalingam, S. Padmanaban, Z. M. Leonowicz et al., "Class e power amplifier design and optimization for the capacitive coupled wireless power transfer system in biomedical implants," Energies, vol. 10, no. 9, pp. 1 – 20, 2017.

[285]J. J. Casanova, Z. N. Low, and J. Lin, "Design and optimization of a class-e amplifier for a loosely coupled planar wireless power system," IEEE Transactions on Circuits and Systems II: Express Briefs, vol. 56, no. 11, pp. 830 – 834, 2009.

[286]G. Bhargava, P. K. Rath, and S. Majumdar, "Gan-based class-f power amplifier for 5g applications," in 2022 IEEE Microwaves, Antennas, and Propagation Conference (MAPCON), 2022, pp. 1444 – 1449.

[287]G. Bhargava and S. Majumdar, "Highly Linearized GaN HEMT Based Class E/F3 Power Amplifier," 2021 Devices for Integrated Circuit (DevIC), Kalyani, India, 2021, pp. 564-568, doi: 10.1109/DevIC50843.2021.9455844.

[288]S. C. Cripps et al., RF power amplifiers for wireless communications. Artech house Norwood, MA, 2006, vol. 250.

[289]Cree GaN-HEMT Datasheet, “ Cree CG2H40010F packaged discrete transistor, ” 22-April-2022, https://assets.wolfspeed.com/uploads/2020/12/CG2H40010.pdf.

[290]Gaurav Bhargava, Shubhankar Majumdar & Farid Medjdoub (2024) Importing Experimental Results via S2D Model in ADS Tool for Power Amplifier Design, IETE Journal of Research, DOI: 10.1080/03772063.2024.2326588.

[291]Zhang Y, You C, Yuan W, et al. Joint Beam Scheduling and Power Allocation for SWIPT in Mixed Near-and Far-Field Channels[J]. arXiv preprint arXiv:2304.07945, 2023.

[292]Zhang Y, You C, Chen L, et al. Mixed Near- and Far-Field Communications for Extremely Large-Scale Array: An Interference Perspective[J/OL]. IEEE Communications Letters, 2023, 27(9): 2496-2500.

[293]Zhang Y, You C. SWIPT in Mixed Near- and Far-Field Channels: Joint Beam Scheduling and Power Allocation[J]. [J/OL] 2023, arXiv:2310.20186.

[294]Huang C, Hu S, Alexandropoulos G C, et al. Holographic MIMO Surfaces for 6G Wireless Networks: Opportunities, Challenges, and Trends[J]. IEEE Wireless Communications, 2020, 27(5): 118 – 125.

[295]Huang Q, Hu J, Zhao Y, Yang K. Holographic Integrated Data and Energy Transfer[J]. arXiv: 2404.04927, 2024.

[296]Sherman J. Properties of Focused Apertures in the Fresnel Region[J]. IRE Transactions on Antennas and Propagation, 1962, 10(4): 399–408.

[297]Poon A, Brodersen R, Tse D. Degrees of Freedom in Multiple-antenna Channels: A Signal Space Approach[J]. IEEE Transactions on Information Theory, 2005, 51(2): 523–536.

[298]Zhang Z, Chen J, Liu Y, Wu Q, He B, and Yang L, On the secrecy design of STAR-RIS assisted uplink NOMA networks[J]. IEEE Transactions on Wireless Communications, 2022, 21(12): 11207-11221 .

[299]Zhang H, Shlezinger N, et al, Beam focusing for near-field multiuser MIMO communications[J]. IEEE Transactions on Wireless Communications, 2022, 21(9): 7476-7490 .

[300]Anaya-Lopez G J, Gonzalez-Coma J P, et al, Spatial degrees of freedom for physical layer security in XL-MIMO[J]. in Proc. IEEE 95th Veh. Technol. Conf. (VTC-Spring), Helsinki, Finland, 2022.

[301]Z. Zhang, et al, "Physical layer security in near-field communications," arXiv: 2302.04189, 2023.

[302]Liu J, Yang G, Liu Y, and Zhou X, RIS empowered near-field covert communications, arXiv preprint arXiv:2401.13564, 2024, https://arxiv.org/abs/2401.13564.

[303]Li Long, Xue Hao, Feng Qiang. Research Progresses in Theory and Applications of Vortex Electromagnetic Waves[J]. Journal of Microwave Science, 2018,34 (02): 1-12. DOI: 10.14183/j.cnki.1005-6122.201802001.

[304]Kou N, Yu S, Li L. Generation of high-order Bessel vortex beam carrying orbital angular momentum using multilayer amplitude phase modulated surfaces in radiofrequency domain [J]. Applied Physics Express, 2017, 10: 016701.

[305]Hu Y, Zheng S, Jin X, et al. Simulation of orbital angular momentum radio communication systems based on partial aperture sampling receiving scheme[J]. IET Microwaves, Antennas & Propagation, 2016, 10(10): 1043 – 1047.

[306]Yan Shi, Ting Ting Hu, Zan Kui Meng, Quan Wei Wu, Tie Jun Cui. Demodulation method of orbital angular momentum vortex wave by few fields sampled on an extremely small partial aperture in radiation region [J]. Appl. Phys. Rev. 1, 2023, 10 (3): 031418.

[307]Ding W, Yang G, Liu J, Liang Y.-C., Near-field wide-band intelligent beamforming based on deep reinforcement learning[J]. submitted to IEEE Transactions on Communications, Jan. 2024.

[308]Deepa N P, Sudha K L. Investigation of inter and intra chip wireless channel modelling[C]// 2017 International Conference on Computing Methodologies and Communication (ICCMC). Erode:IEEE, 2017: 657-662.

[309]Dhillon A S, Melanson F, Liboiron-Ladouceur O. Intra-Chip Wireless Communication using RF On-Chip Antennas in Silicon Photonics[C]//2023 Photonics North (PN). Montreal: IEEE,2023:1-2.

[310]Al-Alem Y, Kishk A A, Shubair R M. Employing EBG in Wireless Inter-chip Communication Links: Design and Performance[C]//2020 IEEE International Symposium on Antennas and Propagation and North American Radio Science Meeting. Montreal:IEEE,2020:1303-1304.

[311]Paudel B, Li X J. A Terahertz On-Chip Antenna for Intra-chip Wireless Communications[C] //2022 IEEE Conference on Antenna Measurements and Applications (CAMA), Guangzhou:IEEE, 2022: 1-3.

[312]Cheema H M, Shamim A. The last barrier: on-chip antennas[J]. IEEE Microwave Magazine,

2013,14(1): 79-91.

[313]Narde R S, Venkataraman J, Ganguly A. Disc-Loaded, Vertical Top-Hat Monopole Antenna at 225 GHz for On-Chip Wireless Communications[C]//2019 IEEE International Symposium on Antennas and Propagation and USNC-URSI Radio Science Meeting. Atlanta:IEEE,2019:1883-1884.

[314]Liu Wenliang, Yi Chupeng, Liu Xin et al. On chip antennas for 6G wireless communication based on GaN technology [C]//Chinese Electronics Society. Compilation of papers at the National Microwave and Millimeter Wave Conference in 2023 (II). Xi'an University of Electronic Science and Technology, 2023:3.

[315]A. Fazzi et al., "3D Capacitive Interconnections with Mono- and Bi-Directional Capabilities," 2007 IEEE International Solid-State Circuits Conference. Digest of Technical Papers, San Francisco, CA, USA, 2007, pp. 356-608

[316]C. Lee, J. Park, J. Y oo, and C. Park, "Study of the coil structure for wireless chip-to-chip communication applications," Prog. Electromagn.Res. Lett., vol. 38, pp. 127–136, Mar. 2013.

[317]C. Lee, J. Park and C. Park, "Zigzag-Shaped Coil Array Structure for Wireless Chip-to-Chip Communication Applications," in IEEE Transactions on Electron Devices, vol. 61, no. 9, pp. 3245-3251, Sept. 2014

[318]S. Hwangbo, Y. -K. Yoon and A. B. Shorey, "Millimeter-Wave Wireless Chip-to-Chip (C2C) Communications in 3D System-in-Packaging (SiP) Using Compact Through Glass Via (TGV)-Integrated Antennas," 2018 IEEE 68th Electronic Components and Technology Conference (ECTC), San Diego, CA, USA, 2018, pp. 2074-2079.

[319]Y. Jiang, F. Gao, and S. Jin, "Electromagnetic Property Sensing: A New Paradigm of Integrated Sensing and Communication," arXiv e-prints, p. arXiv:2312.16428, Dec. 2023.

List of Terms and Abbreviations

3GPP	3rd Generation Partnership Project
AoA	Angle of Arrival
ASPP	Atrous spatial pyramid pooling
ASPP-RDN	Atrous spatial pyramid pooling-based residual dense network
BS	base stations
C&S	communication and sensing
CAP	Continuous-aperture
CE	channel estimation
CIR	Channel Impulse Response
CNFFFT	Spherical near-field to Far-Field Transformation
CoA	Curvature of Arrival
CRBs	Cramer-Rao Bounds
CS	compressive sensing
CSI	Channel State Information
DC	direct current
DFT	discrete Fourier transform
D-MIMO	distributed MIMO
DoFs	degrees of freedom
DRL	deep reinforcement learning
EBG	Electromagnetic bandgap
EDoFs	effective DoFs
EH	energy harvesting
ELAA	Extremely large-scale antenna array
EM	Electromagnetic
FFT	Fast Fourier Transform
FRFT	Fractional Fourier Transform
FRFT	fractional Fourier Transform
FSK	frequency-shift keying
GBSM	Geometry-based Stochastic Channel Model
GMMV	generalized multiple measurement vectors
GS	GerchbergSaxton
HMIMO	holographic MIMO
ID	information decoding
IRS	intelligent reflecting surface
ISAC	integrated sensing and communication
ISI	inter-symbol interference
ITU	International Telecommunication Union
ITU-R WP5D	International Telecommunication Union's 5D Working Group on

	Wireless Communications
IUI	inter-user interference
LDMA	location division multiple access,
LNA	low noise amplifier
LoS	line-of-sight
MA	Movable Antenna
Massive IoT	Massive Internet of things
MCP	multi-chip packaging
MEMS	microelectromechanical system
MHCM	Map-based Hybrid Channel Model
MIIT	Ministry of Industry and Information Technology
MIMO	Multiple-Input-Multiple-Output
MISO	multiple-input-single-output
mMTC	massive machine-type communications
mmWave	Millimeter wave
MPT	Microwave Power Transfer
MRC	Maximum Ratio Combining
MRT	（Maximum Ratio Transmission，）
NFC	Near-field Communications
NF-JCEL	near field joint channel estimation and localization
NLoS	non-line-of-sight
NMSE	normalized mean-square error
NOC	network-on-chip
NOMA	Non-Orthogonal Multiple Access
NUSW	non-uniform spherical wave
OAM	Orbital Angular Momentum
OFDM	Orthogonal Frequency Division Multiplexing
OMA	Orthogonal Multiple Access
OMP	Orthogonal Matching Pursuit
OTFS	orthogonal time frequency space
PA	power amplifier
PAA	phased array antenna
PAS	power angular spectrum
PCB	Printed Circuit Board
PD-OMP	power-diffusion-aware orthogonal matching pursuit algorithm
PEB	positioning error bound
PLS	Physical Layer Security
PLS	power location spectrum
PMI	Precoding Matrix Indicator
P-MRDN	polar-domain multiple residual dense network
P-MSRDN	polar-domain multi-scale residual dense network

P-OMP	polar-domain orthogonal matching pursuit
PT	polar-domain transform
RB	resource block
RCS	radar cross section
RDN	residual dense network
RF	radio frequency
RIS	Reconfigurable Intelligent Surface
rKA	randomized Kaczmarz
RMSE	root mean square error
RSS	received signal strength
RTC	ring-type codebook
SDMA	spatial division multiple access,
SE	spectral efficiency
SIC	Successive Interference Cancellation
SIMO	single-input-multiple-output
SiP	System-in-Packaging
SNR	signal to noise ratio
SoC	System-on-a-Chip
SPD-MIMO	spatially discrete MIMO
SPIM	spatial path index modulation
SWIPT	Simultaneous Wireless Information and Power Transmission
SWSS	spatial wide-sense stationarity
TDoA	time difference of arrival
TGV	through glass via
THz	terahertz
ToA	Time of Arrival
ToF	time of flight
TPD	Triple Parametric Decomposition
TSV	through silicon via
TTD	true time delay
UCA	Uniform Circular Array
UCPA	uniform circular planar array
ULA	uniform linear array
UM-MIMO	ultra-massive multiple-input-multiple-output
UPW	uniform plane wave
URA	Unsourced random access
USW	uniform spherical wave
VNA	Vector Network Analyzer
VNAs	Vector Network Analyzers
VR	visibility region

WEH	Wireless Energy Harvesting
WMMSE	weighted minimum mean square error
WPBC	wireless-powered backscatter communication
WPCN	wireless-powered communication networks
WPT	Wireless Power Transfer
WRC-23)	World Radiocommunication Conference 2023
XL-arrays	extremely large-scale arrays
XL-IRS	extremely large-scale IRS
XL-MIMO	Extremely Large-Scale MIMO
XL-RIS	Extremely Large-Scale RIS